UNIVERSIDAD DE GRANADA

PROGRAMA DE DOCTORADO EN FÍSICA Y MATEMÁTICAS

OUTFLOWS IN LOW LUMINOSITY ACTIVE GALACTIC NUCLEI

Laura Hermosa Muñoz

Supervisors:

Dr. Isabel Márquez Pérez
Dr. Sara Cazzoli

INSTITUTO DE ASTROFÍSICA DE ANDALUCÍA

CONSEJO SUPERIOR DE INVESTIGACIONES CIENTÍFICAS

September, 2022

"She made broken look beautiful and strong look invincible. She walked with the Universe on her shoulders and make it look like a pair of wings."

by Ariana Dancu

"Lunática creciente, loca menguante, con el desequilibrio nuevo y la desorientación llena. No le faltaba ni una fase lunar."

by Rosa Muro

"Happiness can be found, even in the darkest times, if one only remembers to turn on the light."

by A.P.W.B. Dumbledore

"It is our choices, Harry, that show what we truly are, far more than our abilities."

by J.K. Rowling

"En lo más profundo del invierno finalmente aprendí que en mi interior habitaba un verano invencible."

by A. Camus

"Never once had they opened the door which leads to the soul; never once did they dream of taking a blind leap into the dark."

by Henry Miller

A mi familia

Agradecimientos

Desde pequeña las estrellas han sido una guía de vida para no sentirme sola y recordar mi lugar en el mundo. Pronto aprendí las historias encerradas tras esos puntitos brillantes, y las convertí en alas que me arrastraron hasta este momento en el que estoy. El cielo ha guiado mi vida, y ahora estoy rodeada de otras estrellas que me dieron y dan luz. Personas que forman parte de este pequeño gran sueño, sin las que esta tesis no existiría...

A la **Osa Menor** siempre se le resta importancia, por ser la más pequeña, siempre detrás de la Osa Mayor, muchas veces escondida… Pero es la que señala al Norte, y la que marca la dirección incluso en los momentos de tormenta. Es la que demuestra que los segundos nunca han sido malos. Esto va por las que han sido mi Norte mientras estuve en el Sur, porque esta tesis es vuestra.

Isa:
Tengo una libreta llena de consejos, de lecciones de vida, de ciencia, y de palabras que calaron muy hondo. Gracias por la luz cuando las cosas se pusieron más oscuras, por tu puerta abierta, por enseñarme tanto y por **siempre** confiar en mí.

Sara:
El reloj a tu lado se pasó demasiado rápido, construyendo historia y recuerdos, con momentos muy nuestros. Gracias por tu apoyo, sinceridad, lecciones y tus manos abiertas **siempre** a cualquier coste.

Pepa:
Siempre has tenido la habilidad de ver el lado bueno, de cuidarme a mí y a los que te importan y de hacernos sentir parte de algo. Gracias por la guía en las formas de la ciencia, en cómo hacernos valer, y en la vida.
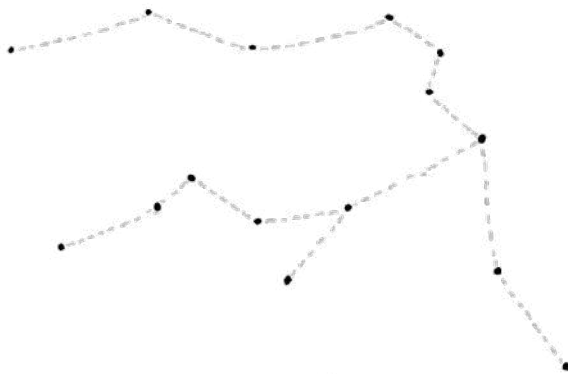
POLARIS
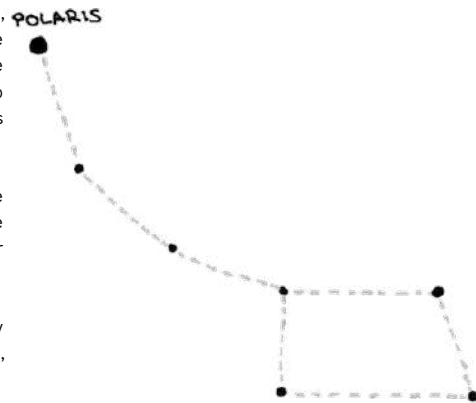
URSA MINOR

Aquarius para mí representa el comienzo de mi vida científica, con una pequeña enana perdida en una esquina. Y si ese comienzo tuvo lugar, fue por la gente que confió en mí y me enseñó, paso a paso, a caminar…

Mar, Ánxel, Koke, Visi, Diego:
Cada clase la convertisteis en un pequeño escalón al que me iba subiendo hasta llegar aquí. Gracias por vuestro empeño.

Luigi, Joaquín:
Fuisteis los primeros con los que descubrí lo que era la astrofísica, y los primeros que me hicisteis pensar en tantas cosas que daba por hecho. Gracias por ayudarme a dar el siguiente gran paso.

María Jesús:
Mi paso por Granada ha sido por ti, nunca te lo podré agradecer lo suficiente.

Giuseppina, Salvatore:
Voi mi avete insegnato cosa significa fare ricerca, essere cauti nell'analisi dei dati e dei resultati, mettere tutto in discussione, scrivere tutto… Grazie di cuore per queste preziose lezioni.

AQUARIUS

viii

En **Sagitario** está el agujero negro supermasivo de nuestra galaxia. Y al final de esto va la tesis, de los pequeños monstruos que habitan en el corazón mismo de las galaxias. Esta rama de la ciencia avanza día a día gracias a mucha gente, pero ha habido gente en particular gracias a la que he podido avanzar y terminar esto.

Omaira, Mirjana, Lorena:

Gracias por los consejos, por abrir camino y por verme como una más desde el principio. Habéis sido y sois una inspiración para saber lo que quiero en mi carrera en la ciencia.

Chony, Jaime, Bea:

Gracias por acompañarme durante todo este tiempo, por la ayuda cuando hizo falta, y por los consejos.
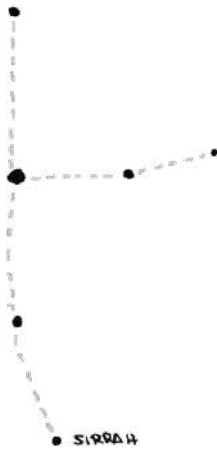
Armando, África, Mario:

MEGARA sin vosotros no existiría. Gracias por las enseñanzas y la ayuda.

Roberto, Mirko, Alice, James, Asia, Sim, Andrin:

Thank you for hosting me in Cambridge and for opening to me a new perspective into the AGN world. It was really helpful to learn from you.
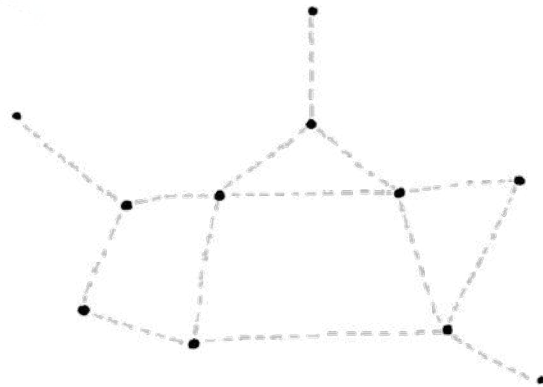
Andrómeda es una mujer fuerte, liberada, salvada por gente que la quiere, que ha sufrido, pero ahí sigue. Que ha llegado a ver la luz incluso en los momentos más oscuros. Su última estrella, es *Sirrah...*

Antonio, Salva, Feli:

Habéis sido Pegaso cuando me quedé sin alas, Oráculo cuando necesitaba consejo, y me habéis dado vida cada minuto que hemos estado juntos. Guardaré cada palabra, cada risa y cada mirada para cuando llegue el invierno. Un gracias se queda corto. Os quiero mucho.

Doran:

Quién nos hubiera dicho que estaríamos hoy donde estamos, tras años hablando por todos los rincones del instituto, y siempre acompañándonos por el camino. Esto no habría sido lo mismo sin ti.

Guille:

Si una cosa me ha enseñado el tiempo, es que el silencio a veces guarda los mejores regalos y, a veces, esconde maravillas. Tu estrella está más que merecida.

Leire:

Me has enseñado que todo son caminos, y que es tan válido seguirlos adonde lleven, como dar marcha atrás. Bendito el día en que nuestros pasos se cruzaron, persona vitamina.

Casiopea representa a la madre de Andrómeda, castigada en el cielo por creerse la más bella de entre mortales e inmortales. Un poco sufre lo que la ciencia, que a veces se cree superior a todas las demás ramas de conocimiento. Pero no sería nada si no hubiera gente preocupada por llevarla y defenderla ante el público. A lo largo de estos años, la divulgación me ha salvado la vida de muchas más formas de las que pudiera describir aquí, y ha sido gracias a muchísima gente.

Asociación Cielos Despejados (en especial a Llara, Belén y Andrés):

Mis primeros pinitos fueron interpretaciones del cielo de vuestra mano. Mil gracias.

Scenio (Nebesu, Arcadi, Adri, Alberto, Roberto, Ignacio, Pepelu, Jose Luis, Gisela, etc.):

Gracias por inspirarme día a día y por construir una comunidad tan guay como Scenio y ScenioTV.

Manu, Emilio:

Ni en mis mejores sueños hubiera imaginado poder tener la suerte y la oportunidad de aprender de vosotros de primera mano sobre lo que es la divulgación. Habéis sido fuente de inspiración desde el minuto uno que pisé el IAA, y siempre con una palabra amable y una mano amiga. Gracias por enseñarme a contar historias y a que dejarse llevar a veces está bien.

Lucía:

Lo que unió la astro que no lo separe nadie. Gracias por confiar en mí en tu gran aventura del Allande Stars y en todo lo que se vino (y vendrá) después. Una suerte para mí poder llamarte amiga.

Y por supuesto, a toda esa gente que me ha invitado a algún vídeo/charla/directo/podcast y a todos los que me dedicaron un ratito de sus vidas. Esto solo tiene sentido si hay alguien escuchando al otro lado.

SAGITTARIUS

ANDRÓMEDA

SIRRAH
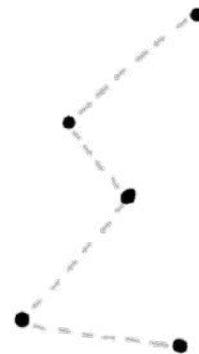
CASSIOPEIA
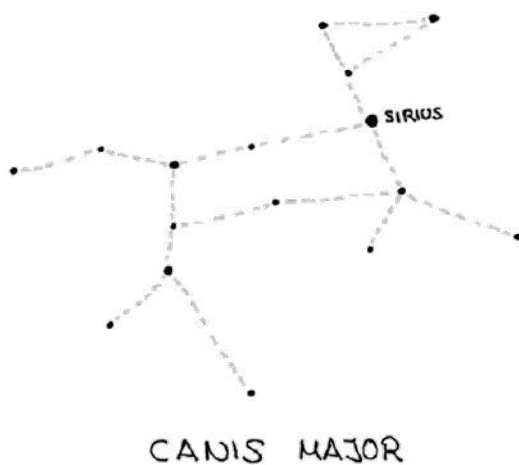
Canis Major es el fiel perro de caza que siempre acompaña a Orión, que está a su lado pase lo que pase. Lo mismo ocurre con la familia, la escogida y la que toca, que siempre son hogar donde volver.

Mamá, papá:
Gracias por vuestros desvelos para que pudiéramos cumplir nuestros sueños, por sacrificaros por nosotros y por poneros delante de lo que hiciera falta para protegernos. Esta tesis es vuestra, porque era un sueño que fue también vuestro. Os quiero.

Javi:
Ya hace mucho que no nos hacen falta palabras para entendernos. No sé que hubiera sido de mí sin ti. Te quiero.

Ángel, Charli, Miguel, Pablo, Mer, Cris, Marián, Sergio, Tere, Maite, tío Carlos, güelu, abuelitos, Tomás, Carlos, Javi, Ana, Marga, Pedro:
Hoy soy quien soy en gran parte gracias a vosotros que, un día, os parasteis a escuchar las historias de la "friki" de las estrellas.

Lau, Adri, Olaya, Vero, Raq, Sara:
Gracias por ser parte de mi familia escogida y por apoyarme en mis decisiones, a pesar de la distancia.

Lyra siempre está en lo más alto en los meses de verano. Esos meses de noches cortas pero que conocemos muy bien, las noches en las que me enamoré de la astronomía y por cómo empezó todo. Vega siempre como referencia, una de las estrellas más brillantes y fáciles de ver. Incluso tú, aunque normalmente yo sea tus ojos para mirar al cielo.

Solo que tú eres mis ojos para mirar a la vida. *Xuan*, gracias por acompañarme durante todo este tiempo, por recorrer conmigo la Vía Láctea, las nebulosas, las galaxias, las estrellas a golpe de láser, cámara y telescopio. Juntos hemos construido todo un nuevo Universo, nuestro camino de vida.

CienciaXL, Scenio, ScenioTV, Cielos Despejados, Tenerife, Granada, Tiedra, Ginebra… todo es gracias a ti. Y esta tesis, también.

Gracias por ser mi red cuando el salto parece vacío, y por siempre dar perspectiva. Te quiero.
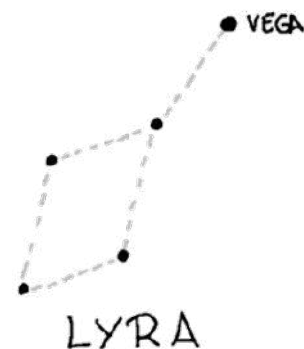
Me gustaría dar un gracias especial al Instituto de Astrofísica de Andalucía-CSIC y a todas las personas en él que han hecho de esta experiencia algo aún más especial. En primer lugar a toda la administración, recursos humanos, el equipo de dirección y gerencia por el apoyo en la burocracia y demás trámites. Y especialmente a Laly, Antonio Lorenzo, Paco, Estefanía, Teresa y demás predocs, postdocs y técnicos/as del IAA por haber ayudado a pasar mucho mejor estos años.

Y a mí *yo* de niña que soñaba con el cielo sin saber que de esto se podía hacer carrera, ¡enhorabuena, lo conseguimos!.

Abstract

This thesis is aimed to provide insights into the relevance of feedback processes in galaxies harbouring at its centre an Active Galactic Nucleus (AGN). Feedback is believed to impact the evolution of galaxies by regulating the star formation and AGN activity. In particular, these processes can be triggered by outflows, that are detected with various tracers related to different gas phases (e.g. ionised or hot gas). In this thesis, we focused on the exploration of the processes at the low end of the AGN luminosity function, in particular with Low-Ionisation Nuclear Emission-line Regions (LINERs). These objects are the largest AGN family in the Local Universe, representing more than 60% of the local population (Ho 2008). Their relative faintness make their detection and characterisation more difficult than for other AGN types, although their proximity gives these objects an advantage, since spatially resolved studies can be made. This is specially important for the characterisation of feedback processes, particularly in the search for outflows.

During the last 20 years, outflows have been detected in a variety of systems, from star-forming galaxies to AGNs. The increasing number of works dedicated to the study of feedback processes seem to conclude that outflows are ubiquitous in both types of galaxies. Many efforts now are dedicated to analysing their properties and evaluating their impact in the evolution of the host galaxy from pc to kpc-scales. However, in the case of AGNs their study has been mainly focused on luminous systems, where outflows are expected to be more powerful and thus easier to detect and characterise. Nevertheless, it remains unclear if outflows are also common or even ubiquitous in LINERs, as this AGN population has been largely unstudied.

In this thesis we address this topic with three different methodologies that will be described along the corresponding chapters.

Optical spectroscopy of type-2 LINERs. We first present the analysis of long-slit spectroscopic data for nine type-2 LINERs obtained with the Hubble Space Telescope (HST) and the Palomar Survey. This work complements the previous work by Cazzoli et al. (2018) on type-1 LINERs. The objectives are twofold: (i) detect a broad line region component in the Balmer emission lines, and (ii) search for outflows as a broad ($\sigma \leq 500\,\mathrm{km\,s^{-1}}$), blueshifted

component in the emission lines. We detected a broad component for 67% of the HST spectra and 25% of the Palomar spectra. As for the outflows, we found that 35% of the type-2 LINERs are good candidates to host them.

A search for ionised gas outflows in an Hα imaging atlas of nearby LINERs. We then systematically searched for outflows in a sample of 70 nearby LINERs by analysing the ionised gas distribution in these systems, using proprietary ALFOSC/NOT and archival HST narrow band imaging. We were able to identify the main morphologies of the Hα gas and detect possible outflows as extended gas for 32% of the objects. Afterwards, by combining imaging with kinematic data from the literature, we found that ~50% of the local LINERs host an outflow in different gas phases. These results indicated that outflows are common in low luminosity AGNs as LINERs.

Analysis of the candidate outflows in LINERs with MEGARA/GTC integral field spectroscopic data (IFS). Finally, we used IFS data to confirm or not the outflow candidates identified from the previous two works on a spatially-resolved basis. For that purpose we used MEGARA/GTC data of nine LINERs in three spectral bands in the optical range. We study as a first case the prototypical LINER NGC 1052 (complementing with proprietary MUSE/VLT data). We detected in this object an ionised gas outflow probably driven by the jet, propagating in a region of turbulent gas, and triggering kpc-scale bubbles.

Then we analysed the other eight objects, finding a kinematical signatures of an ionised gas outflow in four of these LINERs (i.e. 50%). The LINER NGC 4438 is the only object in our sample for which we found three resolved kinematical components in all the emission lines with the MEGARA data. These probe the gaseous disc and an outflow with a bubble-like structure, previously detected with high spatial resolution imaging.

Resumen

Esta tesis tiene como objetivo proporcionar información sobre la relevancia de los procesos de retroalimentación en galaxias que poseen en su centro un núcleo activo de galaxias (AGN en inglés). Se cree que los procesos de retroalimentación afectan a la evolución de las galaxias a través de la regulación de la formación estelar y de la actividad nuclear. En particular, estos procesos se pueden desencadenar por los llamados 'outflows', los cuales se detectan usando varios trazadores relacionados con las distintas fases del gas (por ejemplo, gas ionizado o caliente). En esta tesis nos centramos en la exploración de estos procesos en el límite inferior de luminosidad en los AGNs, en particular en las llamadas regiones nucleares de líneas de emisión de baja ionización (LINERs por sus siglas en inglés). Estos objetos son la familia más numerosa de AGNs que encontramos en el Universo Local, representando a más del 60% de la población local (Ho 2008). Su relativa debilidad hace que sean más difíciles de detectar y caracterizar que otros tipos de AGNs, aunque su proximidad les da la ventaja de permitir realizar estudios espacialmente resueltos. Esto aplica especialmente para el análisis de procesos de retroalimentación y, en particular, para la búsqueda de 'outflows'.

Durante los últimos 20 años se han detectado 'outflows' en una gran variedad de sistemas, tanto galaxias con formación estelar como en AGNs. El aumento del número de trabajos dedicados al estudio de procesos de retroalimentación parecen concluir que los 'outflows' aparecen de manera ubicua en los sistemas anteriormente mencionados. Hay muchos esfuerzos dedicados al análisis de sus propiedades y a evaluar su impacto en la evolución de la galaxia anfitriona en escalas de pc a kpc. Sin embargo, en el caso de los AGNs los estudios se han centrado en los sistemas más luminosos, donde se espera que los 'outflows' sean más poderosos y, por tanto, más fácil de detectar y caracterizar. Aún no está claro si los 'outflows' son también comunes, o incluso su presencia ubicua, en LINERs, ya que su presencia en esta población de AGNs ha sido en gran medida no explorada.

En esta tesis abordamos este tema utilizando tres metodologías distintas que se van describiendo en los capítulos.

Espectroscopía óptica de LINERs de tipo 2: Presentamos en primer lugar el análisis de datos de espectroscopía de rendija larga de nueve LINERs de tipo 2, obtenidos con el Tele-

scopio Espacial Hubble (HST) y de la muestra del Palomar. Este trabajo complementa al estudio anterior de Cazzoli et al. (2018) con LINERs de tipo 1. Los objetivos principales son dos: (i) detectar en las líneas de emisión de Balmer una componente ancha originada en la región de líneas anchas, y (ii) buscar indicadores de 'outflows' en las líneas de emisión como una componente ancha (σ' $500\,\mathrm{km\,s^{-1}}$) desplazada hacia el azul. Detectamos una componente ancha en las líneas de Balmer en el 67% de los espectros del HST y en el 25% de los espectros del Palomar. En cuanto a los 'outflows', encontramos que el 35% de los LINER de tipo 2 son buenos candidatos para albergarlos.

Una búsqueda de 'outflows' en gas ionizado en un atlas de imágenes de Hα de LINERs cercanos. A continuación, buscamos sistemáticamente 'outflows' en una muestra de 70 LINERs cercanos, analizando la distribución del gas ionizado en estos sistemas con imágenes de ALFOSC/NOT e imágenes de archivo del HST de banda estrecha. Pudimos identificar las principales morfologías del gas Hα y detectar posibles 'outflows' en forma de gas extendido en el 32% de los objetos. Después, combinando las imágenes con datos cinemáticos de la literatura, descubrimos que el 50% de los LINER locales tienen 'outflows' que se detectan en distintas fases del gas. Estos resultados indican que los 'outflows' son comunes en AGNs de baja luminosidad, como los LINERs.

Análisis de LINERs candidatos a tener 'outflows' con datos de espectroscopía de campo integral (IFS) con MEGARA/GTC. Por último, utilizamos los datos de IFS para confirmar o no los candidatos a 'outflows' identificados en los dos trabajos anteriores, pero esta vez resolviendo la emisión espacialmente. Para ello utilizamos los datos de MEGARA/GTC de nueve LINERs en tres bandas espectrales distintas en el rango óptico. Estudiamos como primer caso el prototípico LINER NGC 1052 (complementando con datos propios de MUSE/VLT). Detectamos en este objeto un 'outflow' en gas ionizado, probablemente impulsado por un 'jet', que se propaga en una región de gas turbulento provocando burbujas a escalas de kpc.

A continuación analizamos los otros ocho objetos de la muestra. Encontramos indicaciones cinemáticas de la presencia de 'outflows' de gas ionizado en cuatro de estos LINERs (es decir, el 50%). El LINER NGC 4438 es el único objeto de nuestra muestra para el que detectamos, con datos de MEGARA, tres componentes cinemáticas espacialmente resueltas en todas las líneas de emisión. Estas se relacionan con el disco de gas de la galaxia y con un 'outflow' con forma de burbuja, que ya había sido detectado anteriormente con imágenes de alta resolución espacial.

Table of contents

List of figures

List of tables

Chapter 1

Introduction

1.1 The Active Galactic Nuclei family

Active Galactic Nuclei (AGNs) are defined as very compact regions in the centre of some galaxies surrounding the supermassive black hole where large amounts of emission in all spectral bands are produced due to accretion processes. They basically consist on an accretion disc that feeds the supermassive black hole (SMBH), producing the emission of large amounts of energy in all the spectral bands. In these objects, the total released energy is larger and the spectral energy distribution (SED) different than any expected emission from stellar processes, which distinguish them as one of the most luminous objects in the Universe. The luminosity produced by the accretion is usually referred to as Eddington Luminosity or Eddington limit, which is defined as the maximum luminosity that a body can reach when the radiation acting outward and the gravitational force acting inward are balanced. The accretion is maintained as long as the gravitational force remains larger than the emitted radiation, allowing material to fall into the inner body (in this case, into the SMBH). Progressively, the higher the accretion rate the higher the luminosities of the AGNs (such as quasars; see Sect. 1.1.2) and viceversa (low Eddington luminosities for low-accreting AGNs; e.g. Low Ionisation Nuclear Emission-line Regions or LINERs).

The first AGNs to be discovered were Seyferts (see Sect. 1.1.2), named after Carl Seyfert who observed for the first time their optical spectra (Seyfert 1943). He detected strong and broad permitted and forbidden emission lines of unknown origin at that time. A few years later, the radio frequency domain started to be commonly used for analysing the Universe. Many radio sources were discovered, some of them with an optical counterpart also showing broad emission lines (see e.g. Baade & Minkowski 1954). These sources were initially named quasi-stellar objects, or quasars (Matthews & Sandage 1963; Schmidt 1963; Hazard
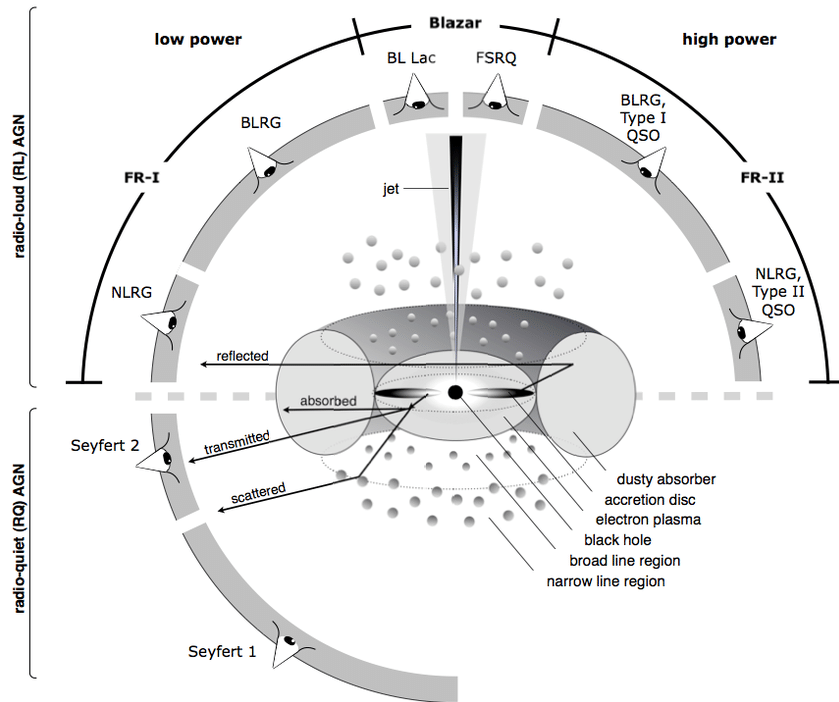
Fig. 1.1 Schematic view of an AGN under the Unified model (Beckmann & Shrader 2012).

et al. 1963), as they morphologically resembled to stellar-like objects. It was found that, in reality, the emission lines in the spectra of these sources were similar to those seen in nebulae, but considerably redshifted. This changed the interpretation of these objects as extragalactic, very luminous (in both radio and optical), compact objects. With time, more and more objects with peculiar spectra that could not be explained by stellar contributions (i.e. very strong non-thermal emission) were discovered. The great majority of them were not radio-active systems (Sandage 1965). Astronomers started to realise the similitude between the spectra of Seyferts and quasars, with broad, redshifted emission lines, but also about the differences in their spectra. This lead to the creation of models that aimed to explain the different observational characteristics of these systems (see e.g. Shields 1999).

1.1.1   The Unified Model of AGNs

Nowadays, all AGNs are believed to be well represented within the framework of what is called 'The Unified Model' (Antonucci 1993; Urry & Padovani 1995). This model relies on the idea that there are several common components in all AGNs, and the visible differences in the results derived from a variety of data sets simply come from the different orientations

of each object with respect to our line of sight (see Fig. 1.1, from Beckmann & Shrader 2012). The main components of AGNs, from the innermost to outermost regions, are:

- *Supermassive black hole* of masses larger than $10^6 M_\odot$ (Kormendy & Richstone 1995).

- *Accretion disc*: Circumnuclear structure formed by diffuse material in orbital motion around the SMBH that lies in the central parts of the galaxies. This diffuse material falls towards the central SMBH through the loss of gravitational energy, which is converted into electromagnetic radiation. They can have different sizes and thickness, as well as different column densities (see Netzer 2013). They are usually assumed to be optically thick and geometrically thin discs, although these characteristics may vary depending on the luminosity of the AGN (i.e. the accretion rate).

- *Torus*: A compact, dusty, obscuring toroidal structure with a total size of few parsecs, believed to be composed by dense, rotating clouds (Elitzur 2006). Their relative small sizes (i.e. 0.1 - 10 pc Netzer 2015) make it difficult to detect them, except for a few local cases (e.g. NGC 1068; García-Burillo et al. 2019), although their existence is inferred as they obscure the emission from the central regions from a certain point of view (see below). Its geometry and composition are still not clear, and there are multiple models that attempt to explain its structure based on the study of the SED specially in the mid-infrared (MIR) range (see González-Martín et al. 2019a,b, for a complete review on dusty torus models). It is a matter of debate if all AGNs have a torus, particularly for LINERs, as there are evidences in multiple wavelength ranges, such as variability on the ultraviolet (UV), that could be an indicator of the disappearance of this structure in the lowest luminous AGNs (Elitzur & Shlosman 2006; Müller-Sánchez et al. 2013; Hernández-García et al. 2014).

- *Broad Line Region* (BLR): Nuclear region found inside the torus formed by dense gas clouds ($\sim 10^{10}$ cm^{-3}, Netzer 2013) ionised by the SMBH where broad permitted emission lines (Full-Width at Half Maximum; FWHM > 1000-2000 km s^{-1}; Netzer 2015) are originated. This region is located very close to the SMBH (e.g. pc or sub-pc distances in high luminous AGNs), leading the clouds to rotate at very large velocities (~ 3000 km s^{-1}, Netzer 2013), thus broadening the emission lines.

- *Narrow Line Region* (NLR): Extended region of low-density ($\sim 10^4$ cm^{-3}; Netzer 2013), ionised gas clouds emerging from the innermost parts of the AGN towards distances of hundreds of parsecs. The NLR produces the emission of permitted, semi-forbidden and intense forbidden emission lines. These latter are a consequence of the low densities in this region, so that few collisions between atoms occur, and thus the forbidden

transitions are maintained enough time to form intense emission lines. In general the emission lines produced in this region are narrower than the ones produced in the BLR (Netzer 2013, 2015). It is believed that the NLR is stratified, such that the emission line widths are wider closer to the SMBH (i.e. their width is correlated with the level of ionisation of the different species), based on both optical and infrared observations (Netzer 2013). When this region is extended up to distances of several kpc or more, we refer to it as an extended narrow line region (ENLR).

- *Jet*: Collimated emission of hot plasma emerging from the central regions of the galaxy at very large distances, that can even surpass the size of the host galaxy. Jets are launched by collimated magnetic fields related to the accretion disc, and propagate through the medium at relativistic velocities. They can sometimes be detected on different wavelength ranges, such as in the optical (e.g. NGC 4486 or M 87), or in X-rays (e.g. NGC 0315, González-Martín et al. 2009). The majority of AGNs are radio-quiet (>90%; see Padovani et al. 2011 and references therein) but have relativistic jets. This motivated the recent work by Padovani (2017), who suggested the classification of AGNs as jetted or non-jetted instead of radio-loud versus radio-quiet.

Under this picture, the complex interplay between each component of the AGN generates distinctive features as analysed through imaging, spectroscopic or polarimetric techniques in various wavelength ranges (see Sect. 1.1.2). The understanding of the physical processes occurring in these objects, lead to an optical division of AGNs in two large groups depending on if a very broad component (also referred to as 'BLR component') is detectable or not in the Balmer emission lines (i.e. H$\alpha\lambda$6563Å or H$\beta\lambda$4861Å). If the central source is not obscured by the torus, we can detect in the nuclear spectrum of these sources very broad line profiles in Hα and/or Hβ. We classify them as **type-1 AGNs**. There are additional sub-categories for these type-1 AGNs, such as type-1.5, 1.8 or 1.9. They essentially differ on the relative intensities of the different components (narrow and broad) that model the emission lines. More specifically, type-1.5 have strong broad and narrow components, type-1.8 have strong narrow and weak broad components, and the same applies for type-1.9, but for them the broad component is not visible in Hβ.

On the contrary, if the central source is obscured by the torus, the optical spectrum will show only narrow line profiles in all the emission lines (FWHM $< 1000\,\mathrm{km\,s^{-1}}$; Netzer 2015), with no signatures of a broad component. In this case we classify them as **type-2 AGNs**. This group is divided into two classes, as for some type-2s there is a detection of a broad component with polarimetric measurements not detected with regular spectroscopy. These are the so-called *true* type-2 AGNs (Hawkins 2004). Their spectra have narrow emission

lines with no indications of broad components on the Balmer lines, and almost no X-ray absorption, which points towards an unobscured continuum (Elitzur 2006). However, the true-2 AGNs are often misclassified due to a poor data resolution or a lack of polarimetric information (Ramos Almeida et al. 2016; Bianchi et al. 2019a).

Under the old Unified Model, the mentioned differences are produced mainly due to orientation effects, such that the narrow emission lines come from the NLR, which is always visible as it extends out from the nuclear region, whereas the broad emission lines (coming from the BLR) are only visible when the AGN is oriented face-on. However, recent observations suggest that the variations between AGN types may be also a consequence of intrinsic differences on their nature (see Netzer 2015, for a review), such as on the structure and composition of the torus, or that some AGNs may lack any of the previous mentioned components, such as the torus in LINERs (see Sect. 1.1.3).

1.1.2 AGN types and differences

All the studies performed on active galaxies allowed us to distinguish between a variety of AGN types (see Fig. 1.1). The physical constraints between them, beyond their luminosity and orientation effects, are diffuse, but yet the main families are:

- *Quasars*: Their name comes from *quasi-stellar* objects (QSOs), as historically they were detected as star-like objects emitting in radio frequencies (Schmidt 1963; Hazard et al. 1963; Sandage 1965). In reality, they are the most luminous and powerful AGNs, typically found at large redshifts (maximum number of QSOs detected at z~2; Schmidt et al. 1995) and the majority of them are radio-quiet. The large distances together with their high luminosity make it difficult to detect the host galaxy.

- *Blazars*: Radio loud AGNs, highly variable, with a strong continuum and an associated jet. We can distinguish two main types in this category: BL-Lacs, characterised by showing a spectrum with no emission lines, as the jet is pointing towards the observer and obscures the AGN emission (see top-left panels in Fig. 1.2); and Flat Spectrum Radio Quasars (FSRQs) (Netzer 2015).

- *Seyferts*: High-luminosity AGNs named after Carl Seyfert, who first discovered them (Seyfert 1943). Their optical spectra shows intense high- and low-ionisation emission lines (see example in top-right panels of Fig. 1.2).

- *LINERs*: Low-luminosity AGNs characterised by showing relatively more intense low-ionisation emission lines than high-ionisation ones, contrary to more luminous AGNs

([Heckman 1980](#)). A typical spectrum of a LINER is illustrated on the bottom-left panel of Fig. [1.2](#). They will be further discussed on Sect. [1.1.3](#).

An example of each type is represented on Fig. [1.2](#), where we can see the redshift-corrected optical spectra of a variety of AGNs in comparison with a non-active galaxy. The blazar (top-left) has a flat spectrum with no particular features, whereas the quasar shows very broad and strong emission lines, particularly the very broad Hβ line. The differences between type-1s and type-2s are clearly appreciated in the right panels, where a very broad component is visible in the Balmer lines of the Seyfert-1 galaxy, in contrast to narrow profiles in the Seyfert-2. These AGNs have very intense high ionisation emission lines, such as [O III]$\lambda\lambda$4959,5007Å. This is in contrast to the LINER spectrum, in which low ionisation lines such as [N II]$\lambda\lambda$6548,6584Å or [S II]$\lambda\lambda$6716,6731Å are very intense and high ionisation lines are rather faint. In normal galaxies, the spectrum is dominated by the stellar emission, including emission coming from H II regions when there is on-going nuclear star formation. The variations on the continuum for every type are also noticeable, with the host galaxy contributing much more in LINERs (similar spectrum to the normal galaxy, differing on the presence of forbidden lines) and on the Seyfert-2 (edge-on AGN with the nuclear contribution obscured by the torus), and other variations (e.g. flat continuum in blazars, or a steep contribution towards the UV in type-1 AGNs).

The emission lines typically seen in the AGN spectra (see Fig. [1.2](#)) allow us also to characterise the physical conditions of the interstellar medium (ISM) in which they were produced. For example, the ratio between the [S II] doublet lines is used to estimate the electron density of the gas ([Osterbrock & Ferland 2006](#)), and the ratio between Hα and Hβ can be used to measure the galactic reddening ([Osterbrock & Ferland 2006](#)). Other emission line ratios are good tracers for identifying the main ionising source of the gas. For example in LINERs, the ratio between the [O I] 6300Å line, produced by ionisation of neutral gas, with respect to Hα is stronger than for more luminous AGNs or H II regions. By combining the fluxes of forbidden and Balmer emission lines[1], we can create the standard diagnostic diagrams (see Fig. [1.3](#)), *Baldwin, Phillips & Terlevich* or BPTs ([Baldwin et al. 1981](#); [Veilleux & Osterbrock 1987](#); [Kauffmann et al. 2003](#); [Kewley et al. 2006](#)). These classify the ionising source of the detected emission as produced by an AGN (Seyferts vs LINERs) or by star-forming processes. The advantage of these diagnostic diagrams is that they are reddening-independent thanks to the relatively nearness in wavelength of the used emission lines. There exist additional diagnostic diagrams based, for example, on infrared emission lines that are also

---

[1]When the spectral fitting of the emission lines require more than one component, the narrowest-one is used for these diagrams.
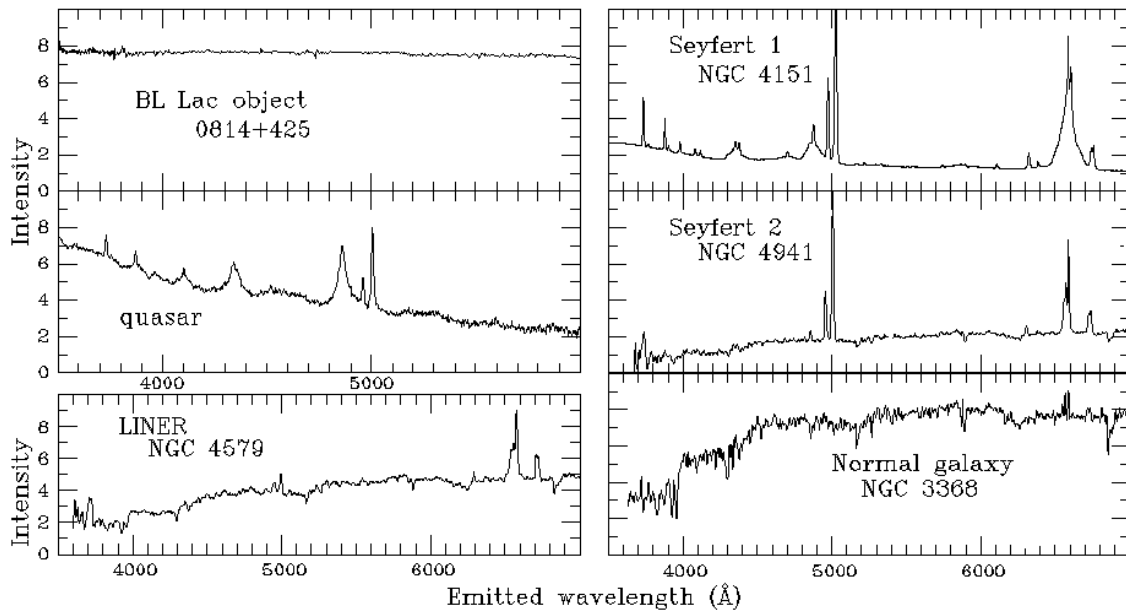
Fig. 1.2 Comparative of the redshift-corrected optical spectra for different active and non-active galaxies. Image edited from W.C.Keel (http://pages.astronomy.ua.edu/keel/agn/spectra.html).

close in wavelength (see e.g. Sturm et al. 2002). Although these diagrams are a good tool to disentangle the ionising source, they are not free from degeneracies. Apart from AGNs or starbursts, the emission may also be produced by shocks or post-asymptotic giant branch (AGB) stars, so these models are often included in BPT diagrams (see e.g. Cazzoli et al. 2018, and Fig. 1.3). Additionally, it has to be considered that they remain useful only on the relative local Universe (< 0.1-0.2), because at larger distances the lower luminous AGNs will not be detected due to their intrinsic faintness, creating a selection bias on statistical surveys (Netzer 2015).

1.1.3   Low-Ionisation Nuclear Emission-line Regions (LINERs)

In the low-luminosity end of the AGN family, we find LINERs. They were firstly identified by Heckman (1980), as a distinctive group of AGNs characterised by their relative high intensity of the low-ionisation emission lines (as [O I]$\lambda\lambda$6300,6364Å) with respect to higher ionisation emission lines (as [O III]). These differences are associated to peculiar characteristics of their NLR with respect to more luminous AGNs (Netzer 2013). They constitute the largest percentage of AGNs in the local Universe ($\sim$30% of the galaxies; Ho 2008). Their true nature as AGNs has been largely discussed in the literature (Ho 2008; Singh et al. 2013; Márquez et al. 2017), as other mechanisms such as shocks (Dopita & Sutherland 1995; Dopita et al.
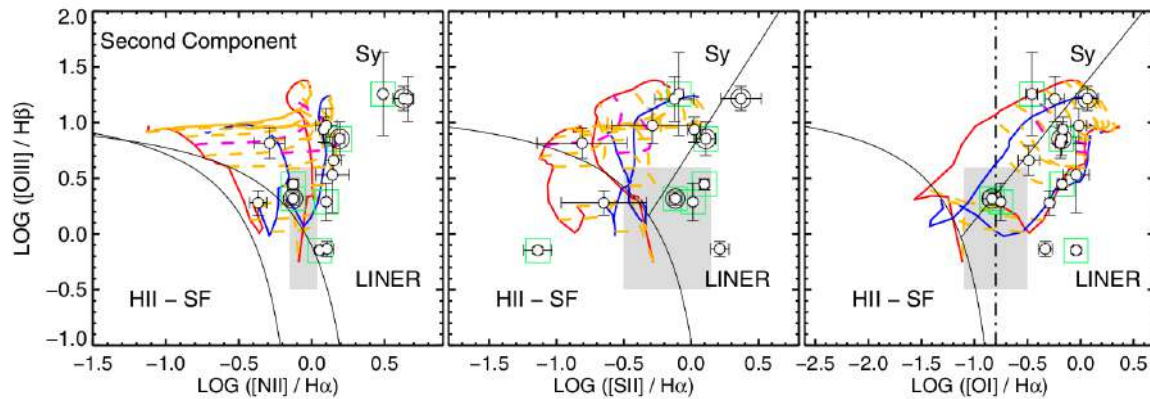
Fig. 1.3 BPT diagrams (Baldwin et al. 1981; Veilleux & Osterbrock 1987), with the dividing lines defined by Kauffmann et al. (2003) and Kewley et al. (2006), separating between AGNs and star-forming regions. On the y-axis, it is always represented the ratio between [O III] and Hβ lines, whereas different low-ionisation lines are compared to Hα on the x-axis. Grey boxes show photoionization models by pAGB stars (Binette et al. 1994), and the AGN and shock ionisation models are overlaid as the coloured lines (red, blue, green, pink and yellow). Image reproduced from Cazzoli et al. (2018) (see for a complete description).

1996) or post-AGB stars (Binette et al. 1994; Stasińska et al. 2008; Cid Fernandes et al. 2011; Papaderos et al. 2013) are able to ionise the medium and reproduce the observed line ratios for some targets. This discussion was fuelled by the discovery of LINER-like emission in the non-central regions of galaxies (Sarzi et al. 2010), referred to as LIERs (Low Ionisation Emission-line Regions; see e.g. Belfiore et al. 2016). For example, Singh et al. (2013) used a sample of 48 LINER-like objects from the CALIFA survey (Sánchez et al. 2012) to find that the emission out from the nucleus could not be produced simply by the AGN photoionisation, but most likely by post-AGB stars (see also Stasińska et al. 2008). All these results point towards LINER-like objects generally lacking young stellar populations and justify the fact that they are frequently found in massive, old galaxies, as this is the only way that a sufficiently large amount of post-AGB stars can produce the detected line ratios (Cid Fernandes et al. 2011; Singh et al. 2013).

However, later on, the AGN classification of the large majority of LINERs has been confirmed based on multi-wavelength data, specially relying on the detection of a nuclear source in X-rays (González-Martín et al. 2006; Ho 2008; González-Martín et al. 2009; González-Martín et al. 2009; Mason et al. 2012; Hernández-García et al. 2013, 2014; González-Martín et al. 2015) and on their radio emission (Nagar et al. 2000), or also in other ranges (for example in the infrared Dudik et al. 2009). In fact, going from a single wavelength range study to multi-band data imply an enhancement of AGN classification for LINERs up to 75-90% of confirmation for them (González-Martín et al. 2009; González-Martín et al. 2009,

2015). The detection of other hints of their nature, as for example a broad component in the Balmer lines associated to the BLR, may be a challenge in some cases due to the high obscuration that some LINERs suffer on the optical and UV regimes.

In the optical range, the emission of these objects is dominated by the stellar component of the host galaxy. Thus a correct subtraction from the underlying stellar population is needed to detect and characterise the true emission from the AGN. The intrinsic low luminosity of these LINERs, together with a poor galactic continuum subtraction, may result into a misclassification of the AGN type (i.e. type-1, -2 or any of the intermediates) due to a non-detection of a relatively faint (in flux) broad component from the BLR, which is diluted by the host contribution. This can be specially relevant when the spatial resolution of the spectroscopic data is low, diluting the AGN emission in favour of the host.

The main classification of type-1 and type-2 LINERs comes from the Palomar Survey, based on optical, long-slit, spectroscopic data. This survey of galaxies in the nearby Universe was done by Ho et al. (1995, 1997a,b), using data obtained with the Hale 5-m telescope at Mount Palomar. They found a large percentage of type-1.9 LINERs (i.e. Hβ not detected) and a correlation with the host galaxy type, with LINERs typically present on early-type galaxies (Ho 2008).

The existence or not of a broad component in LINERs was further studied by several authors, mainly for individual sources (see e.g. Ho et al. 2003; Balmaverde & Capetti 2014; Constantin et al. 2015). The first systematic search of this kind is Cazzoli et al. (2018), where they analysed the optical nuclear spectra of 22 nearby type-1 LINERs. They compared the ground-based vs space-based optical spectra (TWIN/CAHA and ALFOSC/NOT vs HST), finding that the differing resolutions affect the detection of a broad component. In the HST data, all the galaxies had this feature (9/9), although only 33% (7/21) of the data from ground-based facilities had it. These results highlight the difficulty of using the broad component detection as a probe for claiming the true nature of LINERs as AGNs. Additionally, Cazzoli et al. (2018) found various kinematical components on the emission lines of the nuclear spectra, that revealed a complex structure in the ionised gas of these galaxies, associated to non-rotational motions most probably related to the presence of outflows (see Sect. 1.2.1).

1.2   Feedback processes: Outflows

During the last decades, one key topic regarding AGN and galactic evolution has been the action of feedback processes driven by outflows (see e.g. Harrison et al. 2018). These are defined as phenomena that launch gas out of the galaxy powered either by intense star for-

mation processes (such as supernovae) or by an AGN, that may propagate at large distances from the galaxies. The initial phase of outflows are small bubbles or winds of hot gas pressured by the energy released from either the accretion into the SMBH or by starburst processes. Due to the high pressure, they are driven out of the inner regions interacting first with the ISM and, at later times, with the intergalactic medium (IGM), generating shock fronts during the expansion. Given that the gas is a fundamental component of the galaxy, these processes can potentially alter considerably its evolution and environment (Kormendy & Ho 2013). Depending on their effect, we can distinguish between two types of feedback: (i) negative feedback, related to the heating or blow out of the gas from the galaxy, preventing star formation to occur; and (ii) positive feedback, where the gas cools, favouring the formation of new stars (see e.g. Silk 2013; Harrison 2017). For the latter, star formation is triggered either by compression of the gas that favours the formation of molecular clouds (see Cresci et al. 2015; Harrison 2017), or directly the gas forming the outflow cools and fragments, producing star formation in the outflow itself (Maiolino et al. 2017).

The energy produced by the AGN affects the galaxy at different scales, mainly its ISM and the IGM. There are two main ways in which the energy is released towards the outer parts of the galaxy, that are defined as the two feedback modes. These modes depend on the luminosity of the AGNs (i.e. the accretion rate) and are called the **radiative** or quasar mode, and the **kinetic** or jet mode. These are defined as:

- *Radiative mode:* It is more important for high luminosity AGNs which are radiatively efficient (i.e. have moderate to high accretion rates; Eddington ratios >0.01; Harrison 2017). It occurs in smaller timescales than the kinetic phase and is more effective for gas-rich galaxies (Fabian 2012; Heckman & Best 2014). However it is the most intense mode, dragging out large amounts of gas from the galaxy to typically small distances (Costa et al. 2014) that potentially could lead to gas depletion of the host (Fabian 2012). The radiative feedback can be produced either through energy transfer, radiation pressure or moment transfer from the AGN radiation, depending on how the gas interacts with the ISM (Harrison 2017).

- *Jet mode:* It is more commonly found for radiatively inefficient AGNs, such as those at the low luminosity end (e.g. LINERs). The energy in these cases is kinetic and generally driven by jets, thus these AGNs are active radio sources (see e.g. Fabian 2012). The jet generates large cavities and bubbles spatially coincident that can be detected particularly in clusters using both radio and X-ray data (see Fabian 2012, and references therein). The gas in the bubbles is typically not turbulent, making this mode much less violent than the radiative one.

The most probable situation to explain how outflows are launched is to account for both modes acting in AGNs during its evolution, although every mode would act at different evolutionary stages (see e.g. Fabian 2012).

There is a debate about whether outflows in powerful AGNs can shut down the star formation and quench the galaxy (see e.g. Fabian 2012; Cresci et al. 2015; Bongiorno et al. 2016; Fiore et al. 2017). Theoretical predictions of the galactic luminosity function invoke AGN feedback to justify the lack of stellar formation detected in massive galaxies (see e.g. Silk & Mamon 2012; Tacchella et al. 2016; Beckmann et al. 2017). This is predicted by analytical models and in hydrodynamical simulations (see e.g. Bower et al. 2006; Vogelsberger et al. 2014; Tremmel et al. 2019). Indeed observational works found interesting relationships between the AGN and galactic parameters, such as the star formation rate and the SMBH accretion rate, that evolve similarly with time (see e.g. Heckman & Best 2014; Kormendy & Ho 2013). However, it has been suggested that outflows alone are not sufficient to quench the star formation in galaxies, but other additional mechanisms are needed, such as starvation due to the heat of the circumgalactic medium produced by jets (see e.g. Fabian 2012; Cicone et al. 2014; Fluetsch et al. 2019; Trussler et al. 2020).

Now it is known that outflows appear commonly in galaxies, even in our own Milky Way (Su et al. 2010). The outflow in our galaxy is referred to as the *Fermi Bubble* and has been studied since its discovery with a variety of telescopes and satellites in many wavelength ranges (in gamma-rays Su et al. 2010; in X-rays Nakashima et al. 2019, Ponti et al. 2019, Predehl et al. 2020; in UV Fox et al. 2015, Bland-Hawthorn et al. 2019). These bubbles emerge symmetrically from the Galactic centre, spanning a total length of approximately 50000 light-years in gamma-rays. It is still debated if these bubbles were launched by starburst processes or AGN activity. The latter hypothesis seems more likely given the required energy to power the bubbles, and the X-ray and stellar properties of the Galactic centre (see e.g. Bland-Hawthorn et al. 2019; Ponti et al. 2019; Veilleux et al. 2020).
In general, the distinction between when an outflow is powered by an AGN or by star-forming processes is still diffuse, although strong, massive outflows that suppress the star formation in massive galaxies are associated to AGN activity (Fabian 2012), and those triggered by starbursts regulate the star formation in galaxies with stellar masses $<10^{10} M_\odot$ (see e.g. Harrison 2017; Fluetsch et al. 2019, and references therein).

Outflows are detected in various wavelength ranges leaving signatures in both emission and absorption lines, each related to a given gas phase. Depending on the temperature, the gas

presents distinct properties, contributing differently to the parameters of the mass, energetics and evolution of the outflow. Thus, their complexity may only be understood considering their multi wavelength nature and the interplay between all the phases (Cicone et al. 2014; Fluetsch et al. 2021). Among the several phases, there are three relevant in this thesis (in order of importance): ionised, neutral and molecular gas. The most studied here is the warm ionised phase of the gas.

- The **ionised** phase can be traced in its warm phase (T$\sim$10^4 K; Harrison et al. 2018) using the brightest emission lines in the optical range ([N II], [S II], [O III] and Balmer lines; see e.g. Cazzoli et al. 2018), or the hot phase (T $>$ 10^6 K) observed in X-rays (see e.g. Tombesi et al. 2013). Their mass outflow rates reach values up to few hundreds of M$_\odot$/yr (smaller than that of the molecular gas, see below), although they can reach larger distances out of the galaxy, extending out to a few kpc (Harrison et al. 2014). Their velocities and masses are correlated with the luminosity when the outflows are AGN-driven (Fiore et al. 2017). The ionised phase typically traces the borders of the expanding bubbles (Veilleux et al. 2020).

- The **neutral** gas (T$<$10^{4}K) in the optical range can be studied using the sodium doublet $\lambda\lambda$5890,5896Å (NaD) absorption lines (see e.g. Cazzoli et al. 2016; Perna et al. 2017). The neutral phase along with the molecular phase are very important, as typically the cool gas is correlated with the star formation of the galaxies, and thus may affect the evolution of the host. This phase has been mostly studied in Ultra/Luminous Infrared Galaxies (U/LIRGs; see e.g. Cicone et al. 2014; Cazzoli et al. 2014, 2016).

- The coolest phase is the **molecular** gas (T$\sim$10-10^2 K; Kennicutt & Evans 2012), that is generally traced through the CO emission lines (see e.g. Cicone et al. 2014; Fluetsch et al. 2019). This phase shows the largest mass outflow rates of all, up to 1000M$_\odot$/yr (see e.g. Cicone et al. 2014; Carniani et al. 2015; Fiore et al. 2017; Fluetsch et al. 2019), accounting for even 60% of the total outflow mass rate (for U/LIRGs) or even higher for AGNs (Fluetsch et al. 2021). It also traces denser gas than other phases (density $>$10^{3}cm^3).

To fully understand the feedback phenomena and their impact on the evolution of galaxies, one has to first characterise their properties, such as energetics, mass or velocities, among others. There are many efforts in the literature to obtain the physical relations between all the parameters affecting the outflows depending on the gas phase (see e.g. Carniani et al. 2015; Cresci et al. 2017; Fiore et al. 2017; Venturi et al. 2021). For example, the kinetic power of an outflow is used to identify the power source of the outflows, as launched by stellar

processes or AGNs and, in case it is produced by an AGN, if it is more likely powered by the AGN itself or by the jet. The calculations mainly rely on observational parameters, as the line width, velocity, extension and fluxes (e.g. [O III] luminosities) of the emission lines. The main parameters that we derive in this work are the mass, mass outflow rate, kinetic energy and the kinetic power of the outflowing ionised gas. The mass outflow rate is estimated as in Cresci et al. (2015) (see also Fiore et al. 2017):

$$\dot{M}_{\mathrm{OF,ion}} = 3 \times \frac{V_{\mathrm{OF,ion}}}{R_{\mathrm{OF,ion}}} \times M_{\mathrm{OF,ion}} \qquad (1.1)$$

Depending on the velocity of the outflow ($V_{\mathrm{OF,ion}}$), its extension ($R_{\mathrm{OF,ion}}$) and the total mass of the ionised gas ($M_{\mathrm{OF,ion}}$), which is calculated as in Venturi et al. (2021) with the following expression:

$$M_{\mathrm{OF,ion}} = 3.2 \times 10^5 \left(\frac{L_{\mathrm{H\alpha}}}{10^{40}\,\mathrm{erg\,s^{-1}}} \right) \left(\frac{n_{\mathrm{e^-}}}{100\,\mathrm{cm^{-1}}} \right) \qquad (1.2)$$

The mass is dependent of the electron density of the gas ($n_{\mathrm{e^-}}$), that can be estimated from the ratio of the [S II] doublet lines (Osterbrock & Ferland 2006), and the Hα luminosity. The kinetic energy and the kinetic power of the outflow are estimated as:

$$E_{\mathrm{OF,ion}} = \frac{1}{2} \times \sigma_{\mathrm{OF,ion}}^2 \times M_{\mathrm{OF,ion}} \qquad (1.3)$$

$$\dot{E}_{\mathrm{OF,ion}} = \frac{1}{2} \times \dot{M}_{\mathrm{OF,ion}} \times (V_{\mathrm{OF,ion}}^2 + 3\sigma_{\mathrm{OF,ion}}) \qquad (1.4)$$

These depend on the mass, mass outflow rate, the outflow velocity and the average velocity dispersion of the Hα line. These formula will be used in Chapter 4.

1.2.1   State of the art: outflows in LINERs

The work by Fiore et al. (2017) is a systematic exploration of the possible scaling relations existing between outflows and the host galaxies. They collected observational data of AGN outflows for a total sample of 94 galaxies detected in their different phases. They estimated outflow parameters, such as the mass outflow rate or the outflow kinetic power, searching for correlations between their properties with that from the galaxy and/or the AGN. However, the sample was constituted by objects whose lower bolometric luminosity is larger than $10^{43.11}$ erg s^{-1} (see Fig. 1.4) with only a 4% of the objects with luminosities comparable to the typical values for LINERs (i.e. $L_{\mathrm{bol}} < 10^{44}$ erg s^{-1}, Ho 2008). Thus, the largest works up
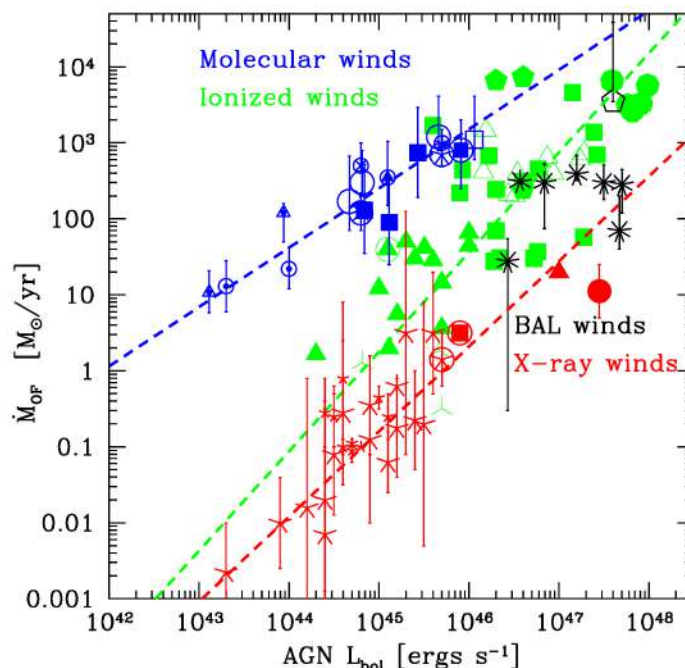
Fig. 1.4 Mass outflow rate versus the AGN bolometric luminosity from Fiore et al. (2017).

to date characterising outflows do not explore the low luminosity end of the AGN family.

So far, the discovery of outflows in LINERs has been mainly by chance, only studied in individual objects (Dopita et al. 2015; Brum et al. 2017) and not through a systematic search, except for the work by Cazzoli et al. (2018). This apparent lack of outflows in LINERs is in contrast to the idea that many works propose about the ubiquitous of outflows in AGNs (see Veilleux et al. 2005, for a review). It may be partly justified if we take into account that the power of the outflow is correlated to the AGN luminosity (Fluetsch et al. 2021), thus implying that outflows must be faint (both in energetics and in extension) in LINERS. The first studies of feedback processes went on the search for powerful outflows that could be 'easily' detected to measure their main properties (i.e. mass rates, energy, energy rate, etc.). Then the scarcity of detection of outflows in LINERs may be a bias towards searching more powerful outflows rather than actually a lack of them at these low luminosities.

There is evidence for extended ionised gas emission in LINERs that could be ascribed to outflows in past works (Pogge et al. 2000; Masegosa et al. 2011). In particular, Masegosa et al. (2011) analysed Hα images from the Hubble Space Telescope (HST) for 32 LINERs. They found that for 42% of the galaxies the ionised gas morphology showed bubble-like, filamentary structures that could be explained as outflows. This was the case for NGC 4438, a

nearby LINER for which a small (projected length of 1 kpc), ionised gas bubble-like structure was detected with imaging data, with the typical shape of an outflow (Fig. 1.5; Masegosa et al. 2011; see also Kenney & Yale 2002).

However, as mentioned previously, outflows are better characterised through the use of spectroscopic techniques. Cazzoli et al. (2018) performed a systematic search for outflows in a sample of 22 type-1 LINERs. They analysed the optical nuclear spectra using long-slit data and performed a kinematical decomposition of the emission lines. In this process, they fitted two kinematical components per forbidden emission line (Hα, [N II], [O I] and [S II]) plus the BLR component (see Sect. 1.1.3). Whereas the narrowest component could be explained by rotational motions for all cases (i.e. gaseous disc), the broader component could be interpreted as an outflow for 40% of the sample, showing blueshifted velocities and a velocity dispersion (σ) larger than $400\,\mathrm{km\,s^{-1}}$. This work together with the morphological analysis of Masegosa et al. (2011) constitute the larger samples of LINERs up-to-date searching systematically for outflowing signatures in both spectra and images. They are however limited in number of objects, in the existence of projection effects on the classification of morphologies with the imaging data and with the long-slit spectroscopic data only covering the nuclear region. Thus both long-slit spectroscopic and imaging data are not able to fully capture and characterise the possible outflow (see Sect. 1.3). Integral Field Spectroscopic (IFS) data at different wavelengths is hence a need to fully characterise outflows in different AGN types (see e.g. Dopita et al. 2015), as explained below.

1.3   Observational methods to study outflows in LINERs

Historically, the analysis of the AGN emission was based on long-slit spectroscopy, which was very useful for characterising the global properties of the nuclei. For LINERs, it was particularly important for the first classification of these AGNs as type-1 or type-2 objects (Ho et al. 1995). However, the information from a single nuclear spectrum of the inner regions of the galaxy is insufficient for obtaining a complete description of the properties of the AGN and its host. As mentioned, there are many studies focused on evaluating the impact of AGN feedback processes in galaxies (see Harrison et al. 2018 for a review), as they could potentially end up the star formation of the galaxy by releasing the gas and dust to the interstellar medium. Although long-slit spectroscopy is useful for identifying candidates of outflows, it remains insufficient for tracing their full extension. Thus, feedback studies benefit from the development of IFS, that allow us to obtain a more complete perspective of

Fig. 1.5 Optical image of NGC 4438 obtained with the HST. The ionised gas is represented in red. Credit: NASA/ESA, Jeffrey Kenney and Elizabeth Yale (Yale University).

the physical processes occurring in galaxies.

Briefly, the IFS technique consists on the acquisition of a spectrum for every pixel in the Field of View (FoV) of the instrument, formed by what its commonly referred as *spaxels* (spectral-pixel). This technique allows us to work with the two spatial directions (RA and DEC) plus an additional dimension, the wavelength. The resulting observations are referred to as data cubes.

It has to be noted that many works (see Harrison et al. 2018, and references therein) do not resolve outflows due to signal-to-noise issues, providing global values of their properties, instead of tracing their properties on a spatially-resolved basis. IFS technique is indeed a powerful tool for studying outflows, but with some limitations. For characterising completely the outflow, both large spatial and spectral resolutions are required along with a large FoV to account for the full extension of the outflow, specially in those more powerful and extended. For example, two known Integral Field Unit (IFU) instruments that can be complemented nicely are MUSE and MEGARA; they have high spatial resolution and high spectral resolution, respectively, but not both simultaneously. If the individual results are not considered carefully, the instrumentation limitations could bias the interpretation of the results to some

extent. One of the most useful targets to study outflows are nearby galaxies, where they are more easily traced given that they could be spatially resolved (e.g. $\sim 60\,\text{pc}$ for targets at $z \lesssim 0.003$). However, now it is known that outflow power scales with the AGN luminosity (Fluetsch et al. 2019) which, as already mentioned, unequivocally would lead to LINERs having small outflows compared with more powerful AGNs. Although the proposed ubiquity of outflows in AGNs together with LINERs being the largest population of AGNs in the local Universe makes them ideal targets to characterise feedback processes on them, they would show faint, compact outflows, difficult to detect even at the largest resolutions.

The optical data analysed in this thesis make use of imaging, long-slit spectroscopy and IFS techniques. We have mainly used four instruments: the Hubble Space Telescope (HST) for imaging and long-slit data; ALFOSC at the Nordic Optical Telescope (NOT) for imaging data; and MEGARA at the Gran Telescopio de Canarias (GTC) and MUSE at the Very Large Telescope (VLT) for IFS data. Here we briefly describe the main characteristics of the telescopes and instruments.

- *HST*: Spatial telescope with a mirror of 2.4 meters in diameter. It has several instruments for obtaining imaging and spectroscopic data. In this thesis we used the Space Telescope Imaging Spectrograph (STIS) instrument, a camera and spectrograph with a total wavelength coverage from the ultraviolet (UV) to the near-infrared (1150 to 10000Å). We studied long-slit spectroscopic data using the intermediate resolution grating G750M (R~5000, ~50 km s^{-1}), with a wavelength coverage from ~5500 to 10000Å. The slit widths were 0.1"and 0.2", allowing for detecting the emission from the nucleus without much contamination from the stellar component of their hosts (see Chapter 2). Additionally, we used narrow and broad band imaging data from the Wide Field Camera (WFC3) to characterise the morphologies of the ionised gas emission in LINERs (see Chapter 3).

- *NOT*: This telescope is located at the Roque de los Muchachos Observatory, in La Palma, and has a primary mirror of 2.56 meters in diameter. It can be used in several observing modes, such as imaging, spectroscopy and polarimetry in the UV, optical and near-IR ranges. We used the Alhambra Faint Object Spectrograph and Camera (ALFOSC) instrument in imaging mode, that has a total FoV of 6.4'×6.4'. The data used in this thesis consist on broad-band and Hα narrow-band images of nearby LINERs (see Chapter 3). The great advantage of ALFOSC with respect to other instruments is the large availability of filters centred in the Hα line, allowing the selection of the most adequate filter depending on the redshift of our targets.

- *GTC*: This 10.4-meter telescope is located at the Roque de los Muchachos Observatory, in La Palma. We used data from the Multi-Espectrógrafo en GTC de Alta Resolución para Astronomía (MEGARA) instrument. It has two observing modes, a Multi-Object Spectrograph (MOS) and an IFS instrument. The first has a FoV of 3.5"×3.5"and the latter a FoV of 12.5"×11.3"and a spatial scale of 0.62". MEGARA has three different spectral resolutions for each mode: low-resolution (LR) with R~ 5500, medium-resolution (MR) with R~ 12000, and high resolution (HR) with R~ 20000. Each resolution has different Volume Phase Holographic (VPHs) covering a variety of wavelength ranges in the optical, from ~3600 to ~9600Å. In this thesis we used the IFS mode with three VPHs at the LR mode and one VPH in the HR mode (see Chapters 4 and 5).

- *VLT*: These 8.2-meter telescopes are located in the Paranal Observatory at Cerro Paranal, Chile. The data used in this thesis comes from the second generation instrument called Multi Unit Spectroscopic Explorer (MUSE), installed at the UT4 telescope. It is an IFU with two observing modes, the wide field mode (WFM; 1'×1'), with a spatial resolution of 0.3-0.4", and the narrow field mode (NFM; 7.5'×7.5') that can reach a spatial resolution of 0.03-0.04". We obtained WFM IFS data with high spatial resolution (0.2") at low spectral resolution (median R~3000) of the prototypical LINER NGC 1052 (see Chapter 4).

Our methodology consists on applying the three mentioned techniques with data from the above telescopes to our sample of galaxies to identify and characterise the possible ionised gas outflows in the objects. In Sect. 1.3.1 we summarise it with a case of study.

1.3.1   NGC 4750 as a case of study

In this thesis we have applied all the techniques mentioned in Sect. 1.3 with a few galaxies that are candidates of hosting an outflow. Given that we considered also the candidates coming from Pogge et al. (2000); Masegosa et al. (2011) and Cazzoli et al. (2018), we note that all the galaxies from the samples in this thesis are analysed in one of those previous works and at least in one of the Chapters 2, 3, 4 and 5. In this section we summarise all the steps followed during the analyses of the data for the candidates, using as an example the results for the LINER NGC 4750[2]. This target is one of our best candidates of hosting an outflow, showing signatures of it in all the studied datasets (see Fig. 1.6).

---

[2]The main characteristics of this LINER are described in Chapters 3 and 5

The long-slit spectroscopic data analysis was done in Cazzoli et al. (2018) using both HST and CAFOS/CAHA. They classified this target as candidate of hosting an outflow based on its ground-based long-slit nuclear spectrum, with the detection of a kinematical component in the emission lines with velocity dispersion of $\sim$380$\pm$42 km s^{-1} and a velocity of -296$\pm$21 km s^{-1}. Then in Chapter 3 we analyse the optical Hα image using HST data (see Fig. B.7). The emission is concentrated in a region of 4"$\times$6" around the nucleus, and present a peculiar bubble-like shape that make it an outflow candidate (see 'Bubble' definition in Chapter 3). As both works classified this galaxy as a candidate for an outflow, we obtained IFS data using MEGARA/GTC using all the low resolution VPHs explained in Sect. 1.3 (i.e. LR-B, LR-V and LR-R). We characterise the spectra in Chapter 5 (see Fig. 5.9). The analysis of the possible neutral gas phase of the outflow, measured with the NaD lines, is left as future work (see Chapter 8). We found two kinematical components per emission line, with the secondary being clearly blueshifted (mean velocity of -92 km s^{-1}) and broader than the first, narrow component (mean σ of 297 km s^{-1}). The secondary component has a bubble-like morphology that emerges westward from the nucleus out to $\sim$2.5". It is consistent with being an outflow, confirming our previous classifications with long-slit and imaging data. Further constraints on the characteristics of the outflow will allow us to understand its origin (see Chapter 5).

1.4   Outline of the thesis

The main open question on outflows is how often we can find them in LINERs, and if indeed they are ubiquitous as has been found for more luminous AGNs. As already mentioned, outflows may have an impact on the evolution of the host galaxy, thus feedback processes are very important for understanding the global galactic evolution. In this thesis we study the presence of ionised gas outflows in LINERs as well as characterised their properties (velocity, flux, length, energetics, etc.). To that aim, we explored all the three techniques described in Sect. 1.3.

In Chapter 2 the study a sample of nine type-2 LINERs with spectroscopic data from HST and from the Palomar survey is presented to explore the existence of a BLR component in those galaxies. We also looked for kinematical signatures in their nuclear spectrum to classify them (or not) as candidates of hosting an outflow, following the lines of Cazzoli et al. (2018). In Chapter 3 we present the results of a systematic search for outflows in LINERs through Hα narrow band imaging data obtained with ALFOSC/NOT and HST for 70 galaxies, expanding the data analysed in previous works (Pogge et al. 2000; Masegosa et al. 2011). We use spectroscopic information from the literature to kinematically confirm the morphological
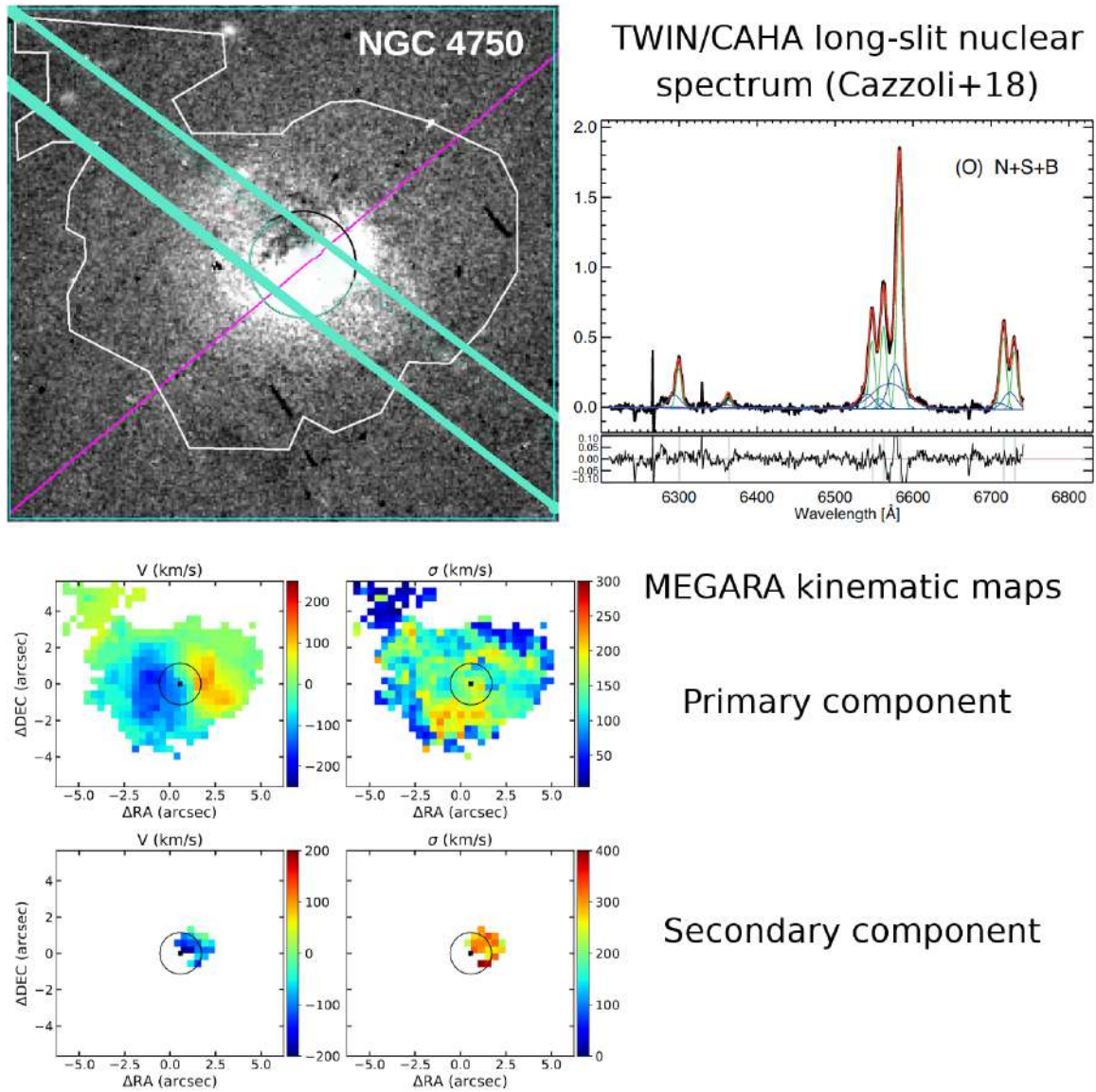
Fig. 1.6 Example of our methodology and the analysed data for NGC 4750. *Top-left:* Hα narrow band image obtained with ALFOSC/NOT, superimposed by the contours of the Hα emission measured with MEGARA (white contours), the major axis position angle of the galaxy (purple line), the slit used in Cazzoli et al. (2018) to obtain TWIN/CAHA spectra (in cyan), and the MEGARA PSF (black circle). *Top-right:* nuclear spectrum of NGC 4750 extracted along the indicated slit, analysed in Cazzoli et al. (2018). *Bottom:* kinematic maps (velocity and σ) for the two components detected in the ionised gas of the galaxy observed with MEGARA/GTC (see Chapter. 5 for a full description).

signatures of outflows in our sample. Additionally, we study soft X-ray data looking for a possible correlation between this emission and the ionised gas of the galaxy.

In Chapters 4 and 5 we start an IFS analysis of the candidate galaxies of hosting an outflow from the previous chapters. Given the variety of data available, we systematically observed all the nine candidates using MEGARA/GTC to characterise the possible outflow. We present in Chapter 4 the analysis of the prototypical LINER NGC 1052, for which we also had data from MUSE/VLT, and then in Chapter 5 the results of the remaining eight objects.

Chapter 2

Optical spectroscopy of type-2 LINERs

Abstract

Type 2 Low-ionization Nuclear Emission-line Regions (LINERs) have been optically classified with the Palomar data as not presenting a broad component in the Balmer emission lines that are associated with the broad-line region (BLR) of the active galactic nuclei (AGN). We aim to unveil the presence of different kinematic components of emission lines in the nuclear region of a sample of local ($z \leq 0.022$) type 2 LINERs. We focus on the analysis of the true nature of LINERs by means of the detection (or nondetection) of a broad component that originated in the BLR of the AGN. Additionally, we search for the possible presence of nonrotational motions such as outflows in these LINERs. We applied a decomposition of the nuclear emission lines using an spectroscopic analysis of the optical spectra of nine type 2 LINERs of intermediate-resolution spectroscopic data retrieved from the Hubble Space Telescope (HST) archive. The study is completed with archival spectra from the Double Spectrograph from the Palomar Observatory. The emission line fitting reveals the presence of a broad component associated with the BLR in six out of the nine galaxies for the space-based data, and for two out of the eight from the ground-based spectra. The velocity dispersion for two galaxies (NGC 4486 and NGC 4594) measured in HST/STIS data suggest the presence of outflows. The results indicate that the spatial resolution plays a major role in the detection of the BLR, as it appears diluted in the ground-based data (even after removing stellar contribution). This is also true for the emission line diagnostics, as the contaminant light contributes to lower emission line ratios toward the star-forming area of standard BPTs.

We propose to reclassify NGC 4594 as a type 1 LINER, since a BLR component is seen in both space- and ground-based spectra. We find ambiguous results for the BLR component of NGC 4486. The modest outflow detection in our sample may indicate that they are not be as frequent as seen for type 1 LINERs.

2.1 Introduction

Low-ionization Nuclear Emission-line Regions (LINERs) are among the lowest luminosity active galactic nuclei (AGN) found in the Universe. Defined for the first time by Heckman (1980), their spectra is dominated by low-ionization lines in contrast with the importance of high-ionization emission lines ([O III]λ5007 or He IIλ4686) in more luminous AGNs, such as Seyferts. The initial separation between LINERs and Seyferts was defined by Heckman (1980) based on the relative ratios between the intensity of several emission lines ([O II]λ3727 to [O III]λ5007 and [O I]λ6300 to [O III]λ5007).

LINERs may be the most numerous type of AGNs in the local Universe (Ho et al. 1997a), although their true AGN nature is still a matter of debate (Ho 2008; Márquez et al. 2017). Their spectral features cannot be explained only with stellar formation processes (Heckman 1980), and an AGN is not the only valid explanation. Other mechanisms that could reproduce their spectral features are, for example, shock ionization (Heckman 1980; Dopita & Sutherland 1995; Dopita et al. 1996) and photoionization by post-AGB stars (Binette et al. 1994; Stasińska et al. 2008; Papaderos et al. 2013).

The morphology of the circumnuclear Hα emission as seen by the HST imaging indicates the possible presence of outflowing material in some of the systems (Pogge et al. 2000; Masegosa et al. 2011). In these cases, the outflow could contribute to the broadening of emission lines such as Hα-[N II], [O I], and [S II]. This could compromise the detection of the weak emission of Balmer lines from the broad-line region (BLR) in their nucleus. Shocks associated with outflows may also be important in ionizing the nuclear gas (and surroundings) (Dopita et al. 1996; Molina et al. 2018). However, these are observed at lower velocities (Molina et al. 2018) than those needed by the shock models (Groves et al. 2004) to reproduce LINER-like line ratios.

As Seyfert galaxies, LINERs appear as type 1.9 or type 2, depending on if the BLR is detected on their nucleus. The BLR is identified as a very broad component in the profiles of the Balmer lines. There are only a few systematic works studying the AGN nature of LINERs (Ho et al. 2003; Cazzoli et al. 2018), with most of them being individual discoveries (Bower et al. 1996; Ho et al. 1997a).

In the work by Cazzoli et al. (2018), the spectra for a sample of nearby (z < 0.025) type 1.9 LINERs obtained with both ground- and space-based telescopes are analyzed. A broad component indicative of the BLR is required for the fitting of ground-based data in only a third of the targets, despite the fact that they were all classified as type 1.9 by Ho et al. (1997a). Nevertheless, the modeling of the spectra of the targets obtained with the Space Telescope Imaging Spectrograph (STIS), mounted on the Hubble Space Telescope (HST), requires a broad Hα feature.

As with type 2 LINERs the BLR is not detected, the AGN nature of these systems is still controversial. Other components, such as post-AGB stars or low-mass X-ray binaries may play an important role in explaining their optical spectra (see Ho et al. 1997a; McKernan et al. 2010).

In this Chapter, we analyze HST spectra of nine type 2 LINERs selected from the sample of González-Martín et al. (2009) with available data in the archive to investigate if they present a broad component in the Balmer lines that could be associated with the existence of a BLR in their nuclei. We completed the study with a comparison to the ground-based spectra from Ho et al. (1995), since the majority of the targets were classified as type 2 objects on that work. We also revisited the possible influence of the outflows in the broadening of Balmer lines, following Cazzoli et al. (2018).

This Chapter is organized as follows: In Section 2.2 we describe the sample and the data reduction process. Section 2.3 indicates the spectral line fitting for each nuclear spectra. Section 2.4 and Section 2.5 show the main modeling results for space- and ground-based spectra, respectively. In Section 2.6, we discuss the modeling results, the possible presence of a BLR in some of the targets, and a comparison of the two datasets for both kinematics and line ratios. Finally, in Section 2.7, we present a summary and the main conclusions of the work.

2.2 Sample and data processing

The sample selection is drawn from the survey by González-Martín et al. (2009) of 82 LINERs selected at X-rays. From this sample, we selected all type 2 LINERs classified as AGNs from the analysis of their features in the wavelength range from X-rays to the near-infrared. The final sample of 12 galaxies comprises all the objects with available spectra in the HST/STIS archive with the intermediate resolution grating G750M (R ~ 5000). This grating covers a total wavelength range from 5450 - 10140Å, centered at 6581 or 6768 Å. This range has been chosen due to the availability of the [S II]; [N II]; and Hα lines in all the spectra and [O I] in those where the grating was centered at 6581Å (all except NGC

4594 and NGC 4676B). Two out of 12 were discarded because the low signal-to-noise ratio (S/N) of the spectra (NGC 4261 and NGC 5055, for which Constantin et al. 2015 already reported the poor quality of the nuclear spectrum of the latter), and also NGC 6240, because even though its spectrum is archived as nuclear, the emission lines were not visible. This leaves a total of nine galaxies in the final sample of type 2 LINERs. Basic information is provided in Table 2.1.

The full calibrated 2D spectra were retrieved from the HST archive. In Table 2.2, the main observing details of each nuclear spectrum analyzed are listed. Then, we extracted the 1D flux and wavelength-calibrated nuclear spectra of the sources. Some of them (namely NGC 4698, NGC 4552, NGC 4676B) showed abundant cosmic rays (CR). The results could be improved by performing a new CR correction with the L.A. Cosmic algorithm (van Dokkum 2001) to the flat-fielded frames also downloaded from the archive. After this correction, we applied the last step of the reduction process following the HST pipeline, which is the x2d task (under the stsdas package in IRAF[1]). This task generates the final calibrated frame and corrects the geometrical distortion.

For the galaxies with several nuclear exposures available, they were realigned and combined with the IRAF tasks imshift and imcombine. These tasks improved the S/N after the CR rejection. If there was only one nuclear spectrum available, and the CRs fell close to the lines in the majority of the nuclear rows, we extracted each row individually and did the CR removal manually. Then, the individual rows were combined to form the final nuclear spectra. If a CR fell on the continuum of these spectra, it was masked in the analysis.

The final nuclear spectrum was extracted using apall task in IRAF. The number of extracted and combined rows depends on the slit width and the binning of the CCD. The majority of the targets were measured with a slit width of $52'' \times 0.2''$, a plate scale of $0.05''$ pixel^{-1}, and no binning. For these, the five central rows (pixels) were extracted to form the final spectra. For the spectra binned to $0.1''$pixel^{-1}, the three central rows were extracted. All the galaxies observed with a slit width of $52'' \times 0.1''$ were unbinned, and therefore we extracted five rows. The number of pixels extracted for each galaxy and its equivalent spatial scale are indicated in Table 2.2 (column 6).

However, the data for two of the objects (NGC 4552 and NGC 4676B) had low S/N that did not improve with the combination of multiple exposures. For NGC 4552, there were additional spectra from regions near the very center, so a line-fitting was possible for the nuclear spectrum (see Sect. 2.3). We also fit the NGC 4676B spectrum, but it was finally excluded due to the low significance of the obtained modeling, as is discussed in Section 2.6.

---

[1]IRAF is the Image Reduction and Analysis Facility distributed by the National Optical Astronomy Observatories (NOAO) for the reduction and analysis of astronomical data.

Additionally, we searched for the spectra of the nine objects within the sample by Ho et al. (1995) in order to compare the space-based and ground-based spectra. The latter were retrieved from the archive. They were observed with the Double Spectrograph (Oke & Gunn 1982), located in the Cassegrain focus of the Hale 5 meter telescope at Palomar Observatory during 1984 and 1985. The long-slit spectra were measured with a $1200 \, \text{line} \, \text{mm}^{-1}$ grating blazed to cover a wavelength range $\sim 6210 - 6860 \text{Å}$. The spectral resolution was R ~ 2500 for a $2''$-length slit and R ~ 4000 for a $1''$-length slit. Spectra for eight out of the nine galaxies (all except NGC 4676B, member of a merging system, which is located at approximately ten times the distance of the rest of the targets, see Table 2.1) were retrieved already reduced from the NASA/IPAC Extragalactic Database (NED)[2] archive. The width of the slit was $2''\times128''$ for all the targets, except for NGC 4486, which was $1''\times128''$. The total extraction window was $2''\times4''$ (for NGC 4486 was $1''\times4''$), equivalent to summing up the central seven pixels of the CCD. The mean seeing of the observations is $1.5''$. The spectral and spatial resolutions were $\sim2.5\text{Å}$ and $0.58'' \, \text{pix}^{-1}$, respectively.

---

[2]The NASA/IPAC Extragalactic Database (NED) is funded by the National Aeronautics and Space Administration and operated by the California Institute of Technology.

Table 2.1 General properties for nine type 2 LINERs discussed in this Chapter. (2) RA and (3) DEC: coordinates of the galaxy; (4) Morphology: Hubble classification; (5) z and (6) scale: heliocentric redshifts and scale distance from the Local Group from NED; (7) i: inclination angle from Ho et al. (1997a); (8) V_{rot} and (9) P.A.: maximum rotation velocity corrected from inclination and position angle from HyperLeda, respectively.

ID	RA (hh:mm:ss)	DEC (dd:mm:ss)	Morphology	z	Scale (pc arcsec^{-1})	i (°)	V_{rot} (km s^{-1})	P.A. (°)
(1)	(2)	(3)	(4)	(5)	(6)	(7)	(8)	(9)
NGC 2685	08 55 34.71	+58 44 03.83	(R)SB0+pec[a]	0.0029	70	60	146±4	38
NGC 3245	10 27 18.387	+28 30 26.79	SA(r)0[b]	0.0045	90	58	-	177
NGC 4374	12 25 03.74	+12 53 13.14	E1[c]	0.0034	65	-	189±15	135
NGC 4486	12 30 49.42	12 23 28.04	E0+pec[d]	0.0043	84	-	-	160
NGC 4552	12 35 39.81	+12 33 22.83	E[a]	0.0011	17	-	-	-
NGC 4594	12 39 59.43	-11 37 22.99	SA(s)a[a]	0.0034	59	68	408±11	90
NGC 4676B	12 46 11.24	+30 43 21.87	SB(s)0/a+pec[a]	0.0220	472	-	397±31	-
NGC 4698	12 48 22.91	+08 29 14.58	SA(s)ab[a]	0.0034	64	53	518	203±3
NGC 4736	12 50 53.061	+41 07 13.65	(R)SA(r)ab[a]	0.0010	25	36	182±5	105

[a] Ho et al. (1997a); [b] Wardle & Knapp (1986); [c] Huchtmeier (1994); [d] Huchtmeier & Richter (1986).

Table 2.2 Observing log of HST/STIS data. Columns indicate: (1) galaxy name; (2) other name; (3) file name of the analyzed spectra as indicated in the archive; (4) proposal ID of the observations; (5) position angle of the slit (north-eastward); (6) extraction window and its corresponding scale in parsecs; (7) date of the observation; (8) exposure time of the spectra; (9) filter used for the sharp-divided image (Márquez & Moles 1996) obtained also from the HST archive. The latter are shown in Appendix B.

ID	Other name	Filename	Proposal ID	PA	Extr. window	Obs. date	Exp.Time	Im.Filter
		(_sx2/_x2d)		(°)	pix (pc)	(yy-mm-dd)	(s)	
(1)	(2)	(3)	(4)	(5)	(6)	(7)	(8)	(9)
NGC2685*	IRAS 08517+5855	o63n01020	8607	54	3 (21)	2001-05-06	3097	F814W
NGC3245	IRAS 10245+2845	o57205030	7403	203	5 (23)	1999-02-02	2715	F547M
NGC4374	M 84	o3wn01010/2010	7124	104	5 (17)	1997-04-14	1993/2223	F814W
NGC4486	M 87	o67z01010/2010	8666	164	5 (21)	2001-03-25/27	1360	F606W
NGC4552	M 89	o51203020	8472	78	5 (4)	2000-06-19	1440	F555W
NGC4594	M 104	o4d303030	7354	250	5 (15)	1999-02-05	280	F814W
NGC4676B*	IC 820	o67q09030	8669	195	3 (144)	2002-02-20	740	F814W
NGC4698	IRAS 12458+0845	o4e022010/20/30	7361	259	5 (16)	1997-11-24	900/933/840	F606W
NGC4736	M 94	o67110030	8591	50	5 (6)	2002-07-15	1440	F555W

Notes. *: spectrum obtained with a slit width whose plate scale was 0.102″ pix^{-1}. It is 0.051″ pix^{-1} for the rest of the objects.

2.3   Analysis of the nuclear spectra

The host galaxy contribution on the nuclear spectra of a low-luminosity AGN may be significant, thus the starlight should be subtracted to robustly measure the kinematics and fluxes of the emission lines. However, due to the small wavelength range covered for the HST/STIS data (572 Å), we decided not to perform the subtraction as the line-free continuum regions of the spectra are small for a proper stellar continuum modeling. Moreover, Constantin et al. (2015) (hereafter C15) proved that the correction is negligible for HST/STIS spectra in this wavelength range due to the small aperture of the instrument, which reduces the contaminant starlight from the host galaxy.

The starlight was modeled and subtracted for the Palomar data using a penalized PiXel fitting analysis (PPXF version 4.71 Cappellari & Emsellem 2004; Cappellari 2017). This differs to the stellar modeling applied by Ho et al. (1993), in which template galaxies were used instead (see Sect. 2.5.2). The methodology of the stellar subtraction was done following a similar technique as in Cazzoli et al. (2018) (hereafter C18), similarly to the modeling of the spectral emission lines, which is explained in below. For each object, the restframe velocity used in the analysis is defined as: $c \times z$ (column 5, Table 2.1). The starlight decontamination for the Palomar data and all the line modelings to the different spectra are found in Appendices A.1 and A.2, respectively.

2.3.1   Emission line fitting

Each of the emission lines present in the spectra ([S II], [N II], Hα and in some cases [O I], Table 2.3 column 4) were fit with Gaussian functions to derive their properties: central wavelength, line width (σ) and full width half maximum (FWHM), flux, and f_{blend}, defined as the percentage of the broad component flux with respect to the total flux of the Hα-[N II] lines. The fitting was performed using a nonlinear least-squares minimization and curve-fitting routine (LMFIT) implemented in PYTHON, which is an extension of the Levenberg-Marquardt method found in the SCIPY package.

The modeling of the lines was performed with three different methods using either [SII], [OI], or both as templates for the Hα-[N II] complex (Cazzoli et al. 2018 and references therein). As Hα and [N II] lines are generally blended, we do not use them directly, because the overall fit could be affected. Among those emission lines available, the best lines are the [O I] lines, as they are separated enough between them to serve as good templates. However, these lines are not always available or have low S/N (e.g., see Fig. A.13), so we have to rely on [S II] lines like in previous works (Ho et al. 1997a; Balmaverde & Capetti 2014; Constantin

et al. 2015). Therefore, the three different models we can apply are [S II], [O I], or both (if available) as the reference lines, because they are usually not strongly blended as Hα-[N II]. Following Cazzoli et al. (2018), the first method is known as S-method, and it consists of fitting the [S II] lines and then tie to them the central wavelengths and widths of all the other narrow lines. The second method (O-method) is the same as S-method, but it uses the [O I] lines as references. The third model is a mixed model (M-model), which uses [S II] and [O I] lines simultaneously as a template for the Hα-[N II] blend.

We tested different methods of fitting since the forbidden lines ions of the spectra have different critical densities ([S II] $\sim 10^3$ cm^{-3}, [O I] $\sim 10^6$ cm^{-3}, and [N II] $\sim 10^4$ cm^{-3}, respectively) caused by the possible stratification in the NLR. Therefore, the profiles of each line could be different (see Balmaverde & Capetti 2014).

The fluxes of the two [N II] lines and the two [O I] lines were set to follow the relations 1:3 and 1:2.96, respectively (Osterbrock & Ferland 2006). For more details on the methods and the constraints, we refer to C18.

As with C18, in order to prevent over fitting, we calculated a parameter, ε_c, which is the standard deviation of a region of the continuum that did not have any absorption or emission line. This parameter was always calculated in a 50Å -length region of the spectra. We compared it with the standard deviation of the residuals under each emission line, and if $\varepsilon^{line} < 3 \times \varepsilon_c$, then the fit is considered to be reliable. For the cases where ε_c was not sufficient in order to differentiate between two different fits, we used the χ^2 of the fit and/or visual inspection as the last criteria to select the final model.

The procedure was organized in three steps. Firstly, we fit the continuum to a linear least squares model using the regions between the emission lines visible in the spectra.

Secondly, all lines were fit to a single Gaussian profile (hereinafter, "narrow component") with the same parameters for all of them. If the fit was satisfactory for the reference lines ([S II] or [O I]), but not for [N II] and Hα, then a broad Gaussian profile was added to Hα (hereinafter, "broad component"). However, if the fit was not reliable in any of the lines, or if the narrow component had a large velocity (≥ 300 km s^{-1}), then a second component was added to all the lines (hereinafter, "secondary component").

Thirdly, if the Hα-[N II] blend was not well-reproduced (significant residuals) with a narrow plus a secondary component, then we added a broad component in Hα. All the line modelings are presented in the figures of Appendix A.2.

This method was not sufficient for the most complicated cases, for which additional restrictions were required. For example, the modeling of the reference lines for the NGC 4594 HST/STIS spectrum was good enough, but the maximum of the profiles of [N II] and Hα seemed to be shifted (~ 1 - 3 Å) from the maximum of the Gaussian profiles. Therefore, we

shifted 1Å the maximum of the secondary Gaussian component to improve the fit. This produced a change in the velocity compatible within the initial error estimation.

For the HST/STIS spectra of two galaxies (namely NGC 4374 and NGC 4552), the [S II] lines were so blended, and the [O I] lines almost absent, that it was challenging to perform the modeling using them as reference (Fig. A.11 and A.13). Therefore, we decided to fit the spectrum of a region situated a few pixels away from the nucleus and use this result to model the narrow component of the nuclear region. This was motivated by the assumption that the narrow component is tracing the kinematics of the disc of the galaxy, thus it should also be visible in regions outside the very center of the system. Moreover, by moving to an outer part of the galaxy, the contribution of the BLR (if present) should disappear due to its unresolved nature at HST scale. As the disc should be rotating with the same velocity dispersion, a modeling of this component in the spectra of an outer region would give approximately the same contribution we should expect in the nucleus, but with a shift in velocity. We note, though, that for some galaxies this condition is not completely true, as the disk velocity dispersion was found to increase towards the center (for NGC 3245 and NGC 4594 see Barth et al. 2001; Emsellem & Ferruit 2000, respectively). This is discussed in more detail for each individual case in Sect. 2.6.3.

An additional assumption was made for NGC 4374. If the narrow component was fixed as it was with the previous method, when proceeding with the rest of the modeling, the secondary component was broad enough to be compatible with a very broad AGN component of $\sigma >$ 800 km/s. The addition of a third Gaussian in the Hα-[N II] complex instead generated a narrow profile to fit a peak that is visible in the spectrum (see Fig. A.11). Therefore, we exchanged the secondary and broad components to improve the fit.

We fixed the velocity dispersion of the narrow component for NGC 4374 and NGC 4552 with this method and allowed the velocity to vary in the nuclear spectra. This improved the final residuals (also visually) with respect to the normal fitting process.

The velocities (V) and line widths (σ_{line}) obtained for each galaxy, as well as the number of components and the model used to fit the reference lines, are indicated in Table 2.3. The S-method was used for all cases except for the Palomar spectrum of NGC 4552, for which we used the O-method. The line width has been corrected from the instrumental width by doing $\sigma_{\text{line}} = \sqrt{\sigma_{\text{obs}}^2 - \sigma_{\text{inst}}^2}$, where the value of σ_{inst} ($\sim$1.34 Å) has been taken from the HST/STIS handbook, and from Ho et al. (2009) for the Palomar data ($\sim$2.2 Å).

2.4 Modeling of HST/STIS data

Table 2.3 Results from the analysis of the optical spectra. From left to right: ID: object designation; Inst.: HST/STIS or Palomar spectra; Comp.: components used for the best-fitting model with N, S and B referring to narrow, second, and broad components, respectively; [OI]: if these lines are present in the spectrum or not (Yes/No); velocity (V) and velocity dispersion (σ) for each component for each of the reference emission lines; f_{blend}: contribution of the broad component to the total flux of the Hα-[N II] complex.

ID	Inst.	Comp.	[OI]	$V_N^{[SII]}$ (km s^{-1})	$\sigma_N^{[SII]}$ (km s^{-1})	$V_S^{[SII]}$ (km s^{-1})	$\sigma_S^{[SII]}$ (km s^{-1})	$V_B^{H\alpha}$ (km s^{-1})	$\sigma_B^{H\alpha}$ (km s^{-1})	f_{blend} (%)
(1)	(2)	(3)	(4)	(5)	(6)	(7)	(8)	(9)	(10)	(11)
NGC 2685	HST/STIS	N	N	80 ± 1	63 ± 12	-	-	-	-	-
	Palomar	N	Y	-10 ± 1	70 ± 10	-	-	-	-	-
NGC 3245	HST/STIS	N + B	N	134 ± 29	172 ± 6	-	-	424 ± 12	998 ± 6	47
	Palomar	N + S	Y	-216 ± 9	25 ± 40	94 ± 17	136 ± 21	-	-	-
NGC 4374	HST/STIS	N + S + B	Y	-275 ± 13	146 ± 14	362 ± 5	281 ± 24	693 ± 7	1432 ± 37	65
	Palomar	N + S	Y	117 ± 4	51 ± 29	33 ± 56	395 ± 71	-	-	-
NGC 4486	HST/STIS	N + S	Y	395 ± 4	198 ± 22	-101 ± 378	**655 ± 18**	-	-	-
	Palomar*	N + S + B	Y	-478 ± 4	238 ± 5	96 ± 6	286 ± 9	-285 ± 145	908 ± 141	5
NGC 4552†‡	HST/STIS‡	N + S + B	Y	-103 ± 47	157 ± 18	501 ± 38	249 ± 50	541 ± 53	1360 ± 20	70
	Palomar†	N	Y	56 ± 59	282 ± 68	-	-	-	-	-
NGC 4594	HST/STIS	N + S + B	N	70 ± 15	108 ± 26	66 ± 152	**554 ± 6**	519 ± 120	1677 ± 18	16
	Palomar	N + B	Y	-11 ± 4	215 ± 7	-	-	698 ± 26	956 ± 41	33
NGC 4676B*‡	HST/STIS‡	N + B	N	527 ± 40	198 ± 12	-	-	336 ± 16	748 ± 12	89
NGC 4698	HST/STIS	N + B	N	55 ± 19	90 ± 5	-	-	273 ± 97	1375 ± 9	39
	Palomar	N	Y	-7 ± 2	98 ± 8	-	-	-	-	-
NGC 4736	HST/STIS	N + B	Y	127 ± 14	84 ± 12	-	-	330 ± 1	738 ± 4	82
	Palomar	N	Y	23 ± 4	105 ± 10	-	-	-	-	-

Notes. The galaxies in bold show a secondary component in the HST/STIS spectrum classified as outflow (see Sect. 2.6.2 and Fig. 2.2). * indicates that the broad component detection in Hα-[N II] lines is not well-constrained (Sect. 2.6.3). † the data for which the O-model was used to model the emission lines (see Sect. 2.3.1). ‡ marks the spectra with low S/N (Sect. 2.2).

After the summary of the overall modeling of the HST/STIS spectra, we compare the results with the work by Constantin et al. (2015). All the results from the spectra modeling are found in Appendix A.2.

2.4.1   Overall modeling summary

Despite there being three possible models to fit the lines, we selected the S-method to model all the HST/STIS spectra for different reasons. For five LINERs, the spectrum was lacking the [O I] lines either for the wavelength range coverage or because they were not detected (Table 2.3 column 4). For two LINERs, NGC 4374 and NGC 4552, the S/N of the [O I] lines was rather faint and difficult to model (see Sect. 2.3.1). For NGC 4736, the fit presented no significant difference when applying S-/O-/M-models, so we decided to use the simplest model that could explain the observed spectra, in this case, the S-model. For the remaining object, NGC 4486, although one of the [O I] lines is clearly visible (Fig. A.12), the modeling was better with the S-method (the χ^2 improved about ~30%). All the fits to the different spectra can be found in the Appendix A.2.

Generally, the modeling of both [S II] and [O I] lines are inside the $3\varepsilon_{\text{line}}$ limits for all LINERs except for NGC 4374 (see Fig A.11). However, in the case of [N II] - Hα, ε_{c} is approximately equal to $3\varepsilon_{\text{line}}$ for NGC 4594 and $\sim 4\varepsilon_{\text{line}}$ for NGC 4374 despite the addition of the very broad component (Fig A.14). In all the other objects, ε_{c} is within $3\varepsilon_{\text{line}}$ limits, thus we consider the fit not to be well-constrained for these two cases.

We find that NGC 2685 is the only spectrum that can be modeled with a single narrow component in all the emission lines, and NGC 4486 is the only spectrum well-reproduced with a narrow plus a secondary component. No very broad component is required for them (Fig. A.9 and A.12). For the other seven LINERs, we found that four out of nine need one narrow Gaussian component to model all the forbidden lines, and an additional broad (BLR) component in Hα (see Table 2.3 column 3). On the other hand, the remaining three LINERs need a secondary component to model the forbidden lines and narrow Hα in addition to a very broad component in Hα. In summary, a secondary component is needed in four out of the nine analyzed galaxies, and a very broad component in Hα is needed in seven out of the nine LINERs.

2.4.2   Comparison with Constantin et al. 2015 (C15)

Most of the galaxies shown here (7 out of 9; 77% of the sample) have already been analyzed by C15, where they report, for the first time, the detection of broad components in eight objects of their total sample. They have studied a total of 113 AGNs with HST/STIS and
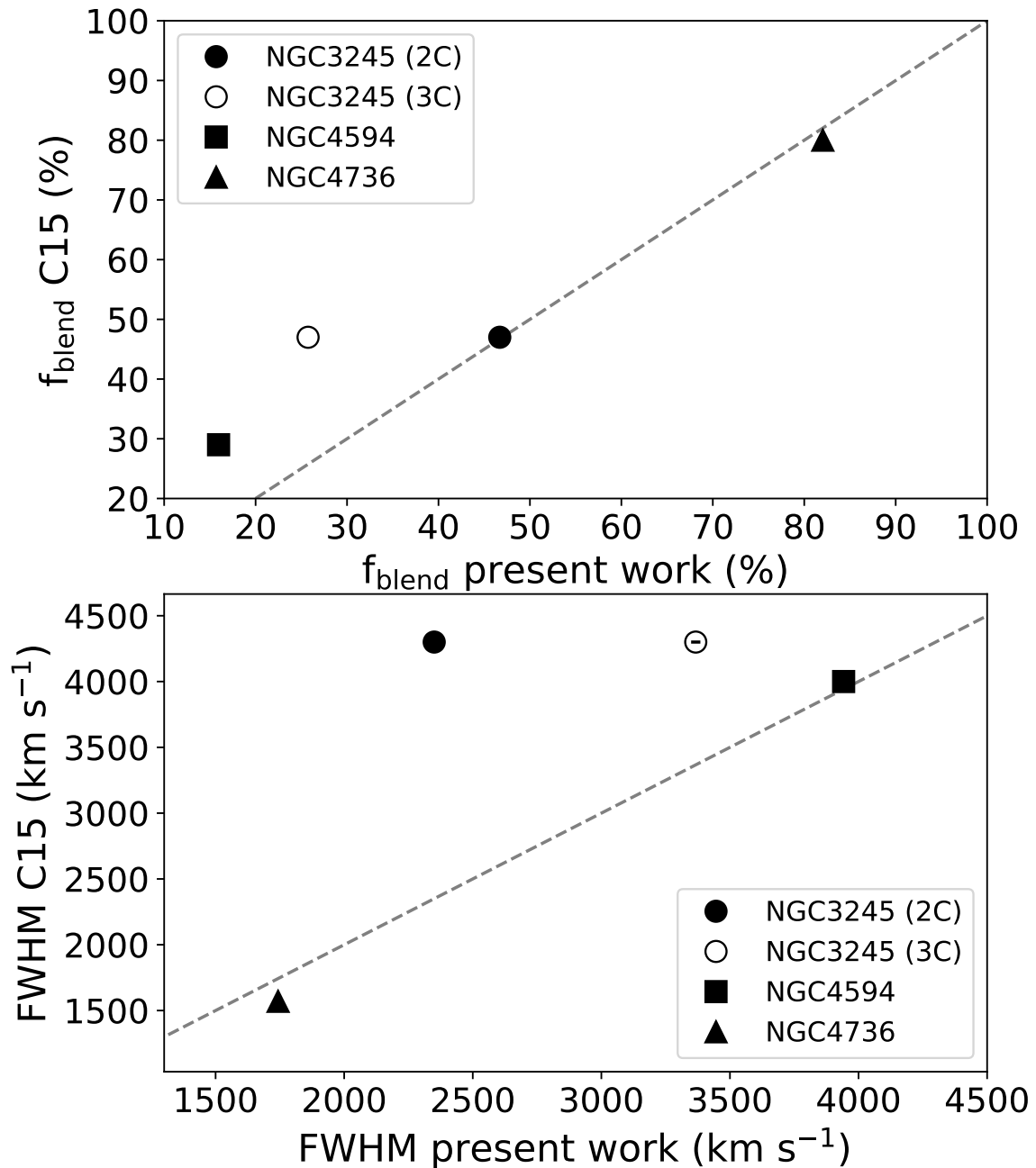
Fig. 2.1 Comparison of the contribution in percentage of the broad component of Hα to the total flux of the Hα-[N II] complex (upper panel) and the FWHM of the very broad component (lower panel) derived in this work versus C15. Each symbol represents a different LINER as indicated in the legend. The filled (empty) circle represents the two- (three-) component fit to NGC 3245. The gray dashed line is the one-to-one comparison.

MMT (Multiple Mirror Telescope) spectroscopic data to analyze the emission lines and to give constraints on the ionizing mechanisms present in the galaxies. The reduction process of the HST/STIS data and the line modeling, for which they used the [S II] lines as template for the Hα-[N II] blend, follow a similar technique to ours. For the galaxies in common, they found a broad Hα emission for three of them (NGC 3245, NGC 4594, NGC 4736) in agreement with our findings (see Table 2.3 and Fig. A.10, A.14 and A.17).

A direct comparison of the contributions of the very broad component to the Hα-[N II] complex and the FWHM for these three galaxies can be seen in Fig. 2.1. Galaxy NGC 3245 is represented with an empty or filled symbol depending on the number of components used for the modeling. Figure 2.1 shows that, if we consider our two-component modeling, the contribution of the very broad component to the Hα - [N II] complex is compatible in both analyses. Nevertheless, the FWHM is more similar in the case of the three-component fit. This could be a direct consequence of the number of components. If we have two Gaussians for each emission line plus a broad component, its contribution to the global fit is going to be smaller than for a modeling of a single Gaussian plus a broad component, as the total flux of Hα - [N II] is going to be distributed among more components.

The number of components for the modeling of NGC 4594 and NGC 4736 is the same as C15 (see Table 2.3; Fig. A.14, A.17), thus no more additional models were considered. In both cases, the results are in agreement with C15, although these authors indicate that the very broad component of NGC 4594 is very difficult to interpret (see Sect. 2.6.3). This very broad component dominates over the narrow to the Hα line flux in both analyses, as can be seen in Fig. A.14. The broad component for NGC 4736 contributes significantly to the total flux of both Hα and the whole Hα-[N II] complex, as can be seen in Fig. 2.1.

For three galaxies (NGC 4374, NGC 4552 and NGC 4698; Fig. A.11, A.13, A.16, respectively) we derive a very broad component ($> 1300\,\mathrm{km\,s^{-1}}$) that C15 do not report in their analysis. According to our modeling, the fit is improved in the three galaxies by adding a very broad Hα component to the Hα-[N II] complex. These detections are individually discussed in Sect. 2.6.3.

2.5 Modeling of Palomar data

After the summary of the overall modeling of the Palomar spectra, we compare the results with the work by Ho et al. (1997a). All the results from the spectra modeling are found in Appendix A.1.

2.5.1 Overall modeling summary

The Palomar data was analyzed by Ho et al. (1997a) (hereinafter H97), who were also looking for the possible presence of a very broad component in the spectra. We analyzed eight galaxies from their sample by testing all three different fitting methods as described in Section 2.3. This is possible for the ground-based dataset, as the [O I] lines are visible in all cases (Table 2.3, column 4; see figures in Appendix A.2).

The best fitting is obtained with the S-method for nearly all the spectra (7 out of 8), as no significant improvement was seen when using the other methods. The galaxy NGC 4552 was the only one for which we selected the O-method, due to the severe blending of the [S II] lines (see Fig. A.13).

We find that four galaxies (NGC 2685, NGC 4552, NGC 4698, and NGC 4736) can be modeled with a single narrow component in all the emission lines, and three galaxies (NGC 3245, NGC 4374, and NGC 4486) need a narrow plus a secondary component, with NGC 4486 requiring a very broad component to obtain a proper model of the spectrum (see Sect. 2.6.3). Galaxy NGC 4594 is the only one whose spectrum is modeled with a narrow Gaussian component for all the forbidden lines and an additional broad Hα component (see Fig. A.14). In summary, a very broad component in Hα is needed in two out of the eight galaxies, and a secondary component is needed in three out of the eight LINERs (see Table 2.3).

2.5.2 Comparison with Ho et al. 1997 (H97)

In the search for broad emission lines carried out by H97, they analyzed the data of the galaxies from Ho et al. (1995), whose line profiles showed (or at least hinted at) the presence of a broad Hα emission. This reduced the total sample from 486 to 211 galaxies, from which only in 34 objects this broad feature was detected. The possible existence of a broad component in eight of the common objects is discussed below.

The methodology used in H97 to analyze the spectra consisted of an initial stellar subtraction using the spectra of galaxies devoid of emission lines (i.e., "template galaxies method", Ho et al. 1993 and references therein) and then a line modeling. The template galaxies method was also tested by C18, although when applying the PPXF routine to the spectra of the templates (see Sect. 2.3), some weak emission lines were visible in six out of the ten template galaxies. Thus, we used the PPXF method instead of the template galaxies method , as they need to be treated very carefully in order to avoid the inclusion of emission lines produced by the interstellar medium (see C18 for further details).

The line modeling in H97 consisted of a single Gaussian fit to the [S II] lines, considering them as reference to model the Hα-[N II] lines. Similarly to our methodology, an additional broad component could be added to the Hα line only when necessary (see Sect. 2.3.1).

The spectra modeling for four of the galaxies (NGC 3245, NGC 4486, NGC 4594, and NGC 4698) is shown in H97. Three of them (namely NGC 4552, NGC 4594, and NGC 4698) are among their null detection of a broad component, whereas NGC 2685, NGC 3245, and NGC 4486 are among the ambiguous cases. For these, according to H97, the cause of ambiguity is the template chosen for the starlight subtraction.

In our analysis, thanks to the use of ppxf, we minimized possible source of ambiguity related to the stellar modeling and subtraction (see Sect. 2.3 and C18). In our modeling for these same spectra, we find a broad component in two out of the eight common objects (NGC 4486 and NGC 4594). Only for NGC 4594 is this broad component also visible on the HST/STIS spectra (see Fig. A.14). This result indicates that the two objects, or at least NGC 4594, could initially have been classified as type 1 LINERs also with ground-based spectroscopy using a different starlight decontamination method and a different line modeling. For the other galaxy, NGC 4486, the existence of a broad component has been a matter of debate in previous works with both ground- and space-based spectroscopy (e.g., Harms et al. 1994; Ho et al. 1997a; Walsh et al. 2013; Constantin et al. 2015, see Sect. 2.6.3). It was described in H97 as showing weak wings at either side of [N II] lines. Although when adding a broad component to the fitting their residuals improve, they say that this component could be a product of some ambiguities with the modeling, so they decided not to include it in the analysis. Its contribution to the global fit is rather weak (5%), but we also improve the residuals from our fitting by including it (Fig.B4). We discuss its presence or absence in our ground and space data in Sect. 2.6.4.

2.6   Results and Discussion

We note that, given the difference among the slit widths between Palomar and HST/STIS data (see Sect. 2.3.1), we consider the latter results as the most accurate in characterizing the innermost parts of the AGN. Hence, the following kinematical analysis is only focused on them. Apart from this, the possible discrepancies between the measured narrow-component velocities from ground- to space-based data (see Table 2.3) may be produced by the different alignment of the slits.

2.6.1   Overall summary of kinematics

The wavelength-shift and line-width of each of the Gaussian components used to model the spectra are converted into a measurement of velocity and velocity dispersion of the ionized gas kinematics. We can associate them to a kinematic component of the galaxy. With this aim, we followed the velocity-velocity dispersion (V-σ) classification similar to the one used in C18, which is shown in Fig. 2.2.

This figure is divided into four different regions, associated with rotation, outflows, inflows and candidates for rotational motions. Dividing limits of the regions have been established by C18 by measuring the gas velocity field from the 2D spectra of the type 1.9 LINERs within their sample, and estimating the maximum broadening of the emission lines associated with rotational motions. The C18 conservative upper limit for this component is $\sim 400\,\mathrm{km\,s^{-1}}$, although the typical value of velocity dispersion ($\sim 200\,\mathrm{km\,s^{-1}}$) in their sample is well below this limit (see Sect. 5.2 in C18). This limit is supported by the fact that the ionized gas in rotation usually produces a broadening of the lines that is translated into velocity amplitudes up to $\sim 300\,\mathrm{km\,s^{-1}}$ (see e.g., Cappellari et al. 2007; Epinat et al. 2010). They found that the regions outside the nuclear zone in the 2D spectra had amplitudes $\sim 300\text{-}400\,\mathrm{km\,s^{-1}}$, thus associating this part of the V-σ diagram to candidates for broadening produced by rotational motions.

As for the velocities, the narrow component of type 1.9 LINERs typically has values $\pm 50\,\mathrm{km\,s^{-1}}$. Thus, when the σ is larger than $300\,\mathrm{km\,s^{-1}}$, these broadenings cannot be addressed as rotational motions, but instead as nonrotational motions. Then, we would consider them as candidates for the presence of outflows or inflows. For the intermediate cases, the targets are considered as candidates for nonrotational motions.

For the secondary component, C18 found that the velocity dispersion present typically values from 400 to $800\,\mathrm{km\,s^{-1}}$. In this case, the broadening is probably related to turbulent nonrotational motions. We can see in Fig. 2.2 that the velocities for the secondary component of type 1.9 LINERs present typical values ranging from $-200 \leq V_S \leq 100\,\mathrm{km\,s^{-1}}$ (see C18). For this analysis, we decided to apply similar limits to C18, because the complete study of the gas velocity field could not be done with the present dataset. Thus, it has to be noted that the region limits could be different for type 2 LINERs if a similar analysis is considered. However, the physical interpretation of the position in the diagram for the galaxies with a secondary component is unlikely to change dramatically, given their large velocity dispersion $>500\,\mathrm{km\,s^{-1}}$, and hence their position on Fig. 2.2.
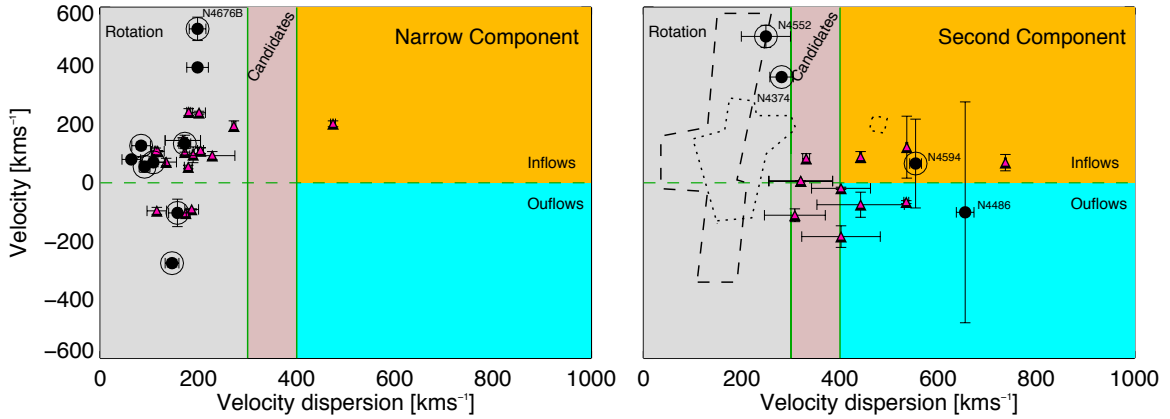
Fig. 2.2 Velocity dispersion versus velocity derived for narrow (left panel) and secondary (right panel) components used to model the HST/STIS spectra for both type 1.9 from C18 (red triangles) and type 2 (black filled circles) LINERs. An additional black circle marks those cases for which a broad component is needed in HST/STIS spectra. All type 1.9 LINERs from C18 show a broad component. Each of the marked regions indicates to which kinematic component the modeled component can be associated. The orange region indicates inflows, the blue region indicates outflows, the pink region indicates candidates for both inflows and outflows, and the gray region indicates rotation. On the right panel, the contours of the narrow components are shown for both type 1.9 (dotted lines) and type 2 (dashed lines) LINERs.

2.6.2 Classification of the velocity components

As mentioned in the previous section, if the velocity dispersion is in the range up to $300 \, \text{km s}^{-1}$, the component may be associated with the presence of a rotating disk in the galaxy. The broad Hα component is not considered in this figure, as it is interpreted unequivocally as a manifestation of the BLR of the AGN. The narrow component, present in all the ground- and space-based spectra, shows velocity dispersions consistent with being produced by rotation. On the other hand, the secondary component is always broader than the narrow one, and it has a higher spread on the velocity dispersion for both type 1.9 and type 2 LINERs, with typical values higher than $\sim 400 \, \text{km s}^{-1}$. These values are consistent with the presence of nonrotational motions (outflows or inflows).

In Fig. 2.2, only four galaxies of the HST/STIS sample (NGC 4374, NGC 4486, NGC 4552, and NGC 4594) needed a secondary component on the line modeling. From these, only for NGC 4374 and NGC 4486 is a second component added to the Palomar spectra. NGC 4486 and NGC 4594 line widths of the secondary component are consistent with being caused by the presence of nonrotational motions, which was also suggested by previous results (e.g., the Hα morphology of NGC 4486 shown in Masegosa et al. 2011). For the remaining cases, the line widths are compatible with being produced by rotational motions, although NGC 4374

could be a possible inflow candidate. Also in Masegosa et al. (2011), the possible presence of an outflow seen with the Hα emission was discarded (or inconclusive) for this galaxy due to the dust lanes that obscure and limit the access to the nuclear Hα morphology. For NGC 4552, a bipolar nuclear outflow was reported by Machacek et al. (2006) with *Chandra* images (0.5 - 2 keV).

The other galaxy in the sample that has been previously reported as hosting an outflow is NGC 3245. The Hα image of this galaxy shows an unresolved nucleus and a structure indicative of the presence of an outflow (Masegosa et al. 2011), which is also supported by the kinematic analysis of (Walsh et al. 2008). However, in our modeling of the HST/STIS spectrum, a secondary component is not needed (see Sect. 2.6.3) and, if used, the resulting velocity and velocity dispersion would be compatible with being caused by rotation ($V_s = -40 \pm 25 \, \mathrm{km \, s^{-1}}$; $\sigma_s = 194 \pm 56 \, \mathrm{km \, s^{-1}}$). Using the Palomar data instead, a secondary component is clearly required to satisfactorily reproduce the line profiles with low residuals (Fig. A.10). In this case, the secondary component also has a velocity, and velocity dispersion in agreement with rotation, so it is not clear if it could be associated with nonrotational motions.

We can directly compare our values with the results from the HST/STIS analysis of 12 type 1.9 LINERs from C18. It is clear that the narrow component for both samples can be explained by rotational motions (see Fig. 2.2). The typical values of velocities and velocity dispersion (see Sect. 2.6.1) are similar except in some cases. Galaxy NGC 4676B has a velocity higher than $500 \, \mathrm{km \, s^{-1}}$. It is a merging galaxy, and its modeling is not well-constrained (see Fig. A.15 and Sect. 2.6.3). In Wild et al. (2014), they quote a big velocity gradient oriented in a similar direction to where the HST/STIS slit is allocated, which may suggest that the velocity of the narrow component could be affected by this. Galaxies NGC 4374 and NGC 4486 have larger velocities of the narrow component than should be expected (see Sect. 2.6.1). For the latter, Noel-Storr et al. (2003) also found that the narrow component was not rest frame in the central spectrum. For the first, they might be produced by the large velocity gradients present in the innermost parts and that we are not considering individually in this analysis (see Sect. 2.6.3). On the other hand, the values for the secondary component are more spread throughout the diagram, including two galaxies in the range in which the broadening could be explained by rotation. Velocities for the secondary component of type 1.9 LINERs are more concentrated than those for type 2 LINERs, with values ranging from $-110 \leq V_S \leq 500 \, \mathrm{km \, s^{-1}}$ for the latter. The velocity dispersion range is more similar for both samples, ranging from $250 \leq V_S \leq 800 \, \mathrm{km \, s^{-1}}$. The proportion of objects within the C18 sample that present a secondary component is slightly higher than that of type 2 LINERs (7 out of 11 versus 4 out of 9). This result could be a consequence of the orientation of the slit, which could not capture the full extension of putative outflows or inflows. However, this

comparison could be not completely representative of these populations, due to the modest amount of type 2 LINERs in the sample.

2.6.3 Individual comments for the galaxies

This section is organized taking into account the components used to fit the HST/STIS spectra, as indicated in Table 2.3 (column 3). The figures with the spectra modeling are in Appendix A.2. As in all cases the BLR components in our analysis have large velocity shifts, we tried to set the velocity of the BLR component to zero in order to statistically confirm its true velocity. The majority of the models presented worse residuals both visually and statistically (i.e., difference in $\chi^2 > 15\%$ worse) than with the final velocities (see Table 2.3). We discuss the results for the galaxies that did not change much with this model individually.

Model with only narrow components

As mentioned in Sect. 2.4, we have been able to model only two of the galaxies (NGC 2685 and NGC 4486) with a narrow or a narrow plus a secondary component (see Table 2.3). The HST/STIS spectra of **NGC 2685** has been analyzed in two works. González Delgado et al. (2004) compare the main ionizing mechanism of this LINER measured with both ground- and space-based instruments, although the data-set for STIS use the G430L grating. It is the only galaxy in their analysis that requires a single narrow Gaussian component to reproduce the observed spectrum. C15 applied exactly the same modeling for the same data-set using only narrow components. Hence, our results are consistent with previous ones. The galaxy **NGC 4486** is a complex object with a well-known radio jet. Noel-Storr et al. (2003) analyzed this spectrum initially and found that the presence of a broad component improved the global fit of the spectrum visually and statistically with respect to a single Gaussian component per line. The velocity of the narrow component they measure in the central pixel is $\sim 260\,\mathrm{km\,s^{-1}}$. Neither Walsh et al. (2013) nor C15 found a broad Hα component when modeling the emission lines. Walsh et al. (2013) reported the existence of velocity gradients in the innermost regions of the slit, as in the case of NGC 4374 (see Sect. 2.6.3). The velocity dispersion can be as high as $600\,\mathrm{km\,s^{-1}}$ in the central row, and it decays in the following regions. In our case, this structure is integrated in our spectrum. Our fit does not improve significantly by adding a very broad component to a two component fitting (only 5%), thus, only two components were used. In this case, the secondary component is consistent with an outflow (see Table 2.3 and Fig. 2.2). However, a second component with a large width could be also the result of the strong gradient in the velocity dispersion reported by Walsh et al. (2013). For the Palomar spectrum, a broad

component improves the fit by 18%, although the ε_c was already smaller than $3\varepsilon_{line}$ (see the residuals of the fit without the broad component in Fig. A.12). Given this and the unclear detection in previous works, we should consider the (non)detection in the Palomar (HST/STIS) spectrum as ambiguous. The nondetection of the HST/STIS data implies that this component, if it exists, should not be attributed to typical BLR clouds orbiting nearby the black hole, but instead to other phenomena on larger scales (e.g., inflows/outflows).

Models with broad BLR-originated component

The remaining seven galaxies were found to require a very broad component with the emission-line fitting analysis. The galaxy **NGC 3245** was classified as an intermediate case between a LINER and a transition object (Ho et al. 1997a). The HST/STIS data was firstly analyzed by Barth et al. (2001), who studied the dynamics of the ionized gas in this galaxy. They suggested the possible presence of a broad component in Hα, which was modeled by C15 (see Sect. 2.4.2). Their emission line modeling consisted of three Gaussian profiles fitted to [N II] - Hα lines (tied in velocity but allowed to vary in σ). In our case, visual inspection indicates that only one narrow component is sufficient to fit the lines, although with a secondary component, the χ^2 of the fit improves by approximately 16%. We prioritized the simplest model that is able to describe the observed spectrum (S-method; see Fig. A.10). In either case, a broad component in Hα was necessary to model the line profiles.

The spectrum of **NGC 4594** obtained with the TIGER 3D spectrograph shows some irregularities in its nucleus and a strong velocity gradient ($\sim 300\,\mathrm{km\,s^{-1}}$) near the center (Emsellem & Ferruit 2000). However, as neither the HST or Palomar slits are located along the major kinematic axis of the galaxy (see Fig. A.14), we would not expect a strong line broadening caused by the ordinary disk rotation. The Hα emission is concentrated in the spiral arms and in the nuclear region of the galaxy (Masegosa et al. 2011). There has been some debate about the presence of a broad Hα component in the spectra of this galaxy. There are studies supporting both its presence (Kormendy et al. 1996; Walsh et al. 2008) and its absence (Ho et al. 1997a; Nicholson et al. 1998). Therefore, a methodology that takes into account all the different possibilities, like the one presented in this work, is required to understand the true nature of this LINER nucleus. The spectrum presents wings in the Hα - [N II] lines that was initially attributed to the existence of a BLR with data from the HST/Faint Object spectrograph (Nicholson et al. 1998). On the one-to-one row analysis by Walsh et al. (2008), they show that there are large velocity gradients in the nuclear regions covered by the HST/STIS slit. These gradients could be producing the observed line profile, as indicated in Sect. 2.3.1. The best fit to the HST/STIS spectrum is obtained with two components plus a broad component, such as C15 (see Sect. 2.4.2 and Fig. A.14). The residuals are still higher

than $3\varepsilon_{line}$, they have been reduced from 3.2 to 2.7 for [N II]λ6548Å, and the χ^2 of the overall fit is improved by 15% by adding the broad component. If we were to set the velocity of the BLR component to zero, the χ^2 would be only 3% worse, and the σ would be $10\,\mathrm{km\,s^{-1}}$ less broad. However, as this component has a negligible flux contribution to the total Hα-[N II] blend, and it is the broadest line we found in our study (see Table 2.3), statistically we would expect to find no difference between both modelings. However, visually, the red wing of the [N II]6584Å line is better reproduced with the velocity as indicated in Table 2.3. Therefore, we decided not to set the velocity of the broad Hα component to zero.

The galaxy **NGC 4736** is an interesting case, as the broad component is clearly visible in the HST/STIS spectrum (Constantin & Seth 2012, C15), but it has never been reported from ground-based observations (Ho et al. 1997a; Constantin & Seth 2012). The size of the slit aperture is crucial in this object to classify it properly. The broad component has also been reported with a principal component analysis (PCA) tomography method applied to integral field unit (IFU) data taken several years after the HST/STIS spectra (Steiner et al. 2009). In our analysis, all the forbidden lines, except the Hα-[N II] complex, are well-modeled with a single narrow Gaussian component. For Hα, a broad component of $\sigma_{\mathrm{B}} \sim 740\,\mathrm{km\,s^{-1}}$ is needed (see Sect. 2.4.2 and Fig. A.17). The FWHM of this component is within the limit of being associated with the BLR of the galaxy, which is also the case for NGC 4676B (see below). Both σ_{B} are only slightly higher ($\sim 100\,\mathrm{km\,s^{-1}}$) that the σ_{S} for NGC 4486.

C15 did not report additional very broad detections for the other galaxies in common (NGC 2685, NGC 4374, NGC 4486, and NGC 4552; see Sect. 2.4.2). However, in our analysis, two of them present a very broad component, whereas the other two only need a narrow, and a narrow plus a secondary component (NGC 2685 and NGC 4486, respectively), as previously indicated (see Sect. 2.6.3).

For the modeling of NGC 4374 and NGC 4552's nuclear spectra, we used a different technique from the rest of the galaxies. As explained in Sect. 2.3.1, in both cases the [O I] lines are barely detected, therefore only the S-method could be applied, but [S II] are severely blended.

The HST/STIS spectra of **NGC 4374** were first analyzed by Bower et al. (1998), and a few years later by Walsh et al. (2010). In the former work, they used two Gaussian components to fit the lines, considering that they were tracing two dynamically different gas components, (a rotating disk and a low-velocity component unrelated to the disk). The latter showed that the profiles of [N II]-Hα could be affected by the rapidly rotating NLR kinematics, although their analysis does not exclude the presence of a broad component. As is the case of NGC 4594, the presence of a BLR-originated component is debated. In C15, they concluded that a broad component in Hα was not needed (see Sect. 2.4.2). Nevertheless, its presence was not

ruled out by Walsh et al. (2010) in the three innermost rows, where a peaked central velocity dispersion, associated with the emission-line disk, is related to large velocity gradients visible mainly in the central row of the slit (see Sect. 2.6.2). In our analysis, these gradients are integrated in the final spectrum, as we did not perform a one-to-one row analysis (to maximize the S/N). In this sense, our narrow component fit should be properly considered as a lower limit to the velocity dispersion of the disk. Both narrow and secondary components are compatible with rotation (see Fig. 2.2 and Table 2.3), which is somewhat expected from the results of Walsh et al. (2010). In this work, they do not show the values of the three nuclear rows' analyses, as their kinematical profiles are said to be difficult to analyze due to the large gradients. However, the amplitude of the velocities is comparable with that of the secondary component ($\sim$400 km s^{-1}), being coincident with an assumed limit for detecting outflows (Sect. 2.6.2 and Fig. 2.2).

In the case of **NGC 4552**, Cappellari et al. (1999) modeled the emission lines with intermediate width profiles in both permitted and forbidden lines and highlighted the low luminosity of the central engine in comparison with other AGNs. With respect to the HST/STIS spectra, C15 did not consider a broad component. Our modeling, which takes into account a second component in forbidden lines and narrow Hα, reveals the presence of a broad component in both galaxies that contributes significantly ($\sim 65\%$ and $\sim 70\%$, respectively) to the global fit, as can be seen in Figures A.11 and A.13 (see Sect. 2.4.2).

The **NGC 4698** data come from the Survey of Nearby Nuclei with STIS, known as SUNNS, analyzed by Shields et al. (2007). They suggest that the galaxy was erroneously classified as a type 2 Seyfert galaxy by Ho et al. (1997a), on the basis of a decrease in the level of the excitation mechanism, suggesting that it is a LINER or a transition object. These authors did not detect a broad component in Hα in their spectral analysis, as Balmaverde & Capetti (2013) and C15 did when analyzing the same dataset in contrast to our findings. More specifically, we find that, even though the [S II] lines are perfectly modeled with a single narrow component, the addition of a weak broad component improves the χ^2 of the fit $\sim 17\%$ (see Fig. A.16). The lack of detection of this component in previous works could be due to its low contribution to the global fit (39%, Table 2.3) flux in comparison with the narrow component (see Sect. 2.4.2). If we were to set the velocity of the broad component to zero, we find that the χ^2 of the fit would be only 0.5% worse than the fit with the velocity from Table 2.3. As for NGC 4594, the broad component has a rather low contribution to the global flux and is the second broadest component in our analysis, thus statistically we should again expect a small difference. In this case, visually there was also no difference. However, due to the rather low velocity of this component in the previous model (273±97 km s^{-1}; Table 2.3), we decided not to add any constraint to the broad component velocity.

The remaining galaxy, **NGC 4676B**, belongs to the Mice galaxies complex, two interacting spiral galaxies. Both spirals have been told to present features indicative of the presence of outflows (Masegosa et al. 2011; Wild et al. 2014). Its HST/STIS nuclear spectrum has not been studied before, as the S/N is rather low, which makes it difficult to analyze (see Fig. A.15). Despite this, we attempted to model the emission line, that being the unique measurement of this kind for this object with HST/STIS data. Our fit reveals the presence of a broad component for the Hα-[N II] complex, while a narrow component is sufficient to fit the [S II] lines. Even though the χ^2 improved with the addition of this component, the residuals are inside the $3\varepsilon_{\mathrm{line}}$ limits also with a single narrow modeling for all the lines. The presence of this component could be affected by the noise, and the FWHM of this component is not as broad (748 km s^{-1}; Table 2.3) as the other detections in our sample. The results of the test of setting the velocity of the broad component to a zero velocity show the same results in FWHM and ε-indicator. So, it is not clear if it can be associated with the presence of a BLR. To avoid possible ambiguities, in what follows, we have conservatively excluded it as a true detection of a broad component.

2.6.4   BLR in optically classified type 2 LINERs

Type 2 LINERs have been classified by optical, ground-based spectroscopy as not having a broad component in the Balmer emission lines, while this is not the case for type 1-1.9 (Ho et al. 1993, 1995). Nevertheless, we see in our analysis (Sect. 2.6.3) that six out of the nine analyzed galaxies in our sample exhibit this component in space-based spectroscopy. In the case of the 22 type 1.9 LINERs (selected from the Palomar Sky Survey), all the available space-based spectra (12 LINERs) showed a broad component in Hα (see C18 for details). However, the same objects analyzed with the original Palomar spectra from Ho et al. (1997a) do not show this feature, except for two cases in type 2 LINERs (NGC 4486 and NGC 4594), and they do show it in all but four cases in type 1.9 LINERs. Ho's initial classification is mainly supported by this result. However, this enhances the difference of the ground-based spectra with those from space, also based on the results of C18.
The detection of a broad component is favored in space-based spectra because of the spatial resolution (Molina et al. 2018). If the BLR exists in a particular galaxy, a wider slit on a ground-based instrument could prevent it from being detected, as the weak broad Hα component could be diluted. This could be the reason for the initial lack of detection of the BLR in the galaxies of our sample, but also the modeling of the lines (e.g., testing single and multiple components) could be crucial to highlighting its presence (as was our case for HST/STIS spectra of NGC 4374 and NGC 4552).

The galaxy NGC 4486 is the only case in which the broad component is detected on the Palomar spectrum but not in the HST data. As we should expect exactly the opposite behavior (i.e., the detection of this component on HST and not in Palomar spectrum), it is not clear if this galaxy should be reclassified (type 1 instead of type 2). Moreover, if we take into account that the existence of the BLR in this object has been largely discussed in the literature (see Sect. 2.5.2). On the other hand, NGC 4594 is the only object in which a very broad component is detected in both datasets, so it should then be considered as a type 1 LINER.

2.6.5 Line ratios

We analyzed the line ratios for the emission lines available in all spectra. In Fig. 2.3, the [N II]/Hα and [S II]/Hα line ratios for both Palomar and HST data are shown[3]. We estimated the ratios for both the narrow and the secondary components (when present) for all galaxies except NGC 4676B, as its modeling is not well-constrained (see Sect. 2.6.3).

We consider, in Fig. 2.3, the empirically derived separation between an AGN or a star forming (SF) system, like in the BPT diagrams (Baldwin et al. 1981; Kauffmann et al. 2003; Kewley et al. 2006), based only in [N II]/Hα and [S II]/Hα ratios. Since [O III]/Hβ is not available in our data, we consider the star formation as the dominant mechanism of ionization if log([S II]/Hα) is < 0.0. The mechanism would be the AGN ionization when log([S II]/Hα)> 0.0. For the log([N II]/Hα), the limit for SF ionization is < −0.2, for AGN it is > 0.2, and we consider it as a "transition" region elsewhere.

In general, evident differences are seen in both panels of Fig. 2.3 between the space- and ground-based data. For both [N II]/Hα and [S II]/Hα, the ratios are always positive for the HST data, whereas more dispersion in the values exists in Palomar data (Palomar vs HST mean/standard deviation for [N II]/Hα 0.15/0.30 vs 0.54/0.40; and [S II]/Hα 0.02/0.24 vs 0.37/0.26). Specifically, for Palomar (HST) the average and standard deviation are, for log([N II]/Hα), equal to 0.15 and 0.30 (0.54 and 0.40), respectively; for log([S II]/Hα), these values are 0.02 and 0.24 (0.37 and 0.26).

In the absence of [O III]/Hβ (see Sect. 2.2), the ratios are more compatible with the AGN region for the HST spectra than for the Palomar data. The difference could be due to the spatial resolution based on the recent results from Molina et al. (2018). They have analyzed three LINERs with HST data, and performed a detailed study on the line diagnostic diagrams considering the unresolved nuclear source and what they call an "integrated" spectrum, which resembles the spectra of the targets as seen from a ground-based telescope. They found that the line ratios tend to be higher for the unresolved nuclear source than for the integrated

---

[3][O I]/Hα is not considered, as the [O I] line is not available for all HST spectra (Table 2.3, column 4).
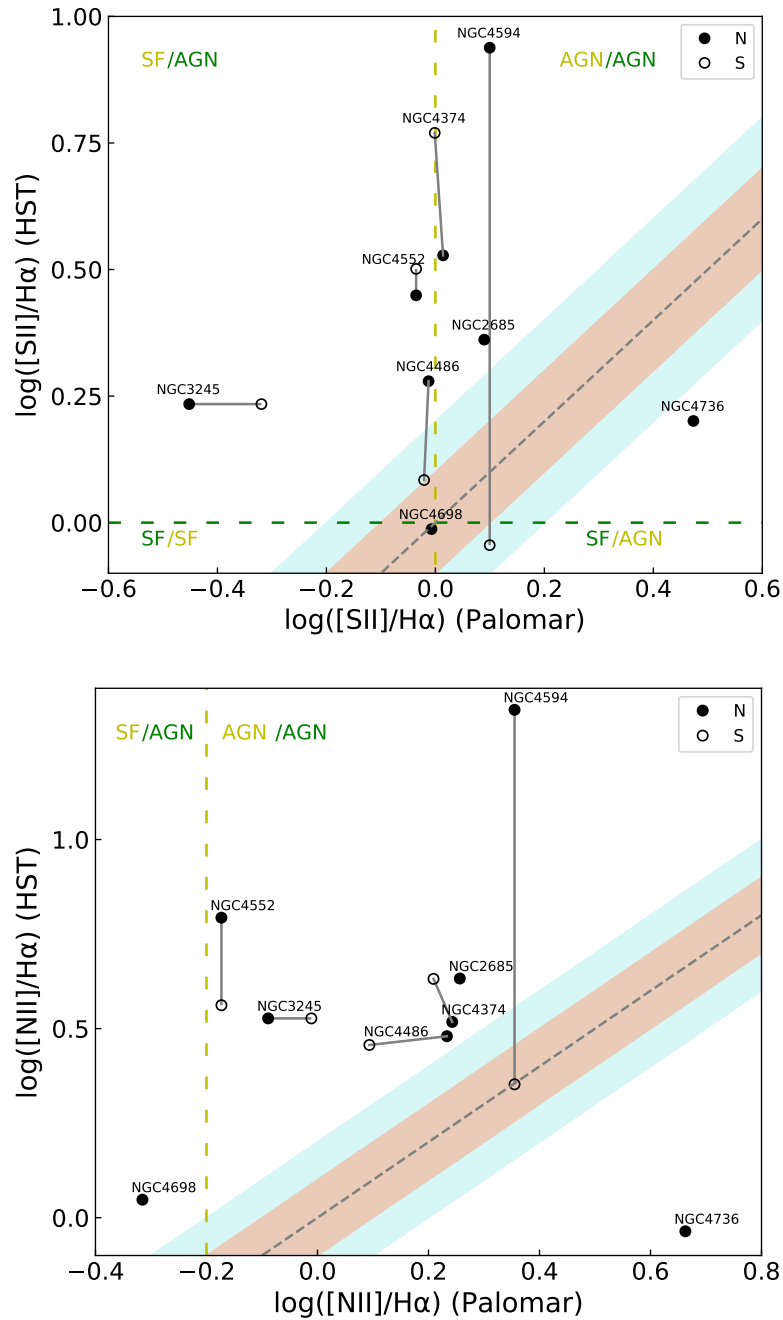
Fig. 2.3 Comparison of line ratios for [S II]/Hα (top) and [N II]/Hα (bottom) for both HST/STIS spectra (y-axis) and Palomar spectra (x-axis). The gray dashed line is the one-to-one comparison. Filled circles represent the narrow component, whereas the empty circles are for the secondary, which is connected to the narrow through a gray solid line when present. The light pink and light blue ranges indicate the 10% and 20% uncertainty levels with respect to the one-to-one comparison, respectively. Green and yellow dashed lines indicate the limits (HST and Palomar, respectively) for the star forming (SF) and AGN regions. The limits were obtained from Kauffmann et al. (2003) and Kewley et al. (2006).

spectrum. They conclude that it could be produced by the addition of a large spatial region of the galaxy (∼100 pc) within the integrated spectrum, where there is influence from gas probably suffering simultaneously photoionization and shock effects. This is reflected on their line ratios being consistent with different ionization mechanisms.

In Fig. 2.3, NGC 2685, NGC 4698, and NGC 4736 only have a single narrow component (black circles), so they appear only once. The difference compared to the one-to-one line could be explained directly with the variation of the Hα profile seen in the HST with respect to the Palomar spectra (see Fig. A.9, A.16 and A.17). Although, except for NGC 4698, they are compatible to being produced by an AGN in both Palomar and HST. For the case of NGC 4698, line ratios correspond to the transition region in both diagrams for the HST data, so this results in an ambiguous classification. The varying Hα profile does not only produce considerable differences in the line ratios for these three objects, but also for NGC 3245 and NGC 4486 (see Fig. A.10 and A.12, respectively).

The differences in the Hα profiles are significant, but there are also dramatic variations for the ratios of the secondary with respect to the narrow component. The most extreme case is NGC 4594 (see Fig. A.14 and Fig. 2.3), in which the Hα contribution to the total flux of the narrow component is almost negligible in comparison to the contribution of the secondary and the broad component. However, the secondary component shows a very similar line ratio to the Palomar spectrum.

In the top panel of Fig. 2.3, considering the [S II]/Hα ratio, the great majority of points for ground-based data are located around the transition region (i.e., log([S II]/Hα)∼0.0). In these cases, the information of the [O III]/Hβ ratio is required to further constrain the source of the ionization field. This is true for all objects except for NGC 4736, which is the only galaxy for which both [N II]/Hα and [S II]/Hα line ratios of the narrow component are consistent with being produced by the AGN, as mentioned above. Our classification, based on the [S II]/Hα ratio, is consistent with the presence of a very broad component (BLR-originated) visible in its HST spectrum (Fig. A.17). On the other hand, for the classification based on [N II]/Hα ratio, the majority of objects (7 out of 8) fall within the AGN region, and only one is consistent with being ionized by a SF region.

2.7 Summary and conclusions

In this work, we present a kinematic analysis and the study of ionization mechanisms of the gas of nine type 2 LINERs with both space- and ground-based spectroscopy obtained from the HST/STIS archive and from the Palomar/Double Spectrograph (Ho et al. 1995), respectively. The main objective is the detection of the existence of a BLR in these galaxies by analyzing

its spectral emission line features, and the possible presence of outflows. Moreover, we addressed the line ratios of the emission lines to study the dominant ionization mechanism for these objects.

We used the [S II] and [O I] lines as templates to model the other forbidden lines ([N II]) and narrow Hα, and considered the addition of a broad component under Hα where necessary. We used a maximum of three Gaussian components called the narrow, secondary, and broad components. Our approach allowed us to explore a larger number of scenarios for modeling emission lines with respect to previous work. These scenarios include possible NLR stratification and nonrotational motions being present, and never explored, for type 2 LINER nuclei (see C18 for type 1 LINERs).

The narrow component is likely to be associated with the rotation from the galaxy disk, whereas the secondary component, of intermediate width, could be related to both rotational and nonrotational motions (as outflows). The broad component of Balmer lines is always associated with the BLR of the AGN.

The secondary component has been detected for four LINERs in the HST spectra and for three in the Palomar data. For two objects from the HST analysis (i.e., NGC 4486 and NGC 4594), this component is found to suggest nonrotational motions, such as outflows. The line width of these components is similar to those found for outflows in type 1.9 LINERs by Cazzoli et al. (2018).

The detection of the BLR in LINERs is crucial to revealing its true AGN nature. Ho et al. (1997a) optically classified eight of the galaxies as type 2 objects, because their line fitting did not require a very broad BLR-originated component to reproduce the Hα-[N II] profile. With our analysis (following C18) of the same Palomar-spectra, we find that for two out of eight LINERs, a broad component is indeed necessary to reproduce emission lines. For the space-based data, a very broad component is needed in six out of the nine analyzed objects. The only detection of this component in the Palomar data but not confirmed with the HST is for NGC 4486. The results for this component are not well-constrained, thus we consider the BLR component detection as ambiguous. The galaxy NGC 4594 is the only one in the sample for which a broad component is needed in both space- and ground-based spectra, indicating that it would be better classified as as a type 1 LINER.

Three of the BLR detections in the HST data (NGC 3245, NGC 4594, and NGC 4736) were already reported by Constantin et al. (2015). Our measurements of both FWHM and flux contribution of the broad component with respect to the total flux of the Hα-[N II] complex agree with Constantin et al. (2015).

The detection of a very broad component is favored with the HST data as the spatial resolution being ten times better than for the Palomar data, decreasing the amount of contaminant

starlight from the host galaxy, and preventing the possible dilution of the broad component. The spatial resolution could be also relevant to the line diagnostic diagrams, as the calculated line ratios vary significantly from ground- to space-based spectra.

Chapter 3

A search for ionised gas outflows in an Hα imaging atlas of nearby LINERs

Abstract

Outflows play a major role in the evolution of galaxies. However, we do not have yet a complete picture of their properties (extension, geometry, orientation and clumpiness). For low-luminosity Active Galactic Nuclei (AGNs), in particular, low-ionisation nuclear emission line regions (LINERs), the rate of outflows and their properties are largely unknown. The main goal of this work is to create the largest, up-to-date atlas of ionised gas outflow candidates in a sample of 70 nearby LINERs. We aim to use narrow-band, imaging data to analyse the morphological properties of the ionised gas nuclear emission of these galaxies and to identify signatures of extended emission with distinctive outflow-like morphologies. We obtained new imaging data from Alhambra Faint Object Spectrograph and Camera (ALFOSC)/Nordic Optical Telescope (NOT) for a total of 32 LINERs, and complemented it with Hubble Space Telescope archival data (HST) for 6 objects. We extracted the Hα emission of the galaxies and used it to morphologically classify the circumnuclear emission. We combined our results with those from the literature for additional 32 targets. We additionally obtained soft X-ray data from Chandra archive to compare this emission with the ionised gas. The distribution of the ionised gas in these LINER indicates that ~32% show bubble-like emission, ~28% show a 'Core-halo', unresolved emission, and ~21% of the sample have a

disky-like distribution. Dust lanes prevent any detailed classification for ~11% of the sample, that we call as 'Dusty'. The soft X-ray emission is in most cases (~60%) co-spatial with the ionised gas. If we account for the kinematical information which is available for a total of 60 galaxies, we end up with a total of 48% of the LINERs with detected outflows/inflows in the emission lines (50% considering only kinematical information based on Integral Field Spectroscopic data). Our results suggest that the incidence of outflows in LINERs may vary from 41% up to 56%, based on both the Hα morphology and the kinematical information from the literature. The ionised gas seems to be correlated with the soft X-ray emission, so that they may have a common origin. We discuss the use of Hα imaging for the pre-selection of candidates likely hosting ionised gas outflows.

3.1   Introduction

Outflows are believed to play an important role in the evolution of galaxies (e.g. Kormendy & Ho 2013; Cresci & Maiolino 2018; Veilleux et al. 2020). Those driven by Active Galactic Nuclei (AGNs) interact with the gas in the host galaxy generating both negative and positive feedback processes that affect the evolution of the host with notable effects, such as the gas-recycling or the suppression of the star formation (e.g. Fabian 2012; Cresci & Maiolino 2018). Outflows are characterised by their multi-wavelength phases (cold, warm and ionised gas), whose analysis is needed to fully understand their importance on the evolution of their host galaxies (e.g. Cazzoli et al. 2014; Cicone et al. 2014; Ramos Almeida & Ricci 2017; Morganti 2017; Veilleux et al. 2020; Fluetsch et al. 2021).

These galactic outflows are commonly seen in all AGN types (e.g. Veilleux et al. 2005; Morganti 2017; Veilleux et al. 2020), including a handful of Low-Ionisation Nuclear Emission-line Regions (LINERs) (Heckman 1980). Given that the presence of outflows has been suggested to be ubiquitous within the AGN population (e.g. Veilleux et al. 2005; Concas et al. 2019), it is also expected to be the case for low-luminosity AGNs, as LINERs. Although that, this field is largely unexplored except for few works (Cazzoli et al. 2018; Hermosa Muñoz et al. 2020). This is probably a result of a bias towards the search of outflows in powerful AGNs, where these outflows are more easily identified, as the outflow rate scales with the AGN luminosity (Fluetsch et al. 2019). Nevertheless, much less is known for the largest population of AGNs in the Local Universe, which is dominated by LINERs (Ho et al. 1997a). Mainly hosted in early-type galaxies (Ho 2008), their AGN nature is not yet clear for all the objects (Márquez et al. 2017), given the existence of other mechanisms, such as shocks (Heckman 1980; Dopita & Sutherland 1995; Molina et al. 2018), that could explain the observed spectra of these systems.

One of the best ways to identify the presence of outflows is using kinematical information via 2D spectroscopy (e.g. Davies et al. 2014; Harrison et al. 2016; Mingozzi et al. 2019; Davies et al. 2020; Cazzoli et al. 2020; Raimundo 2021, Cazzoli et al. in prep). These spectroscopic measurements allow us to obtain resolved information of the gaseous component of a galaxy at low (e.g. Raimundo 2021) and high redshift (e.g. Harrison et al. 2016). In more luminous AGNs, the kinematical component of the emission lines associated to the outflow can dominate and be the more predominant feature of the spectra, above other rotational movements of the internal gas (Davies et al. 2020). However, in the absence of spectroscopic data, outflows may be detected, or at least hinted by using imaging techniques, even when the activity of the host galaxy is low (Masegosa et al. 2011). In the works by Pogge et al. (2000) and Masegosa et al. (2011) they studied the extended ionised Hα emission of several LINER-like galaxies. In the latter work, this emission was classified in different morphological types depending on the distribution of the ionised gas. One of the possible classification is outflow-like, referred to extended filamentary or bubble-like gas extending out of the galaxy nuclei. For some galaxies, this ionised gas emission with morphological signatures of outflowing gas, was later confirmed as an outflow by means of the use of kinematic data obtained from 2D spectroscopy (see e.g. NGC 4676A in Wild et al. 2014).

In this Chapter, our objectives are: (i) to create an atlas of the ionised gas morphology of a sample of nearby (z<0.025) LINERs that almost doubles that previously existing; (ii) search for morphological evidences of possible outflowing gas that could be associated to feedback processes, in order to determine how common outflows/inflows may be for the LINER AGN family; (iii) compare the Hα morphology to that seen in X-rays (when possible), to investigate possible correlations between both emissions, as seen in different AGN types in previous works (Bianchi et al. 2006; Masegosa et al. 2011; Bianchi et al. 2019b); and (iv) look for kinematically-identified outflows in the literature within our targets, in order to test the goodness and eventual relation of the morphological signatures in the actual detection of outflows.

This Chapter is organised as follows: Section 3.2 describes the selection of the sample and the data gathering. In Section 3.3 we present the data reduction. In Section 3.4 we show the main results of the Hα and X-ray morphologies. We discuss the kinematical signatures of outflows identified in the literature for our targets, its relation with the gas morphology, as well as the implications of our work in Section 3.5. Finally, Section 3.6 summarises the main conclusions. Individual comments on each galaxy are in Appendix B.1; all the figures can be found in Appendix B.2.

3.2   Sample and data

The total number of objects analysed in this work is 70 LINERs (see Table B.1), that were selected as explained below. The parent sample of our data set comes from González-Martín et al. (2009), where the X-rays properties of 82 LINERs were analysed, and is complemented with 11 LINERs from Cazzoli et al. (2018) and 2 from Pogge et al. (2000). We included in the sample one additional LINER (NGC 5957) not initially in either of the initial samples, but for which we have integral field spectroscopic data (Hermosa Muñoz et al. in prep). To select the targets, we applied the following criteria: (i) all galaxies should have distances not larger than 100 Mpc in order to ensure that the galaxies fitted in the field-of-view (FoV) allowing to detect parsec-scale structures; (ii) we do not consider systems on a high level of interaction. The first criterion excluded 14 galaxies and the second excluded 5 objects. This lead to 77 objects, from which 36 were already studied either in Masegosa et al. (2011) (hereafter M11) or in Pogge et al. (2000) (32 from the first, 4 from the second). Among the 32 targets in M11 we found NGC 4676A and B, that are on a high interacting level, so we further excluded them. We added NGC 3379 and NGC 4278 to the remaining 41 targets, as they were analysed in M11 based only in the Hβ, but not in the Hα emission. Thus, we end up with 43 LINERs; from them, we were able to gather data for 38 targets (see Table B.2, Table B.3 and Sect. 3.2.1).

To achieve the largest statistics of Hα images possible, our final sample encompass the 38 new targets with those from M11 and Pogge et al. (2000) with previous observations (32 targets, excluding NGC 3379, NGC 4278, NGC 4676A and B). Hence, summing up, the complete sample we analysed is 70 LINERs. We estimated the bolometric luminosity of the sources with the X-ray luminosity (2-10 keV) following González-Martín et al. (2009) (see Fig. 3.1). The typical bolometric luminosity of our sources is $10^{41.8}$ erg s^{-1} (see Table B.1).

3.2.1   Data gathering

We searched for archival data in any available narrow filter from the HST for the 43 objects that corresponded to the Hα line at the redshift of the targets, finding 6 objects with at least one image available (see Table B.2). The selected filters are indicated for each object in Table B.2. We aimed to observe the remaining 37 objects with the Alhambra Faint Object Spectrograph and Camera (ALFOSC), at the Nordic Optical Telescope (NOT), during several observing campaigns (see Table B.3).

The ALFOSC instrument is located at the NOT telescope (2.56 m), in 'Roque de los Muchachos' observatory, in La Palma, Spain. We used its camera in imaging mode, with a total FoV of 6.4'×6.4' and a pixel scale of 0.214"pix^{-1}.
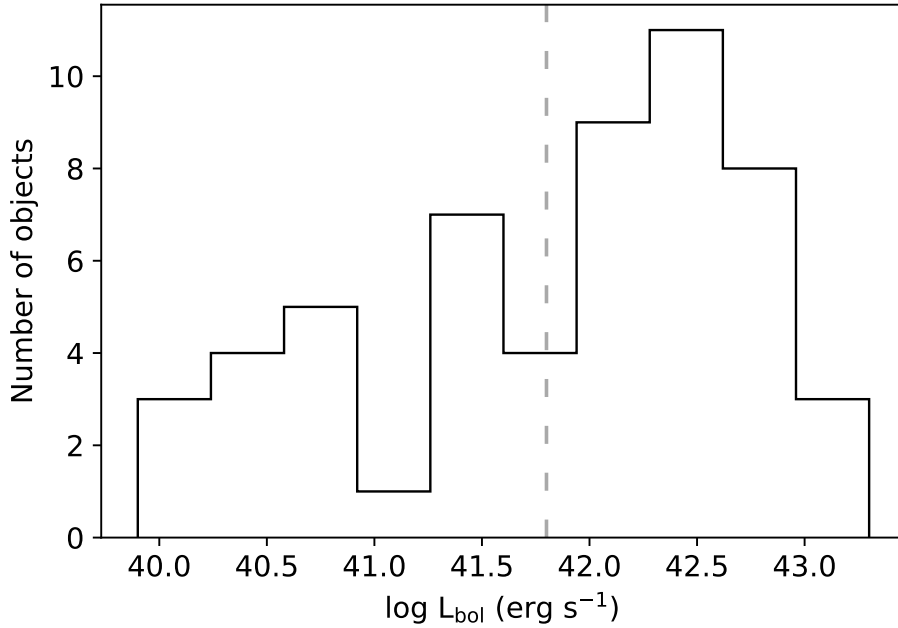
Fig. 3.1 Histogram of the bolometric luminosities (in log units) of the selected sample of LINERs. The luminosities were estimated from González-Martín et al. (2009) (see Table B.1). The dashed grey line indicates the average value ($10^{41.8}$ erg s^{-1}).

The data were gathered in a total of 14 nights (PIs: S. Cazzoli and L. Hermosa Muñoz; see Table B.3). We obtained 3 individual exposures for both narrow and broad band filters per galaxy, with typical exposure times of 1200 s and 300 s, respectively. For some objects, the broad filter images were observed with smaller exposure time to avoid saturation of the galaxy centre. The total time on source per galaxy was 1.25 hours. The average seeing and airmass were 0.92"and 1.24, respectively (the corresponding information for the different nights is listed in Table B.3).

We used the narrow filters from NOT that allowed us to observe the ionised gas of the LINERs at their given redshift, that corresponded to the Hα line. These are (as indicated in the NOT web page[1]): #49 (661_5 - Full Width Half Maximum /FWHM 50Å), #50 (665_5 - FWHM 55Å), #68 (664_4 - FWHM 40Å), #77 (662_4 - FWHM 39Å), #78 ([N II]658_4 - FWHM 36Å) and #123 ([S II] 672_5 - FWHM 50Å). As for the broad filter, we used the standard R band filter from the Sloan Digital Sky Survey (as indicated in the NOT web page: r'_SDSS 625_140 - FWHM 1400Å). The selected narrow filters are wide enough to also include one of the [N II]$\lambda\lambda$6548,6584Å emission lines. However, we have chosen the filters such that the only other emission line that could also fit within the filter is the [N II]λ6548Å line, which is weaker than the [N II]λ6584Å line (relation 1:3, see Osterbrock

[1]http://www.not.iac.es/instruments/filters/filters.php

& Ferland 2006). Contamination of the Hα line due star-formation processes could exist. However, we do not expect this to be important, as all our sources are early-type galaxies (see morphological types in Table B.1), where the star formation is expected to be less important than in later host types.

The presence of several ghosts contaminated the images of NGC 0474 and NGC 0524, observed with the NOT filter #77. This prevented a reliable analysis and therefore, these two galaxies were further excluded from the sample. NGC 5957 was observed while high clouds appeared during at least one individual exposure, dimming the object flux. Finally, due to bad weather conditions and time constraints to finish the last observing run, 3 objects (NGC 0833, NGC 0835 & NGC 2655) were not observed. Thus, the campaign is completed up to a ~90% of the sample (37 objects).

3.2.2   X-ray data

We searched for X-ray data in the Chandra Data Archive for all the new galaxies in the sample (38 objects) for which we obtained optical data, to compare their soft emission (0.3 - 2 KeV) with the ionised gas. We retrieved X-ray images taken with the Advanced CCD Imaging Spectrometer (ACIS) for a total of 28 objects. We estimated the 3σ contours of the emission and superimposed them to the Hα images.

For the data coming from M11, there is a similar analysis with both hard and soft X-ray Chandra images. They gathered data for a total of 26 objects, whose results we discuss in Sect. 3.5.2. The images from their objects can be found in their Fig. 6.

3.2.3   Kinematical information

By searching in the literature, we retrieved kinematical information either for all the LINERs from Integral Field Spectroscopy (IFS) (30 galaxies) or long-slit spectroscopic data (30 galaxies). When a target was analysed with IFS data, we prioritised those 3D results over those coming from long-slit spectroscopy. The previous works analysing the different targets (see Sect. 3.5.1 and Appendix B.1 for more details on the individual sources) discuss the possible presence of outflows/inflows or non-rotational motions in the galaxies for 28 objects. We compare the morphologically-identified outflows with those kinematically-identified (or undetected) in Sect. 3.5.1.

3.3   Data reduction process

The data gathered from the HST archive were already fully reduced and the narrow-band images of the galaxies were already combined in those cases where there was more than one available. However, given that the HST observations are from the archive, some of the selected narrow filter (NF) images were not observed the same night as the broad filter (BF) images (see Table B.2). We tried to select, when possible, the BF with the closest wavelength range to the NF range. Thus, the only procedure applied to HST data was the realignment of the NF and BF images when they were obtained in different observing campaigns (see Table B.2). Specifically, we used the position angles on the header of the different frames to set the images to a common North-East axis reference. Then the outermost, elliptical isophotes were fitted to ellipses, providing us with the centres and position angles that were used to apply the corresponding shift and rotation for alignment. Finally, we trimmed the images to where both had information.

The data from ALFOSC/NOT were reduced following standard procedures (bias and flat-fielding) with both IRAF and PYTHON routines. We performed a dedicated background subtraction to the ALFOSC/NOT images required for a reliable sky determination. An example of the procedure is shown in Fig. 3.2. We used PHOTUTILS routines under a PYTHON environment to mask external stars, galaxies and artefacts from the filter, and estimate a 2D background. We created masks for objects detected at least at 3σ over the background in the BF images (as usually the flux is more extended in this filter) and applied them to the NF ones. The background in the masked pixels could not be estimated, so we used the median value of the background in the rest of the image. Then, we made a smoothing of the background image (100×100 pixels), so that no structures were included due to the masks, and we subtracted the final smoothed background image per each galaxy and filter.

In order to obtain exclusively the emission of the galaxies in the Hα line, we subtracted the continuum of the narrow-band images using broad-band images of the same targets. For ALFOSC/NOT, those BF images were observed the same night as the NF ones. The procedure follows that from M11. The NF images include not only the Hα emission but also the underlying continuum. The line emission is usually less extended than the continuum, which is translated into the fact that, at large scales in the galaxy, both NF and BF images should return comparable emissions. Thus, we scaled the BF image to the NF image and then subtract them to obtain the Hα image.
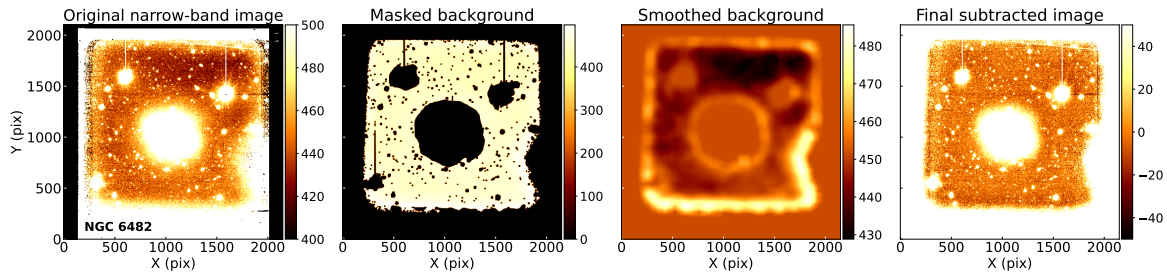
Fig. 3.2 Example of the background subtraction process for NGC 6482. *Left:* Original narrow-band image of the galaxy. *Middle-left:* Mask applied to the original image over imposed to the estimated background. *Middle-right:* Final smoothed background. *Right:* Final narrow-band image with the corresponding background subtracted. The scale on the left and right panels is around the background level to appreciate the differences before and after the subtraction. See Sect. 3.3 for more details.

The peculiar morphologies of the galactic continuum in the studied galaxies are highlighted by the use of sharp-divided images (e.g. Márquez & Moles 1996; Márquez et al. 1999, 2003). Briefly, this technique consists on dividing the BF image by its smoothed version, which is the original image convolved with a median filter of a 20-pixel box. Although simple, this method is very useful specially for detecting asymmetries on the image, such as bars, rings, spiral arms or dust regions. The sharp-divided images of the galaxies are shown in the right panels of Appendix B.2.

The Chandra X-ray images were reduced following the Chandra threads aimed for the ACIS instrument, using the dedicated software CIAO v4.13 and the calibration package CALDB 4.9.5. After downloading the data, we applied the most recent calibrations running the script 'chandra_repro' and restricted to the energy range between 0.3-2 KeV. We extracted background light curves from the event files using the CIAO tool DMEXTRACT in order to eliminate high background events. Based on those background light curves, we generated Good Time Intervals for our images excluding time intervals deviated 1σ from the mean rate of counts in the background using the CIAO tool DEFLARE.

3.4   Results

We have classified the circumnuclear Hα morphologies of the galaxies according to 4 different categories: 'Core-halo', 'Disky', 'Bubble' and 'Dusty'. An example of each morphological type is shown in Fig. 3.3. The properties of the ionised emission included in these categories are fully explained in M11. The basic definitions are: (i) 'Core-halo': unresolved nuclear
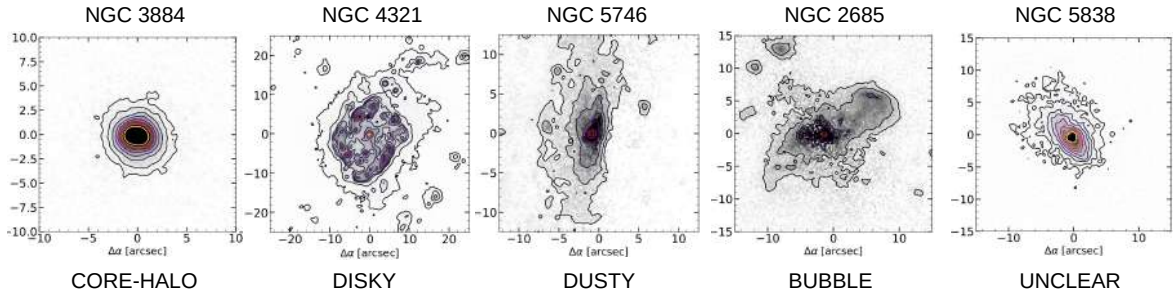
Fig. 3.3 Examples of the five proposed morphological classifications of the nuclear Hα emission (see Sect. 3.4). The complete images are in Appendix B.2.

emission in the galaxy centre; (ii) 'Disky': ionised emission along spiral arms, star forming rings or diffuse emission in the disc; (iii) 'Bubble': equivalent to the 'Outflow' morphology in M11, refers to biconical, filamentary or bubble-like structures emerging from the nucleus; and (iv) 'Dusty': mostly edge-on galaxies with dust lanes obscuring the nuclear emission. We classified all the targets using visual inspection of the Hα images, considering all the emission detected above 3σ from the background. Our classification is given in Table 3.1. We assigned a morphological class when 3 or more authors agreed on the classification. This happened for 87% of the targets from the new data. The remaining 13% (5 out of 38) had ambiguous morphologies that could be included in various classes. To enable a more clear discussion, we defined for them the additional category 'Unclear'. In this Section we account only for the new observed data, as the results for the other targets are presented in M11 and Pogge et al. (2000). More details on the individual galaxies can be found in Appendix B.1; all Hα and sharp-divided images are in Appendix B.2, and the soft X-ray images (in contours) are in Fig. 3.5.

3.4.1   Ionised-gas morphological classification

We have identified a total of 12 LINERs that show 'Core-halo' emission. Among them, NGC 4261, NGC 4589 and NGC 6482 (see Figs. B.5, B.7 and B.9, respectively) show extended emission probably elongated along their galaxy disks; NGC 3884, NGC 4278, NGC 4772 and NGC 5957 (see Figs. B.3, B.5, B.8 and B.9, respectively) have an unresolved, not elongated nuclear emission; in the remaining galaxies, NGC 0410, NGC 4450, NGC 4494, NGC 4698 and NGC 7743 (see Figs. B.1, B.6, B.7 and B.10), the Hα emission is extended and detected at 3σ level at distances larger than >10"from their nuclei.

The 'Disky' morphology is found in 9 galaxies. For NGC 0841, NGC 3642, NGC 4321 and NGC 4457 (see Figs. B.1, B.3, B.5 and B.6) the emission is found along a star-formation ring or arm, where several clumps are easily identified. In 3 galaxies, namely NGC 3185,

NGC 3507 and NGC 5077 (see Figs. B.2 and B.8), the emission shows a twisted and elongated shape that may be ascribed to a bar or to large-scale spiral arms or discs. Finally, for 2 galaxies, NGC 3608 and NGC 3898 (see Figs. B.3 and B.4, respectively), the emission is extended along the disc, with no clumps or evidence of star formation.

There are only 3 objects classified as 'Dusty', as they show clear dust lanes that prevent from analysing their nuclear emission (NGC 3628, NGC 4125 and NGC 5746). However, note that this classification is based on the innermost regions (∼20") of the galaxies. NGC 3628 (Fig. B.3) is known to have extended emission further out from the nuclei, a large scale Hα emission clearly visible in the southern parts of the galaxy (Fabbiano et al. 1990). In our image, this plume is barely detected at 1σ level (see Fig. 3.4), whose analysis is out of the aim of this Chapter. NGC 4125 (Fig. B.4) has some extended emission, but clearly around dust lanes, thus we were conservative in its classification. For NGC 5746 (Fig. B.8), the emission is barely visible through some regions of the galactic disc, thus not reliable for a proper morphological classification.

We have identified 9 LINERs that may have an outflowing emission with complex ionised gas morphologies. NGC 0266, NGC 3414, NGC 4596 and NGC 4750 (see Figs. B.1, B.2 and B.7) show a faint extended emission parting asymmetrically from the photometric centre of the galaxies. NGC 3945 image unveils a filamentary structure (Fig. B.4). For NGC 2685, NGC 3379 and NGC 5813 (see Figs B.1, B.2 and B.9), the Hα emission has a biconical or bubble-like shape oriented almost perpendicular to the major axis of the galaxies (inclination of NGC 2685 is 60∘, not measured for the other two; see Table B.1). NGC 4459 (see Fig. B.6) can also be included in this latter group, as the nuclear emission in the inner 3"×3" resembles the base of a outflowing bubble. All the objects would benefit of detailed spectroscopic information with spatial resolution to determine the extent and origin of their emission.

Finally, there are five galaxies (NGC 4143, NGC 4203, NGC 5363, NGC 5838 and NGC 7331) with 'Unclear' morphologies. NGC 4143, NGC 4203 and NGC 5838 are double classified in this work as 'Bubble' and 'Disky' (see Figs. B.4, B.5 and B.9). In these cases, the emission seems to be extended along the galaxy disc, but with a non-symmetrical distribution. These asymmetry may be produced due to outflows instead of being associated to the disc, which lead to the unclear classification. For the case of NGC 5363 (Fig. B.8), a nuclear dust lane of ∼1 kpc is obscuring the nucleus, although at larger scales (≥20") there is a extended, filamentary emission of ionised gas (see Fig. 3.4). The morphological differences at both scales lead to a double classification as 'Dusty', and 'Bubble'. NGC 7331 (Fig. B.10) is classified as both 'Dusty' and 'Bubble', as we detect some extended emission out of the nucleus, but we cannot ensure this Hα profile to be symmetrical, as a thick dust lane is visible
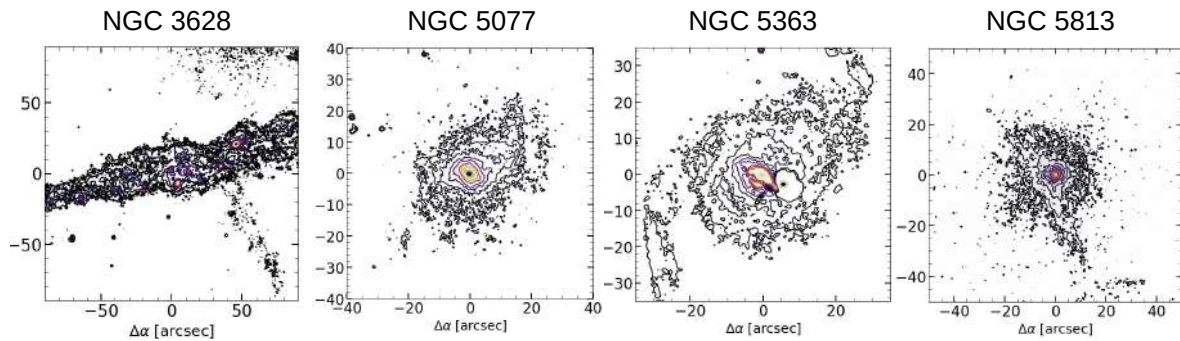
Fig. 3.4 Large-scale Hα images of NGC 3628, NGC 5077, NGC 5363 and NGC 5813. The largest contours indicate the 1σ level over the background signal, except for NGC 5363, that represents 3σ. The corresponding image on smaller scale (∼10"×10") with the 3σ-detection are shown in Appendix B.2.

within the galaxy disc.

There are two galaxies, NGC 3379 and NGC 4278 (Figs. B.2 and B.5), that were observed in our sample despite they were also analysed in M11. The only available data in the HST archival were in the narrow filter corresponding to the [O III] line emission (filter F547M). In our work, we have obtained data for these galaxies in the Hα wavelength range, to have an uniform comparison of all the nuclear emissions in the galaxies from the sample. For M11, NGC 3379 (NGC 4278) was classified as having a 'Disky' ('Core-halo') emission. We agree on the classification of NGC 4278 but, on the contrary, we classified NGC 3379 as having an 'Bubble', as the inner Hα morphology shows an elongated shape that cannot be ascribed to either of the other possible classifications. This elongated emission is coincident with a dust lane crossing the nuclear region, visible in Hβ (Masegosa et al. 2011). It could also be an effect produced by a bar (see individual comments on Appendix B.1), as the sharp-divided image (see Fig. B.2) show an 'X'-like shape which is usually ascribed to barred systems (Laurikainen & Salo 2017).

3.4.2 Soft X-ray images properties

Some previous works have studied the correlation between the soft X-ray and ionised gas emissions for different AGN types (Bianchi et al. 2006, ; M11), such that both emissions are believed to raise from the photoionisation of the gas around the AGN (Bianchi et al. 2006, 2019b). These results are discussed in Sect. 3.5.2. For the new data, we searched for X-ray data with resolution comparable to that of the ALFOSC/NOT 38 Hα images. The soft X-ray contours are shown in Fig. 3.5. The emission for 11 galaxies is mainly point-like around

the nucleus, which would be equivalent to a 'Core-halo' classification (see Sect. 3.4). We find 12 objects with an extended emission and 5 with clumpy emission. Despite the different morphologies, the soft X-ray emission is co-spatial with the ionised gas for 12 galaxies (see Table 3.3).

If we separate those galaxies in which both emissions are coincident, at least, in the direction of the emission, we end up with 12 LINERs (NGC 0266, NGC 0410, NGC 3414, NGC 3884, NGC 3945, NGC 4261, NGC 4450, NGC 4596, NGC 4750, NGC 4772, NGC 5813, NGC 5838). One example is NGC 5813, for which the Hα image, specially at large scales, shows an extended filamentary structure (see Fig. 3.4), with a bubble extending up to 10" in the north-west direction with respect to the centre. The X-ray emission is rather complex, with the same bubble almost co-spatial with the Hα emission (see Fig. 3.5).
The most notable difference in the remaining objects lies in the extension of the emission, being in some cases much more extended in the X-rays (e.g. NGC 4278, see Fig. B.5), and in other cases in Hα (e.g. NGC 4698, see Fig. B.7).

3.4.3 Global picture of ionised gas morphologies in LINERs

For the new imaging data obtained with NOT and HST, as drawn by the detected Hα emission at 3σ level, the nuclear ionised gas in these LINERs is extended ($\geq$5") in the majority of the cases (32 objects; ~84%). This emission is not exclusively along spiral arms or nuclear discs but also due to possible outflows (for example, as filamentary structures), or perhaps other events at large scales (i.e. >1'; see Fig. 3.4), as mergers (e.g. NGC 4125, see Appendix B.1 and Fig. B.4).

Within our new data, as already mentioned in Sect. 3.4.1, we have 9 objects of outflow-like morphologies in the Hα nuclear emission, which corresponds to ~25% of the sample. The same percentage also applies for disky-like emission (9 LINERs), whereas the majority are classified as 'Core-halo' (12 LINERS; ~32%). However, if we consider all the measurements and classifications in previous similar studies, larger statistics can be made. More specifically, in M11 they provided the final morphological classification for 30 LINERs, accounting for the data in Pogge et al. (2000) (see Sect. 3.2).

In this work, we have added a total of 38 new LINERs, considering both NOT and HST data sets. Summing up, we have Hα morphological information for a total of 70 LINERS, such that 32% of them are classified as having outflow-like emission, 29% show 'Core-halo' morphology, 21% are classified as 'Disky', 11% as 'Dusty' and 7% with an 'Unclear'
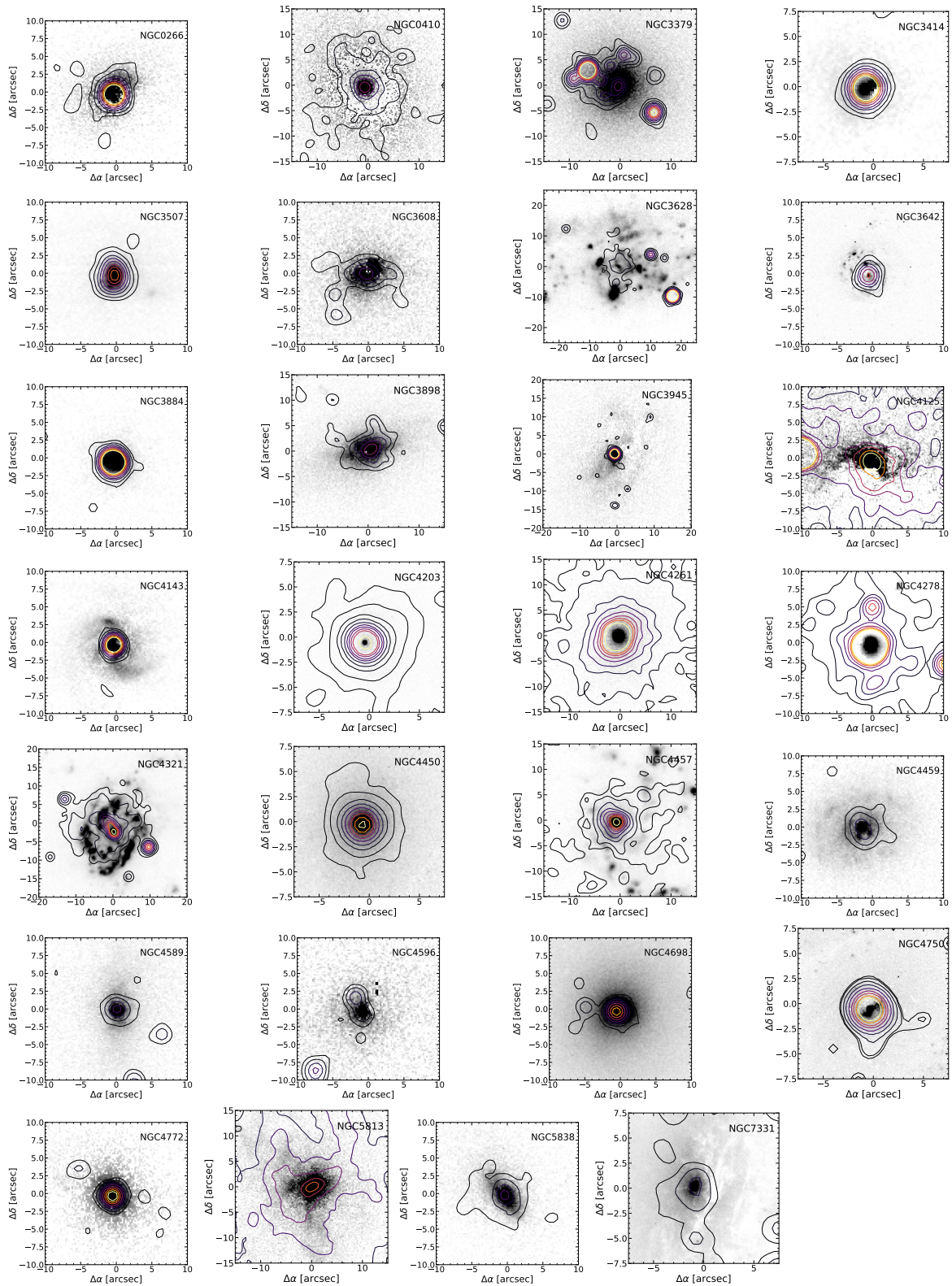
Fig. 3.5 Hα images with overlaid contours of the X-ray emission from Chandra. The contour levels are at 3σ (black), 7σ (black), 15σ (black), 25σ (dark-purple), 40σ (purple), 60σ (light-purple), 80σ (red), 100σ (orange) and 150σ (yellow).
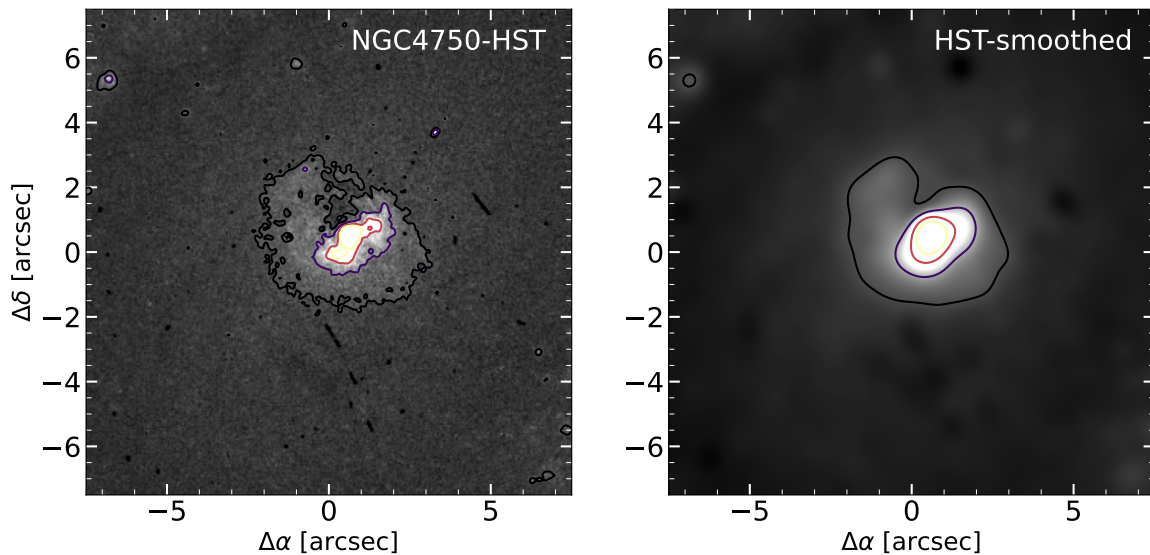
Fig. 3.6 *Left:* Hα emission on NGC 4750 observed with HST (M11). *Right:* Smoothed version of the HST image with a Gaussian filter ($\sigma \sim 5$) to match the ALFOSC/NOT resolution. In both panels, the minimum contour is 3σ over the background and the maximum, yellow contour of 25σ.

morphology. These results indicate that 1 out of every 3 LINERs in the local Universe may have an outflow.

3.5   Discussion

The combined results of the new 38 objects from this work and 32 from previous works (Pogge et al. 2000; Masegosa et al. 2011) constitute the largest sample up to date of ionised gas morphological analysis of LINERs. The morphological features of the 70 galaxies indicate that a high percentage (32%) of LINERs do have outflow-like ionised gas emission. However, we notice that a dedicated spectroscopic follow-up using IFS is needed to firmly confirm what the morphological signatures suggest and capture the full extension of the putative outflow. This specially applies to the targets with long-slit spectroscopic observations, where the outflow will not be detected if the slit is not properly oriented.

We note that, although we classify all the images under the same criteria (see Sect. 3.4), both HST and ALFOSC/NOT data have different spatial resolutions. This implies a loss of detail on the possible substructures present on the images, but it should not produce any relevant change on the classification of the ionised gas morphology, as the categories defined rely on features large enough (as discs or dust lanes) to not depend on pc-scale structures (see Fig. 3.6). Specifically, the mean extension of the Hα emission within the HST data is 0.8

Table 3.1 Morphological classification of the Hα nuclear emission as in M11.

Core-halo (12+8)	Disky (9+6)	Dusty (3+5)	Bubble (9+13)
IC 1459[†]	NGC 0841	NGC 3226[†]	NGC 0266
NGC 0315[†]	NGC 2681[†]	NGC 3607[†]	NGC 0404[†]
NGC 0410	NGC 2841[†]	NGC 3627[†]	NGC 1052[†]
NGC 2639[†]	NGC 3185	NGC 3628	NGC 2685
NGC 2787[†]	NGC 3507	NGC 4125	NGC 3245[†]
NGC 3623[†]	NGC 3608	NGC 4374[†]	NGC 3379*[†]
NGC 3884	NGC 3642	(NGC 5363)	NGC 3414
NGC 3998[†]	NGC 3898	NGC 5746	NGC 3718[†]
NGC 4111[†]	(NGC 4143)	NGC 5866[†]	NGC 3945
NGC 4261	(NGC 4203)		NGC 4036[†]
NGC 4278*	NGC 4314[†]		(NGC 4143)
NGC 4450	NGC 4321		NGC 4192[†]
NGC 4494	NGC 4457		(NGC 4203)
NGC 4589	NGC 4552[†]		NGC 4438[†]
NGC 4698	NGC 4594[†]		NGC 4459
NGC 4772	NGC 4736[†]		NGC 4486[†]
NGC 5055[†]	NGC 5077		NGC 4579[†]
NGC 5957	(NGC 5838)		NGC 4596
NGC 6482	(NGC 7331)		NGC 4636[†]
NGC 7743			NGC 4696
			NGC 4750
			NGC 5005[†]
			(NGC 5363)
			NGC 5813
			(NGC 5838)
			NGC 5846[†]
			(NGC 7331)

Notes. † indicates the galaxies classified in M11 and Pogge et al. (2000). The galaxies in parenthesis have an unclear classification. * indicates targets analysed both with the new data and in M11.
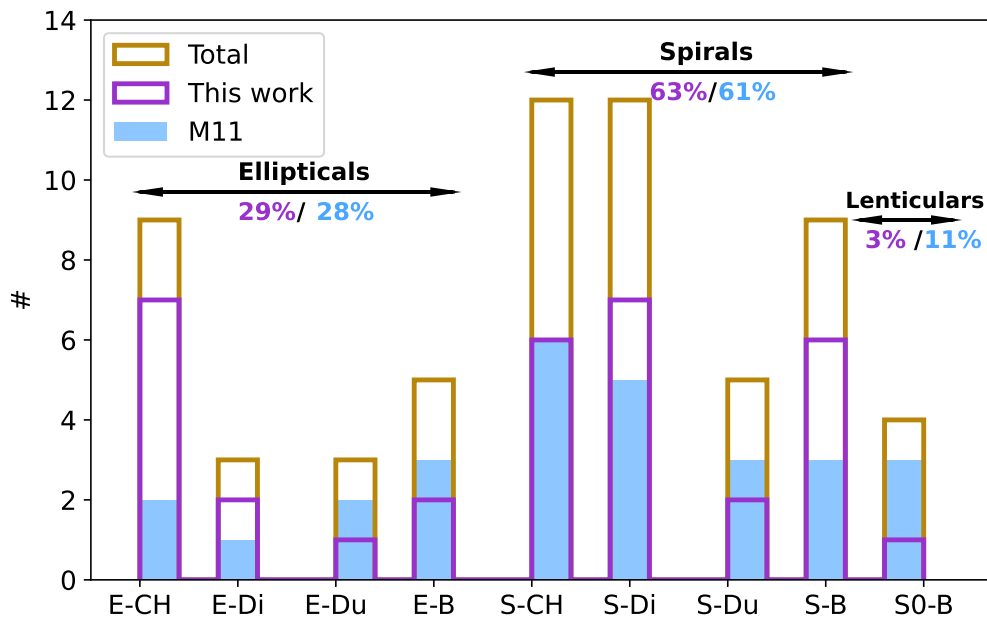
Fig. 3.7 Histogram of the morphological type of the host galaxy and the classification of the nuclear Hα emission. It is divided into ellipticals (E), spirals (S) and lenticulars (S0); 'CH' stands for 'Core-halo', 'Di' for 'Disky', 'Du' for 'Dusty' and 'B' for 'Bubble'. Purple lines indicates the sample from this work; blue for M11; and yellow is the combination of both samples. We have not included unclear cases or irregular galaxies in the figure, and thus the percentages do not sum up 100%.

±0.3 kpc, whereas for the ALFOSC/NOT data is 1.9±1.3 kpc.

We compare the ionised gas morphology with the morphological type of the host galaxy (see Table B.1) in order to see if there exists any relationship with the Hα emission beyond the possible star-forming regions in the centres of those galaxies. We see no correlations of the morphologies in the data from M11, in the new data, or when considering both together (see Fig. 3.7). We note that the Hα nuclear emission of all the lenticular galaxies mixing both works was classified as outflow-like, although the sample is small (5 objects) to firmly state any conclusion about it. All the targets are early types, ranging from E to Sb. This is expected, as within the Palomar sample the largest fraction of AGNs (including higher accretion rates) were found among these morphological types (Ho 2008). We find that the majority of galaxies are spirals both in M11 and in this work (~60%; see Fig. 3.7). This is in contrast to Ho (2008), who stated that for LINERs approximately 35% of the hosts galaxies were ellipticals, ~45% spirals, while lenticulars were 20%. We selected our LINERs based on their distances (see Table B.1) and a previous detection in X-rays that ensured their true nature as AGNs (see Sect. 3.2 González-Martín et al. 2009). The different selection criteria of the samples may be causing the differing percentages.

3.5.1   Outflow candidates with kinematic information

If we take into account all the cases from the sample in this work (see Sect. 3.4.1), M11 and Pogge et al. (2000), 60 LINERs have spectroscopic data (at least, from long-slit spectroscopy) available in some spectral bands. This information from the literature allows us to estimate the total percentage of kinematically-confirmed (or suggested) outflows in the total sample.

For all the targets classified as 'Core-halo', 'Disky' and 'Dusty' (43 targets) in our Hα data, there is kinematic information available for 33 objects, from which there are reported outflows/inflows in 15, as specified below.
From the 20 classified as 'Core-halo', 16 LINERs have kinematical information, and there are outflows reported for 8 LINERs: IC 1459, NGC 0315, NGC 2787, NGC 3884, NGC 3998, NGC 4278, NGC 4450, and NGC 7743. For NGC 0315, NGC 2787 (see also Ruschel-Dutra et al. 2021), NGC 3884, NGC 4278 and NGC 4450 objects the possible outflows (inflow for NGC 4278) were suggested by Cazzoli et al. (2018) with long-slit spectroscopy of the nuclear region. In IC 1459 the outflow was detected using IFU data from GMOS (Ricci et al. 2014, 2015), although the gas is associated to accretion from the surrounding galaxies with MUSE data in Mulcahey et al. (2021). For NGC 3998 there were hints of non rotational motions in Cazzoli et al. (2018), that were compatible with the perturbed kinematics of the [O III]

emission using IFU data of the ATLAS3D survey (Boardman et al. 2017). For NGC 7743 there was an outflow detected in molecular gas using SINFONI (Davies et al. 2014), and several kinematical components detected in the ionised gas studied by Katkov et al. (2011). In the case of the 15 LINERs classified as 'Disky', there is kinematical data for 13 targets. There are outflows/inflows reported only for 4 objects: NGC 2841, NGC 3642, NGC 4594 and NGC 5077. For NGC 2841, Schmidt et al. (2016) detected a small inflow of HI gas, although it is not clear if is caused by gas accretion or minor mergers. For NGC 3642 and NGC 4594 the outflows were detected with long-slit spectroscopy by Cazzoli et al. (2018) and Hermosa Muñoz et al. (2020), respectively. For NGC 5077 there is MUSE IFS data studied in detail by Raimundo (2021), who reports an outflow with the morphology of a hollow cone. The extended ionised emission corresponding to the outflow in that work is similar to what we find at larger scales (see Fig. 3.4).

From the 8 targets classified as 'Dusty', 6 of them have kinematical information in the literature. Outflows have been reported for 4 LINERs: NGC 3226 (Cazzoli et al. 2018), NGC 3627 (inflow in Casasola et al. 2011), NGC 3628 and NGC 5866 (Li 2015). The case of NGC 3628 was already mentioned in Sect. 3.4.1. There are two hints of outflows in this galaxy (see individual comments in Appendix B.1), a kpc-scale Hα plume (see Fig. 3.4) detected in various wavelength bands (Fabbiano et al. 1990; Tsai et al. 2012; Cicone et al. 2014; Fluetsch et al. 2019), and a sub-kpc outflow reported in CO emission (Tsai et al. 2012; Cicone et al. 2014; Roy et al. 2016), that is not visible in our Hα data due to obscuration from the dust lane (it is in the north direction at ≤ 20"from the centre).

From the 22 LINERs classified as 'Bubble' (see Sect. 3.4.1 and Table 3.1), there is kinematical information available for 21 targets, from which 10 have kinematically detected outflows with either IFS or long-slit spectroscopy. For 13 LINERs, namely NGC 0266, NGC 0404, NGC 1052, NGC 2685, NGC 3379, NGC 3414, NGC 4459, NGC 4486, NGC 4579, NGC 4596, NGC 4696, NGC 5813 and NGC 5846, there is IFS data available (see individual comments on each galaxy in Appendix B.1, in Pogge et al. 2000 and M11). The IFS data provided hints for non-rotational motions in the velocity maps which could be associated to outflows only for 6 objects, namely NGC 0404, NGC 1052, NGC 3379, NGC 4486, NGC 4579 and NGC 4696. NGC 0404 images show extended Hα emission ascribed to gas blown out possibly by starburst processes (Pogge et al. 2000), that is shown in Nyland et al. (2017) along with the central soft X-ray emission, which have similar extensions, suggesting the presence of shocks. This galaxy was suggested to have outflows associated to a small jet driven by the AGN using ALMA C0(2-1) data (Nyland et al. 2017), although the same emission was also ascribed to supernovae processes (Pogge et al. 2000; Boehle et al. 2018). NGC 1052 was in-

depth studied with IFS data, with all the works confirming an outflow in ionised gas (Dopita et al. 2015; Dahmer-Hahn et al. 2019a, Cazzoli et al. in prep.). For NGC 3379 the outflow is detected with SAURON data in Shapiro et al. (2006). For NGC 4486 they are mentioned in Hermosa Muñoz et al. (2020), although the emission is defined as ionised gas filaments with unclear nature in López-Cobá et al. (2020); Sánchez et al. (2021). For NGC 4579, the emission is ascribed to an outflow in several works with long-slit spectroscopy (Walsh et al. 2008; Davies et al. 2014; Mazzalay et al. 2014; Balmaverde & Capetti 2014; Molina et al. 2018), although within the NUGA project, there was an inflow detected in molecular gas, affecting on different galactic scales (García-Burillo et al. 2009; Casasola et al. 2011). For the remaining 7 objects, although there is disturbed gas, it is usually ascribed to past mergers or dust lanes that produce asymmetries in the gas velocities. For NGC 4696, Canning et al. (2011) analysed VIMOS/VLT IFU data, finding a filamentary structure with at least two different kinematic components, probably caused due to interactions with the powerful radio jet and with other members of its galaxy cluster. NGC 2685 has a complex structure: a polar ring blended with an outer ring (see Appendix. B.1). It was studied with long-slit spectra in previous works (Eskridge & Pogge 1997; Józsa et al. 2009; Hermosa Muñoz et al. 2020), but the different slits were not oriented in the direction of the possible outflow. Boardman et al. (2017) studied its [O III] emission with the ATLAS^{3D} survey, finding perturbed kinematics likely not produced by mergers, but by gas accretion of unclear origin.

For the other 8 galaxies with bubble-like morphology there is only long-slit spectroscopic data available in the literature. There are outflows reported for 4 targets: NGC 3245 (in Walsh et al. 2008, although not confirmed in Hermosa Muñoz et al. 2020), NGC 4036 (in Walsh et al. 2008, although not confirmed in Cazzoli et al. 2018), NGC 4750 (as an asymmetry in the emission due to dust lanes and spiral arms emerging from the centre Carollo et al. 2002; Cazzoli et al. 2018) and NGC 5005 (from both space and ground-data in Cazzoli et al. 2018) using long-slit spectroscopy. For the other 4 objects there are no outflows detected (NGC 3718, NGC 3945, NGC 4438 and NGC 4636). However, NGC 4438 has an interesting morphological structure (see Fig. 2 in M11). A clear bubble emerging from the nucleus is seen in Hα (M11), although the slit was in a direction of the possible outflow in the study by Cazzoli et al. (2018). The nature of this structure would be analysed with IFS data (Hermosa Muñoz et al. in prep.).

There are 5 galaxies whose morphologies were classified as 'Unclear'. There is kinematical information in the literature for 4 of them (NGC 4143, NGC 4203, NGC 5838, and NGC 7331), where 3 have reported outflows. For NGC 4143 there is only long-slit spectra available, from which the existence of outflows was suggested (Cazzoli et al. 2018). For

NGC 4203, NGC 5838 and NGC 7331, there is resolved kinematical information available in the literature (see Appendix B.1). NGC 4203 is included in the ATLAS^{3D} survey, and the H I shows non-rotational motions and inner dust lanes. H I data from the THINGS survey for NGC 7331 (Schmidt et al. 2016) indicated the presence of inflowing/outflowing emission, also suggested in previous works (Mediavilla et al. 1997; Battaner et al. 2003). Finally, for NGC 5838 there are not reported outflows. The IFS data comes from the SAURON survey (Falcón-Barroso et al. 2003; Sarzi et al. 2006), and although they detect asymmetries in the velocity maps, they ascribe them to dust in the nucleus.

Summarising, the kinematic information available for 60 LINERs indicates that there are a total of 29 objects (48%) for which the presence of outflows/inflows was either found or suggested by means of spectroscopic data. Their Hα morphology is classified here as 'Core-halo', 'Disky', 'Dusty' or 'Bubble', being 3 of them classified as 'Unclear' (see Table 3.1 and Sect. 3.4.1). The derived percentage is larger to the percentage derived from imaging data (32%, see Sect. 3.4.3). In Table 3.2 we have estimated the percentage of kinematically-identified outflows for the morphological classes derived in this work. The percentages in Table 3.2 indicate that, on average, 1 of every 2 LINERs in the nearby Universe may host an outflow. However, we note that we lack of kinematical information for 10 LINERs in the whole sample of 70, thus the rate may actually vary from 41% up to 56% LINERs with outflows.

Table 3.2 shows that among the classes with the largest number of objects (>10), the two categories with the largest percentages are 'Core-halo' and 'Bubble' (50% and 48%, respectively). The objects classified as 'Disky' show the lowest percentage within our classification (31%); this could be a matter of the outflow orientation and the inclination of the disc, that may challenge a possible outflow detection (see Sect. 3.5.3), specially in these low accretion rates where they are expected to be faint. The fraction of LINERs with kinematically confirmed outflows that are morphologically classified as 'Bubble'-like emission is 34% (10 out of 29). This implies that for the majority of the detected outflows, the ionised gas morphology does not show evident features of a bubble-like emission.

If only IFS data are considered for the identification of kinematical outflows (30 objects with IFS data; see Table 3.3), only 15 have detected outflows (50%). Small numbers preclude a separate analysis by morphological class, since all but 'Bubble' morphologies have IFS data for less than 10 objects. There are 13 objects with IFS information between the 'Bubble'-like morphologies, among which 6 (46%) show kinematical evidences of outflows, a slightly larger rate than that of the morphological detection (32%).

Table 3.2 Percentages of the galaxies with kinematically confirmed outflows in the literature depending on their morphological classification of the Hα nuclear emission (see Sect. 3.5.1 and Appendix B.1 for the comments on individual targets).

Morphological class	Kinematical outflows	Targets
Core-halo	50%	8 (out of 16)
Disky	31%	4 (out of 13)
Dusty	66%	4 (out of 6)
Bubble	48%	10 (out of 21)
Unclear	75%	3 (out of 4)
All classes	48%	29 (out of 60)

3.5.2   Soft X-ray / Ionised-gas relationship

It is noticeable that the Hα morphologies and the soft X-ray emission are coincident in a large fraction of the new data (∼30%), as is the case also for the targets analysed in M11. This behaviour has been seen previously for type-2 Seyferts (Bianchi et al. 2006), where the [O III] and the soft X-ray emission correlated. The work by Bianchi et al. (2019b) suggested that Seyferts and LINERs do have similarities in their narrow line regions (see also Pogge et al. 2000), which could lead to the conclusion that these two emissions are produced within the same region of the AGN, and thus a correlation should be expected also in LINERs. The correspondence of the ionised gas morphological signatures, the kinematic results and the X-ray emission for all the galaxies for which we could retrieve data (56 targets: 28 from new data; see Sect. 3.3) is in Table 3.3.

M11 performed a similar analysis with the objects from their sample. They gathered data for a total of 28 LINERs in both soft and hard X-rays using Chandra, 4 of which were NGC 3379, NGC 4278, NGC 4676A and B (thus we consider here 24 objects). The results were that, generally, the soft X-ray emission traced that of the ionised gas, and they were correlated in all but 4 galaxies, that seemed to deviate from that trend (NGC 3226, NGC 4486, NGC 5846 and NGC 5866). From all the galaxies with X-ray data in their sample, 20 out of 24 (∼83%) showed a correlation in the emission.

By taking into account the new data in this work (see Sect. 3.4.2), from the 52 objects with soft X-ray data available in the Chandra archive, 31 of them (60%; see Table 3.3) do show a correlation with the ionised gas emission. According to our results (see Table 3.3), 29 targets have reported outflows or inflows with kinematical information. Only 12 LINERs (namely IC 1459, NGC 2787, NGC 2841, NGC 3245, NGC 3884, NGC 3998, NGC 4036, NGC 4450, NGC 4579, NGC 4594, NGC 4696 and NGC 4750) have both features simultaneously, that is 23% (12 over 52). However, the reported outflows in all the objects but 5 (IC 1459,

NGC 2841, NGC 3998, NGC 4579 and NGC 4696) come from long-slit spectroscopy. As discussed previously (see Sect. 3.5), although useful, these spectra do not fully characterise the AGN and its environment, given the spatial limitations of the technique. This combined with the small number of coincidences, do not allow to draw any firm conclusion about a possible correlation between the presence of an outflow and an extended X-ray emission.

Table 3.3 Galaxies with available X-ray data and its correspondence with the morphological signatures in Hα and the kinematically-confirmed outflows or inflows in the literature (see Sect. 3.5.1, Sect. 3.5.2 and Fig. 3.5).

Galaxy (1)	Morphology (2)	Spectra (3)	Outflow/Inflow (4)	X-ray (5)
NGC 0266	Bubble	IFS	N	Y
NGC 0404[†]	Bubble	IFS	Y	-
NGC 1052[†]	Bubble	IFS	Y	-
NGC 2685	Bubble	IFS	N	-
NGC 3245[†]	Bubble	LSS	Y	Y
NGC 3379	Bubble	IFS	Y	N
NGC 3414	Bubble	IFS	N	Y
NGC 3718[†]	Bubble	LSS	N	-
NGC 3945	Bubble	LSS	N	Y
NGC 4036[†]	Bubble	LSS	Y	Y
NGC 4192[†]	Bubble	-	-	-
NGC 4438[†]	Bubble	LSS	N	Y
NGC 4459	Bubble	IFS	N	N
NGC 4486[†]	Bubble	IFS	Y	N
NGC 4579[†]	Bubble	IFS	Y	Y
NGC 4596	Bubble	IFS	N	Y
NGC 4636[†]	Bubble	LSS	N	Y
NGC 4696[†]	Bubble	IFS	Y	Y
NGC 4750	Bubble	LSS	Y	Y
NGC 5005[†]	Bubble	LSS	Y	-
NGC 5813	Bubble	IFS	N	Y
NGC 5846[†]	Bubble	IFS	N	N
IC 1459[†]	Core-halo	IFS	Y	Y
NGC 0315[†]	Core-halo	LSS	Y	N

Table 3.3 Continue.

Galaxy (1)	Morphology (2)	Spectra (3)	Outflow/Inflow (4)	X-ray (5)
NGC 0410	Core-halo	IFS	N	Y
NGC 2639[†]	Core-halo	-	-	-
NGC 2787[†]	Core-halo	LSS	Y	Y
NGC 3623[†]	Core-halo	-	-	-
NGC 3884	Core-halo	LSS	Y	Y
NGC 3998[†]	Core-halo	IFS	Y	Y
NGC 4111[†]	Core-halo	-	-	Y
NGC 4261	Core-halo	IFS	N	Y
NGC 4278	Core-halo	LSS	Y	N
NGC 4450	Core-halo	LSS	Y	Y
NGC 4494	Core-halo	IFS	N	-
NGC 4589	Core-halo	LSS	N	N
NGC 4698	Core-halo	IFS	N	N
NGC 4772	Core-halo	IFS	N	Y
NGC 5055[†]	Core-halo	IFS	N	Y
NGC 5957	Core-halo	-	-	-
NGC 6482	Core-halo	LSS	N	-
NGC 7743	Core-halo	IFS	Y	-
NGC 0841	Disky	LSS	N	-
NGC 2681[†]	Disky	LSS	N	Y
NGC 2841[†]	Disky	IFS	Y	Y
NGC 3185	Disky	-	-	-
NGC 3507	Disky	IFS	N	N
NGC 3608	Disky	IFS	N	N
NGC 3642	Disky	LSS	Y	N
NGC 3898	Disky	LSS	N	N
NGC 4314[†]	Disky	-	-	Y
NGC 4321	Disky	IFS	N	N
NGC 4457	Disky	IFS	N	N
NGC 4552[†]	Disky	LSS	N	Y
NGC 4594[†]	Disky	LSS	Y	Y

Table 3.3 Continue.

Galaxy	Morphology	Spectra	Outflow/Inflow	X-ray
(1)	(2)	(3)	(4)	(5)
NGC 4736[†]	Disky	LSS	N	Y
NGC 5077	Disky	IFS	Y	-
NGC 3226[†]	Dusty	LSS	Y	N
NGC 3607[†]	Dusty	-	-	Y
NGC 3627[†]	Dusty	IFS	Y	-
NGC 3628	Dusty	IFS	Y	N
NGC 4125	Dusty	-	-	N
NGC 4374[†]	Dusty	LSS	N	Y
NGC 5746	Dusty	IFS	N	-
NGC 5866[†]	Dusty	LSS	Y	N
NGC 4143	Unclear	LSS	Y	N
NGC 4203	Unclear	IFS	Y	N
NGC 5363	Unclear	-	-	-
NGC 5838	Unclear	IFS	N	Y
NGC 7331	Unclear	IFS	Y	N

Columns indicate: (2) the morphological classification according to Sect. 3.4; (3) indicates whether the spectral information was obtained with long-slit spectroscopy (LSS) or IFS; in columns (4) and (5): 'Y' stands for Yes and 'N' for No; (5) indicates if the X-ray emission is co-spatial with the Hα morphology (see Sect. 3.4.2). Targets from Pogge et al. (2000) and Masegosa et al. (2011) are marked with †.

3.5.3   Comparison with other active galaxies

So far, there are two systematic searches of outflows in LINERs with both ground and space-based long-slit spectroscopic data. These were done by Cazzoli et al. (2018) and Hermosa Muñoz et al. (2020), who analysed 22 (type-1) and 9 (type-2) LINERs, finding an outflow detection-rate of 41% and 22%, respectively. Considering the sample number, the rate of outflows we report in this study (48%) is in agreement with that by Cazzoli et al. (2018).

There are several works searching for outflows in the nearby Universe for different active galaxies in different wavelength ranges (Cazzoli et al. 2016; Fiore et al. 2017; Fluetsch et al.

2019, 2021; Ruschel-Dutra et al. 2021), and also at higher redshifts (e.g. Harrison et al. 2016, $0.6 \lesssim z \lesssim 1.7$, with ~50% kinematic detections of ionised outflows). Within the kinematical data from the literature gathered in this work with LINERs in the Local Universe, not all the targets with kinematically-identified outflows are based on ionised gas (19 out of 29 in ionised gas). There are evidences for extended outflows on different spatial scales (from sub-kpc to several kpc), associated to both AGNs and starburst activity (Veilleux et al. 2005, e.g. M 82, see Leroy et al. 2015). Luo et al. (2021) studied the ionised emission for 40 nearby (z<0.1) type-2 AGNs, finding a correlation between the outflow sizes and the [O III] luminosities. The typical sizes of the kinematically-identified outflows varied from 0.9 to 4 kpc (median 2 kpc), which are similar sizes to those quoted by previous works (e.g. mean of 1.8 kpc for luminous z<1 AGNs in Bae et al. 2017; 0.1 to 3 kpc for 6 Seyfert-2 galaxies in Revalski et al. 2021). In this work we focus on the circumnuclear emission of the galaxies as it is expected that the possible outflows are less intense in LINERs. However, the Hα emission in our images has similar extensions, with a mean observed size of 1.9 kpc, ranging in all morphologies from 0.2 to 6 kpc (0.5 to ~2 kpc for only the bubble-like morphologies). Concas et al. (2019), by exploiting SDSS spectra, suggested that although the inclination of the host galaxy is crucial to detect the outflowing emission, if the ionised outflows are AGN-driven and the accretion disc is not connected to the host disc, then the outflow may be launched in another direction, not perpendicular to the host. Fischer et al. (2013) obtained the inclination of the AGN in 17 Seyfert galaxies, finding that the biconical outflows were more easily detected in those that were type-2 AGNs (i.e. oriented edge-on). From our imaging data and the kinematic analysis from the literature, we find that inclination could be important, as the lowest percentages of outflows are in 'Disky' systems (e.g. NGC 4321). Given that the intensity of the outflowing gas scales with the activity of the AGN (Fluetsch et al. 2019; Revalski et al. 2021), and that their extension is typically ~ 1 kpc (one of the largest seen with our images is NGC 3945 ~1.5 kpc; see Fig. B.4), we could be missing outflows due to inclination effects. As already noticed by Fischer et al. (2013), these effects are potentially more relevant for close to face-on targets in which the outflow has a cone-like shape, as the inclination effects may lead to misleading morphological classifications. Within our sample, between the kinematically-detected outflows there are 19 type-1 (5 IFS, 14 LSS) and 10 type-2 LINERs (8 IFS, 2 LSS)[2]. Those detected with long-slit spectroscopy are only nuclear outflows. Curiously, for the IFS outflowing detections in type-1s, the typical sizes are larger than 1 kpc (i.e. ~1 kpc for NGC 1052, ~2.3 kpc for NGC 4696, ~5 kpc for IC 1450), whereas for type-2s the sizes are usually detected on a sub-kpc scale (i.e. ~40 pc NGC 0404

---

[2]The distribution of type-1 and type-2 LINERs in the complete sample is 38% and 62% respectively (based on Ho et al. 1997a; Cazzoli et al. 2018; Hermosa Muñoz et al. 2020)

or ~700 pc for NGC 7743). This would be expected based on the unified model, as type-2 LINERs are oriented edge-on and thus outflows oriented in the polar direction would be more easily detected than on more face-on type-1 LINERs.

3.6 Summary and conclusions

In this work we present a morphological analysis of 70 nearby LINERs with both AL-FOSC/NOT and HST narrow band imaging corresponding to the Hα emission. We have obtained new data for a total of 38 galaxies, whereas the remaining 32 come from previous works (Pogge et al. 2000, M11). The Hα imaging data indicate that among these AGNs there is a variety of morphologies within the ionised gas, that can be classified in 4 different groups, as in M11, plus an additional class for objects with an ambiguous classification. The statistics derived from the total sample of 70 LINERs suggest that ~32% of LINERs have bubble-like ionised gas morphologies, ~29% show compact circumnuclear emission ('Core-halo') and ~21% have emission associated to the disc or the spiral arms of the host galaxy. For ~11% of the sample we cannot state anything on the morphologies, as there is nuclear dust preventing from obtaining a complete vision of the ionised gas. Additionally, the complex distribution of the gas in ~7% of the sample lead us to an unclear classification of the sources based exclusively on imaging information. However, there is kinematical information in the literature for 80% (4 out of 5) of these sources with 'Unclear' morphology that provides more evidences on the possible origin of the emission (see Sect. 3.5.1).

Considering all the kinematic information available, accounting for both long-slit and IFS data, we have data for 60 LINERs. The statistics evidence that 48% of the objects do show outflow kinematic signatures (see Sect. 3.5.1). This percentage is somewhat larger than that derived from the morphological signatures (32%). Since we still miss kinematic information for 10 targets of the 70 LINERs, the total rate could vary from 41% up to 56% LINERs with outflows. With the complete morphological and kinematical information combined, we find that at least 1 out of every 3 nearby (z < 0.025) LINERs may have a galactic outflow, probably associated to the activity of the super massive black hole, given that they are mainly detected in ionised gas.

The morphological signatures combined with the kinematical information suggest that, considering our number statistics, it is equally probable to find an outflow in a LINER in which the ionised gas morphology is bubble-like than if it is core-halo-like (see Sect. 3.5.1).

We found evidences that the soft X-ray emission follows that from the ionised gas in 31 LINERs (~60% above the total with X-ray data) from the galaxies analysed in this work. This means that for the majority of targets there is a correlation between the ionised Hα gas and the soft X-ray, as it was proposed in previous works for higher-luminosity AGNs (Bianchi et al. 2006, 2019b). Both emissions are then expected to be raised in the same spatial region of the AGN. We note though that the results may vary and that we could find (or not) a strong correlation between the emissions as we still lack soft X-ray data for a 25% of the sample (i.e. 18 LINERs). Specifically, the correlation percentage may vary up to 70% (44%) if both emissions are (not) co-spatial for all the remaining targets. We do not see any correlation between the spectroscopically-confirmed outflows and the co-spatiality of these emissions (ionised gas and soft X-rays). Therefore, with the data that we have, we can say that the soft X-ray emission is not a strong predictor of the presence of kinematically evident outflows. As for the Hα imaging, considering all the kinematical information available, our results suggest that those objects with Disky-like structures have less probability of hosting an outflow, probably due to the orientation, whereas for the remaining morphologies, the probability of detection is 55%.

Chapter 4

Unexplored outflows in nearby low luminosity AGNs: The case of NGC 1052

Abstract

Multi-phase outflows play a central role in galaxy evolution shaping the properties of galaxies. Understanding outflows and their effects in low luminosity active galactic nuclei (AGNs), such as low ionisation nuclear emission line regions (LINERs), is essential. LINERs bridge the gap between normal and active galaxies, being the most numerous AGN population in the local Universe. Our goal is to analyse the kinematics and ionisation mechanisms of the multi-phase gas of NGC 1052, the prototypical LINER, in order to detect and map the ionised and neutral phases of the putative outflow. We obtained Very Large Telescope MUSE and Gran Telescopio Canarias MEGARA optical integral field spectroscopy data for NGC 1052. In addition to stellar kinematics maps, by modelling spectral lines with multiple Gaussian components, we obtained flux, kinematic, and excitation maps of both ionised and neutral gas. The stars are distributed in a dynamically hot disc ($V/\sigma \sim 1.2$), with a centrally peaked velocity dispersion map ($\sigma_c = 201 \pm 10\,\mathrm{km\,s^{-1}}$) and large observed velocity amplitudes ($\Delta V = 167 \pm 19\,\mathrm{km\,s^{-1}}$). The ionised gas, probed by the primary component is detected up to $\sim 30''$ ($\sim 3.3\,\mathrm{kpc}$) mostly in the polar direction with blue and red velocities ($|V| < 250\,\mathrm{km\,s^{-1}}$). The velocity dispersion map shows a notable enhancement

($\sigma > 90 \, \text{km s}^{-1}$) crossing the galaxy along the major axis of rotation in the central 10". The secondary component has a bipolar morphology, velocity dispersion larger than $150 \, \text{km s}^{-1}$, and velocities up to $660 \, \text{km s}^{-1}$. A third component is detected with MUSE (and barely with MEGARA), but it is not spatially resolved. The broad-line region (BLR) component (used to model the broad Hα emission only) has a full width at half maximum of 2427 ± 332 and $2350 \pm 470 \, \text{km s}^{-1}$ for MUSE and MEGARA data, respectively. The maps of the NaD absorption indicate optically thick neutral gas with complex kinematics. The velocity field is consistent with a slow rotating disc ($\Delta V = 77 \pm 12 \, \text{km s}^{-1}$), but the velocity dispersion map is off-centred without any counterpart in the (centrally peaked) flux map. We found evidence of an ionised gas outflow (secondary component) with a mass of $1.6 \pm 0.6 \times 10^5$ $M_\odot$, and mass rate of $0.4 \pm 0.2 \, M_\odot \text{yr}^{-1}$. The outflow is propagating in a cocoon of gas with enhanced turbulence and might be triggering the onset of kiloparsec-scale buoyant bubbles (polar emission), both probed by the primary component. Taking into account the energy and kinetic power of the outflow ($1.3 \pm 0.9 \times 10^{53}$ erg and $8.8 \pm 3.5 \times 10^{40} \, \text{erg s}^{-1}$, respectively) as well as its alignment with both the jet and the cocoon, and that the gas is collisionally ionised (due to gas compression), we consider that the most likely power source of the outflow is the jet, although some contribution from the AGN is possible. The hints of the presence of a neutral gas outflow are weak.

4.1   Introduction

Outflows produced by active galactic nuclei (AGNs) and intense episodes of star formation are thought to play a crucial role in regulating the build up of stellar mass and black hole mass growth through negative and positive feedback (see e.g. Kormendy & Ho 2013 and references therein). Recently, it has been shown that outflows can also be driven by radio jets (e.g. Morganti et al. 2005; Harrison et al. 2014; Morganti & Oosterloo 2018; Jarvis et al. 2019; Molyneux et al. 2019; Venturi et al. 2021). The outflows might be an important source of feedback as they evolve and heat the interstellar medium (ISM) preventing the cooling of the gas possibly on large scales.

The different gas phases of outflows have been widely studied in different galaxy populations (Veilleux et al. 2005, 2020, for reviews) mostly via long-slit spectroscopy (e.g. Heckman et al. 2000; Rupke et al. 2002; Arribas et al. 2014; Villar-Martín et al. 2018; Rose et al. 2018; Hernández-García et al. 2019; Saturni et al. 2021) and integral field spectroscopy (IFS, e.g. Cazzoli et al. 2014; Cresci et al. 2015; Ramos Almeida & Ricci 2017; Maiolino et al. 2017; Bosch et al. 2019; Perna et al. 2020, 2021; Comerón et al. 2021) observations.

To date, the vast majority of studies of multi-phase outflows and feedback have focussed

on local luminous and ultra-luminous infrared galaxies (U/LIRGs, e.g. Rupke & Veilleux 2013; Cazzoli et al. 2014, 2016; Pereira-Santaella et al. 2016, 2020; Fluetsch et al. 2021) and luminous AGNs (e.g. quasars or Seyferts galaxies; Feruglio et al. 2010; Müller-Sánchez et al. 2011; Fiore et al. 2017; Brusa et al. 2018; Venturi et al. 2018; Cazzoli et al. 2020). These works demonstrate the power of the 3D IFS in studies of this kind. For example, the wealth of optical and infrared (IR) IFS data enable the exploration of possible scaling relations between AGN properties, host galaxy properties, and outflows (e.g. Kang & Woo 2018, Fluetsch et al. 2019; Kakkad et al. 2020; Ruschel-Dutra et al. 2021; Avery et al. 2021; Luo et al. 2021, Singha et al. 2022, and references therein).

For low luminosity AGNs, such as low ionisation nuclear emission line regions (LINERs), no systematic search for outflows has been done yet. Except for individual discoveries (e.g. Dopita et al. 2015; Raimundo 2021) the only systematic studies are by Cazzoli et al. (2018) and Hermosa Muñoz et al. (2020) of ionised gas outflows in type 1 and type 2 LINERs, respectively. These two works, where 30 LINERS were studied on the basis of optical long-slit spectroscopy, indicate that multi-phase outflows are common in LINERS (detection rate: 60%, Cazzoli et al. 2018), showing an intriguing ionisation structure in which low ionisation lines (e.g. [O I]$\lambda\lambda$6300,6364) behave differently to high ionisation lines (e.g. [O III]$\lambda\lambda$4959,5007). Most of these spectroscopically identified outflows show in their HST-H$\alpha\lambda$6563 image (Pogge et al. 2000; Masegosa et al. 2011; Hermosa Muñoz et al. 2022) a large-scale biconical or bubble-like shape along with evident spatially resolved sub-structures, such as $\sim$ 20-70 pc wide gas clumps.

A 3D description of multi-phase outflows and the quantification of their feedback (mass, energy, and their rates) in low luminosity AGNs like LINERs is lacking. The exploration of outflows and feedback for this AGN family is crucial to improving our understanding of galaxy evolution as these sources are thought to bridge the gap between normal and luminous AGNs, and they belong to the most numerous AGN population in the local Universe (Ho 2008, for a review).

NGC 1052 (MCG-01-07-034, PKS 0238-084) is considered as the prototypical LINER in the local Universe (z $\sim$ 0.005). Table 4.1 summarises the basic properties of this object.

There are four previous IFS studies focussing on NGC 1052: Sugai et al. (2005), Dopita et al. (2015), and Dahmer-Hahn et al. (2019a,b). Sugai et al. (2005) probed the bulk of the outflow with channel maps of the [O III] emission line thanks to Kyoto3DII/Subaru data over the innermost 3″ × 3″. Dopita et al. (2015) (hereafter D15) analysed the stellar and gas kinematics within the inner 25″ × 38″ using WiFeS/ANU data. The authors mapped the emission line properties on scales of hundred of parsecs (spatial sampling $\sim$1.3″), mainly studying shocks with no detailed information on the properties of the different kinematic components.

Dahmer-Hahn et al. (2019a,b) (hereafter DH19a,b) mapped optical and near-IR lines in the inner 3.5''×5"(similar to the work by Sugai et al. 2005) exploiting GMOS/GEMINI data. The richness of tracers provided by the combination of multi-wavelength data offers a more detailed view than the previous works of the complex kinematics in NGC 1052. Nevertheless, the large-scale emission, on kiloparsec (kpc) scales, is not covered by the GEMINI data set. Summarising, all these IFS-based works support the presence in NGC 1052 of an emission line outflow possibly extended on kpc scales.

In this paper we use spectral and spatial capabilities of MUSE/VLT and MEGARA/GTC optical IFS observations to build, for the first time, a comprehensive picture of both stellar and ISM components in NGC 1052 of the outflow, at a resolution of tens of parsec (pc).

This paper is organised as follows. In Section 4.2 the data and observations are presented, as well as the data reduction. In Section 4.3 we present the spectroscopic analysis: stellar subtraction, line modelling, and map generation. Section 4 highlights the main observational results. In Section 5 we discuss the stellar kinematics and dynamics, and the ionised and neutral gas properties with special emphasis on outflow properties and its possible connection with the radio jet; we also estimate the black hole mass, and compare the full width at half maximum (FWHM) of the unresolved broad-line region (BLR) component with previous estimates. The main conclusions are presented in Section 4.6. In Appendix C.1 we summarise the procedure to account for background sources. In Appendix C.2 we present the kinematic flux-intensity maps and flux ratios from our IFS data set. Appendix C.3 is devoted to presenting the 1D position-velocity and position-dispersion diagrams aimed at comparing gas and stellar motions along the three major axes: the major and minor axes of the host galaxy, and the radio jet.

All images and spectral maps are oriented following the standard criterion, so north is up and east to the left.

Throughout the paper, angular dimensions will be converted into physical distances using the scale distance from the Local Group of 110 pc/'' (see Table 4.1).

4.2   Observations and data reduction

In this section we describe MUSE and MEGARA data and their data reduction process (Sections 4.2.1 and 4.2.2, respectively).

Table 4.1 General properties of NGC 1052.

Properties	Value	References
R.A. (J 2000)	$02^h41^m04^s.799$	NED
Decl. (J 2000)	$-08^d15^m20^s.751$	NED
z	0.00504	NED
V_{sys} [km s^{-1}]	1532 ± 6	Karachentsev & Makarov (1996)
D [Mpc]	22.6 ± 1.6	NED
Scale [pc/$''$]	110	NED
Nuclear Spectral Class.	LINER (1.9)	González-Martín et al. (2009)
Morphology	E3-4/S0	Bellstedt et al. (2018)
i [$°$]	70.1	Hyperleda
PA_{phot}	112.7	Hyperleda
R_{eff} [$''$]	21.9	Forbes et al. (2017)
M_{BH} [$M_{\odot}$]	$3.4\,(0.9)\times 10^8$	Beifiori et al. (2012)
PA_{jet} [$°$]	70	Kadler et al. (2004a)
SFR [$M_{\odot}$/yr]	0.09	Falocco et al. (2020)

Notes. V_{sys}, D and Scale is the systemic velocity, distance, and scale, respectively, from the Local Group. Morphology is the Hubble classification. i is the inclination angle defined as the inclination between line of sight and polar axis of the galaxy determined from the axis ratio of the isophote in the B band using a correction for intrinsic thickness based on the morphological type. PA_{phot} is the position angle of the major axis of the isophote 25 mag/arcsec^2 in the B band measured north-eastwards (see Paturel et al. 1997 and references therein). R_{eff} is the effective radius from Spitzer data. The black hole mass (M_{BH}) is derived from a Keplerian disc model assuming an inclination of 33°(81°) and a distance of 18.11 Mpc. PA_{jet} is the position angle of the jet from VLBI data (covering only the central region of NGC 1052). As the PA depends on the different components of the jet, varying from 60° to 80°, in this work we consider the average value of 70°. See Kadler et al. (2004a) and references therein for further details. SFR is the upper limit to the star formation rate from FIR luminosity (2×10^{42} erg s^{-1}) as measured by Falocco et al. (2020).
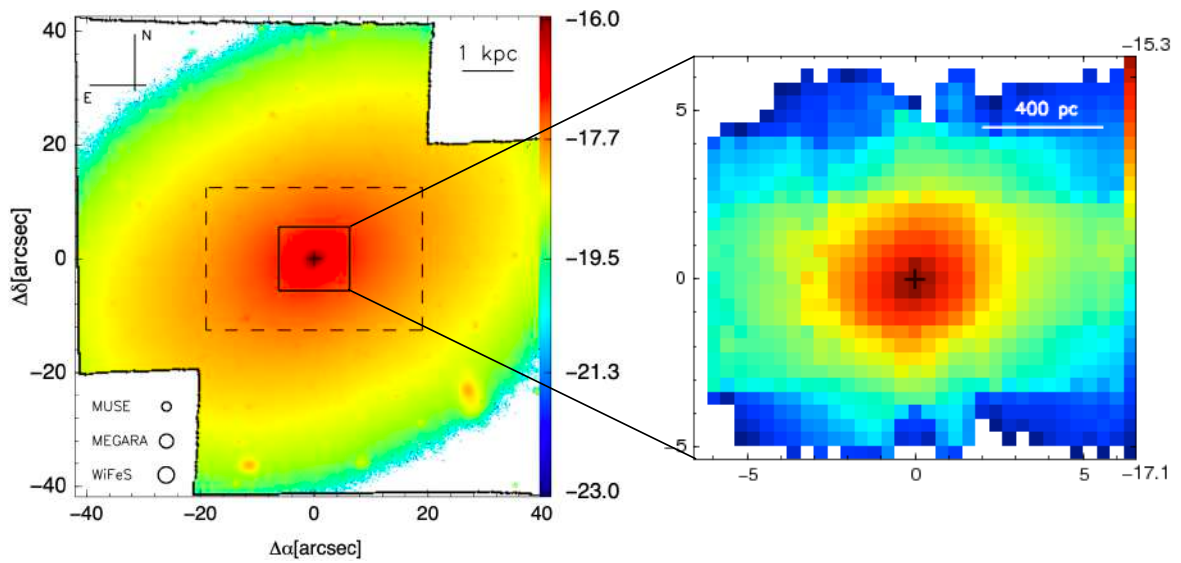
Fig. 4.1 Optical continuum images computed from MUSE (left) and MEGARA (right) in units of $\mathrm{erg\,s^{-1}\,cm^{-2}}$ (logarithmic scale). To obtain these images we considered a 60 Å wide continuum band ($6105 - 6165$ Å). The cross is the photometric centre, and the sizes of the different PSFs for MEGARA and MUSE data are indicated in the bottom left part of the figure (see also Sect. 4.2). As reference we show the field of view (dashed rectangle) and average seeing ($1.4''$, bottom circle) for the WiFeS datacube analysed in D15. The black bar at the upper right represents 1 kpc ($\sim 9''$) at the redshift of NGC 1052 (see Table 4.1). Similarly, the white bar at the upper right, right panel, represents 400 pc ($\sim 3.6''$).

4.2.1   MUSE observations and data reduction

The data were gathered on September 5, 2019, with the Multi-Unit Spectroscopic Explorer (MUSE, Bacon et al. 2010, 2014), mounted at the UT4 of the Very Large Telescope at the Paranal Observatory in Chile as part of programme 0103.B-0837(B) (PI: L. Hernández-García).

They were acquired in the wide-field mode configuration with the nominal setting (i.e. no extended wavelength coverage), covering the spatial extent of 1 arcmin^2 with $0.2''$ pix^{-1} sampling. The MUSE data has a wavelength coverage of 4800 - 9300 Å, with a mean spectral resolution of R ~ 3000 at 1.25 Å spectral sampling. During the observations the average DIMM seeing was 0.62"(varying between $0.48''$ and $0.85''$); the mean airmass was 1.06.

In total we obtained eight exposures with a total integration time of 93 min. Including the overheads the observations took two hours (i.e. two observing blocks). Each block consists of four dithered exposures of 697 s. The relative offsets in RA(DEC) were $10''$, $0.5''$, $-21.5''$, and $0.5''$ ($11''$, $0.5''$, $-21.5''$, and $0.5''$) with respect to the position of NGC 1052 (Table 4.1). The dither pattern also involves a 90° rotation for a better reconstruction of the final cube in order to have a homogeneous quality across the field of view.

The eight pointings constitute a mosaic covering a contiguous area of $80'' \times 80''$, or 8.8 kpc $\times$ 8.8 kpc at the adopted spatial scale (110 pc/$''$, Table 4.1). The radius of the covered area is about 3.5 times the effective radius of NGC 1052 ($21.9''$, Table 4.1). The data reduction was performed with the MUSE pipeline (version 2.8.1) via `EsoRex` (version 3.13.2). It performs the basic reduction steps (bias subtraction, flat-fielding, wavelength calibration, and illumination correction), as well as the combination of individual exposures in order to create the final mosaic. For flux calibration we used the spectrophotometric standard star Feige 110 (spectral type: DOp) observed before the science frames. Since we did not apply any telluric correction, some residuals remain in the region between 7110 and 7310 Å. In this spectral window only the HeIλ7065.3, [Ar III]λ7135.80, and [Fe II]λ7155 lines are detected, but they are not crucial for our analysis. The sky subtraction was performed in the latest step of the processing of MUSE observations using the sky background obtained from the outermost spaxels in each science exposure (no dedicated on-sky exposures were gathered). We performed the astrometry calibration using the astrometric catalogue distributed with the pipeline.

The final cube has dimensions of $418 \times 422 \times 3682$. The total number of spectra is 176 396, of which 28 508 (16 %) are not useful as they correspond to artefacts from the creation of the mosaic (i.e. empty spaxels located in the bottom left and top right corners, and at the edges of the field of view).

The radius of the point spread function (PSF) of the MUSE observations ($0.4''$, see Fig. 4.1)

was estimated from the FWHM of the 2D profile brightness distribution of the standard star used for flux calibration. Throughout the paper, in order to avoid any possible PSF contamination in the kinematic measurements, we conservatively consider as the 'nuclear region' a circular area of radius equal to the width at 5% intensity of the PSF radial profile (i.e. 0.8''). This area does not coincide with any peculiar feature (e.g. dust lanes) visible in the MUSE continuum image shown in the left panel of Fig. 4.1. The nuclear region is indicated (with a circle) in the spectral maps computed from the MUSE datacubes (see Fig. 4.1, but also Sect. 4.3 and Appendix C.2).

We obtained the instrumental profile by measuring the single (not blended) OHλ 7993.332 sky-line (Osterbrock et al. 1996; Bai et al. 2017). We measured it in the fully reduced datacube of the standard star Feige 110 (see above) by selecting a region of size 50×50 spaxels free from stellar emission. On average, the central wavelength and the width of the OH sky-line are 7993.335 ± 0.114 Å and 1.19 ± 0.13 Å, respectively. This instrumental profile correction was further checked with the 5577 Å sky-line. In this case the value of the average instrumental resolution is consistent with that from the OH line (i.e. 1.2 Å).

4.2.2   MEGARA observations and data reduction

The data were taken on December 28, 2019, with the MEGARA instrument (see Gil de Paz et al. 2016; Carrasco et al. 2018) located in the Cassegrain focus of GTC using the Large Compact Bundle IFU mode (GTC94-19B, PI: S. Cazzoli). The 567 fibres that constitute the MEGARA IFU (100 μm in core size) are arranged on a square microlens array that projects on the sky a field of 12.5'' x 11.3''. Each microlens is a hexagon inscribed in a circle with diameter of 0.62'' projected on the sky. A total of 56 ancillary fibres (organised in eight fibre bundles), located at a distance of 1.75–2.0 arcmin from the centre of the IFU field of view, deliver simultaneous sky observations.

We made use of two low resolution volume phase holographic gratings (LR-VPHs) that provide a R $\sim$ 6000 in the central wavelengths of the selected bands: LR-V has a wavelength coverage $5140 - 6170$ Å and LR-R $6100 - 7300$ Å.

We obtained six exposures with an integration time of 900s per VPH in two observing blocks, leading to a total observing time of four hours. The mean signal-to-noise ratio (S/N) in the spectra continuum was 25 for the LR-R and 30 for the LR-V datacube. The data reduction was done using the MEGARA Data Reduction Pipeline (Pascual et al. 2020; Pascual et al. 2021) available as a package inside Python (version 0.9.3). We performed the standard procedures: bias subtraction, flat-field correction, wavelength calibration, and flux calibration using the star HR 4963. Each fibre was traced individually at the beginning of the data reduction and, within the pipeline, we applied additional corrections for the possible differences of each fibre

with respect to the whole image, including an illumination correction based on individual fibre flats. For this correction we used IRAF to smooth the sensitivity curve as (in the case of the LR-R VPH) some structure due to the lamp emission is present (see the MEGARA cookbook). The pipeline also performs the individual exposures combination to generate the final cube (one per VPH), which can be transformed into a standard IFS cube from raw stacked spectra format by means of a regularisation grid to obtain 0.4″ square spaxels (see Cazzoli et al. 2020). The PSF of the MEGARA data was measured as in Sect. 4.2.1 with the star HR 4963, giving a FWHM of 1.2″ (see Fig. 4.1, left).

Considering the wavelength ranges of the VPHs and the emission lines present in NGC 1052 spectra, we decided to combine the two cubes into a single datacube to optimise the stellar modelling and subtraction (increasing the range of line-free continuum, see Sect. 4.3.2). More specifically, the need to combine the two MEGARA cubes to reliably model the stellar continuum is twofold. First, the spectral range of the MEGARA LR-V cube covers only the MgI stellar feature, whereas none are present in the LR-R cube. Second, for the LR-R (red) cube, the stellar continuum emission is limited by the presence of the broad emission features and a telluric band (see Sect. 4.2.2). For the cube combination, we scaled the fluxes for every spaxel to have the continuum at the same level in the common wavelength range of both VPHs (6100 − 6170 Å). The combined datacube was used in the whole analysis.

4.3   Data analysis

In this section we summarise the identification and subtraction of background sources in the MUSE field of view (Sect. 4.3.1), and we describe the stellar continuum modelling (Sect. 4.3.2) and line fitting for MUSE and MEGARA cubes (Sect. 4.3.3).

4.3.1   Background sources in the MUSE field of view

We visually inspected the white light image generated in the last step of the data reduction of MUSE data: the mosaic creation (see Sect. 4.2) and the continuum image in Fig. 4.1. We note that there are a number of sources (both point-like and extended), some of which may not be part of the NGC 1052 galaxy. In Appendix C.1 we summarise the procedure for identifying putative background sources.

We found two background galaxies at redshifts ∼0.03 and ∼0.022. Only the former is identified in NED as *SDSSCGB_67616.02*. Both of these galaxies were masked out from the final MUSE datacube used for the analysis.
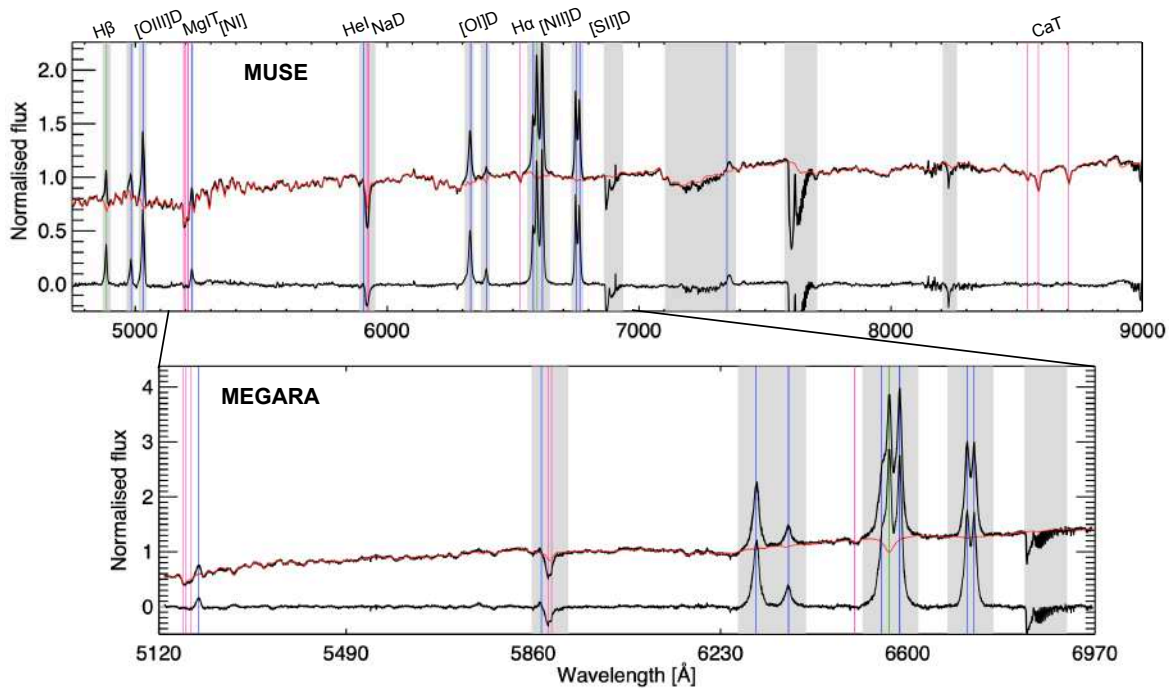
Fig. 4.2 Example of stellar continuum modelling and its subtraction for high S/N nuclear spectra from MUSE (top panel) and MEGARA (bottom panel) data. The red line indicates the modelled stellar spectrum that matches the observed continuum, obtained applying the pPXF (Sect. 4.3.2). The wavelength regions blocked for the modelling are shown in grey. Spectral features are labelled at the top, and Balmer lines, forbidden lines, and absorption lines are shown in green, blue, and pink, respectively. In case of MEGARA we combined the cubes in LR-V and LR-R bands, which have a 70 Å overlap around 6130 Å (see Sect. 4.2.2).

4.3.2   Stellar continuum modelling

For the stellar continuum modelling we used the penalised PiXel-Fitting code (pPXF) by Cappellari & Copin (2003) (see also Cappellari 2017 and references therein) for both MEGARA and MUSE, in different coding environments. We used the pPXF code within the GIST pipeline (see below) for MUSE and within PYTHON for MEGARA.

For MUSE we used the GIST pipeline (v. 3) by Bittner et al. (2019)[1] as a comprehensive tool both to spatially bin the spectra in order to increase the S/N in the continuum and to model the stellar contribution to the observed spectra. The MUSE spectra were shifted to rest frame based on the initial guess of the systemic redshift from NED, $z = 0.005$ (Table 4.1). Then the data were spatially binned using the 2D Voronoi binning technique by Cappellari & Copin (2003) that creates bins in low S/N regions, preserving the spatial resolution of those above a minimum S/N threshold. The S/N has been calculated in the line-free wavelength band

---

[1]http://ascl.net/1907.025

between 5350 and 5800 Å. All spaxels with a continuum S/N < 3 were discarded to avoid noisy spectra in the Voronoi bins. We found that a minimum S/N threshold of 30 results in reliable measurements of stellar kinematics in NGC 1052 as well as an optimum spatial resolution. In general, cells are not larger than 60 spaxels ($2.4\,\mathrm{arcsec}^2$ in area), hence stellar properties are likely to be homogeneous within a Voronoi cell.

For MEGARA data the Voronoi binning was not necessary to achieve a proper stellar continuum modelling as in the spaxels with the lowest S/N (< 15), which constitute ~12% of the total, the resulting velocity and velocity dispersion are consistent with the rest of the cube with higher S/N.

To accurately measure spectral line properties (wavelength, width, and flux), it is necessary to account for stellar absorption, which primarily affects the Balmer emission lines and the NaD absorption doublet. For MUSE we limited the wavelength range used for the fit to $4800 - 9000$ Å, which contains spectral features from Hβ to CaT, and excluded the region of the auroral [S III]λ9069 line[2]. For MEGARA the total wavelength range was from 5150-7000 Å covering the main spectral features in both LR-V and LR-R bands. For both data sets we masked the spectral regions (emission lines and atmospheric and telluric absorptions) affected by emission from the interstellar medium (ISM). Additionally, we excluded the NaD absorption that is not properly matched by the stellar templates owing to the impact of interstellar absorption. For MUSE, we used the Indo-U.S. stellar library (Valdes et al. 2004) as in Cazzoli et al. (2014, 2016, 2018). Briefly, in this library there are 885 stars selected to provide a broad coverage of the atmospheric parameters (effective temperature, surface gravity, and metallicity). The stellar spectra have a continuous spectral coverage from 3460 to 9464 Å, at a resolution of ~ 1 Å FWHM (Valdes et al. 2004). For MEGARA we used the RGD synthetic stellar library (González Delgado et al. 2005; Martins et al. 2005) since it covers the whole spectral range for the combined datacubes, and the spectral resolution is consistent with that from our spectra. The library consisted on 413 stars selected with a metallicity of Z = 0.02, ranging from 4000 to 7000 Å and covering a wide range of surface gravities and temperatures (see González Delgado et al. 2005, and references therein).

Finally, we set up `pPXF` using four moments of the line of sight velocity distribution (LOSVD) for both MUSE and MEGARA: V, σ, h3, and h4. The additive and multiplicative polynomials were set to 4-4 (0-12) for MUSE (MEGARA) in order to, respectively, minimise template mismatch and match the overall spectral shape of the data so that the fit is insensitive to reddening by dust (see Westfall et al. 2019; Perna et al. 2020, and references therein).

An example of the `pPXF` modelling is shown in Fig. 4.2 for both MUSE (top panel) and

---

[2]This line is noisy and only barely detected in a region of radius of ~ 1″, hence no spatially resolved analysis will be done.
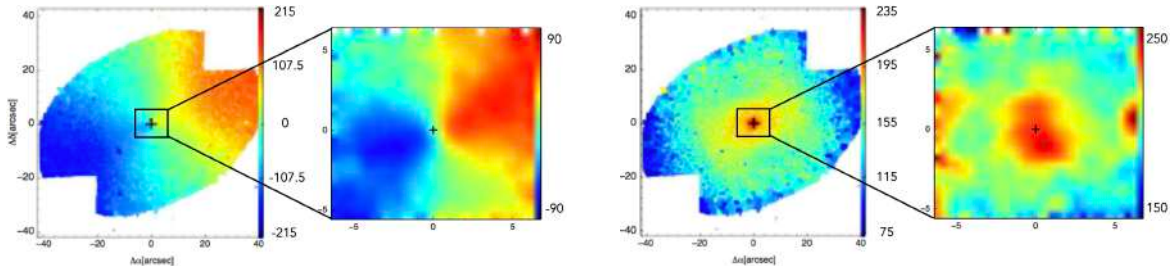
Fig. 4.3 NGC 1052 stellar kinematics maps from our pPXF analysis (Sect. 4.3.2). These maps, velocity (left) and velocity dispersion (right), are displayed in units of km s^{-1}. In both panels the large-scale kinematics are obtained from MUSE data, whereas the insets show the smoothed pPXF-maps from MEGARA datacube. The cross indicates the photometric centre as in Fig. 4.1.

MEGARA (bottom panel) data. The results of the pPXF fits (i.e. the stellar kinematics maps of the first two moments of the LOSVD) are shown in Fig. 4.3, and are discussed in Sect. 4.4.1. A detailed study of higher order moments of the stellar LOSVD (h3 and h4) is beyond the aim of the paper, hence the corresponding maps are not displayed.

Through the analysis we consider formal uncertainties provided by the pPXF tool. These are in good agreement with those from the Monte Carlo simulations performed on MUSE data. Specifically, differences are generally lower than 5 km s^{-1} and 7 km s^{-1} for velocity and velocity dispersion, respectively.

Motivated by the typical small sizes of the Voronoi cells in the MUSE data, we made the simplifying assumption that the stellar populations and kinematics do not change radically within one Voronoi bin. For each spaxel the stellar spectrum of the corresponding bin was normalised and then subtracted from the one observed to obtain a datacube consisting exclusively of ISM absorption and emission features. For the MEGARA data the stellar subtraction was performed on a spaxel-by-spaxel basis. In what follows we refer to this datacube (data − stellar model) as the ISM cube.

4.3.3 Line modelling

From the ISM cube we produced line maps by modelling the spectral lines with multiple Gaussian functions. To achieve this, we applied a Levenberg–Marquardt least-squares fitting routine under both interactive data analysis (IDL) and PYTHON environments, using MPFITEXPR by Markwardt (2009) and LMFIT, respectively (see Sections 4.3.3 and 4.3.3). We imposed the intensity ratios between the [O III]λ4959,5007 (only for MUSE), [O I]λ6300,6363, and [N II]λ6548,6584 to be 2.99, 3.13, and 2.99 (Osterbrock & Ferland 2006). The ratio of the equivalent widths (EWs) of the two lines of the NaD$\lambda\lambda$5890,5896 absorption,
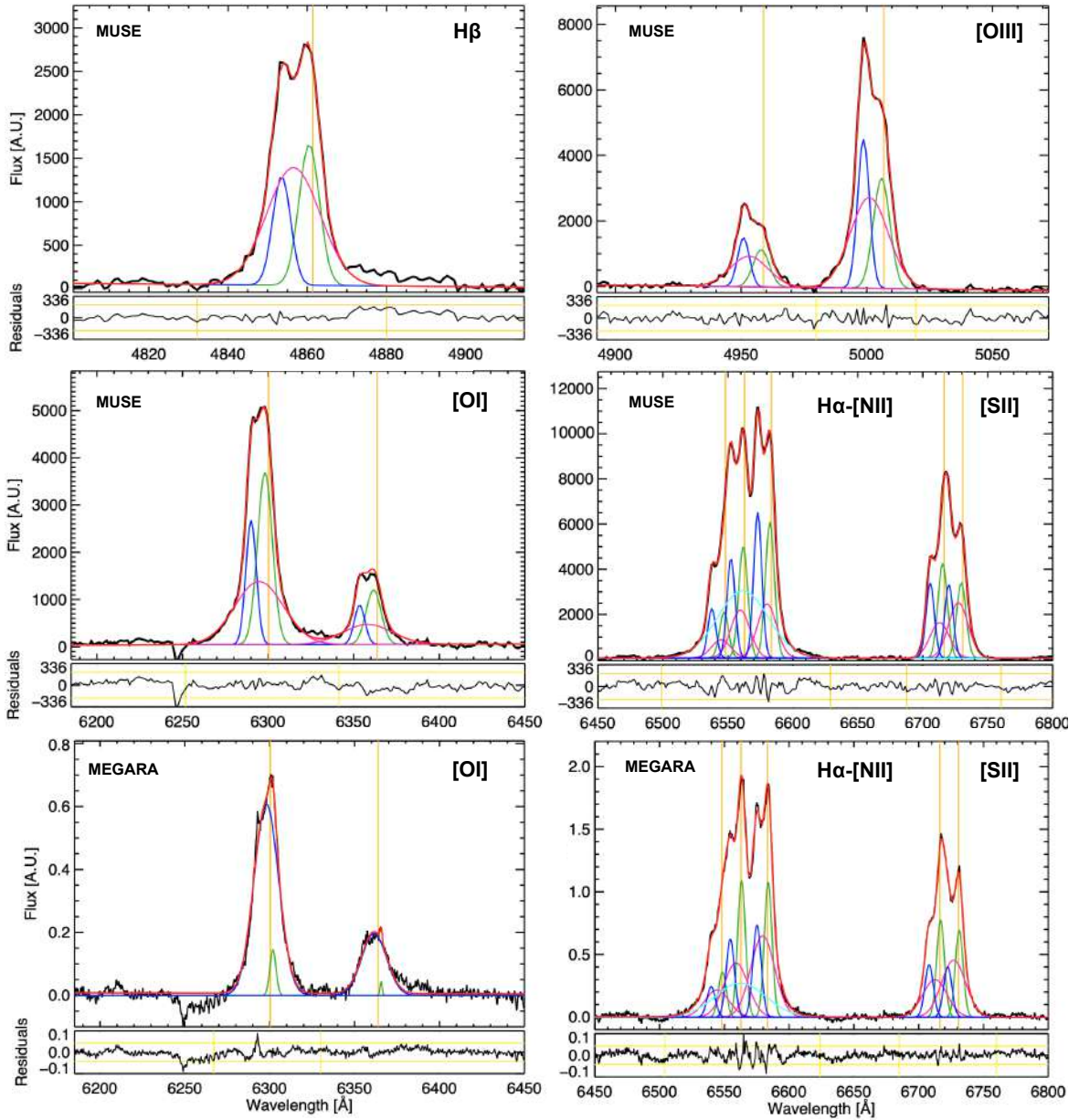
Fig. 4.4 Examples of emission line spectra (black) after stellar subtraction (Sect. 4.3.2) and their modelling from the central region of both MUSE data (R = 0.7″, i.e. 77 pc) and MEGARA data (R = 0.9″, i.e. 100 pc), as indicated top left. As references, the orange vertical lines give the systemic wavelengths of the emission lines which, are indicated top right. For each panel the modelled line profile (in red) and the components (in different colours) are shown. Specifically, the green, blue, and pink Gaussian curves indicate the primary, secondary, and tertiary components used to model the profiles. The cyan line indicates the broad Hα component from the BLR. Residuals from the fit are shown below each panels; the yellow horizontal lines indicate the $\pm 2.5\,\varepsilon_c$ (Sect. 4.3.3) and the vertical yellow lines give the wavelength range considered for calculating ε_{fit} for each line (Sect. 4.3.3). The high residuals redwards of Hβ cannot be fitted with a BLR component (the velocities and widths would be inconsistent with those of the broad Hα component), and are likely due to some residuals from stellar subtraction (Sect. 4.3.2).
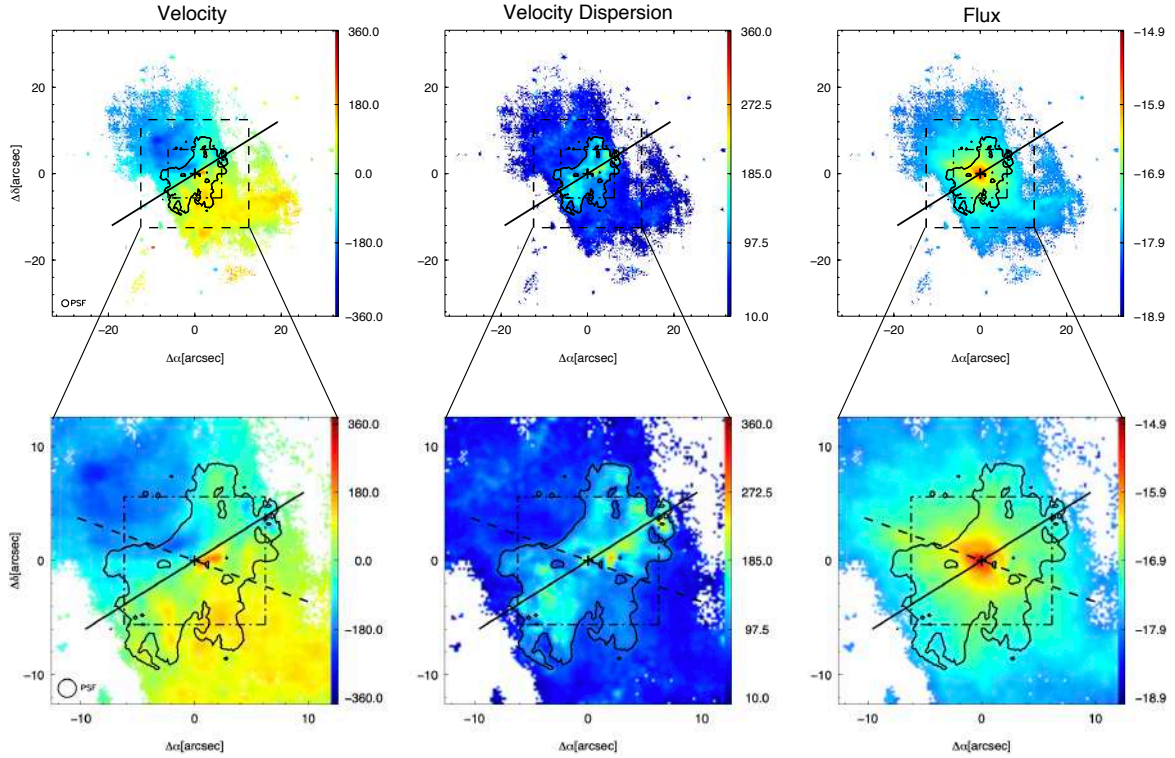
Fig. 4.5 Example of emission line maps produced from the fitting of the [O III]λ5007 line using the MUSE ISM cube (Sect. 4.3.3). Shown, from left to right, are the maps for the primary component: velocity field (km s^{-1}), velocity dispersion (km s^{-1}), and flux intensity (erg s^{-1} cm^{-1}, log scale). The black solid line indicates the major axis of the stellar rotation (Table 4.2). The dot-dashed square indicates the MEGARA field of view. The contours indicate the central region at high velocity dispersion (see Sect. 4.4.2 for details). *Top*: Maps covering a smaller field of view with respect to the original MUSE mosaic ($80'' \times 80''$, Sect. 4.2.1) to highlight weak features. The dashed square indicates the selected zoomed-in view in the bottom panels of this figure and for Figures C.3 to C.15 of the Appendix C.2. *Bottom*: Zoomed-in area. The dashed line indicates the orientation of the radio jet (Table 4.1).

$R_{NaD} = EW_{5890}/EW_{5896}$, is restricted to vary from 1 (optically thick limit) to 2 (optically thin absorbing gas), according to Spitzer (1978).

Emission line modelling

We derived the kinematics of the ISM properties by modelling all the spectral lines available in the cubes. To perform the fitting, and hence discriminate between line models and number of components, we followed the approach proposed by Cazzoli et al. (2018). Specifically, for the MUSE and the MEGARA data, we tested the [S II]-model and the [O I]-model, for which we first fitted in the spectrum only [S II] and [O I] lines (depending on the model) and then used them as reference to tie all the other narrow lines, so they share the same

width and velocity shift. Additionally, we tested the 'mixed' models, using [S II] and [O I] simultaneously as reference respectively for [N II] and narrow Hα or, alternatively, using [O I] for narrow Hα and [N II], with [S II] lines behaving otherwise. For the MUSE data only (see Sect. 4.2.2), the best fit to the Hα ([S II]) line is applied to the Hβ ([O III]) line. However, none of these models provided a good fit for the whole set of lines. In the MEGARA field of view the independent fitting of [O I] and [S II] lines produced differences of $\sim 100\,\mathrm{km\,s^{-1}}$ for the velocity measurements, although the line widths were similar with differences $\leq 50\,\mathrm{km\,s^{-1}}$. For the MUSE data we found that at large spatial scales (R $> 10''$) the kinematics of these lines are similar within $75\,\mathrm{km\,s^{-1}}$ (mostly) when they are fitted independently. Although large discrepancies ($> 100\,\mathrm{km\,s^{-1}}$) arise in the central region (inside the MEGARA field of view; R $< 10''$ oriented E-W), with a peculiar butterfly shape (see Sect. 4.4). A similar behaviour was found comparing [O III] and [S II] kinematics. Moreover, the S/N of the [O I] (Hβ) drops steeply in the NW-SE direction, complicating the tying with Hα-[N II] (Hα) in both MUSE and MEGARA data. Taking all this into account, we decided to fit Hβ, [O III], [O I], and [S II] independently and use the last as a template for the Hα-[N II] blend. Finally, as NGC 1052 is a type 1.9 LINER (Table 4.1), we added a broad AGN component (from the unresolved BLR) with width $> 600\,\mathrm{km\,s^{-1}}$ ($1400\,\mathrm{km\,s^{-1}}$ in FWHM) only in Hα forcing its spatial distribution to be the same as the PSF. Figure 4.4 shows examples of the Gaussian fits of the whole set of emission lines for both MUSE (four upper panels) and MEGARA (two lower panels).

The emission lines present complex profiles with broad wings and double peaks[3] (Fig. 4.4) suggesting the presence of more than one kinematic component, especially within the innermost $10''$ of radius. In order to prevent overfit, we first fitted all emission lines with one Gaussian component, and then more components were added based on the parameter $\varepsilon_{\mathrm{line}}$. This parameter is defined as the standard deviation of the residuals under the emission lines, after a component is added. In the cases where $\varepsilon_{\mathrm{line}} > 2.5 \times \varepsilon_{\mathrm{cont}}$ (standard deviation of the line-free continuum), another Gaussian component is added. This criterion has been already successfully applied to optical spectra of active galaxies both from long-slit (Cazzoli et al. 2018; Hernández-García et al. 2019; Hermosa Muñoz et al. 2020) and IFS (Cazzoli et al. 2020).

Overall, we allowed a maximum of three Gaussians per line plus the BLR component in Hα (Fig. 4.4). This provides a good trade-off between a statistical good fit to the spectra (i.e. residuals are of the same order as the noise without any peculiar structures like spikes or bumps) and the number of components used having a reasonable physical explanation.

---

[3]Double peaks were already detected by DH19a for NGC 1052 (their Fig. 3) and in other LINERs, e.g. NGC 5077 (Raimundo 2021).

For each emission line and component found we ended up with the following information: central wavelength, width, and flux intensity along with their respective fitting uncertainties. These are the formal 1σ uncertainty weighted with the square root of χ^2, as in Cazzoli et al. (2020).

Taking into account both their central velocities and line widths, we identify a primary, a secondary, and a tertiary component. More specifically, the primary component can be mapped over the whole galaxy line-emitting region ($\sim 39''$, i.e. 4.3 kpc), with clear blue and red velocities, with generally the lowest widths (it is also clearly detected by D15b). The tertiary component is not spatially resolved (it is extended within a radius of $\leq 2''$, i.e. PSF size) being generally the broadest. The secondary component has intermediate properties; it is spatially resolved, being mapped up to $R < 5''$ (i.e. 550 pc), with extreme velocities (up to $\sim 660\,\mathrm{km\,s^{-1}}$). Additionally, in order to discriminate between the components (especially primary and secondary) we considered the spatial continuity of both flux and kinematic values. For the former a visual inspection was already satisfactory to prevent wild variations; for the latter we avoided sharp variations of the kinematics between adjacent spaxels. Specifically, we imposed that the values of the velocity fields vary smoothly (differences are less than $200\,\mathrm{km\,s^{-1}}$) and that the secondary component is broader than the primary. Differences in line widths are of $\sim 160 - 180\,\mathrm{km\,s^{-1}}$ on average, for the brightest lines such as [O III] and Hα-[N II]. A minor number of spaxels (< 40) constitute an exception to this general behaviour of velocity dispersion, but they are mainly located either within the PSF or at the largest radii where the secondary component is detected.

For each of these components we created velocity, velocity dispersion, and flux maps. These are shown in the figures in Appendix C.2 (from Fig. C.3 to Fig. C.10 and from Fig. C.11 to Fig. C.13 for MUSE and MEGARA, respectively). An example of these maps is shown in Fig. 4.5 for the [O III] line for MUSE data. In this figure we display both the large and small scales mapped by our IFS data. As the large-scale emission is similar among emission lines, the maps in Appendix C.2 show only the central region ($R \sim 10''$) where the largest differences are observed (see Sect. 4.4 for details).

To obtain velocity dispersion for each spectrum (i.e. on a spaxel-by-spaxel basis), the effect of instrumental dispersion (i.e. σ_{INS}, see Sect. 4.2) was corrected for by subtracting it in quadrature from the observed line dispersion (σ_{obs}): $\sigma_{\mathrm{line}} = \sqrt{\sigma_{\mathrm{obs}}^2 - \sigma_{\mathrm{INS}}^2}$.

We use the [S II] ratio ([S II]$\lambda6716$/[S II]$\lambda6731$, e.g. Fig. C.6, right panel) to estimate the electron density (n_e) in accordance with the relation of Sanders et al. (2016). To investigate the ionising mechanisms across the field of view for each component used to model emission features (forbidden and narrow Balmer lines), the maps of the four line ratios used in standard Baldwin, Phillips & Terlevich (BPTs) diagnostic diagrams (Baldwin et al. 1981) were also

generated. The maps are presented in Appendix C.2 (Figures from C.15 to C.18) and the diagnostic diagrams in Figures 4.6 and 4.7. For the two spatially resolved components (namely primary and secondary), the typical values of kinematics and line ratios are summarised in Tables 4.3 and 4.4.

Sodium doublet modelling

The wavelength coverage of our MUSE and MEGARA data sets allow us to probe the NaD absorption doublet. This feature originates both in the cold-neutral ISM of galaxies and in the atmospheres of old stars (e.g. K-type giants). We modelled the doublet in the ISM cubes (after the stellar subtraction, Sect. 4.3.2) to obtain the neutral gas kinematics, and hence to infer whether the cold neutral gas is either participating in the ordinary disc rotation or entraining in non-rotational motions such as outflows (see e.g. Cazzoli et al. 2014, 2016). For MUSE data the NaD is detected at S/N > 3 up to R ~25.7″ (2.8 kpc); however, most of the absorption (95% of the spaxels at S/N > 3) is concentrated within the inner ~16″ (1.8 kpc). The NaD EW map is presented in Fig. 4.8. The values range from 0.4 to 3.3 Å (1.1 Å, on average).

We prefer to model the NaD doublet on a spaxel-by-spaxel basis in the MEGARA data as it generally has a higher S/N with respect to that of the MUSE data. We considered one kinematic component (a Gaussian function for each line), and we masked the wavelength range between 5900 and 5920 Å due to some residuals from the stellar subtraction.

To infer the presence of a second component we inspected the map of the residuals (i.e. $\varepsilon_{line}/\varepsilon_{cont}$), as was done for the emission lines (Sect. 4.3.3). However, the values are in the range 0.7–2 (1.2, on average), hence there is not a strong indication of the need for multiple components to fit the doublet.

Figure 4.9 shows an example of the modelling of the NaD doublet absorption, and Fig. 4.10 presents the corresponding kinematic and absorbed-flux maps. The results for the NaD absorption doublet are presented in Sect. 4.4.6 and discussed in Sect. 4.5.4.

4.4   Main observational results

In Sect. 4.4.1 we present the results from the pPXF stellar kinematics analysis of both the MUSE and the MEGARA data. The emission lines detected in both MUSE and MEGARA ISM cubes are [S II], Hα-[N II], and [O I], whereas Hβ and [O III] are covered only by MUSE data (see Sect.4.2). In both data sets a maximum of three kinematic components are used to model forbidden lines and narrow Hα (Sect. 4.3.3). These components have different kinematics and spatial distribution indicating that they are distinct components. In
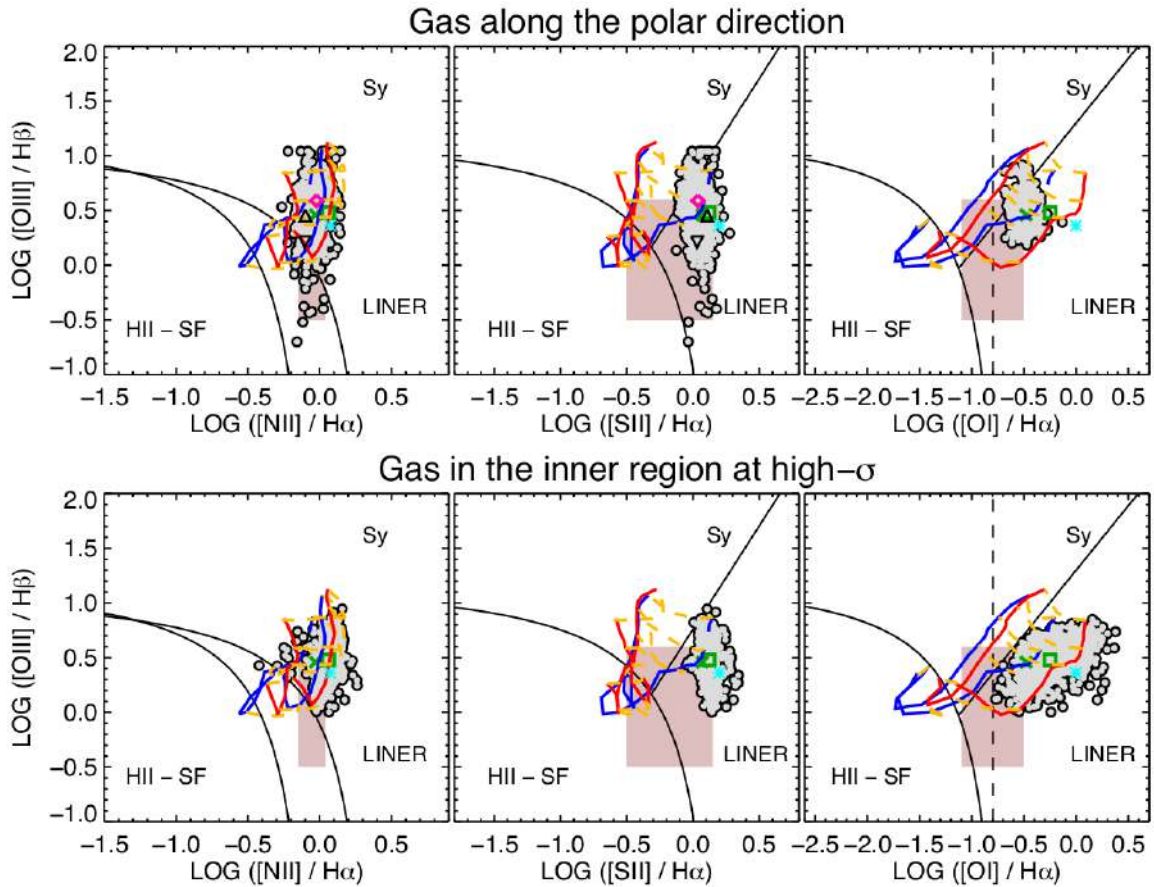
Fig. 4.6 Optical standard BPT diagrams for the primary component for the gas distributed in the polar direction and that in the central region at high-σ (top and bottom panels, respectively) obtained from MUSE data. The grey circles indicate the data points presented in this paper. The black lines in all diagrams represent the dividing curves between H II star-forming regions, Seyferts, and LINERs from Kewley et al. (2006) and Kauffmann et al. (2003). The pink boxes show the predictions of the photoionisation models by pAGB stars for Z = Z$_\odot$, a burst age of 13 Gyr (Binette et al. 1994), and ionisation parameter values (log U) between -3 and -4. Log U is typically -3.5 in LINERs (Netzer 2015). The predictions of shock-ionisation models are overlaid in each diagram. Specifically, following Cazzoli et al. (2018), shock+precursor grids from Groves et al. (2004) are considered with Z = Z$_\odot$ and for different n$_e$. The blue and red curves correspond to models with n$_e$ = 1 cm^{-3} and n$_e$ = 100 cm^{-3}, respectively (see also Sect. 4.4.2). The values plotted correspond to the minimum and maximum preshock magnetic field allowed in each model. In addition, only shock-velocities from 100 to 500 km s^{-1} (yellow dashed lines) are considered as larger σ are not observed for the primary component (Sect. 4.4.2). The dividing line between weak-[O I] and strong-[O I] LINERs (Filippenko & Terlevich 1992) is shown in black with a dashed line (right panels). In all diagrams, green symbols indicate the average values calculated in the polar (cross) and central (square) regions; as reference the cyan star is the typical value in the nucleus (average within the PSF region). In the top panels the pink diamond, black triangle, and black upside down triangle are the average BPT values for the faint features: the arm, the east, and south-east clumps, respectively (see Sect. 4.4.2). These features are not detected in [O I], hence no symbols are displayed in the corresponding diagnostic diagrams.
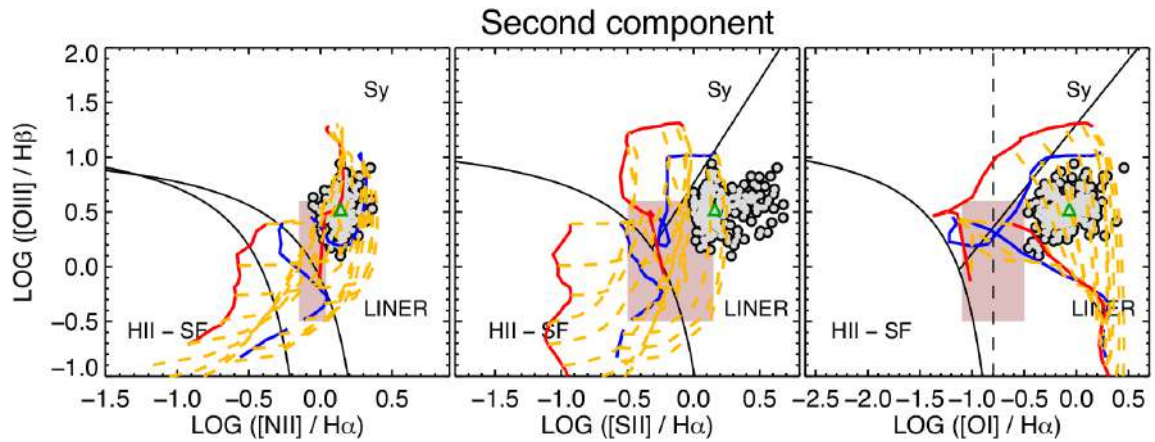
Fig. 4.7 Same as Fig. 4.6, but for the secondary component. Shock models (no precursor) are considered; the blue and red curves correspond to models with $n_e = 100 \, \mathrm{cm}^{-3}$ and $n_e = 1000 \, \mathrm{cm}^{-3}$, respectively (see Sect. 4.4.2). The green triangle indicates the average value of the line ratio distribution.
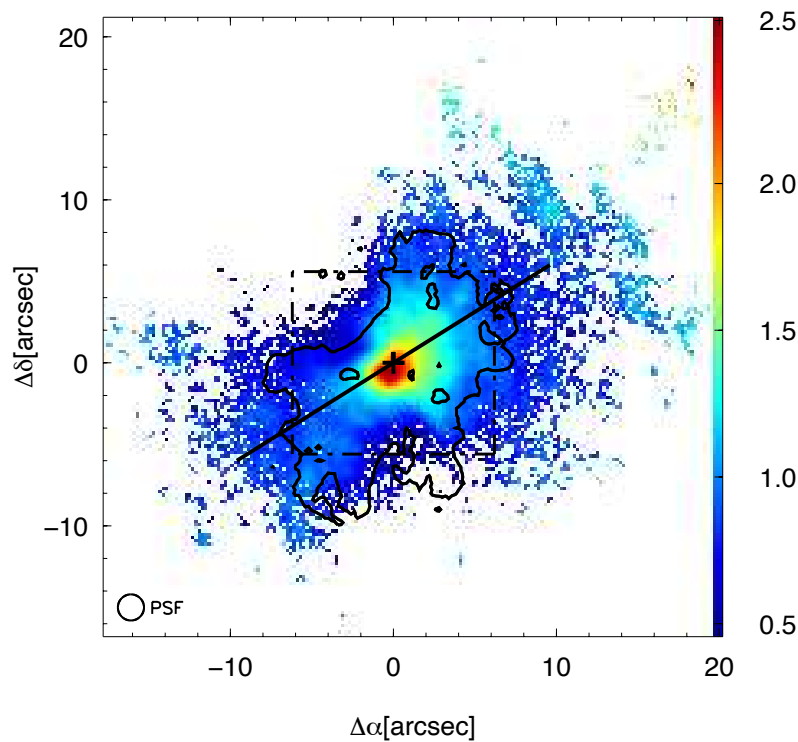
Fig. 4.8 NaD EW map (in Å) from MUSE cube. The dot-dashed square indicates the MEGARA field of view. The black solid line indicates the major axis of the stellar rotation (Table 4.2). The contours indicate the region with enhancement velocity dispersion of emission lines (see Sect. 4.4.2 and e.g. Fig. 4.5).
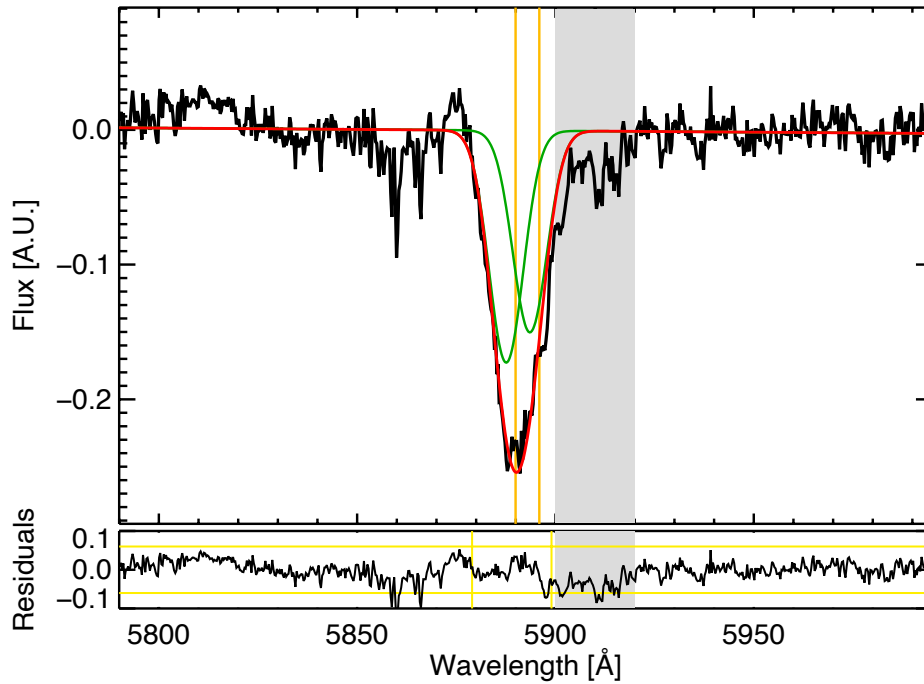
Fig. 4.9 Example of absorption line spectra (black) after stellar subtraction (Sect. 4.3.2) and their modelling from the central region of MEGARA data (R = 1.45″, i.e. 160 pc). The grey band indicates the spectral band blocked during the fitting due to residuals from stellar subtraction (see Sect. 4.3.3). The orange vertical lines and the red and green curves, as well as both vertical and horizontal yellow lines, are as in Fig. 4.4.
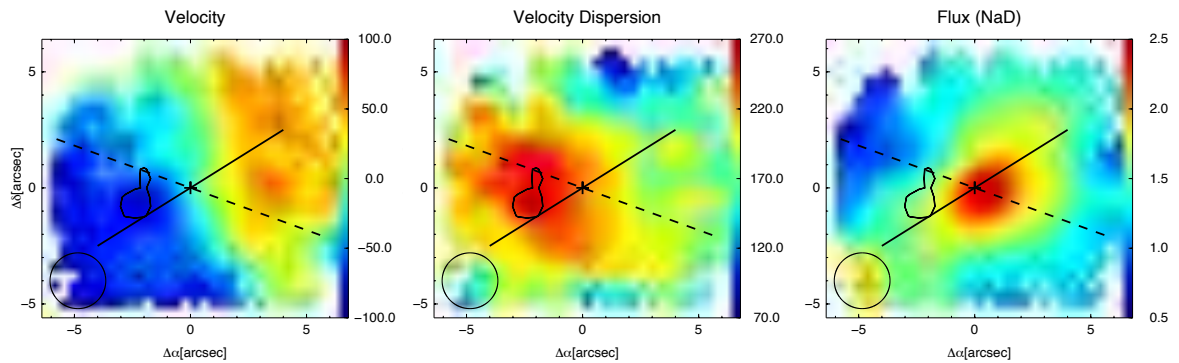
Fig. 4.10 Neutral gas velocity field (km s^{-1}), velocity dispersion (km s^{-1}), and flux intensity (mJy) maps for the single kinematic component used to model NaD. The black lines are as in Fig. C.13. Specifically, the black solid line indicates the major axis of the stellar rotation (Table 4.2). The dashed lines indicate the orientation of the radio jet (Table 4.1). The contours indicate the region at high velocity dispersion (Sect. 4.5.4 for details).

Table 4.2 Stellar kinematic properties of NGC 1052 from MUSE and MEGARA.

IFU_{FoV}	ΔV $km\,s^{-1}$	PA $^\circ$	σ_c $km\,s^{-1}$	σ $km\,s^{-1}$
MEGARA	78 ± 3	112 ± 6	215 ± 13	201 ± 16
$MUSE_{MEGARA}$	75 ± 9	122 ± 5	—	180 ± 6
MUSE	167 ± 19	122 ± 10	201 ± 10	145 ± 22

Notes. ΔV is the observed velocity amplitude; PA is the position angle of the major kinematic axis; σ_c and σ are the central velocity dispersion (at $R < R_{eff}/8$, i.e. 303 pc) and the mean velocity dispersion, respectively (see Sect. 4.4.1). For the velocity dispersion measurement the quoted uncertainties are one standard deviation. The $MUSE_{MEGARA}$ line indicates that the values are measured using the MUSE data but over the field of view (FoV) of MEGARA.

Sect. 4.4.2 we present the spatial distributions of kinematics and ISM properties (e.g. line ratios and electron density) measured for each of the three components in the MUSE data. The comparison between the MUSE and MEGARA results is presented in Sect. 4.4.4. An additional broad Hα component originating in the BLR of the AGN was used to model spectra within the nuclear region (Sect. 4.3.3). Its properties are presented in Sect. 4.4.5 for both data sets. Finally, Sect. 4.4.6 summarises the main results from the modelling of the NaD absorption (Sect. 4.3.3).

4.4.1 Stellar kinematics

As explained in Sect. 4.3.2, we used pPXF to fit the stellar continuum of the spectra for both MEGARA and MUSE datacubes. The maps of the stellar kinematics (velocity and velocity dispersion) for both data sets are shown in Fig. 4.3 and the main properties are summarised in Table 4.2.

The stellar velocity field (Fig. 4.3, left panels) shows the typical spider-pattern consistent with a rotating disc, at both large and small spatial scales mapped by our IFS data. The peak-to-peak velocity (ΔV, Table 4.2) from the MUSE (MEGARA) data is $167 \pm 19\,km\,s^{-1}$ ($78 \pm 3\,km\,s^{-1}$) at a galactocentric distance of $40''$ ($4''$), which corresponds to 4.4 kpc (0.4 kpc). The ΔV from MUSE map within the MEGARA footprint, $75 \pm 9\,km\,s^{-1}$ (Table 4.2) is consistent with that from the MEGARA cube.

The stellar major kinematic axis estimated at the largest scales for the MUSE and MEGARA data are respectively $(122 \pm 10)^\circ$ and $(112 \pm 6)^\circ$ measured north-eastwards (Table 4.2). Both measurements indicate this axis is aligned with the photometric major axis (112.7°, Table 4.1).

Overall, the stellar velocity dispersion varies from 75 to $235\,km\,s^{-1}$ for MUSE and from 100
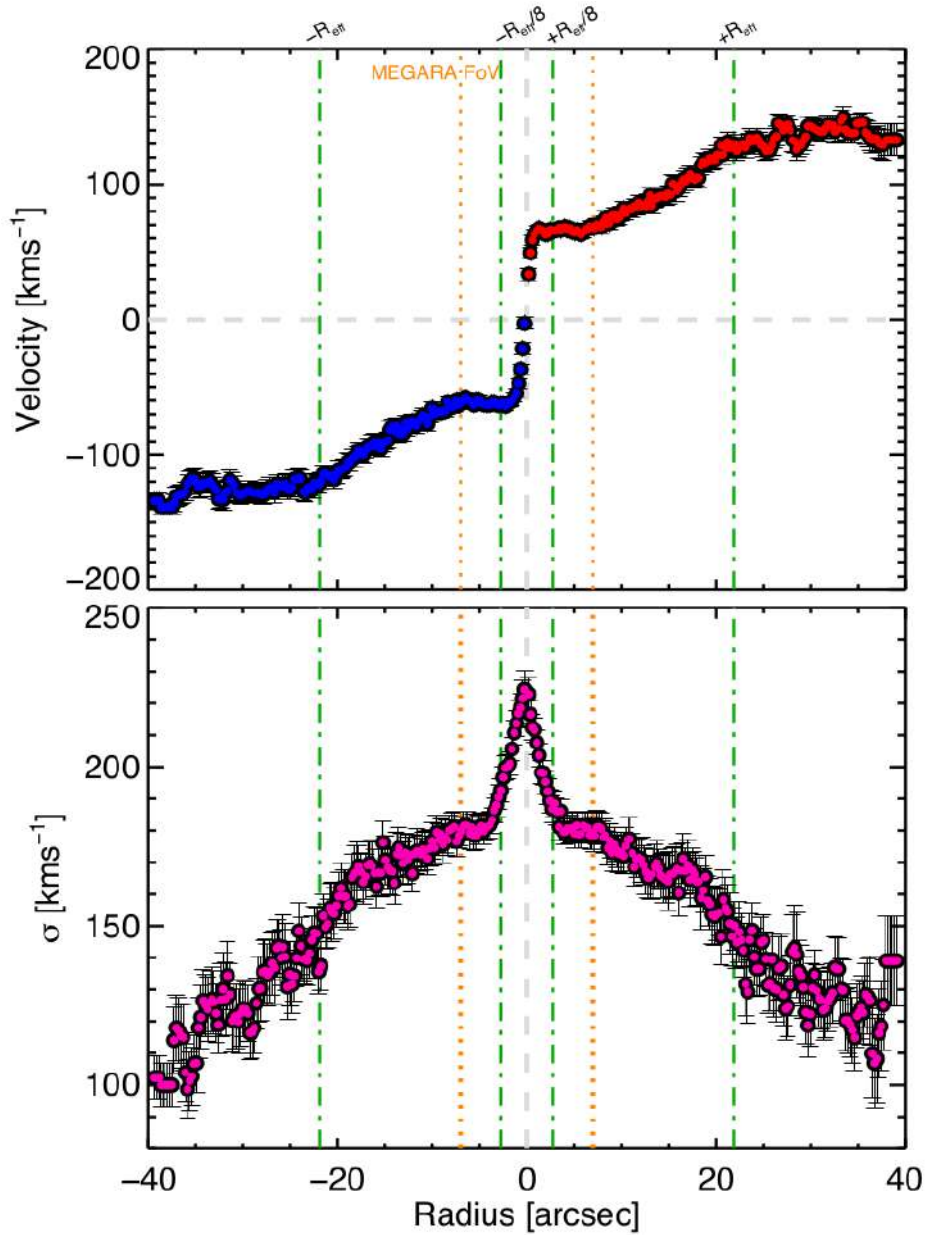
Fig. 4.11 Position-velocity (P-V, top) and position-velocity dispersion (P-σ, bottom) curves of the stellar component of NGC 1052 from MUSE data (Sect. 4.4.1). Both curves were obtained considering a pseudo-slit of $1''$ in width aligned according to the major axis of the rotation (i.e. $112°$, Table 4.2). Velocities are centred to the kinematic centre, and the radius is calculated as the distance from the photometric centre. In the top panel the blue and red symbols indicate the approaching (negative velocities) and receding sides (positive velocities) of the rotation, respectively. The green lines give the R_{eff} ($21.9''$, i.e. 2.4 kpc, Table 4.1) and $R_{eff}/8$ ($2.75''$, i.e. 303 pc, Sect. 4.4.1), as labelled at the top. The grey dashed lines show the zero points for position and velocity, as reference. The field of view of the MEGARA observations is indicated with orange dotted lines. The typical uncertainty (extracted from the uncertainties estimated with pPXF) on the velocity and velocity dispersion measurements are generally $\leq 12\,\mathrm{km\,s^{-1}}$ and $\leq 14\,\mathrm{km\,s^{-1}}$, respectively.

to $250 \, \text{km s}^{-1}$ for MEGARA (Fig. 4.3, right panels). As expected in the case of a rotating disc, the stars exhibit a centrally peaked velocity dispersion map, with a maximum value of $233 \pm 6 \, \text{km s}^{-1}$ and $241 \pm 4 \, \text{km s}^{-1}$, as measured from the MUSE and MEGARA maps, respectively, being in positional agreement within the uncertainties with the nucleus (considered as the photometric centre, i.e. the cross in all maps).

Following Cappellari et al. (2013) for the ATLAS^{3D} legacy project, the central velocity dispersion (σ_c) is calculated at a distance corresponding to $R_{eff}/8$, which is $R < 2.75''$ (303 pc) for NGC 1052. The value for the central velocity dispersion is $201 \pm 10 \, \text{km s}^{-1}$ ($215 \pm 13 \, \text{km s}^{-1}$), whereas the extra-nuclear mean velocity dispersion is $145 \pm 22 \, \text{km s}^{-1}$ ($201 \pm 16 \, \text{km s}^{-1}$) for MUSE (MEGARA) data (see Table 4.2). The mean velocity dispersion from MUSE data within the MEGARA footprint is $180 \pm 6 \, \text{km s}^{-1}$ (Table 4.2), hence consistent within uncertainties with that measured directly from the MEGARA velocity dispersion map.

In addition to the main point-symmetric disc-like pattern, in the MUSE data towards the northeast and south-west and up to $R \sim 30''$ (i.e. $\sim 3.3 \, \text{kpc}$) we observe a smooth local enhancement of the velocity dispersion values. This enhancement is about $150 - 180 \, \text{km s}^{-1}$ (hence above the average, Table 4.2), but it does not match features in either the continuum or ISM maps (Fig. 4.1 and Appendix C.2), and it is not an artefact from cross-talk effects.

Higher velocity dispersion ($\sim 220 \, \text{km s}^{-1}$) with respect to the mean values seems to be present only in MEGARA at $R \sim 5''$, prominent only to the east and to the west. Given its the position, this feature it is likely caused by the lower S/N of the spaxels near the edges (see Sect. 4.3.2). We obtained the position-velocity (P-V) and position-dispersion (P-σ) diagrams shown in Fig. 4.11 in a $1''$-width pseudo-slit along the major axis of rotation listed in Table 4.2. In the (central) region mapped by the two data sets we checked whether the kinematics and curves are in agreement within the uncertainties (Table 4.2). However, as MEGARA observations cover only the innermost region (see Fig. 4.1 and Sect. 4.2), in this work we consider the kinematics from the MUSE cube as the reference for the stellar component.

The large-scale rotation curve (Fig. 4.11, top) is characterised by two plateaus. The first flattening is at a galactocentric distance of $\sim 2''$ (i.e. 220 pc) with velocities of $\sim 70 \, \text{km s}^{-1}$. At large distances, between $10''$ and $20''$, the curve rises slowly reaching values up to $140 \, \text{km s}^{-1}$, and then finally flattens at $30''$. The velocity dispersion profile shows a sharp peak within the innermost $3''$ (i.e. 330 pc) without an exponential decline up to the largest distances mapped by MUSE (Fig. 4.11, bottom).

4.4.2 Kinematics and fluxes of the different ISM components detected by MUSE

Table 4.3 Summary of measurements for the primary component from MUSE and MEGARA.

Line	whole FoV		Polar emission			Central region (high-σ)		
	σ	BPT	σ	ΔV	BPT	σ	ΔV	BPT
	km s^{-1}		km s^{-1}	km s^{-1}		km s^{-1}	km s^{-1}	
Hβ	60 (52) ± 51	–	47 (47) ± 25	247 ± 13	–	128 (118) ± 34	358 ± 51	–
[O III]	66 (62) ± 39	0.47 (0.46) ± 0.16	54 (57) ± 21	251 ± 3	0.46 (0.45) ± 0.16	121 (114) ± 27	215 ± 6	0.48 (0.48) ± 0.15
[O I]	204 (142) ± 151	-0.36 (-0.44) ± 0.21	115 (110) ± 32	207 ± 11	-0.48 (-0.48) ± 0.07	351 (358) ± 106	231 ± 34	-0.25 (-0.30) ± 0.22
Hα-[N II]	66 (54) ± 47	-0.02 (-0.03) ± 0.07	50 (49) ± 17	190 ± 3	-0.03 (-0.03) ± 0.06	149 (134) ± 52	295 ± 6	0.06 (0.05) ± 0.05
[S II]	58 (48) ± 46	0.08 (-0.08) ± 0.06	44 (44) ± 21	200 ± 16	0.07 (0.07) ± 0.06	143 (130) ± 44	260 ± 15	0.12 (0.12) ± 0.04
[O I]	157 (121) ± 115	-0.84 (-0.81) ± 0.34	101 (94) ± 33	520 ± 117	-0.63 (-0.66) ± 0.19	282 (276) ± 66	175 ± 92	-0.53 (-0.59) ± 0.23
Hα-[N II]†	–	0.02 (0.03) ± 0.04	–	–	0.03 (0.03) ± 0.04	–	–	0.01 (0.01) ± 0.03
[S II]	154 (138) ± 69	0.17 (0.17) ± 0.06	78 (78) ± 7	192 ± 80	0.14 (0.15) ± 0.06	170 (155) ± 65	259 ± 97	0.17 (0.18) ± 0.06

Notes. ΔV is the observed velocity amplitude; average velocity dispersion and value of the average line ratio used for standard BPTs in Fig. 4.6 is in log units, and are reported in correspondence with the numerator of the standard line ratios. The values are reported for the different spatial scales labelled at the top, except for the whole field of view (FoV), for which we did not report ΔV as it coincides with that of polar emission. For velocity dispersion and line ratios measurement the quoted uncertainties are one standard deviation. † [S II] and Hα-[N II] lines were fixed to have the same kinematics; only the line ratios differ.

As mentioned at the end of Sect. 4.3.3, Tables 4.3 and 4.4 summarise the most important properties of the two spatially resolved components (primary and secondary). Figures 4.6 and 4.7 show the location of the line ratios for the narrow and secondary emission line components onto standard BPT diagrams (Baldwin et al. 1981). A direct comparison of gas and stellar motions for the primary component is presented in Fig. C.19 that includes the P-V and P-σ along the three major axes (i.e. the major and minor axes of the host galaxy, and the radio jet).

In the following we describe the overall results for each component.

Overall properties of the primary component

The primary component is the narrowest of the three detected (Sect. 4.3.3), with $\sigma \leq$ 66 km s^{-1} on average (except for [O I] which is 204 km s^{-1}). Exceptions to this general behaviour are few spaxels (< 65) mostly within the PSF area (the circle in all maps in Appendix C.2; see also Sect. 4.3). The velocities are generally $|V| < 350$ km s^{-1}, except for Hβ, which are up to 450 km s^{-1} (these extreme values are observed only towards the north-west). The kinematic maps (both velocity and velocity dispersion) lack of any symmetry typical of a rotation dominated system (left and central panels of Fig. 4.5). A clear distinguishable feature in the velocity dispersion map is the σ-enhancement crossing the galaxy from east to west (along the major axis of rotation) with a butterfly-shape (contours in Fig. 4.5 and Figures C.3 to C.6). The gas here presents complex motions that differ markedly from gas elsewhere.

For the identification of this region with high-σ, we consider as reference the average velocity dispersion in two square regions of side 15$''$ (1.65 kpc) in the outer part of the maps lacking of any peculiar σ feature. Specifically, at a distance of 15$''$ from the photometric centre towards the north-east and south-west. In the case of [O I], the box size and distance are 5$''$ and 8$''$ (550 and 880 pc), respectively, due to the decrease in S/N already visible at a radius of 10$''$ (1.1 kpc).

The final threshold (i.e. 2σ above the average velocity dispersion) is 90 km s^{-1} for all the emission lines but [O I], for which it is 180 km s^{-1}. Hereafter we consider as polar[4] emission all the spaxels with velocity dispersion below those thresholds (Sect. 4.4.2). These are mostly distributed along the minor axis of rotation in the NE-SW direction. The properties of the intriguing feature with high-σ in the central region of NGC 1052 is described separately from that of the emitting gas organised along the polar direction (Sect. 4.4.2).

Maps of line fluxes (Fig. 4.5 and Figures C.3 to C.6, right panels) show a similar general

---

[4]Throughout this paper the polar direction (NE-SW) corresponds to that of the minor photometric kinematic axis. It is not related to the direction of the AGN ionisation cones.

morphology that is very different from the smooth continuum flux (Fig. 4.1). More specifically, the gas emission within the inner 3″ resembles a mini-spiral, while it appears extended along the NE-SW direction with some filaments and irregularities especially relevant up to R ∼ 10″ (mostly within the central region at high-σ). However, flux maps do not show any butterfly morphology matching that of the innermost region at high velocity dispersion. Outside the inner 10″ × 9″ (i.e. 1.1 kpc × 1.0 kpc, see Sect. 4.4.2), the flux maps do not reveal any peculiar morphology (e.g. filaments or clumps). Taking all this into account, we prefer to describe the morphology of line fluxes only in this section and not separately for the polar and central region (Sections 4.4.2 and 4.4.2).

At all scales, line ratios from standard BPT diagnostic indicate LINER-like ionisation (see Table 4.3 for typical values and Fig. C.15). These line ratios are discussed in Sect. 4.5.2 together with the weak-[O I] and strong-[O I] LINER classifications by Filippenko & Terlevich (1992), as in Cazzoli et al. (2018).

The [S II] line ratio varies from 1.2 to 1.7 (Fig. C.6) excluding extreme values (i.e. the 5% at each end of the line ratio distribution). This ratio is 1.47 ± 0.2 on average, indicating a gas with relatively low density ($n_e < 100\,\mathrm{cm}^{-3}$).

Polar emission on kiloparsec scale

The velocity fields of the primary component for all the lines show a similar overall pattern (see Fig. 4.5 for [O III]), with well-defined blue and red sides oriented along the minor axis of rotation (polar direction, i.e. NE-SW). Even so, the velocities do not show rotating disc features (spider diagram) in any emission line (Fig. 4.5 and Appendix C.2).

The region with negative velocities extends from the photometric centre towards the northeast up to 30″ (i.e. 3.3 kpc) and 12″ for [O I] (i.e. 1.3 kpc; see Figures 4.5 and C.4, left) with an opening angle of 105° as measured from the velocity maps of [O III]. The most blueshifted value of the observed velocity field is ∼ 250 km s^{-1}, located at a distance of ∼ 11.5″ (i.e. 1.3 kpc) as measured from the [O III] line (Fig. 4.5, top left). Similar negative velocities (within the uncertainties) are seen for all the other emission lines. The unique exception is [O I], for which the maximum blueshifted velocity is of about -250 kms at a radius of 7.5″ (825 pc) in the NE direction (Fig. 4.5, top left).

It is worth noting that these blueshifted velocities do not decrease smoothly to its minimum. Instead, the maps show three concentric arcs that do not cross each other (see Fig. 4.5). These arcs are not symmetric since they are absent where positive velocities are observed (see Figures 4.5 and C.19) towards the south-west and up to 25″, corresponding to 2.75 kpc (15″, i.e. 1.65 kpc for [O I]). We checked the possibility that extinction due to the galaxy dusty stellar disc might have caused this asymmetry. By comparing the velocity maps of the ionised

gas and that of the ratio of Hα to Hβ fluxes we did not find evident dusty structures at the location of the arcs. Hence, we excluded this possibility.

The average velocity dispersion is typically of about $50\,\mathrm{km\,s^{-1}}$ varying between 44 ± 21 and $54 \pm 21\,\mathrm{km\,s^{-1}}$ for [S II] and [O III], respectively (Table 4.3). The [O I] emission represents the exception, with an average velocity dispersion of $115 \pm 32\,\mathrm{km\,s^{-1}}$ (Table 4.3 and Fig. C.8). The [N II]/Hα, [S II]/Hα, and [O I]/Hα line ratios for the large-scale gas distribution are homogeneous (Fig. C.15, see values in Table 4.3 and the discussion in Sect. 4.5.2). The typical standard deviation of the values in the maps is 0.08 in log units; the scatter for the [O III]/Hβ ratio is larger, about ~ 0.2 (Fig. C.15, left). We note that low log [O III]/Hβ ratio values (< 0.1) corresponding to both log [N II]/Hα and log [S II]/Hα of about ~ -0.1 - 0.0, are sparsely observed at large distances from the nucleus (R $> 10''$) and towards the north-east and the south where faint clumpy features are detected (see Sect. 4.4.2).

High-σ feature in the central region of NGC 1052

For all emission lines, the region of higher velocity dispersion with $\sigma > 90\,\mathrm{km\,s^{-1}}$ ($\sigma > 180\,\mathrm{km\,s^{-1}}$ for [O I]; see Figures C.3 and C.4 and Sect. 4.4.2) is located in the innermost parts of the maps, $10'' \times 9''$ (i.e. $1.1\,\mathrm{kpc} \times 1.0\,\mathrm{kpc}$, Table 4.3, contours in Fig. 4.5 and Figures C.3 to C.6). It is mostly aligned with the major axis of the stellar rotation, with a PA of $\sim 124°$ and opening angle of $\sim 70°$ measured from [O III] line (Fig. 4.5). This region is partially mapped also with the MEGARA data (see Section 4.4.4 and Figures C.11 and C.12).

The line-emitting gas is spatially resolved with MUSE into streams of filamentary strands with a tail (clearly visible especially in [O III] line maps, Fig. C.3) departing from the photometric centre towards the south, with velocities up to $150\,\mathrm{km\,s^{-1}}$. In this central region, the velocity of the narrow component does not closely match the motion of the large-scale gas in the polar direction.

Similar patterns in kinematics maps are seen for all emission lines (Figures C.3, C.5, C.6, and C.19) except [O I] (Figures C.4 and C.19), for which we summarise the main results separately.

For the Balmer features and the [O III], [N II], and [S II] lines, high blueshifted (redshifted) velocities up to -290 (260) $\mathrm{km\,s^{-1}}$ are detected towards the east and west of the centre of the butterfly region. The southern tail generally has redshifted velocities from 100 to 180 $\mathrm{km\,s^{-1}}$, with a typical velocity dispersion that varies from 90 to 110 $\mathrm{km\,s^{-1}}$. The σ map shows non-symmetric clumpy structures in the west strands. This clumpiness is particularly evident in the Hα-[N II] velocity dispersion map (Fig. C.5, central panel).

For the [O I] line the morphology of the high-σ region is characterised by two well-defined regions with a triangular projected area (contours in Fig. C.4). The apex of the east projected

triangle is at 2" from the photometric centre, whereas that of the west one is at the photometric centre.

The velocity distribution is skewed to negative (blueshifted) velocities (60% of the spaxels in this region). The main difference of [O I] kinematics with respect to the common patterns of all other lines is seen to the east. Specifically, at this location in the velocity map two thick strands are clearly visible at negative velocities, ~ 200 and ~ 160 km s^{-1} in the northern and southern directions, respectively (Fig. C.4, left panel). For other emission lines, at the same spatial location, the velocities are negative and positive, hence partially kinematically distinct from that found for [O I].

The values of the [O I] σ-map increase gradually from the photometric centre both to the east and to the west, from ~ 200 km s^{-1} up to ~ 500 km s^{-1} (Fig. C.4, central panel). The highest values are seen in correspondence with the most extreme velocities (e.g. the two strands towards the east).

Apart from the flux features summarised in Sect. 4.4.2, in the innermost 10″ the maps do not reveal any peculiar morphology (e.g. clumps or filaments), but only a gradual decrease towards the external part of this region.

At the location of enhanced sigma, the line ratios indicate LINER-like emission (Fig. C.15). More specifically, the [O III]/Hβ line ratio is typically > 0.1 in log units (on average 0.46 ± 0.16, Table 4.3), except for an elongated region from the east to the south-west crossing the photometric centre. At this location line the log [O III]/Hβ varies between 0.005 and 0.3. This peculiar structure does not match any feature of any other map for the narrow component. However, it overlaps with the location of the secondary component. Any putative link between the properties of these two components is discussed in Sect. 4.5.2.

The main feature of the [N II]/Hα ratio map (Fig. C.15 second panel) is the presence of two clumps of similar size (diameter 1.2″, i.e. 130 pc). One clump is located within the PSF region (Sect. 4.2) with log [N II]/H$\alpha \sim 0.2$. The other clump with log [N II]/H$\alpha \sim -0.3$ is located 2.6″ (290 pc) westward to the photometric centre.This clump is embedded in an area with a local enhancement of the [N II]/Hα ratio. Specifically, this region emerges from the photometric centre and extends for 8″ towards the west, and partially matches the region where the velocity dispersion is higher (about 250 - 350 km s^{-1}) with respect to the butterfly average (i.e. 149 ± 52 km s^{-1}; Table 4.3). Local [N II]/Hα ratios are also enhanced at a distance of 7″ to the north and to the west.

Similarly, two clumps with log [S II]/H$\alpha \sim 0.03$ (hence lower than the average, i.e. 0.07 ± 0.06; Table 4.3) are detected to the north of the photometric centre at R ~ 1.5″ (Fig. C.15, right). The observed values of the log [O I]/Hα vary between -0.69 and 0.25 (-0.48 ± 0.07 on average; Table 4.3). The morphology of this line ratio closely matches that seen in the [O I]

Table 4.4 Summary of measurements for the second component from MUSE and MEGARA.

Line	σ	ΔV	BPT
	km s^{-1}	km s^{-1}	
Hβ	313 (316) $\pm$ 128	637 $\pm$ 59	–
[O III]	267 (277) $\pm$ 44	582 $\pm$ 12	0.52 (0.53) $\pm$ 0.14
[O I]	637 (704) $\pm$ 167	371 $\pm$ 51	-0.07 (-0.07) $\pm$ 0.18
Hα-[N II]	281 (277) $\pm$ 105	569 $\pm$ 12	0.14 (0.14) $\pm$ 0.08
[S II]	260 (256) $\pm$ 96	571 $\pm$ 14	0.16 (0.11) $\pm$ 0.14
Hα-[N II]	–	–	0.05 (0.05) $\pm$ 0.09
[S II]	445 (434) $\pm$ 106	430 $\pm$ 175	0.28 (0.28) $\pm$ 0.09

Notes. The same as Table 4.3, but for the secondary component. For the MEGARA data, the [S II] and Hα-[N II] lines were fixed to have the same kinematics (Sect. 4.3.3); we do not report measurements for [O I], due to its low S/N.

kinematic maps (with well-defined strands) at the same position (Fig. C.15, third panel). For a detailed discussion of ionisation mechanisms from BPTs, see Sect. 4.5.2.

Properties of the secondary component

For the MUSE data the spatial distribution of the secondary component has a bipolar shape extended up to 7.2″, which corresponds to 790 pc (Figures C.7 to C.10); its properties are summarised in Table 4.4. This emission is aligned with the radio jet (PA = 70°, Table 4.1) with a PA of ~ 75°, not centred but slightly more extended to the south of the photometric centre. The morphology is almost symmetric with respect to the photometric centre with a redshifted region towards the west of the nucleus, and a blueshifted region towards the east. Overall, the velocity distribution is large, with velocities ranging from -680 to 730 km s^{-1} (Table 4.4). The line profile is broad, generally with $\sigma > 150$ km s^{-1}. The average values of the σ-maps are within 260 and 320 km s^{-1} for all emission lines, except for [O I] which is 637 ± 167 km s^{-1} (Table 4.4, Fig. C.8). Despite these high values, there is a σ-decrement ($\sigma \sim 80$ km s^{-1}) that mostly corresponds to the PSF region. This feature is more evident in the Hβ, [O III], and [O I] maps with respect to the same maps for [S II] and Hα-[N II]. The unique feature of the flux maps outside the PSF region is a shallow elongation towards the south-west (Figures from C.7 to C.10, right panels).

The average value for the [S II] line ratio is 1.2 ± 0.5 (Fig. C.10) indicating a gas with relatively high density ($100 < n_e < 1000$ cm^{-3}). The values of the standard BPT line ratios (see Table 4.4 for average values, and Fig. C.16) indicate the LINER-like AGN photoionisation

as the dominant mechanism for the gas of this component (see Fig. 4.7). See Sect. 4.5.2 for further discussion.

Faint features

All emission line maps from MUSE (e.g. [O III], Fig. 4.5, top panels), except [O I] due to the lower S/N (Fig. C.4), show two peculiar faint features with typical fluxes of about 3×10^{-18} erg s^{-1} cm^{-2} with kinematics (velocity and velocity dispersion) consistent with the values observed in the polar direction (Sect. 4.4.2).

On the one hand, towards the west, a stream is clearly visible in [O III] (Fig. 4.5, top) and Hα-[N II], whereas it is weakly or barely detected in the [S II] and Hβ maps. It extends for 18$''$ (2 kpc) as measured from the Hα-[N II] maps considering only the detached region to the west. The same measurement in the [O III] map (Fig. 4.5) is more difficult because the stream is connected to the main body of NGC 1052, and no peculiar feature in the kinematic and flux maps allows us to disentangle the stream from the body of the galaxy. This stream is found to have nearly systemic velocities (i.e. ± 60 km s^{-1}) and low velocity dispersion (< 50 km s^{-1}, generally). A small clump of radius 0.4$''$ (45 pc) is detected at high-σ (> 100 km s^{-1}) in [O III] only.

On the other hand, towards the south and south-east, there are two detached clumps. Both clumps show redshifted velocities, but the one to the south shows the most extreme kinematics. Specifically, at this location the observed velocities vary from 80 to 150 km s^{-1} (130 ± 16 km s^{-1}, on average), whereas towards the south-east the velocity maps show values between 65 and 115 km s^{-1} (95 ± 7 km s^{-1}, on average). Between these two clumps the differences in velocity dispersion are mild. The average values are 45 ± 13 km s^{-1} and 28 ± 9 km s^{-1} for the south and south-east clumps, respectively.

The location of the line ratios for all these faint features on the standard BPT diagrams (Fig. 4.6 top panels, black and pink symbols) are generally consistent with those observed in AGNs (LINER-like) considering the dividing curves proposed by Kewley et al. (2006) and Kauffmann et al. (2003). This result excludes star formation as the dominant ionisation mechanism in these clumps.

4.4.3   Main kinematic properties of the third spatially unresolved component

For the MUSE data this component is generally the broadest one ($\sigma > 400$ km s^{-1}) for Hβ and oxygen lines. For [S II] and Hα-[N II] the average line widths are 134 ± 45 and 217 ± 104 km s^{-1}, respectively. Its velocity distribution is skewed to blueshifted velocities (typically

within -600 and 200 $km\,s^{-1}$).

In none of the earlier works but D19b, has the detection of a broad (FWHM $\sim 1380\,km\,s^{-1}$) and blueshifted (V $\sim 490\,km\,s^{-1}$) unresolved component in narrow lines been reported. D19b found such a broad component only in [O III], whereas with our current MUSE data we detect it in all emission lines.

The FWHM of the [O III] line is $1053 \pm 84\,km\,s^{-1}$, on average, hence lower than the measurements by D19b. Despite this discrepancy, considering such a large FWHM of the [O III] and the AGN-like BPT ratios measured for this third component, it could probe either an unresolved AGN component as proposed by DH119b or a more recent AGN-driven outflow, which is very central and therefore unresolved. However, as mentioned in Sect. 4.3.3, this component is found only in the central region affected by the PSF (Sect. 4.2), hence no spatially resolved analysis can be done.

4.4.4   Comparison between MUSE and MEGARA results

Similarly to the case of the MUSE data, with MEGARA we map three different kinematic components in narrow lines and the BLR emission in Hα. Among the detected emission lines in the MEGARA ISM cube (Sect. 4.4), [O I] has the lowest S/N. Hence we focus on the results from the modelling of [S II] and Hα-[N II]. These lines were tied to share the same kinematics (Sect. 4.3.3).

The field of view of MEGARA data is almost completely coincident with the region at high-σ, with a minor fraction of a few spaxels ($\sim$14%) corresponding to the polar emission. Hence, we focus the comparison between the results from the MUSE and MEGARA ISM cubes on the butterfly region. However, we summarised the properties of the polar emission from MEGARA in Table 4.3 for the sake of completeness.

For the primary component, the velocity maps for the [S II] and [O I] lines from the MEGARA data set (Figures C.11 and C.12, left panels) show a rotation pattern, with larger positive velocities in the [O I] (systematically $\sim 100\,km\,s^{-1}$ higher). For both lines, there is a velocity decrement at R $\sim 5''$ north-westwards from the photometric centre which continues spatially up to ~ 770 pc, as seen from MUSE maps (e.g. Fig. C.3), at larger distances. This decrement is spatially coincident with the high-σ region, and divides the two strands seen in the butterfly region defined by the MUSE maps (see Sect. 4.4.2). Additionally, the velocity map of the [S II] line (Fig. C.11, left) clearly shows an arc at almost rest frame velocities at approximately $3''$ northwards of the photometric centre, which is also seen in the MUSE maps (see Sect. 4.4.2; Fig. C.6).

The velocity dispersion shows an average value of the [S II] lines of $154 \pm 38\,km\,s^{-1}$, broadly consistent within the uncertainties with that of MUSE in the same innermost region (Ta-

ble 4.3). The [S II] and [O I] lines share the same structure (Figures C.11 and C.12), with increasing values in the western and eastern regions of the photometric centre (for MUSE, see Sect. 4.4.2). The photometric centre has lower values ($\sim 100\,\mathrm{km\,s^{-1}}$) than the eastern and western parts of the map (generally $> 200\,\mathrm{km\,s^{-1}}$), which emerge in a biconical shape (defining the wings of the butterfly) from the centre in a similar way to the MUSE maps (e.g. Figures C.4 and C.6).

The flux maps for the narrow component of all the emission lines in the MEGARA data are not centrally peaked, but show instead a spiral-like shape with high fluxes (right panels in Figures C.12 and C.11). It does not correspond to any peculiar feature in the kinematic maps (velocity or velocity dispersion). This structure is also present in the MUSE maps limited to the region of the MEGARA field of view, being the only noticeable feature in the maps (as mentioned in Sect. 4.4.2).

The limited spectral coverage of MEGARA data allows us to estimate the [S II]/Hα, [N II]/Hα, and [O I]/Hα line ratios (see Sect. 4.4). The [S II]/Hα ([N II]/Hα) ratio in log for the primary component ranges between -0.17 and 0.44 (-0.19 and 0.18), with an average value of 0.17 ± 0.06 (0.02 ± 0.04). For the [O I]/Hα ratio the values range from -1.6 to 0.3, on average -0.84 ± 0.34 in the complete MEGARA field of view (see Table 4.3 and Fig. C.17). In the maps of this last ratio (Fig. C.17 centre), a clump is present near the photometric centre, within the PSF, that is spatially coincident with an enhanced region of this ratio, also in the MUSE maps. Table 4.3 shows that the ratios are consistent within the uncertainties independently of the high-σ–polar emission splitting. We have also estimated the electronic density using the [S II] line ratio (Fig. C.11, right), which indicates a low density regime, as for MUSE data (see Sect. 4.4.2). The density maps of this component are homogeneous, with small deviations only in the outer parts of the field of view (with lower S/N).

The second component detected in the MEGARA data (Fig. C.13) has the same spatial extension as in MUSE, accounting for the differences in the spatial resolution of the two data sets. For the [S II] and [O I] velocity maps the same structure is seen, with a clear velocity distribution ranging up to an absolute value of $\sim 400\,\mathrm{km\,s^{-1}}$ for both lines. For this component the velocities of both lines are in close agreement, also with the MUSE data (see Table 4.4). For the velocity dispersion this component is the broadest of all the components detected in the MEGARA data (excluding the broad Hα in Sect. 4.4.5). The values are consistent for all lines, although the [O I] measured in MEGARA differs considerably to that from MUSE (average of 359 ± 64 vs $627 \pm 167\,\mathrm{km\,s^{-1}}$), probably due to the lower S/N of this line in the MEGARA data. Therefore, we cannot ensure a proper determination of the properties of the secondary component with the [O I] lines.

The flux maps of all the lines show a centrally peaked distribution, with no peculiar features.

However, as in MUSE, the line ratios present elongated substructures both east and south-west from the photometric centre in both [S II]/Hα and [N II]/Hα that do not correspond to any kinematic feature (Fig. C.18). The mean values of these ratios are summarised in Table 4.4. For the MUSE and the MEGARA data sets the [S II] flux ratio of the second component (Fig. C.13) indicates a gas with high density, $n_e \sim 1000\,\text{cm}^{-3}$.

As already mentioned, MEGARA also identified a third spatially unresolved kinematic component in the emission lines. However, unlike the MUSE data, this component is detected only in [S II]. Its main kinematic properties are velocities ranging between -365 and 221 km s^{-1} (mean error 72 km s^{-1}), and an average velocity dispersion of 127 ± 47 km s^{-1}. These results are in broad agreement within the uncertainties with those obtained with the MUSE data for the [S II] lines (see Sect. 4.4.3).

4.4.5 BLR component

The broad Hα component from the spatially unresolved BLR of NGC 1052 is observed only within the PSF radius (i.e. 0.8″ and 1.2″ for MUSE and MEGARA respectively, Sect. 4.2) in both data sets. For this component we obtained, on average, velocities near rest frame, i.e. -38 km s^{-1} (-60 km s^{-1}) as measured from MUSE (MEGARA) data. Overall, the average velocity dispersion is 1031 ± 141 km s^{-1} and 998 ± 200 km s^{-1} (2427 and 2350 km s^{-1} in FWHM) for the MUSE and MEGARA data, respectively.

In the end, we note that our final modelling of the Hβ line does not require a broad component confirming the type 1.9 AGN classification of the active nucleus in NGC 1052 (see Table 4.1). The FWHM of this AGN component is compared to that of previous works in Sect. 4.5.5.

4.4.6 NaD Absorption

Figure 4.8 shows the equivalent width map of the NaD absorption corresponding to spaxels with S/N ≥ 5 in the MUSE ISM cube. Its overall spatial distribution has an intriguing morphology similar to that of the central butterfly-like region at high-σ described in Sect. 4.4.2. It is oriented in the SE-NW direction with the north-west side more prominent (EWs generally > 1.5 Å).

Our kinematic maps obtained from the MEGARA data indicate a complex neutral gas kinematics (Fig. 4.10). Specifically, the velocity map shows the blue–red pattern of a rotating disc (velocities from -96 to 57 km s^{-1}), but with a flat gradient (ΔV is 77 ± 12 km s^{-1}, Fig. 4.10, left). However, the peak of the velocity dispersion map is off-centred (Fig. 4.10, centre). It peaks at 2.5″ (277 pc) eastwards with a value of 263 ± 10 km s^{-1}. Moreover, high velocity dispersion values (> 220 km s^{-1}, higher than the central velocity dispersion of the stars, σ_c

in Table 4.2) are observed up to 4.8″ (530 pc) towards the north-east. These high values do not have any counterparts in either velocity or flux maps (Fig. 4.10, left and right).

The maps of the ratio of the NaD fluxes indicate that the gas is optically thick ($R_{NaD} = 1.3 \pm 0.1$, on average) similarly to what was estimated for the nuclear spectrum analysed in Cazzoli et al. (2018) ($R_{NaD} = 1.0$), so far the only study of the NaD-absorption in NGC 1052.

4.5 Discussion

The results obtained with the MUSE data are in general agreement with those from the MEGARA cube at higher spectral resolution (Sections 4.4.4 and 4.4.5). In Sect. 4.5.1, we discuss the stellar kinematics and dynamics using the full data set, whereas the discussion in Sect. 4.5.2 is mostly based on the results from the MUSE data only in order to exploit its capabilities (spectral range, spatial sampling, and field of view; Sect. 4.2). Sections 4.5.3 and 4.5.4 are dedicated to exploring the kinematics and energetics of the multi-phase outflow (ionised and neutral gas). Finally, in Sect. 4.5.5 we compare the FWHM of the unresolved BLR component with previous measurements. The estimation of the black hole mass based on the stellar kinematics and the broad Hα components is discussed in Sect. 4.5.1 and Sect. 4.5.5, respectively.

4.5.1 Kinematics and dynamics of the stellar disc

As mentioned in Sect. 4.4.1, the stellar component of NGC 1052 shows features of rotational motions on small scales (MEGARA) and on large scales (MUSE). These include a spider pattern in the velocity field and a centrally peaked velocity dispersion map (Fig. 4.3). In addition, the kinematic major axis coincides with the photometric major axis, which further confirms the presence of rotation-dominated kinematics.

NGC 1052 is classified as an oblate galaxy of E3-4/S0 type (Bellstedt et al. 2018, Table 4.1). Its stellar kinematic properties (e.g. large velocity amplitude; Table 4.2 and Fig. 4.11, bottom) suggest that NGC 1052 is more likely a lenticular-S0 galaxy (see Cappellari 2016 for a review). The motivation for this classification is twofold. First, the lack of the exponential decline in the P-σ curve (Fig. 4.11, bottom) indicates the presence of relevant random motions. Second, the combination of a large velocity amplitude and a symmetric velocity field (Table 4.2, Fig. 4.11, top) suggests that NGC 1052 has a prominent rotating disc.

The rotational support of the stellar disc can be drawn from the observed (i.e. no inclination

corrected) velocity-to-velocity dispersion (V/σ) ratio[5], calculated as the ratio of the amplitude to the mean velocity dispersion across the disc. For MUSE (MEGARA) the dynamical ratio is ~ 1.2 (0.8), indicating a strong random motion component, hence a dynamical hot disc. The results from the analysis of the stellar kinematics from present IFS data are generally in agreement with those from previous works by D15 and DH19a with optical IFS from WiFEs and GMOS/GEMINI, respectively, although these data are limited in either spectral range or in field of view, and in spatial sampling (see Sect. 4.1). For both these past works, the stellar velocity field shows clearly a smooth rotation. However, a 1:1 comparison is not possible as no velocity amplitude measurements are given by the authors. The velocity dispersion shows a central cusp ($\sim 200\,\mathrm{km\,s^{-1}}$ and $\sim 250\,\mathrm{km\,s^{-1}}$, as measured by D15 and DH19a, respectively). This is qualitatively consistent with the shape of the P-σ curve (Fig. 4.11, bottom). Finally, our results are broadly consistent with those by Bellstedt et al. (2018) obtained with DEIMOS/Keck: a rotational velocity and central velocity dispersion of $\sim 120\,\mathrm{km\,s^{-1}}$ and $\sim 200\,\mathrm{km\,s^{-1}}$, respectively.

Thanks to our measurement of the stellar dynamics, we can provide an estimate of the black hole mass (M_{BH}) based on the central velocity dispersion of stars measured in MUSE data ($201 \pm 10\,\mathrm{km\,s^{-1}}$, Table 4.2) and Eq. 8 by Bluck et al. (2020) (see also Saglia et al. 2016) yields M_{BH} of $2 \pm 0.5 \times 10^8$ $M_\odot$. This value is in good agreement with the previous estimates by Beifiori et al. (2012) listed in Table 4.1. We note that the use of other prescriptions can return different black hole masses (see e.g. Ho 2008 and references therein), as briefly discussed in Sect. 4.5.5.

4.5.2   Multi-phase ISM properties

Early-type galaxies were traditionally thought to be uniform stellar systems with little or no gas and dust (Falcón-Barroso et al. 2006b). The spatial distribution and kinematics of the ionised gas in NGC 1052 challenges this view, as ISM and stars seem completely decoupled indicating a complex interplay between the two galaxy components. The proposed scenario is summarised in the cartoon shown in Fig. 4.12.

In what follows we mostly focus on spatially resolved components (i.e. primary and secondary for emission lines and for the NaD absorption). We note that a third component is needed to reproduce line profiles in all forbidden lines and narrow Hα (see Sect. 4.3.3). The presence of this component is reported in Dahmer-Hahn et al. (2019b), but only in [O III] with FWHM $\sim 1380\,\mathrm{km\,s^{-1}}$. These authors propose that it is tracing the interaction between

---

[5]Some authors (e.g. Perna et al. 2022 and references therein) use the inclination-corrected velocity to calculate the dynamical ratio. For NGC 1052 such a correction does not strongly affect the V/σ ratio; it would be 1.23 instead of 1.16, hence ~ 1.2 in both cases.
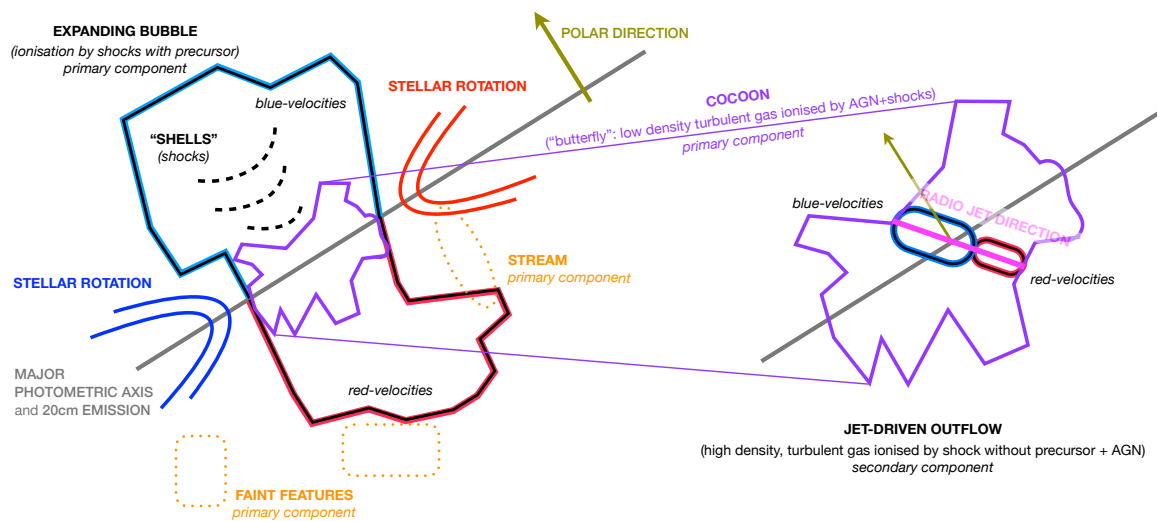
Fig. 4.12 Cartoon illustrating the proposed scenario for the stellar component and the ionised ISM for NGC 1052 (see text for details).

the jet and the ISM-environment. Even though we were able to map this component for all emission lines (from Hβ to [S II]), it is spatially unresolved (see Sect. 4.4.2). Due to this limitation we do not investigate this component further. However, its general properties are summarised in Sect. 4.4.3.

Intriguing ISM kinematics in NGC 1052

For NGC 1052, the presence of non-rotational motions such as an AGN-driven outflow has been suggested in many previous works on the basis of *HST* imaging (Pogge et al. 2000; Walsh et al. 2008) and 1D and IFS spectroscopy (Sugai et al. 2005; Dopita et al. 2015; Cazzoli et al. 2018; Dahmer-Hahn et al. 2019b), mostly in the optical band.

Generally, the detection of outflows is widely based on the comparison between the observed velocity field and line width distribution and that expected in the case of a rotating disc (see e.g. Veilleux et al. 2020 and references therein). However, for NGC 1052 the deviations from the disc-like behaviour (i.e. outflow signatures) in the kinematics maps of the two spatially resolved components are ambiguous.

On the one hand, for the primary ISM component a clear velocity gradient is observed in the perpendicular direction with respect to the stars (SE-NW direction, see Figures 4.5 and C.19). This feature can be explained in terms of either large buoyant bubbles or a polar disc[6]. This

---

[6]We discard the scenario in which the polar gas arise from the AGN's narrow line region (NLR). Indeed, by means of the relation between the X-ray luminosity and size of the NLR for LINERs by Masegosa et al. (2011) (see their Fig. 4), for NGC 1052 the NLR physical size would be ∼ 600 pc. Hence, the NLR is much less extended than the polar emission detected at a distance > 3 kpc.

bipolar velocity field is not perfectly symmetrical (see Sect. 4.4.2 and Figures 4.5 and C.19) indicating that the putative disc could either be a perturbed rotator or a complex kinematic object according to the classification by Flores et al. 2006.

On the other hand, the velocity dispersion map is not centrally peaked as expected for rotating discs (see Figures 4.5 and C.19). Instead, a σ enhancement[7] $> 90\,\mathrm{km\,s^{-1}}$ is present at a galactocentric distance smaller than $10''$ with a peculiar butterfly shape (see Sect. 4.4.2 and contours in Fig. 4.5, Figs. C.3 – C.6, and Fig. C.19). At this location the maximum velocity gradient is oriented nearly along the stellar major axis of rotation (black solid line in Figures in Appendix C.2). The morphology and the kinematics of this butterfly feature are suggestive of the presence of two bubbles outside the plane of the galaxy similarly to the well-known superwind in NGC 3079 (an optically thin bubble with blue and red sides from the front and back volumes, e.g. Veilleux et al. 1994). Indeed, if two bubbles (or biconical outflows) are moving away in the polar direction, high velocity dispersion is expected along the major axis of rotation due to the overlap of the blue and red clouds to the line of sight. The observed butterfly feature may represent this effect.

This twofold behaviour of the ionised gas on different spatial scales might indicate that the gas probed by the primary ISM component is tracing two different substructures that are possibly related. Neither of them is likely probing a rotating disc due to the irregularities in the kinematics and the significance of shocks in ionising the gas (as discussed in Sect. 4.5.2). For the second ISM component the blue to red velocity gradient is mostly aligned with the radio jet (70°, Table 4.1) with large widths (Table 4.4) extended mostly within $5''$ from the photometric centre (see e.g. Fig. C.7).

As mentioned in Sect. 4.4.6 the spatial distribution of the NaD absorption has a morphology similar to that of the central region at high-σ described with a prominent north-west side (Fig. 4.8). However, the kinematics maps do not show clear evidence of a neutral gas outflow (Fig. 4.10; Sections 4.4.6 and 4.5.4). Hence, by using the kinematics only we cannot claim the robust detection of a multi-phase outflow. In the next section we explore the ionisation structure and the possible connection with the radio jet in order to pinpoint the location of the outflow and hence study the kinematic, energetic and power source.

Line ratios and ionisation structure

We used the observed spatially resolved narrow emission line fluxes and line ratios to investigate the excitation mechanisms at work in NGC 1052 by means of the standard diagnostic diagrams by Baldwin et al. (1981), also known as BPT diagrams (Figures 4.6 and 4.7).

---

[7]This line width enhancement cannot be explained in terms of beam smearing because the scale on which we observe it is much larger than the spatial resolution of the observations.

For the MUSE data, the Hβ and [O I] lines are the weakest of those detected. Therefore, they constrain the spatial regions where the BPT analysis can be carried out (see maps in Appendix C.2). For the MEGARA data the main limitation is that the observed spectra lack both Hβ and [O III], preventing us from exploiting the BPT diagnostics.

In this section we mainly compare our results for ionisation mechanism with those in D15, due to the similarities in spatial and wavelength coverage. This comparison would be more difficult with the results from DH19b, as these authors present the analysis of the [N II]/Hα ratio, complemented by near-IR BPT diagrams, in the central region of NGC 1052 (i.e. 3.5″×5.0″). However, their general findings (i.e. LINER-like line-ratios throughout the whole GMOS/GEMINI field of view and a combination of shocks and photoionisation mechanisms in act in NGC 1052) are in broad agreement with our results (see Sect. 4.4 and below). For the primary (narrowest) component, we exclude the pAGB or H II-ionisation scenarios in favour of a mixture of AGN photoionisation and shock excitation as the dominant mechanisms of ionisation. On the one hand, the large majority of the line ratios lie above the empirical dividing curves between H II- and AGN-like ionisation by Kewley et al. (2006) and Kauffmann et al. (2003). These line ratios are not fully reproduced by pAGBs models by Binette et al. (1994). Furthermore, the observed [O I]/Hα ratios indicate that NGC 1052 is a strong-[O I] object (i.e. genuine AGN) according to the criterion for dividing weak-[O I] and strong-[O I] LINERs, proposed by Filippenko & Terlevich 1992, that is [O I]/Hα > 0.16. Hence, these findings indicate the need of an ionisation mechanism more energetic than star formation or pAGB-stars, such as AGN photoionisation. We note that only for a small number of spaxels (50, i.e. < 1% of the map), the AGN scenario is disfavoured as the log ([O III]/Hβ) ratio is < 0.3 and log ([N II]/Hα) is < 0.2. However, these spaxels are sparsely distributed at large distances (R > 20″, i.e. 2.2 kpc), where faint gas-clumps are detected (see Sect. 4.4.2). On the other hand, shock models with a photoionising precursor (grids in Fig. 4.6) are able to reproduce the large majority of the observed line ratios in the [N II]/Hα and [O I]/Hα diagrams, and only partially in the [S II]/Hα diagram.

The match between data points and shock models is more accurate for the gas distributed along the polar direction (Fig. 4.6, top) than for that within the central region at high-σ (Fig. 4.6, bottom). The same two dominant sources of ionisation (AGN and shocks) acting in NGC 1052 were identified by D15. These authors propose that part of the ionised line-emitting gas is photoionised by the AGN with a central region (R < 1″) that appears shock excited. Emission lines have been modelled with a dusty plasma having a three times solar abundance and via a double-shock model. The latter combines an accretion shock with velocities of about 150 km s^{-1} and a cocoon shock at higher velocities of 200 − 300 km s^{-1}. Such a model explains the high densities observed ($\sim 10^4 − 10^6$ cm^{-3}) in the WiFes data and

provides a good fit to the observed emission line spectrum. The proposed physical scenario establishes the existence of a higher ionisation cone and a large-scale bipolar outflow (energised by the jet) and a turbulent flow along the major axis of the galaxy. However, the model by D15 only marginally fits our measurements, as explained below.

On the one hand, our 2D mapping of the primary component reveals a central region at high velocity dispersion consistent with the accretion shocks proposed by D15, $\sigma \sim 120 - 150 \, \text{km s}^{-1}$, (except for [O I] for which $\sigma \sim 350 \, \text{km s}^{-1}$; Table 4.3). Generally, the high velocity dispersion region seen in the WiFES data match that of our IFS data. However, thanks to the high sensitivity and spatial resolution of MUSE we can map this region on a larger area and spatially resolve substructures in flux and kinematics.

On the other hand, the discrepancy is threefold. First, we do not find any indication of such extremely high density. We rather measure two regimes of gas densities, both at lower densities (i.e. $n_e < 10^4 \, \text{cm}^{-3}$) for the primary and second components, as mentioned in Sections 4.4.2 and 4.4.2. Second, by using the line-flux maps from MUSE, in the central region we measured a metallicity of 8.18 ± 2.059 (the solar value is 8.69; Asplund et al. 2009) following Pérez-Díaz et al. (2021), using the HII-CHI-MISTRY tool by Pérez-Montero (2014). Hence, there are no hints of the extreme metallicities adopted by D15. Third, velocities consistent with the cocoon shock velocities ($200-300 \, \text{km s}^{-1}$) in the model by D15 are observed for the secondary component (Table 4.4, except for [O I]). This is a separated component with respect to that distributed on kpc scales being extended to $7.2''$, which corresponds to 790 pc (hence not only in the central R $<1''$, Sect. 4.4.2) and oriented similarly to the radio jet.

For the secondary component, shock models (without a precursor) are able to reproduce satisfactorily the observed [N II]/Hα and [O I]/Hα ratios. Nearly half of the data points in the [S II]/Hα diagram are too high to be modelled either with shocks or pAGBs models (Fig. 4.7, grids and pink boxes, respectively).

Taking into account all this, we conclude that the emission line ionisation in NGC 1052 cannot be explained by one mechanism alone, as proposed by D15 and DH19b. The ionisation in the central region (R $< 10''$) is a mixture of AGN photoionisation and shock ionisation, while at larger galactocentric distances the shock mechanism is dominating. Finally, we note that we used different shocks models (with and without a precursor) to reproduce the line ratios of the two spatially resolved components. The gas probed by the primary component is self-ionising, including both shocks and a precursor. For the secondary component, the gas is collisionally ionised by the shock (i.e. no precursor) likely as a consequence of the passage of the radio jet, given the alignment between the axis of the radio jet and the secondary component.

It should be noted that although the [O I] kinematic-properties are different from those of

other lines (e.g. Hα), they are consistent with the current scenario (see e.g. Fig. 4.12). Indeed, [O I] is highly sensitive to shocks (especially shock heating), and it is enhanced in the region where the butterfly feature is observed.

Connection between ISM and radio jet

NGC 1052 is a radio-loud AGN ($L_{1-100\,GHz} \sim 4.4 \times 10^{40}\,ergs^{-1}$, Wrobel 1984) with a twin radio jet strongly interacting with its environment (Kadler et al. 2004a; Mukherjee et al. 2018). The jet has been detected in numerous observational studies (Falocco et al. 2020 and references therein) associated with an X-ray emitting region (spatially coincident with radio emission at 1.5 GHz, Kadler et al. 2004b).

Radio jets can produce gaseous outflows impacting the host-galaxy on sub-kpc and kpc scales (e.g. Harrison et al. 2014, Hernández-García et al. 2018, Jarvis et al. 2019, Molyneux et al. 2019 and Venturi et al. 2021) with different observational features. On the one hand, powerful AGNs show high velocity dispersion along the full extent of the radio emission (e.g. Oosterloo et al. 2019). On the other hand, an enhancement of the emission-line velocity width is found to be perpendicular to the direction of the AGN ionisation cones and jets (e.g. Venturi et al. 2021).

In NGC 1052 the footprints of the interaction between the jet and the gas in the galaxy disc are probed by the primary and secondary components. Specifically, the alignment between the radio emission and ionised gas in the inner $\sim$ 1-1.2 kpc is indicative of the radio jet interacting with the ISM (PAs are about 70°, Table 4.1 and Sect. 4.4.2). Such an interaction can trigger an outflow and can induce large turbulence and kpc-scale bow-shocks (i.e. a jet-induced outflow acting on both sub-kpc and kpc scales). In this scenario, the outflow is probed by the second component, whereas the primary component traces both the cocoon of gas surrounding the expanding jet-induced outflow (with enhanced turbulence) and the large-scale gas (extended up to $\sim$ 2-3 kpc) expanding perpendicular to the axis of the jet. The shells seen in the blue part of the velocity field of the primary component along the polar direction could indicate shock waves propagating in a smooth medium. These could be absent on the red side of the polar emission at positive velocities, due to ISM anisotropy.

The proposed scenario for NGC 1052 is similar to that presented by Morganti et al. (2021) for PKS 0023–26 (a far-IR bright source hosting a young powerful radio source) on the basis of the results from ALMA CO (2−1) and 1.7 mm continuum data. In PKS 0023–26, the highly perturbed gas tends to follow the edge of the radio emission on sub-kpc scales, whereas the relatively mild expansion of the cocoon, created by the interaction between jet and ISM, is pushing the gas aside. For NGC 1052 the strong coupling between radio jets and the ISM is limited to the innermost 7.2″, corresponding to 790 pc (Sect. 4.4.2), with

large buoyant bubbles extending up to 30″, which corresponds to 3.3 kpc (Sect. 4.4.2). As for PKS 0023–26, the cocoon does not reach extreme velocities but injects turbulence into the ISM, triggering the creation of the bubbles along the polar direction. With the present data set we cannot infer the presence of cavities devoid of dense gas at larger radii, due to the maintenance phase of outflow, nor any relation between radio lobes and the ISM, as the former are absent for the jet in NGC 1052.

Although the comparison between PKS 0023–26 and our results for NGC 1052 is illustrative, it has to be taken with caution as we are tracing different gas phases within the jet–ISM interaction.

4.5.3 Ionised gas outflow kinematics and energetic

On the basis of the morphology and kinematics of the different components, and taking into account that shocks are a crucial mechanism of ionisation in NGC 1052, we claim the detection of an ionised gas outflow. It is probed by the secondary component, with a bipolar morphology and velocity dispersion $> 150 \, \mathrm{km \, s^{-1}}$. The outflow is strongly interacting with the surrounding ISM mapped by the primary component. Such an interplay is suggested by both the high-σ ($> 90 \, \mathrm{km \, s^{-1}}$) region with a peculiar butterfly-like morphology and the presence of two kpc scale buoyant bubbles.

In this section we summarise the main properties (kinematics and energetic) of the outflow as well as its power source (i.e. verify the jet-driven scenario proposed in Sect. 4.5.2). We assume a simple outflow model, with inclination-corrected velocities and distances, that considers the outflow oriented perpendicular to the plane of the disc.

We estimated the total mass of the emitting ionised hydrogen gas following Venturi et al. (2021) (see also Carniani et al. 2015, Cresci et al. 2017). We calculated the Hα luminosity corrected for extinction ($L_{H\alpha}$), considering the corresponding distance (i.e. 22.6 Mpc, Table 4.1) and using the attenuation law by Calzetti et al. (2000) for galactic diffuse ISM ($R_V = 3.12$) and an intrinsic ratio (Hα/Hβ) = 2.86 (for an electron temperature of 10^4 K, Osterbrock & Ferland 2006). The intrinsic Hα luminosity is converted in mass of the ionised gas with the Eq. 1 in Venturi et al. (2021) using the median value of the electron density (i.e. $360 \, \mathrm{cm^{-3}}$). We obtain a total $L_{H\alpha}$ of $(1.8 \pm 0.7) \times 10^{40}$ erg s^{-1} and a total mass of ionised gas in the outflow of $M_{OF,ion} = (1.6 \pm 0.6) \times 10^5 \, M_\odot$ with our data.

The mass outflow rate is $\dot{M}_{OF,ion} = (0.4 \pm 0.2) \, M_\odot \mathrm{yr^{-1}}$, estimated with $3 \times V_{OF,ion}/R_{OF,ion} \times M_{OF,ion}$ as in Cresci et al. (2015). We note that, in this estimation, we assumed $V_{OF,ion}$ to be the maximum of the velocity field from the map of the secondary component ($\sim 655 \, \mathrm{km \, s^{-1}}$). We also estimated the kinetic energy and power of the outflowing ionised gas, $E_{OF,on} = 0.5 \times \sigma^2_{OF,ion} M_{OF,ion}$ and $\dot{E}_{OF,ion} = 0.5 \times \dot{M} \times (V^2_{OF,ion} + 3\sigma^2_{OF,ion})$, using an average velocity

dispersion of Hα ~280km s^{-1}. We obtained E$_{OF,ion}$ = $(1.3 \pm 0.9) \times 10^{53}$ erg and Ė$_{OF,ion}$= $(8.8 \pm 3.5) \times 10^{40}$ erg s^{-1}.

An upper limit on the outflow mass and energy could be estimated by considering the whole outflow phenomenon, which is the outflow core (secondary component) plus the buoyant bubbles (primary component, excluding the faint features described in Sect. 4.4.2). Hence, the mass of the ionised gas associated with the outflow phenomenon (bubbles) is $1.8 \pm 1.1 \times 10^6$ M$_\odot$ $(1.7 \pm 1.1 \times 10^6)$ M$_\odot$ and the corresponding energy is $1.9 \pm 1.5 \times 10^{53}$ $(8.1 \pm 1.1 \times 10^{52})$ erg.

We excluded the star formation as a power source of the outflow since the kinetic power of the starburst associated with supernovae is low ($\sim 6.3 \times 10^{40}$ erg s^{-1}, as calculated following Veilleux et al. 2005 from the total star formation rate, SFR, i.e. 0.09 M$_\odot$yr^{-1}; Table 4.1). In what follows we focus on distinguising between the two most likely scenarios: AGN-driven versus jet-driven outflow.

The energy rate is of the order of 0.01 of the bolometric luminosity of NGC 1052 (L$_{bol}$ = $10^{42.91}$ erg s^{-1} Onori et al. 2017b). This is in broad agreement with the results of Fiore et al. (2017) (see their Fig. 1, right) that showed that the average ratio Ė$_{OF,ion}$/L$_{bol}$ for AGN-driven ionised outflows is generally below 0.1. As in Venturi et al. (2021), in order to infer whether the jet is energetic enough to power the observed features, we compared the total kinetic energy of the jet (E$_{jet}$) with the kinetic energy of the outflow. By assuming the power and travelling time of the jet (10^{45} erg s^{-1} and 0.7 Myr, respectively) used in Mukherjee et al. (2018) to simulate the observed kinematics and morphology of the ionised gas in NGC 1052, we obtain a total energy of the jet of E$_{jet}$ = 2.2×10^{58} erg.

The comparisons Ė$_{OF,ion}$ versus L$_{bol}$ and E$_{jet}$ versus E$_{OF,ion}$ indicate that both the AGN and the jet in NGC 1052 are capable of injecting the required energy into the ISM to power the outflow. However, taking into account the alignment between the radio jet, the secondary component, and the cocoon with enhanced turbulence, we consider that the most likely power source of the outflow is the jet, although some contribution from the AGN is possible.

4.5.4 Neutral gas outflow detection

As mentioned in Sect. 4.5.2, the mapping of the neutral gas properties does not show evident outflow features (e.g. a broad kinematic component with significant blueshifted velocities). Hence, the identification of the neutral gas outflow and the corresponding estimates provided in this section is exploratory, and hence must be taken with caution. To identify the putative neutral gas outflow we used the velocity dispersion map (Fig. 4.10, centre), which shows the clearest deviations from the rotating disc behaviour among those obtained from the NaD modelling (Sect. 4.4.6).

As a threshold to identify the outflowing neutral gas, we consider the 75th percentile of the distributions of the velocity dispersion, that is, $\sigma_{thr} > 245\,\mathrm{km\,s^{-1}}$. The selected region (with $\sigma > \sigma_{thr}$) is marked with contours in the maps shown in Fig. 4.10. It is extended up to a galactocentric distance of 4.8″ (530 pc), with an elongated morphology (oriented north-south), and a projected area of 3.8 arcsec². The region is characterised by a mild kinematics with velocity and velocity dispersion of $63 \pm 21\,\mathrm{km\,s^{-1}}$ and $251 \pm 5\,\mathrm{km\,s^{-1}}$, respectively, on average. The EW is, on average, 1.2 ± 0.3 Å. This value is converted into column density of the wind (N_H) via reddening (E_{B-V}) following the approach by Cazzoli et al. (2014, 2016), already used for the MEGARA data by Catalán-Torrecilla et al. (2020). On average, the column density of the outflow is $(2.8 \pm 0.7) \times 10^{21}\,\mathrm{cm^{-2}}$. As in Catalán-Torrecilla et al. (2020) we assumed that the outflow is organised in a series of thin shells, and to obtain the deprojected velocities, distances, and solid angle we used a simple geometrical model of a conical outflow that emerges perpendicular to the disc.

Following these prescriptions, the total mass of neutral gas contained in the outflowing region is $(7.1 \pm 2.8) \times 10^6$ M$_\odot$ and the outflow rate is (0.86 ± 0.30) M$_\odot\mathrm{yr^{-1}}$. We also derived the total energy of the neutral outflow which is $(1.1 \pm 0.4) \times 10^{55}$ erg.

Cold neutral gas outflows in LINERs and early-type galaxies (ETGs), probed by the NaD absorption, have been less studied compared for example to ionised and molecular outflows in Seyferts or U/LIRGs (e.g. Arribas et al. 2014; Pereira-Santaella et al. 2016; Venturi et al. 2018; Pereira-Santaella et al. 2020; Wylezalek et al. 2020; Perna et al. 2021; Comerón et al. 2021; Riffel et al. 2021). However, there are two systematic studies of neutral gas in LINERs in large samples by Lehnert et al. (2011) and Sarzi et al. (2016). Lehnert et al. (2011) detected neutral ISM gas in about one-third of their sample of 691 radio-loud ETGs on the basis of SDSS data. The detected NaD profiles suggest the presence of outflows with low velocities ($\sim 50\,\mathrm{km\,s^{-1}}$) and broad profiles ($\sim 500\,\mathrm{km\,s^{-1}}$). On the contrary, Sarzi et al. (2016) found that only a dozen radio AGNs (out of 103 objects) show NaD absorption from ISM, but the neutral gas never appears to be outflowing.

The unique study of the NaD absorption in NGC 1052 is by Cazzoli et al. (2018) on the basis of slit spectroscopy. In this work, the neutral gas kinematics has been interpreted as being due to rotation. However, slit observations give only a partial description of the outflow phenomenon, hence in the case of NGC 1052, IFS observations could have been the key for our (tentative) detection of the neutral gas outflow.

4.5.5   Comparison with current and previous Hα broad component measurements

The BLR component in NGC 1052 has been observed in polarised light (Barth et al. 1999) and at different wavelengths (Onori et al. 2017a, Cazzoli et al. 2018, Dahmer-Hahn et al. 2019a and references therein). Onori et al. (2017a) modelled the BLR component in both optical and near-IR bands with *HST*/FOS (R $\sim$ 2800) and ISAAC (R $\sim$ 730) spectra. The near-IR He I$\lambda 1.083\mu$m line was modelled with a broad Gaussian curve with width of 2455 km s^{-1}, a slightly smaller value (i.e. 2193 km s^{-1}) was used for Hα. The broad Hα emission was also measured by Balmaverde & Capetti (2014) (FWHM $\sim$ 2240 km s^{-1}), Constantin et al. (2015) (FWHM $\sim$ 2800 km s^{-1}), and Cazzoli et al. (2018)[8] (FWHM $\sim$ 2915 km s^{-1}) with *HST*/STIS slit spectra, all obtaining values that are in fair agreement.

There are three measurements of the width of the broad Hα component with optical IFS. Two of them are from the present MEGARA and MUSE IFS data: 2427 ± 332 and 2350 ± 470 km s^{-1}, respectively. These values are consistent within the uncertainties, but are smaller than the value of $\sim$ 3200 km s^{-1} reported by DH19a from their GMOS/GEMINI cube (R $\sim$ 1700 and final angular resolution 0.7$''$).

We considered as the main sources of discrepancies the number of components used to model emission lines and the different spectral–spatial resolution of the different data sets (see e.g. Cazzoli et al. 2020). Another possibility for explaining the differences in the FWHM of the broad component is AGN variability (see e.g. Hernández-García et al. 2014), which is beyond the aim of the paper.

The FWHM and luminosity of the broad Hα component determined from the best-fitting model of the Hα broad component can be converted in black hole mass using the virial relation. For NGC 1052, we found that M_{BH} is $\sim 3 \times 10^5$ M$_\odot$ from Eq. 3 in Koss et al. (2017). Considering that the assumed value of luminosity is a lower limit as we did not apply any correction for reddening, the estimate of the black hole mass from Hα is in broad agreement with that by Onori et al. (2017b) using the virial relation of $\sim 4 \times 10^6$ M$_\odot$ (Table 4.1).

However, the determination based in the broad Hα has been explored the most for luminous type 1 AGNs (see e.g. Greene & Ho 2005 for details), hence for type 1.9 LINERs like NGC 1052 (Table 4.1) it could be uncertain; in other words, it is challenging to isolate the AGN contribution unambiguously. Therefore, we consider the M_{BH} from the stellar velocity dispersion to be more reliable because it is the result of coevolution between the host galaxies and the supermassive black holes.

---

[8]They found evidence for the BLR only in *HST*/STIS and not in ground-based CAHA/CAFOS data, due to a less reliable fit to the Hα emission line in ground- and space-based data sets.

4.6   Conclusions

On the basis of optical MUSE and MEGARA IFS data we have studied the properties of the stellar and ionised and neutral gas components in the LINER 1.9 NGC 1052, using as tracers both emission lines (from Hβ to [S II]) and the NaD absorption doublet.
The conclusions of this study can be summarised as follows:

1. *Kinematics and dynamical support for the stellar component.* The stellar velocity field is characterised by ordered large-scale rotational motions ($\Delta V = 167 \pm 19 \, \mathrm{km \, s^{-1}}$), although the velocity dispersion is generally high as measured from the MUSE ($145 \pm 22 \, \mathrm{km \, s^{-1}}$) and MEGARA data ($201 \pm 16 \, \mathrm{km \, s^{-1}}$). The rotational support is low, however. The dynamical ratio $V/\sigma = 1.2$ (0.8) from the MUSE (MEGARA) data is indicative of a dynamically hot disc with a significant random motion component. In both data sets the stellar major axis is well aligned with the photometric axis. The kinematic and dynamics of the stellar disc of NGC 1052 favour its classification as an S0-type. The black hole mass estimated from stellar dynamics is $2 \pm 0.5 \times 10^8 \, \mathrm{M_\odot}$.

2. *Ionisation mechanisms.* By combining the location of line ratios onto BPTs, theoretical models of shocks and pAGBs ionisation, and the weak or strong [O I] classification, we exclude star formation and pAGB scenarios in favour of a mixture of shock excitation and AGN activity as the main mechanisms of ionisation in NGC 1052. The general behaviour is that the ionisation in the central region ($R < 10''$) is a mixture of AGN photoionisation and shocks, while at larger galactocentric distances the shock excitation is dominating.

3. *The intriguing properties of the ionised gas probed by the primary component.* The velocity field shows a large-scale structure extended in the polar direction (NE-SW direction) up to $\sim 30''$ ($\sim 3.3 \, \mathrm{kpc}$) with blue and red velocities (typically $< |250| \, \mathrm{km \, s^{-1}}$). The velocity dispersion map lacks any symmetry typical of a rotation dominated system with a notable enhancement ($\sigma > 90 \, \mathrm{km \, s^{-1}}$) crossing the galaxy along the major axis of rotation in the central $\sim 10''$ (also called butterfly region within the main text). We consider that both features are likely related to the presence of an ionised gas outflow instead of, for example, a polar disc.

4. *Ionised gas outflow.* The outflow is probed by the secondary component with a bipolar morphology, velocity dispersions $> 150 \, \mathrm{km \, s^{-1}}$, and velocities up to $660 \, \mathrm{km \, s^{-1}}$. The outflow (with mass of $1.6 \pm 0.6 \times 10^5 \, \mathrm{M_\odot}$, and mass rate of $0.4 \pm 0.2 \, \mathrm{M_\odot yr^{-1}}$) is propagating in a cocoon of gas with enhanced turbulence (the butterfly region) and

triggering the onset of kpc-scale buoyant bubbles (polar emission). Considering the energy $(1.3 \pm 0.9 \times 10^{53}$ erg$)$ and energy rate $(8.8 \pm 3.5 \times 10^{40}$ erg s$^{-1})$ of the outflow, both the AGN and the radio jet are able to launch the outflow. However, taking into account its alignment with the jet and with the cocoon, and that the gas is collisionally ionised, we consider that the most likely power source of the outflow is the jet, although some contribution from the AGN is possible.

5. *Neutral gas content*. The kinematics maps of the NaD absorption obtained with MEGARA data indicate optically thick neutral gas with complex kinematics. The velocity field is consistent with a slow rotating disc $(\Delta V = 77 \pm 12 \, \mathrm{km \, s^{-1}})$, but the velocity dispersion map is off-centred with a peak value of $263 \pm 10 \, \mathrm{km \, s^{-1}}$ observed at 2.5″ (277 pc) eastwards of the photometric centre without any counterpart in the (centrally peaked) flux map. The hints of the presence of the neutral gas outflow are weak, and our identification its tentative. The putative neutral gas outflow is extended to the west with a projected area of 3.8 arcsec^2 with mild kinematics (i.e. with velocity and velocity dispersion of $63 \pm 21 \, \mathrm{km \, s^{-1}}$ and $251 \pm 5 \, \mathrm{km \, s^{-1}}$, respectively). The mass, the mass rate, and the energy of the neutral would be $(7.1 \pm 2.8) \times 10^6 \, \mathrm{M_\odot}$, $(0.86 \pm 0.30) \, \mathrm{M_\odot yr^{-1}}$, and $(1.1 \pm 0.4) \, 10^{55}$ erg, respectively.

6. *BLR properties*. In the nuclear region of NGC 1052 ($\leq 1''$) the broad Hα component that originated in the (unresolved) BLR of the AGN is modelled with a Gaussian component with FWHM of respectively 2427 ± 332 and $2350 \pm 470 \, \mathrm{km \, s^{-1}}$ for the MUSE and MEGARA data.

7. *Unresolved component*. This component has been detected with the MUSE data (barely with MEGARA) in all emission lines. It is observed in the central region, with a spatial extension matching that of the PSF, with an average FWHM $\sim 1380 \, \mathrm{km \, s^{-1}}$ and line ratios indicating AGN ionisation. It could probe either an unresolved AGN component, as proposed by DH119b, or a more recent AGN-driven outflow. However, with the current data set it is not possible to distinguish between the two scenarios.

As a final remark, we highlight that studies of this kind provided valuable insight into our general understanding of multiphase outflows in low luminosity AGNs.

Chapter 5

The MEGARA view of outflows in LINERs

5.1 Introduction

Feedback processes, and outflows in particular, are known to affect the evolution and composition of galaxies in different aspects, as already mentioned in the previous chapters. They are believed to be ubiquitous in galaxies that host an active galactic nuclei (AGN), as they are powered either by the activity of the supermassive black hole (SMBH), triggered by the kinetic energy injected by the jet, or by a mixture of both processes (e.g. Veilleux et al. 2005; Fabian 2012; Kormendy & Ho 2013; Heckman & Best 2014).

The results from Chapter 3 suggest that outflows are common also in low luminosity AGNs, in particular in Low Ionisation Nuclear Emission-line Regions (LINERs) (~50% detection), but their characteristics (extension, energetics, mass, velocities, etc) are still not fully understood. The work in Chapter 3 relies on the detection of extended ionised gas in imaging data. It also uses the available information on kinematics, coming from various sources and different wavelength ranges, to estimate the reliability of images as a tracer of such structures, as the kinematic information is typically more reliable than the imaging data. That is because the signatures of outflows in the emission lines are easily identified as an additional kinematical component on the line profiles, whereas an extended emission on imaging data may be produced by other phenomena that may mimic the behaviour of outflowing/inflowing gas. However, the different spectral and spatial resolution of data coming from different instruments may affect the detection and characterisation of the outflows to its full extension. This is specially the case for those coming from long slit spectroscopy, since the signatures of outflows will not be retrieved if the slit is not well aligned with the corresponding feature.

Thus we need uniform spectroscopic data to establish unified criteria to confirm or not the detection rate reported in Chapter 3.

To that aim, we obtained data with the MEGARA (Multi-Espectrógrafo en GTC de Alta Resolución para Astronomía) instrument for nine LINERs that are candidates to host an outflow either by imaging data or by kinematic information (see Masegosa et al. 2011; Cazzoli et al. 2018, and Chapters 2 and 3). We have already shown our pilot study of characterisation of outflows with the case of the prototypical LINER NGC 1052, finding evidence for an outflow seen with both MUSE/VLT and MEGARA/GTC data (see Chapter 4). In this chapter, we analyse optical spectroscopic data for the remaining eight galaxies with the aim to: (i) model the emission lines of the ionised gas to detect possible outflow signatures; (ii) compare the information from the kinematic signatures and the imaging data from HM22; and (iii) characterise the main properties (kinematics, energetic, mass etc.) of the outflows. To fulfil our objectives, we will extract first the stellar component of the galaxies, and characterise their kinematics, to obtain exclusively the ionised gas emission.

This chapter is organised as follows: In Sect. 5.2 we explain the sample selection; in Sect. 5.3 we describe the data reduction process of the data cubes, as well as the modelling of both the stellar continuum and the emission lines. In Sect. 5.4 we present the kinematic maps resulting of our analysis for each galaxy, that are discussed in Sect. 5.5. Finally, the conclusions and future work on these data is presented in Sect. 5.6.

5.2 Sample and data

The total number of objects analysed in this chapter is eight LINERs (see Table 5.1), that were selected as explained below. The parent sample of our data set comes from Cazzoli et al. (2018) and Hermosa Muñoz et al. (2020), where the long-slit spectroscopic properties of 21 and nine LINERs, respectively, were characterised; and from Hermosa Muñoz et al. (2022), where imaging data for 70 LINERs were analysed. We selected those targets showing non rotational motions that could be ascribed to outflows, presumably associated to the AGN. We were able to systematically gather data for nine targets, one of which was NGC 1052, already analysed in Chapter 4 (see also Cazzoli et al. 2022). The complete information of our observations is summarised in Table 5.2 and Sect. 5.2.1, and the nine galaxies, considering NGC 1052, are shown in Fig. 5.1.
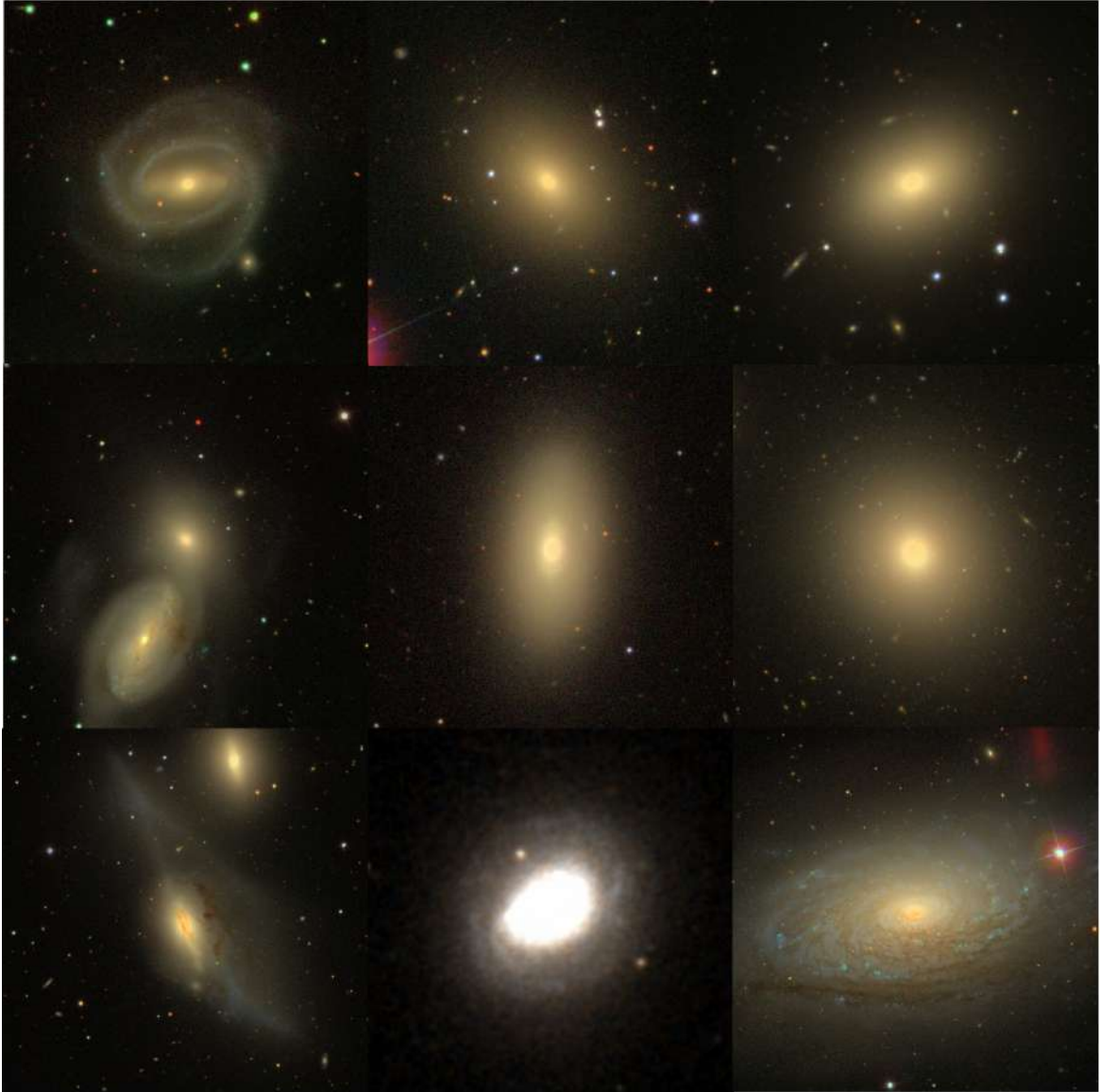
Fig. 5.1 Optical images of the nine LINERs observed with MEGARA. From left to right, up to down: NGC 0266, NGC 0315, NGC 1052, NGC 3226, NGC 3245, NGC 4278, NGC 4438, NGC 4750 and NGC 5055. All images have been obtained from the Sloan Digital Sky Survey DR9, except for NGC 4750, that is from the Digitalized Sky Survey. In all images, north-east is up-left.

5.2.1   Data gathering

We observed the objects with the MEGARA instrument, attached at GTC telescope (10.4 m), in Roque de los Muchachos observatory, in La Palma, Spain. The MEGARA instrument is an Integral Field Unit (IFU) with a FoV of 12.5"×11.3" and a spatial scale of 0.62" per fiber. It uses several Volume Phase Holographics (VPHs) available at different spectral resolutions. In this work we use three different VPHs at low-resolution and one at the highest resolution. Specifically, they are: LR-B, LR-V and LR-R; and the high-resolution VPH HR-R. The main properties of these VPHs for our targets (z<0.02), obtained from the MEGARA cookbook[1], are listed here:

- *LR-B:* The total wavelength range is 4330-5200 Å with an average resolution R = 6060; corresponding to 0.23 Å pix^{-1}. The relevant emission lines observable in this wavelength range are [O III]$\lambda\lambda$4959,5007 Å and Hβ.

- *LR-V:* The total wavelength range is 5140-6170 Å with an average resolution R = 6080; corresponding to 0.27 Å pix^{-1}. The relevant absorption line observable in this wavelength range is the NaI doublet.

- *LR-R:* The total wavelength range is 6100-7300 Å with an average resolution R = 6100; corresponding to 0.31 Å pix^{-1}. The relevant emission lines observable in this wavelength range are [S II]$\lambda\lambda$6716,6731 Å, [N II]$\lambda\lambda$6548,6584 Å, H$\alpha\lambda$6563Å and [O I]$\lambda\lambda$6300, 6364 Å.

- *HR-R:* The total wavelength range is 6440-6840 Å with an average resolution R = 18700; corresponding to 0.09 Å pix^{-1}. The relevant emission lines observable in this wavelength range are the [S II] doublet, [N II] doublet and Hα.

The data were gathered in a total of 10 nights (PIs: S. Cazzoli and A. Gil de Paz). We obtained two (three) individual exposures for VPH per galaxy, with typical exposure times of 1200 s (900 s) for the data obtained through the MEGADES (MEGARA Galaxy Disks Evolution Survey; Chamorro et al. in prep.) survey (open time), each forming an observing block (OB). The average airmass were 1.22 (LR-B), 1.25 (LR-V) and 1.3 (LR-R) (see Table 5.2).

---

[1]http://www.gtc.iac.es/instruments/megara/media/MEGARA_cookbook_1I.pdf

Table 5.1 General properties for all the 8 LINERs analysed in this chapter. Columns indicate: (3) RA and (4) DEC: coordinates; (5) Morphology, (6) z and (7) scale distance: from the Local Group from NED; (8) inclination angle and (9) V magnitude from HyperLeda; and (10) bolometric luminosity estimated from González-Martín et al. (2009).

#	ID	Other name	RA	DEC	Morphology	z	Scale	i	V mag	L_{bol} (10^X)
			(hh mm ss)	(dd mm ss)			(pc per ")	(deg)		(erg s^{-1})
(1)	(1)	(2)	(3)	(4)	(5)	(6)	(7)	(8)	(9)	(10)
1	NGC 0266	UGC 508	00 49 47.80	+32 16 39.79	SB(rs)ab	0.0155	351	16	11.8	–
2	NGC 0315	UGC 00597	00 57 48.88	+30 21 08.81	E+	0.0165	370	57	11.6	43.30
3	NGC 1052	IRAS 02386-0828	02 41 04.80	-08 15 20.75	E4	0.005	108	70	11.0	42.77
4	NGC 3226	ARP 094	10 23 27.01	+19 53 54.68	E2 pec	0.0044	86	69	12.9	42.33
5	NGC 3245	IRAS 10244+2845	10 27 18.39	+28 30 26.56	SA0^0(r)	0.0044	90	62	10.8	42.29
5	NGC 4278	IRAS 12175+2933	12 20 06.82	+29 16 50.72	E1-2	0.0021	42	16	10.2	42.53
6	NGC 4438	IRAS 12252+1317	12 27 45.59	+13 00 31.78	SA(s)0/a pec	0.0002	–	73	10.9	<42.36
7	NGC 4750	IRAS 12483+7308	12 50 07.27	+72 52 28.72	(R)SA(rs)ab	0.0054	129	32	12.1	–
8	NGC 5055	M 63	13 15 49.33	+42 01 45.40	SA(rs)bc	0.0017	40	55	8.6	41.09

5.3   Data reduction process

The data from MEGARA/GTC were reduced following the MEGARA Data Reduction Pipeline (Pascual et al. 2019). All the software and packages used throughout this analysis were within in a PYTHON environment. The full process is described in Gil de Paz et al. (2018) and Cazzoli et al. (2020); here we briefly describe the main steps. The pipeline applies the standard procedures to the data, as bias subtraction, flat-field correction and wavelength and flux calibration (with the respective standard stars observed each night for each target). The pipeline considers the information from all the fibers individually, to trace them over the field-of-view (FoV) and apply for each of them a specific illumination correction. Finally, it combines the individual exposures for each target to create the final *RSS* file[2]. For two objects (namely NGC 0266 and NGC 0315), the different OBs for a given VPH were not observed during the same night, so the individual exposures were shifted in spatial position. In these cases, to obtain the final combined cube, we created a mosaic with the task HYPERMOSAIC under the MEGARA-TOOLS package (v.0.1.0; de Paz et al. 2020). After that, for all targets we transformed the final *RSS* file to a data cube by applying a regularisation grid to obtain 0.4" square spaxels (see Cazzoli et al. 2020, and Chapter 4).

Once the cubes were fully reduced, we combined the LR-V and LR-R data cubes for all the targets. The procedure was based on our previous experience with NGC 1052 (see Chapter 4), in which the wavelength range corresponding to the LR-R VPH (see Sect. 5.2.1) lacked from sufficient stellar features to obtain a good modelling of the stellar component of the galaxies. We decided to combine LR-R with the LR-V data cube to increase the continuum features in the total wavelength range and obtain a satisfactory modelling in the LR-R range. For two targets (namely NGC 4278 and NGC 4750) we additionally obtained LR-B data cubes (see Table 5.2). At their redshifts, in the spectral range of this VPH the emission lines available are located at the reddermost part of the available wavelength range. This implies that these data cubes have sufficient stellar features to obtain a proper stellar modelling without combining with the other VPHs (i.e. LR-R & LR-V). Finally, NGC 4278 was observed with both the lowest (LR-B and LR-V) and highest resolution mode of MEGARA (VPH HR-R instead of LR-R). In the HR-R, the spectral band is small ($\Delta\lambda \sim 400$ Å; see Sect. 5.2.1) and the continuum featureless, so the stellar subtraction was not performed.

For two objects (namely NGC 0315 and NGC 4750), the cubes to be combined (LR-R and LR-V) were not aligned, as each VPH was observed in a different night. To estimate the

---

[2]A Raw Stacked Spectra (*RSS*) file is the final product of the data reduction; an image containing the spectra of the 623 fibers.

Table 5.2 Observing log of MEGARA/GTC data. Columns indicate: (1) object; (2) date of the observation; (3) VPHs used; (4) exposure time; (5) average airmass per VPH; and (6) average seeing per target. $^{(*)}$ indicates the objects observed within the MEGADES survey (see Sect. 5.2.1).

Galaxy	Observing date (yy-mm)	VPH	Exposure time (s)	Airmass	Seeing (")
(1)	(2)	(3)	(4)	(5)	(6)
NGC 0266	2020-08	LR-V	900	1.02	
		LR-R	900	1.20	
NGC 0315	2019-09	LR-V	900	1.08	1.1
	2019-10	LR-R	900	1.18	1.1
NGC 3226	2018-12	LR-V	1200	1.15	0.8
		LR-R	1200	1.68	0.6
NGC 3245	2021-02	LR-V	900	1.60	1.0
		LR-R	900	1.15	0.9
NGC 4278$^{(*)}$	2019-05	LR-B	1200	1.01	0.6
		LR-V	1200	1.07	0.5
		HR-R	1200	1.22	0.5
NGC 4438	2019-01	LR-V	1200	1.06	1.0
		LR-R	1200	1.05	1.0
NGC 4750$^{(*)}$	2019-05	LR-B	1200	1.43	0.7
		LR-V	1200	1.40	0.7
		LR-R	1200	1.55	0.6
NGC 5055$^{(*)}$	2020-01	LR-V	1200	1.64	1.2
		LR-R	1200	1.31	1.2

photometric centre of every cube, we created a broad band-like image by collapsing along the wavelength dimension and fitted them to ellipses. The central position of the ellipses was taken as a reference of the photometric centre. When the position differed significantly (>2 square-spaxels) from the LR-V datacube to the LR-R, we shifted the cubes to set their photometric centres at the same spatial positions. Finally, for combining the individual spectra at each position of the FoV, we checked the signal-to-noise ratio (S/N) of the continuum of the cubes, to ensure smooth variations between different VPHs.

5.3.1   Stellar modelling

We used the PPXF software by Cappellari & Copin (2003) (see Cappellari 2017 and references therein) to subtract the stellar contribution from the host galaxy. This is crucial for low-luminosity AGNs, such as LINERs, where the nuclear emission is usually heavily

absorbed by the stellar absorption, especially in the Balmer lines. As mentioned in Sect. 5.3, we combined the LR-V and LR-R cubes to increase the range of continuum in the spectra and improve the overall fitting by including more stellar features. For the correct modelling of the stellar population, we masked all the emission, absorption, telluric and atmospheric lines (see example for NGC 4750 in Fig. 5.2). We used the additive and multiplicative Legendre polynomials to adjust the continuum shape of the selected templates, with the lowest order possible to obtain a proper modelling. We set the additive and multiplicative polynomials to be 8 and 4, respectively, for all the targets. As for the LR-B data cubes, we fitted them individually (see Sect. 5.3; additive and multiplicative polynomials 4 and 4, respectively). We used the synthetic stellar library by González Delgado et al. (2005), which provides a total spectral coverage from 4000 to 7000Å, enough to cover the spectral range of our data cubes with the same resolution. The 413 synthetic stellar spectra correspond to a metallicity of 0.02 $Z_\circ$, and cover a whole range of other parameters, such as the temperature or the gravity (see González Delgado et al. 2005; Martins et al. 2005; Cazzoli et al. 2022, for more details).

In total, we fitted the combined LR-V + LR-R cubes for 7 LINERs, namely: NGC 0266, NGC 0315, NGC 3226, NGC 3245, NGC 4438, NGC 4750 and NGC 5055; and the LR-B cubes for 2 LINERs, namely NGC 4278 and NGC 4750. From the modelling we obtained the main kinematical properties on a spaxel by spaxel basis and generated the final maps for each galaxy. The main results are found on the top panels of Figs. 5.4 to 5.10, where we show the velocity, velocity dispersion (σ) and the galactic continuum or Hα flux maps of each LINER. For NGC 0266, NGC 0315 and NGC 4750 we had to shift the LR-V and the LR-R cubes to match their photometric centres, as mentioned in Sect. 5.3; consequently their final maps cover a smaller field of view.

5.3.2   Emission line modelling

We modelled the emission lines using a Non-Linear Least-Squares Minimization and Curve-Fitting package, LMFIT (Newville et al. 2014). We applied a similar technique as in previous works (Cazzoli et al. 2018, 2020, see Chapters 2 and 4). The main aspects are briefly summarised here.

We used the [S II] lines as a reference for the remaining emission lines (i.e. [N II] doublet, Hα and [O I] doublet when possible), fixing their central wavelength (associated to the gas velocity) and its width (associated to the velocity dispersion). We imposed the intensity ratios between the [O III] (LR-B), [O I], and [N II] doublets to be 2.99, 3.13 and 2.99 (Osterbrock & Ferland 2006). The velocity dispersion was estimated subtracting the measured value
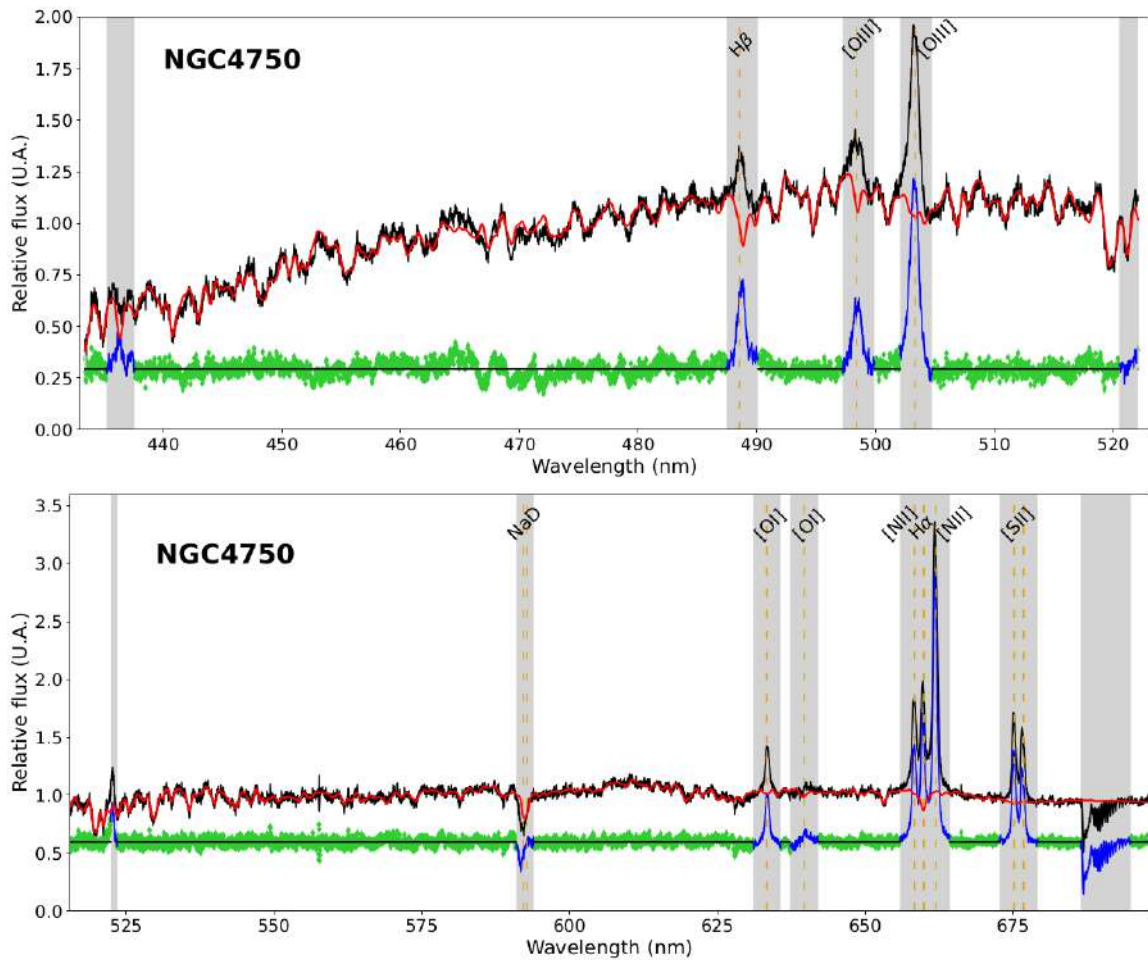
Fig. 5.2 Examples of the stellar modelling of the LR-B (top) and LR-V+LR-R (bottom) spectra extracted at the photometric centre of NGC 4750. In both panels: the red line shows the best fitting using PPXF, the green line shows the residuals of the fit, and the blue line is the final subtracted spectrum. The main emission and absorption lines are indicated with dashed vertical lines. Grey regions have been masked during the fitting.

from the instrumental value as follows: $\sigma = \sqrt{\sigma_{obs}^2 - \sigma_{inst}^2}$. Not only we can use the [S II] as reference (the so-called S-method), but also the [O I] 6300Å emission line (the O-method). This serve us to test which of the S- or O- methods better reproduce the profiles of the emission lines and the physical implications behind, such as a possible stratification of the gas in the NLR of the AGN. However the [O I] line is detected with enough S/N (>5) only in three galaxies from the sample (i.e. NGC 3226, NGC 4750 and NGC 5055), and typically only in the inner regions (<2" from the centre). In general, we found that the kinematics derived from the [S II] lines reproduced better the profiles of the [N II]-Hα blend (i.e. with lower residuals), while the [O I] behaved differently.

For the line modelling, we allowed up to three Gaussian components per emission line, plus an additional very broad component (FWHM>1000 km s^{-1}) only in the Balmer lines within the PSF region, originated in the BLR. In order to evaluate the number of components preventing overfitting, we used the ε criterion (Cazzoli et al. 2018, Chapters 2 and 4). This parameter is defined as the standard deviation of the residuals under the lines when fitted with a Gaussian component, with respect to its value in the continuum (ε_c) on a 50Å-wide region with no emission lines. We considered the inclusion of an additional component whenever the ε was larger than 3, as this means that the standard deviation of the remaining residuals could not be explained simply as continuum variations. We visually inspected the spectra when it varied between 2 and 3.

To test whether there was a very broad component in the Balmer lines for each galaxy, we created a high S/N spectrum integrating the individual spectra in the PSF region, so that the BLR component could be more easily detected and not as diluted as in the individual spaxels. If the presence of a BLR component was significant, we included it in the PSF region for the individual spaxels. An example of the ionised gas modelling of the integrated spectrum in the PSF of NGC 4438 is shown in Fig. 5.3.

5.4   Results

In this Section we describe the results from both the stellar and ionised gas components of the galaxies (see Sect. 5.4.1). We show the kinematic and flux maps for all the galaxies, accounting for the different kinematical components that may appear in the stellar component and the emission lines in Figs. 5.4 to 5.10.

The following sections are based on seven out of the eight targets of the sample (see Table 5.2). We prioritised the targets with available IFS cubes in both R and V band at the same (low) resolution in order to optimise their wavelength coverage. We have the LR-R+LR-V data
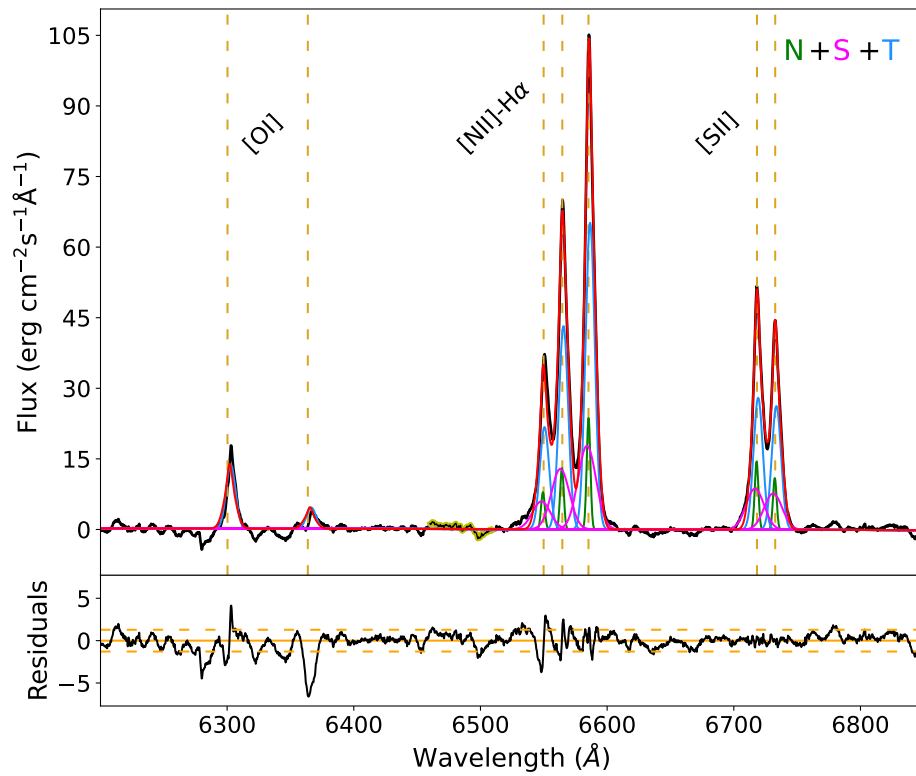
Fig. 5.3 Example of the ionised gas modelling of the integrated LR-R spectrum on the PSF region of NGC 4438. In the top panel the green, pink and blue Gaussians represent the narrow, secondary and third kinematical components, respectively. The global fit is in red and the region where we estimated the ε from the continuum (ε_c) is marked in yellow. In the bottom panel the residuals of the fit are shown in black, with the horizontal, dashed, yellow lines indicating $3\varepsilon_c$ (see Sect. 5.3).

cubes for the majority of the targets (~90%; see Table 5.2). Lowest priority, has been given to
the other targets with either data in the R band but at the highest resolution (i.e. NGC 4278) or
with additional cubes in B-band. Hence, the excluded targets in this Chapter are NGC 4278
and the LR-B cube of NGC 4750. The analysis of these latter objects is ongoing, an it will be
presented in a forthcoming paper (Hermosa Muñoz et al. in prep.).

We focus on the emission line gas (ionised gas) to benefit the experience in handling the data
acquired from previous works by our team (see Cazzoli et al. 2018, 2020, Chapters 2 and 4).
The modelling and analysis of NaD absorption lines will be covered in the future paper by
the team.

As mentioned in Sect. 5.3.1, we modelled the stellar component of the LR-V+LR-R combined
cubes (when possible) or LR-V cubes for our LINERS using pPXF. The stellar subtraction
allow us to obtain the spectra of exclusively the ionised and neutral gas emission without
the contamination from the stars in the host galaxy. An example of the stellar modelling for
both the LR-V+LR-R combined cube and the LR-B cube is shown in Fig. 5.2. As for the
ionised gas components, we obtained the kinematic maps using as reference the kinematics
from the [S II] doublet emission lines for all galaxies whenever their S/N was larger than 5
(S-method, see Sect. 5.3.2), in order to ensure a proper fitting to the other emission lines.
Here we describe the main results and features obtained per each galaxy individually, which
will be discussed in Sect. 5.5. The derived parameters from the stellar maps and the kinematic
components of the ionised gas maps are shown in Table 5.3.

5.4.1   Main results per individual galaxy

The main considerations taken into account in the result description are the following:

- We always consider the S-method for the line modelling. The O-method has not been
  used given the generally low S/N of the [O I] line.

- Given that the parameters of the lines (central wavelength and width) have been tied,
  the derived kinematic values are equal for all. We show exclusively the Hα flux map
  throughout the paper, the rest of the flux maps will be presented in our forthcoming
  paper (Hermosa Muñoz et al. in prep.).

- In general, the position angle (PA) has been estimated measuring from north to east,
  using as reference the receding side of the velocity maps. In case this convention is not

used in a particular object, it is properly indicated. We estimated the PA of the ionised gas for the primary component whenever it resembled to a gas disc.

- From now on, we will refer to the three Gaussian components and the broad (associated to the BLR) as the primary, the secondary, the third and the broad, respectively. They were ordered in such a way that generally the primary component has smaller widths than the secondary component, ensuring the continuity in the final maps.

- We found exclusively one component in the forbidden and permitted emission lines for two galaxies (NGC 0266 & NGC 5055), two components for four galaxies (NGC 0315, NGC 3226, NGC 3245 and NGC 4750), and three components for NGC 4438 and NGC 1052 (see Chapter 4).

NGC 0266 (Fig. 5.4): The stellar component of this galaxy is rotating with a clear pattern. The higher velocities are found in the inner regions immediately out of the PSF up to ~4" in diameter in the major axis direction (PA~121°). The velocity dispersion map is rather homogeneous, with a median value of $189\,\mathrm{km\,s^{-1}}$, probably caused by the known bar in this galaxy (Font et al. 2017). At the photometric centre, $\sigma = 205\,\mathrm{km\,s^{-1}}$, out of the PSF (~1.2" in radius) it radially goes down to ~$170\,\mathrm{km\,s^{-1}}$, and then gets uniform at larger radii ($> 2.5''$).

We detect ionised gas elongated towards the major axis of the stellar component. The number of spaxels with S/N>5 in the [S II] lines comprises ~40% of the total number of spaxels in the cube. In general, the emission line profiles are narrow (median σ in the map of $116\,\mathrm{km\,s^{-1}}$) and were properly fitted with a single narrow Gaussian component all over the FoV. The structure of the ionised gas velocity map clearly differs from that of the stars, being much closer to a traditional spider-pattern (see Fig. 5.4). The inner parts of the velocity map show a twisted shape oriented towards the north direction, whereas the outer parts (>2.5") show a rotating-like pattern oriented along the stellar major axis. The semi-amplitude velocity of the gas is ~$212\,\mathrm{km\,s^{-1}}$. The Hα flux is concentrated on a spiral-like shape, that is spatially coincident with the twisted region of nearly flat rotation in the gas velocity map. The gas velocity dispersion map is centrally peaked ($\sigma_{\mathrm{gas,N}}^{\mathrm{PSF}} = 173\,\mathrm{km\,s^{-1}}$; see Table 5.3) and drops radially out from the centre.

NGC 0315 (Fig. 5.5): The stellar component of this galaxy shows homogeneous velocity and velocity dispersion fields, with no significant variations (median values of -3 $\mathrm{km\,s^{-1}}$ with respect to the systemic and σ ~$330\,\mathrm{km\,s^{-1}}$). This galaxy is elliptical, so no strong features were expected on the stellar kinematic maps, neither on the galactic continuum.
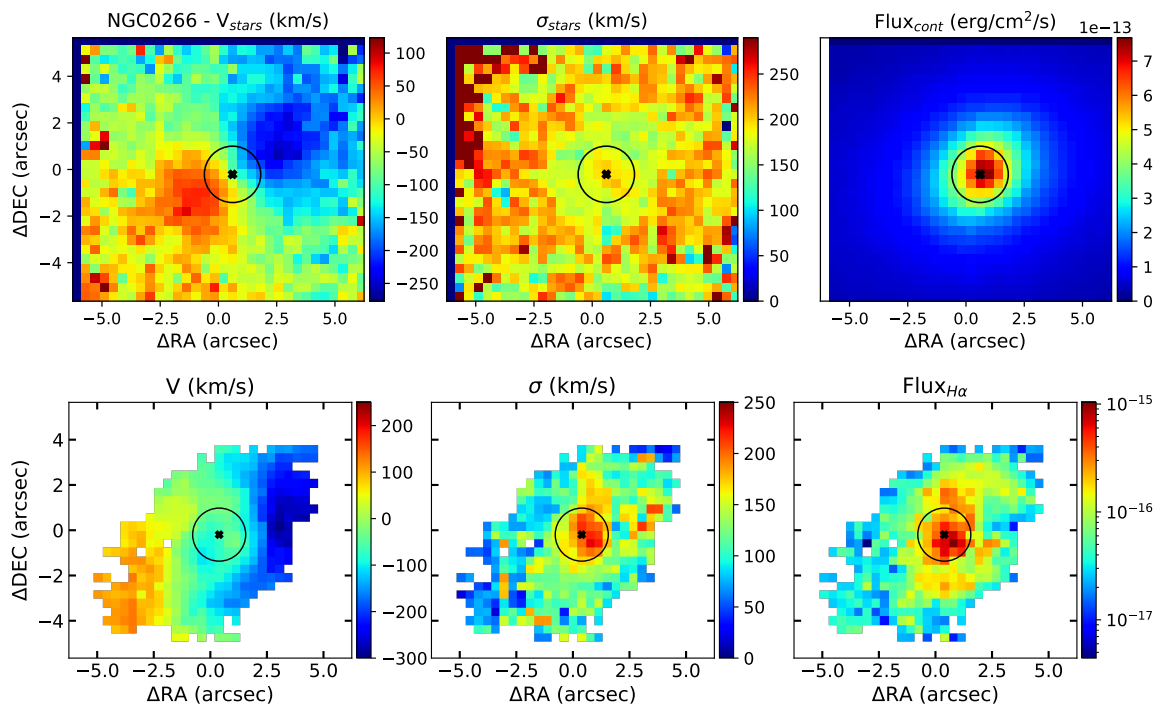
Fig. 5.4 Kinematic maps for the stellar (top panel) and ionised gas (bottom panel) components of NGC 0266. The stellar kinematics was calculated using the combined LR-V+LR-R data cube, whereas the ionised gas kinematics is that of the Hα emission line (see Sect. 5.3). In all panels from left to right: corrected velocity in km s^{-1}, velocity dispersion in km s^{-1} and integrated flux per spaxel (stars) or integrated Hα flux (gas) in erg s^{-1} cm^{-2}. The black cross indicates the photometric centre, and the PSF is marked with a black circle.

We tried modelling the emission lines using not only [S II] but also the [O I] line as reference, but it produced larger structure in the residuals under the Hα-[N II] blend. The emission corresponding to the ionised gas in this galaxy, measured with the S-method, is concentrated around the nucleus, and reaches only distances of $\sim$2" in radius from the photometric centre. In general, the emission lines show complex profiles, with various kinematical components difficult to disentangle. The majority of the emission ($\sim$70%) is located inside the PSF, and thus is unresolved. We detect two kinematic components per forbidden line plus a very broad component under Hα. The primary component is barely resolved, with a rotational pattern that differs from the velocity map of the stars, with a semi-amplitude velocity of 156 km s^{-1}. The velocity dispersion has a median value of 199 km s^{-1}, and a central value of 195$\pm$38 km s^{-1} (see Table 5.3). The secondary and broad components under Hα are unresolved, with an average velocity of 96 km s^{-1} and -53 km s^{-1}, and an average σ = 480 km s^{-1} and σ = 1077 km s^{-1}, respectively.

NGC 3226 (Fig. 5.6): The stars of this galaxy are rotating, creating a velocity map with a regular pattern (PA$_{\text{stars}}$=49°; see Table 5.3). The semi-amplitude velocity is 106 km s^{-1}, and the velocity dispersion peaks at the photometric centre with a central value of 210 km s^{-1} (see Table 5.3). The velocity dispersion drops radially from the centre out to the FoV limits[3]. The rotational pattern from the stars is oriented in the north-east direction as the ionised gas velocity map, but with a different position angle (PA$_{\text{gas}}$ = 19°; see Table 5.3). In total, we identified two kinematical components per emission line in this galaxy plus an spatially unresolved broad component in Hα. The primary component is oriented on the north-east south-west direction and shows a strong rotational pattern, with a semi-amplitude velocity of 219 km s^{-1}. The Hα flux is oriented in the same direction as the velocity map. In general, this component is very narrow ($\sigma \leq 100$ km s^{-1}) although a nuclear structure with wider profiles ($\sigma \sim 200$ km s^{-1}) is visible oriented almost perpendicular to the major axis of the velocity map (PA $\sim$107°). The secondary kinematic component of the emission lines is unresolved and completely embedded in the PSF region. It is clearly blueshifted (average velocity of -91 km s^{-1}) with an average velocity dispersion of 262 km s^{-1} (see Table 5.3). We detect a very broad component (average σ of 979$\pm$65 km s^{-1}) with an average velocity of 269$\pm$20 km s^{-1}. We checked its presence by modelling the integrated PSF spectrum, whose χ^2 improved by a 36% with the addition of this component with respect a two-component fit.

NGC 3245 (Fig. 5.7): The Hα emission line within the nuclear region was strongly absorbed in comparison with other galaxies. Consequently, in order to ensure a proper modelling of

---

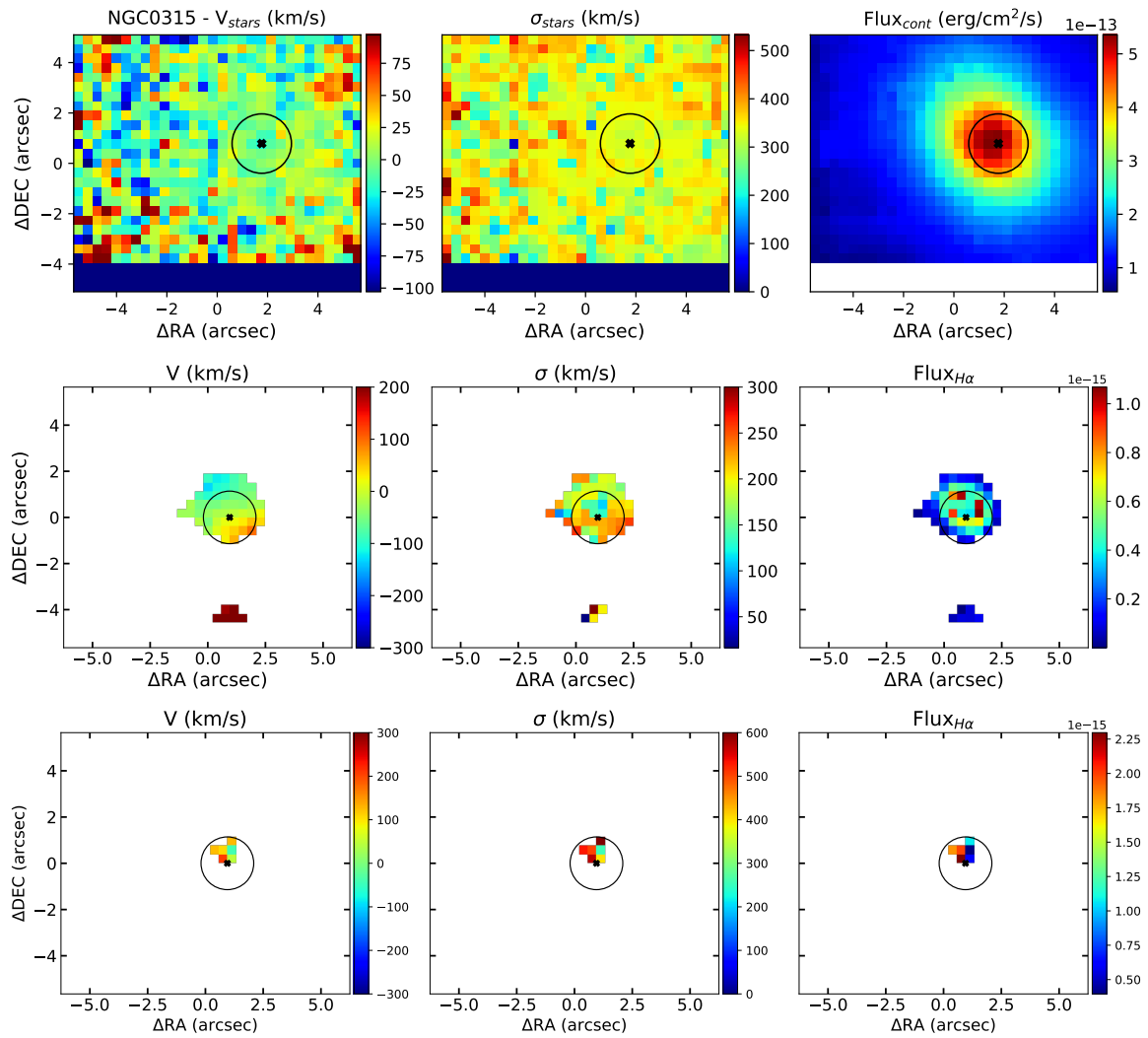[3]The structures on the borders of the FoV are due to S/N issues.

Fig. 5.5 Kinematic maps for the stellar (top panel) and ionised gas components of NGC 0315. The spectra of this galaxy was modelled with a narrow (second panel) and a secondary, unresolved (third panel) kinematical components per emission lines. Full description in 5.4.
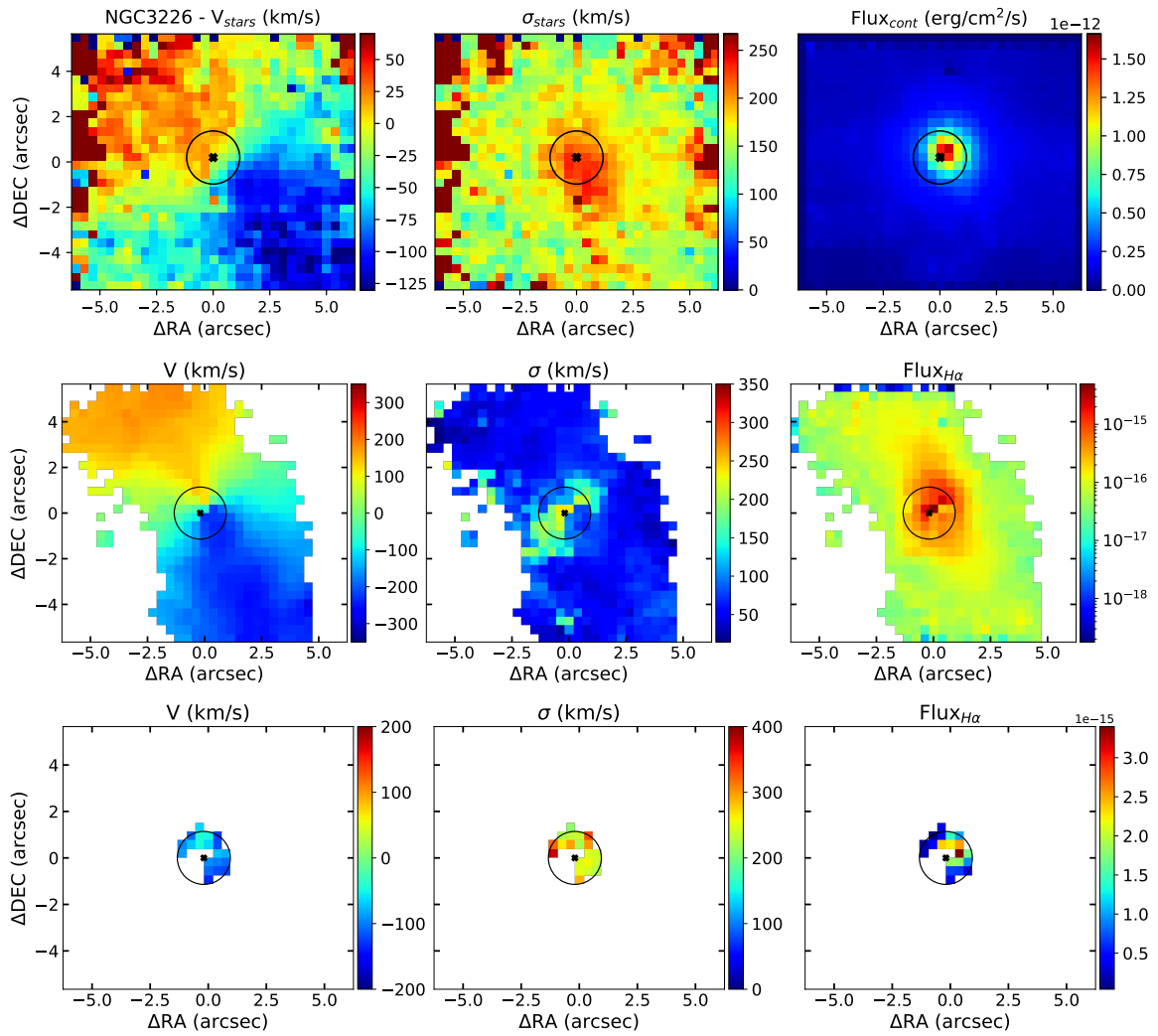
Fig. 5.6 Kinematic maps for the stellar (top panel) and ionised gas components of NGC 3226. The spectra of this galaxy was modelled with a narrow (second panel) and a secondary (third panel) kinematical components per emission lines. Full description in 5.4.

the stellar component in this region, we used higher additive polynomials than for the other targets (10 vs 8). The kinematical maps show a regular spider-pattern velocity field with a centrally-peaked velocity dispersion map (central value of 245 km s^{-1}; see Table 5.3). The semi-amplitude velocity of the stellar component is 137 km s^{-1}.

The ionised gas in the inner regions of the galaxy has a complex structure with double components per emission line. There is no strong statistical evidence of a very broad component in the Hα-[N II] blend, as the total contribution of that component would have been less than 5% for all the spectra in the PSF region. We tested its presence by fitting an integrated PSF spectrum and testing the number of components needed to reproduce the emission line profiles, finding only two kinematic components and no BLR component. Overall in the FoV, the narrow kinematic component shows a strong rotation pattern (semi-amplitude velocity ~232 km s^{-1}) despite its relatively low extension (~8"-diameter in the north-south direction and ~4"-diameter in the east-west direction). The velocity dispersion map shows an enhanced region ($\sigma > 140$ km s^{-1}) in the east-west direction resembling a bicone, that does not correspond to any particular feature in the velocity or flux maps. The secondary component is almost completely blueshifted (v < 50 km s^{-1}) and its average value in the PSF region is similar to that of the primary kinematic component (average $\sigma_{\mathrm{gas,S}}^{\mathrm{PSF}} = 198$ km s^{-1} vs median $\sigma_{\mathrm{gas,N}}^{\mathrm{PSF}} = 154$ km s^{-1}: see Table 5.3). Both the velocity and velocity dispersion maps show a clear bimodality, with a narrower, more blueshifted component in the north part of the PSF, with respect to the south part. It has to be noted that this secondary component is embedded in the PSF, so no strong claims about its origin can be made.

NGC 4278 (Fig. 5.8): Contrary to the previous galaxies, for NGC 4278 we obtained the properties of the stellar component by using the LR-B and LR-V data cubes individually and not the combined LR-R+LR-V datacube, as we have the HR-R cube instead of the LR-R (see Table 5.2 and Sect. 5.2.1). The kinematic maps for the LR-V cube (which are very similar to that from the LR-B) reveal a velocity map for the stars following a spider pattern (semi-amplitude velocity of 104 km s^{-1}; see Table 5.3) and a centrally peaked velocity dispersion (central value in the PSF of 336 km s^{-1}; see Table 5.3) that drops gradually from the centre. The modelling of the emission lines in the LR-B wavelength range (i.e. [O III] and Hβ will be done as a future work (Hermosa Muñoz et al. in prep., see Sect. 5.6).

NGC 4750 (Fig. 5.9): The behaviour of the stellar component in this galaxy creates a velocity map with regularly rotating spider-pattern along a major axis with a PA of 130° (receding side from south-west; see Table 5.3). The velocity dispersion map shows no particular features,
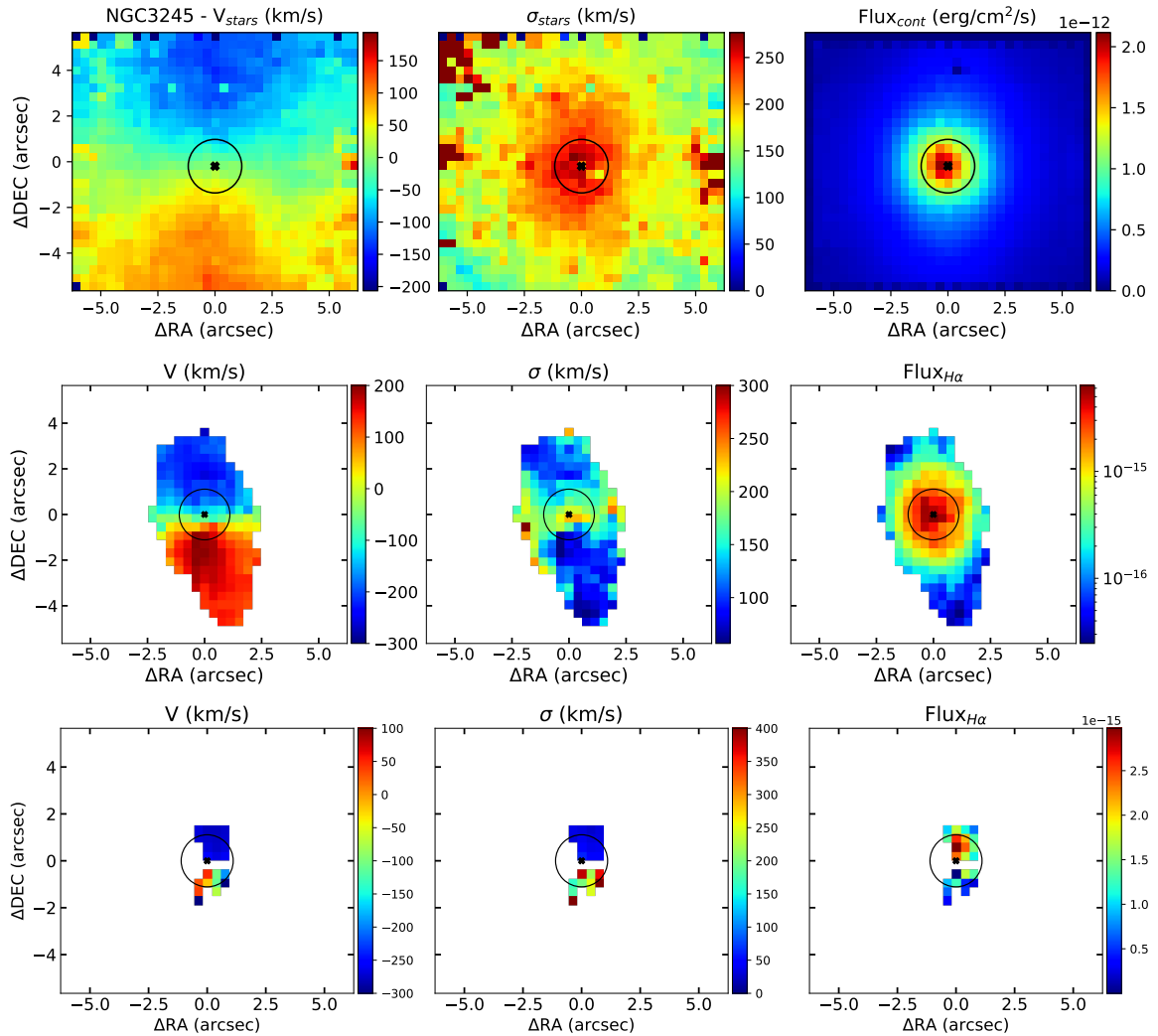
Fig. 5.7 Kinematic maps for the stellar (top panel) and ionised gas components of NGC 3245. The spectra of this galaxy was modelled with a narrow (second panel) and a secondary (third panel) kinematical components per emission lines. Full description in 5.4.
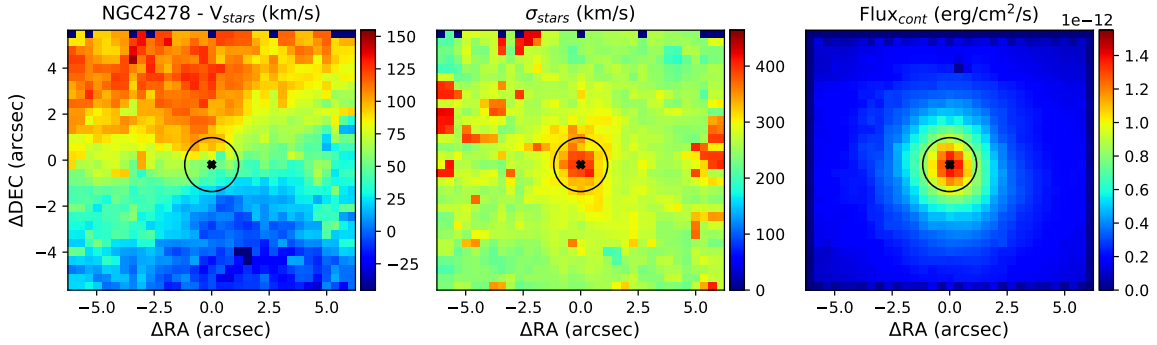
Fig. 5.8 Kinematic maps for the stellar component of NGC 4278. For this galaxy we modelled the stellar component using only the LR-V cube (see Sect. 5.3). Full description in 5.4.

but a rather homogeneous distribution with a median value of $121\,\mathrm{km\,s^{-1}}$ (in the PSF, the average value is $134\,\mathrm{km\,s^{-1}}$; see Table 5.3).

However, this galaxy has the most peculiar kinematic maps for the ionised gas of the sample. We found a total of two components per emission line plus an additional very broad component associated to the BLR. For the narrowest component, we find in the velocity map two blobs clearly distinguishable from the rest of the map, which is barely rotating (average velocity out of blobs $\sim$-5 km s^{-1}). These two regions located eastward (receding side) and westward (approaching side) from the nucleus do not correlate with another particular feature visible in the velocity dispersion map (average σ in all the map of $120\,\mathrm{km\,s^{-1}}$), that is a S-like structure of high σ (i.e. $>200\,\mathrm{km\,s^{-1}}$). The position angle of the rotating region of the ISM velocity map differs slightly from that of the stellar component (PA$\sim$175° vs 130°; see Table 5.3). The flux map shows an enhanced region located at 4" north-east from the nucleus, corresponding to a low velocity dispersion region ($\sim$50 km s^{-1}) of approximately 2×2" in diameter. Comparing with a pure Hα image (see Fig. 5.13 and B.7) and considering the different spatial resolutions, this region is probably a star forming region from one of the spiral arms of the galaxy.

As for the secondary component, it is barely resolved although it is extended out of the PSF west from the nucleus (up to 2.5"). It is mainly blueshifted (average velocity = -92 km s^{-1}) and broader than the primary component, with a central velocity dispersion of $297\,\mathrm{km\,s^{-1}}$ (see Table 5.3). As for the very broad component associated to the BLR, it has an average velocity 156±18 km s^{-1} and average σ of 929±127 km s^{-1}.

NGC 5055 (Fig. 5.10): This LINER is a very massive galaxy with a very important contribution of the stellar component in the observed spectra, specially in the nuclear region (within the PSF). The spectra inside the PSF region hence have strong features in the continuum
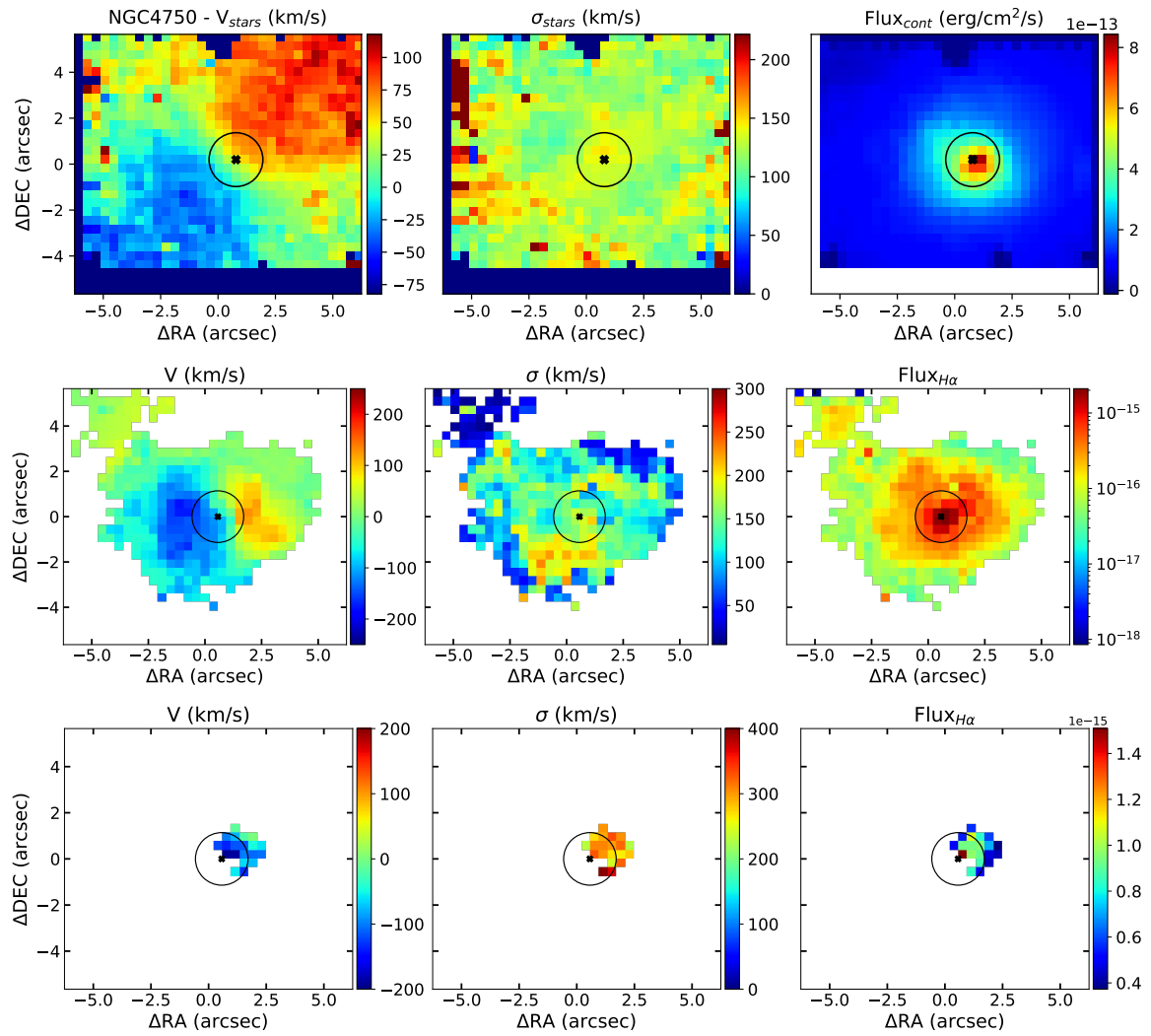
Fig. 5.9 Kinematic maps for the stellar (top panel) and ionised gas components of NGC 4750. The spectra of this galaxy was modelled with a narrow (second panel) and a secondary (third panel) kinematical components per emission line plus a broad component under Hα. Full description in 5.4.

which difficulted the modelling. Due to this, we created an integrated spectrum within the PSF to increase the S/N and ensure a better fit to the stellar contribution, considering that the Hα-[N II] blend is highly absorbed (see Fig. 5.11). We increased the polynomials from the standard (in our data) 8-4 to 10-4 to improve the fit and overall residuals. The stellar maps show a clear rotation field and an homogeneous velocity dispersion. The semi-amplitude velocity derived from the velocity map is ~90 km s^{-1}, and the velocity dispersion has a median value of 115 km s^{-1}.

After the stellar subtraction, we find in general the S/N of the emission lines to be larger than 5 and no [O I] detected in the whole FoV. The line profiles are quite narrow ($<$200 km s^{-1}), with only one kinematic component in all the emission lines, including the PSF region (see integrated spectrum in Fig. 5.11). The median velocity of the primary component is -32$\pm$11 km s^{-1} and the median σ is 40$\pm$20 km s^{-1}. The velocity map shows a rotating pattern with a semi-amplitude velocity of 126 km s^{-1}. The velocity dispersion map peaks at the photometric centre, but then it becomes asymmetric in the north-east part with respect to the south-west region. Finally, the flux map of Hα has a slightly different morphology to that of the other two kinematical maps. It peaks at the central regions (i.e. PSF), showing two enhanced regions with blobs again in the north-east and south-west direction. However, the enhanced regions are anti-correlated with the regions where the σ is more prominent (i.e. north-east). This may indicate that these blobs correspond to star-forming regions, where the σ is expected to be low, as in the case of NGC 4750.

5.4.2   The intriguing case of NGC 4438

From our eight LINERs, NGC 4438 is the most particular case, as it is the only galaxy in the sample for which we find a third kinematical component per forbidden emission line resolved out of the PSF region (see integrated spectrum of the PSF in Fig. 5.3). As mentioned in Sect. 5.2, the systematic search for outflows in LINERs with MEGARA started with the prototypical LINER NGC 1052 in Chapter 4. In the kinematical decomposition of the emission lines, we found three kinematical components for this LINER, as for NGC 4438, but the third component of NGC 1052 was unresolved.

This galaxy is known to have an ionised gas bubble (Kenney & Yale 2002) that we targeted with MEGARA data. We traced the north-western region of the bubble by centring it in the FoV of MEGARA instead of the galaxy nucleus. As a consequence, we barely detect any emission south-east from the nucleus. Due to this shift and contrary to the rest of the galaxies in our sample, here the stellar velocity field is slightly shifted towards detecting the reddermost rather than the bluemost velocities, simply because is not centred in the FoV.
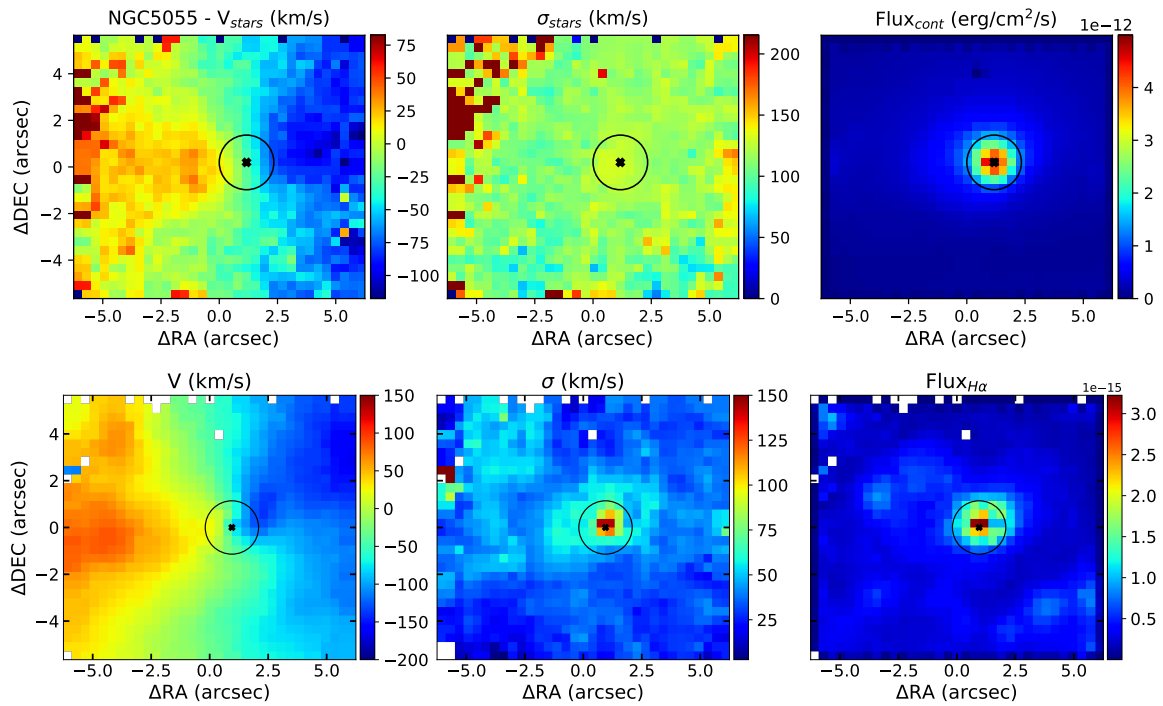
Fig. 5.10 Kinematic maps for the stellar (top panel) and ionised gas (bottom panel) components of NGC 5055. The spectra of this galaxy was modelled with a single narrow component on the emission lines. Full description in 5.4.
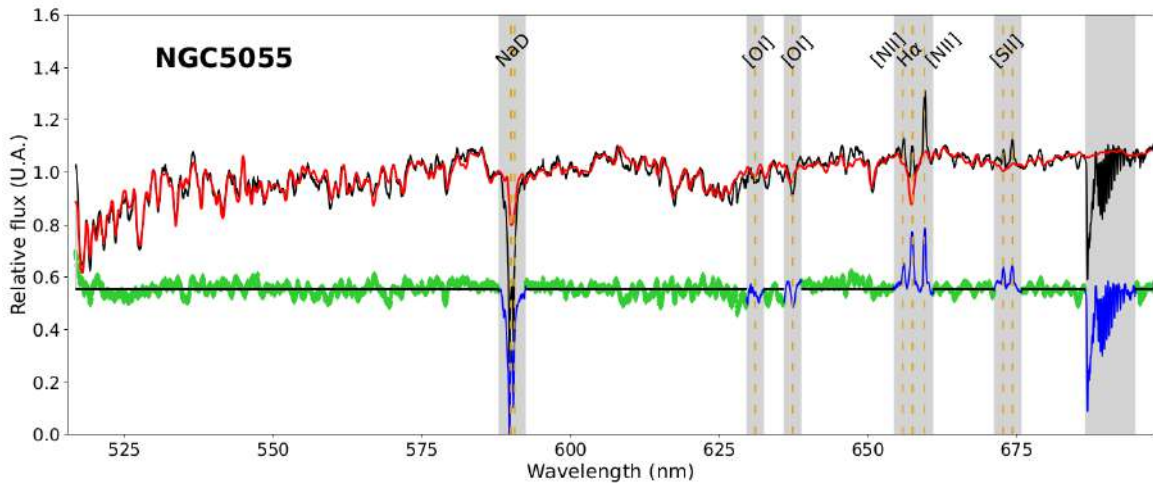

Fig. 5.11 Stellar component modelling of the integrated PSF region for NGC 5055. Same description as in 5.2.

Table 5.3 Kinematical parameters derived from the stellar modelling of the LR-R+LR-V data cubes and the the individual components of the gas modelling of the LR-R cubes. Columns indicate: (1) object; (2) position angle of the stellar velocity maps; (3) semi-amplitude velocity and (4) central velocity dispersion in the PSF of the stellar maps; (5) position angle of the primary component of the ionised gas; (6) and (7) semi-amplitude velocity and central velocity dispersion (in the PSF) of the primary component of the ionised gas; (8) and (9) average velocity and velocity dispersion integrated in the PSF for the secondary component of the ionised gas.

Galaxy	PA_{stars}	Δv_{stars}	σ_{stars}^{PSF}	PA_{gas}^{N}	$\Delta v_{gas,N}$	$\sigma_{gas,N}^{PSF}$	v_{gas}^{S}	$\sigma_{gas,S}^{PSF}$
	(°)	(km s^{-1})	(km s^{-1})	(°)	(km s^{-1})	(km s^{-1})	(km s^{-1})	(km s^{-1})
(1)	(2)	(3)	(4)	(5)	(6)	(7)	(8)	(9)
NGC 0266	121±7	172	182±14	–	–	173±28	–	–
NGC 0315	–	–	335±13	225±8	156	195±38	96±77	480±120
NGC 3226	49±4	106	210±17	19±4	219	136±55	-91±27	262±42
NGC 3245	178±3	137	245±18	174±6	232	154±46	-214±142	198±173
NGC 4278	20±1	104	336±35	–	–	–	–	–
NGC 4438	27±2	111	148±7	28±6	154	99±28	-8±35	256±57
NGC 4750	130±10	134	134±7	–	–	153±29	-92±50	297±41
NGC 5055	99±4	79	50±4	107±11	126	69±26	–	–

However, the velocity map shows a regular rotating stellar disc with a PA of 27°. The velocity dispersion is homogeneously distributed (average central value of 148 km s^{-1}, see Table 5.3), with slightly larger values (~180 km s^{-1}) and smaller velocities on the same location as the ionised gas bubble. The stellar continuum morphology is elongated along the disc, with no particular features.

We analysed the spectra of the ionised gas emission lines, deriving the presence of three different kinematical components per line, as mentioned. The narrowest component (average central σ of 99 km s^{-1}) is detected with S/N>5 in almost the whole FoV. Its velocity field is very similar to that of the stellar component (PA = 28°), with a semi-amplitude velocity of 154 km s^{-1} (see Table 5.3). The Hα flux is mainly oriented towards the galactic disc, indicating that this primary component is probably tracing a regular rotating gas disc. The flux is also enhanced in the direction of the bubble. As for the σ map of the primary component, it is rather homogeneous except in the FoV limits (due to a lower S/N), with values ≤250 km s^{-1}.

The secondary component spatially matches the full extension of the bubble, so it is probably gas associated to it. Indeed the Hα flux map shows a bubble-like structure along with receding velocities in the north-west direction. In the velocity map (see Fig. 5.12) we distinguish a receding and an approaching side, oriented at the same PA of the bubble (~123°). The velocity

dispersion is higher than the primary component in the whole extension ($\sigma < 200\,\mathrm{km\,s^{-1}}$ only in 10% of the spaxels). It is tracing the borders of the bubble, with lower values in the inner parts of it, which may indicate a hollow bubble, as the imaging data suggested (Kenney & Yale 2002; Masegosa et al. 2011).

Finally, we find a third component in the emission lines, present in the spaxels distributed elongated in the north-west direction, the same direction in which the bubble is extended. This component of the emission lines is generally narrow (average value of $135\,\mathrm{km\,s^{-1}}$), receding (redshifted) and with a filamentary structure. Its velocity dispersion is comparable to that of the primary component of the gas ($\sigma_{\mathrm{gas,N}}^{\mathrm{PSF}} \sim 100\,\mathrm{km\,s^{-1}}$, see Table 5.3), but with a very different morphology.

5.5   Discussion

The discussion is mainly focused on the kinematic maps that trace every component used to model the emission lines for all the galaxies, including NGC 1052 (see Chapter 4). In general, we find extended emission for all galaxies except for NGC 0315, which is unresolved (see Sect. 5.4). Including the results for NGC 1052 (see Chapter 4), we find at least two different kinematical components per emission line in six out of the eight objects (i.e. 66% of the sample). The secondary component is generally unresolved (i.e. contained in the PSF region), except for a few cases (NGC 1052, NGC 4438 and NGC 4750). We found a third component only for two galaxies: unresolved in NGC 1052 (see Chapter 4) and resolved in NGC 4438 (see Fig. 5.12 and Sects. 5.4.2 and 5.5.3). We detect a very broad component associated to the BLR for four LINERs, namely NGC 0315, NGC 1052, NGC 3226 and NGC 4750, that are discussed separately in Sect. 5.5.4. The flux maps of all galaxies, except for NGC 0266, NGC 4438 and NGC 4750, are centrally peaked and with no particular morphologies. Further discussion of these maps will be made when we estimate the line ratios, also accounting for the Hβ and [O III] lines (Hermosa Muñoz et al. in prep.).

We compare the results from the MEGARA data with the detection (or not) of outflows in our previous works in Sect. 5.5.1. Additionally, the kinematic maps show a big variety of morphologies and properties, that are individually discussed in Sects. 5.5.2 and 5.5.3. There are four targets with radio detections in the sample (namely NGC 0266, NGC 0315, NGC 1052 and NGC 4438; see Nagar et al. 2005; Hota et al. 2007; Baldi et al. 2018). There are two radio jets, for NGC 1052 that was already discussed in Chapter 4, and for NGC 0315, whose emission is barely resolved in our data and a possible correlation between the radio
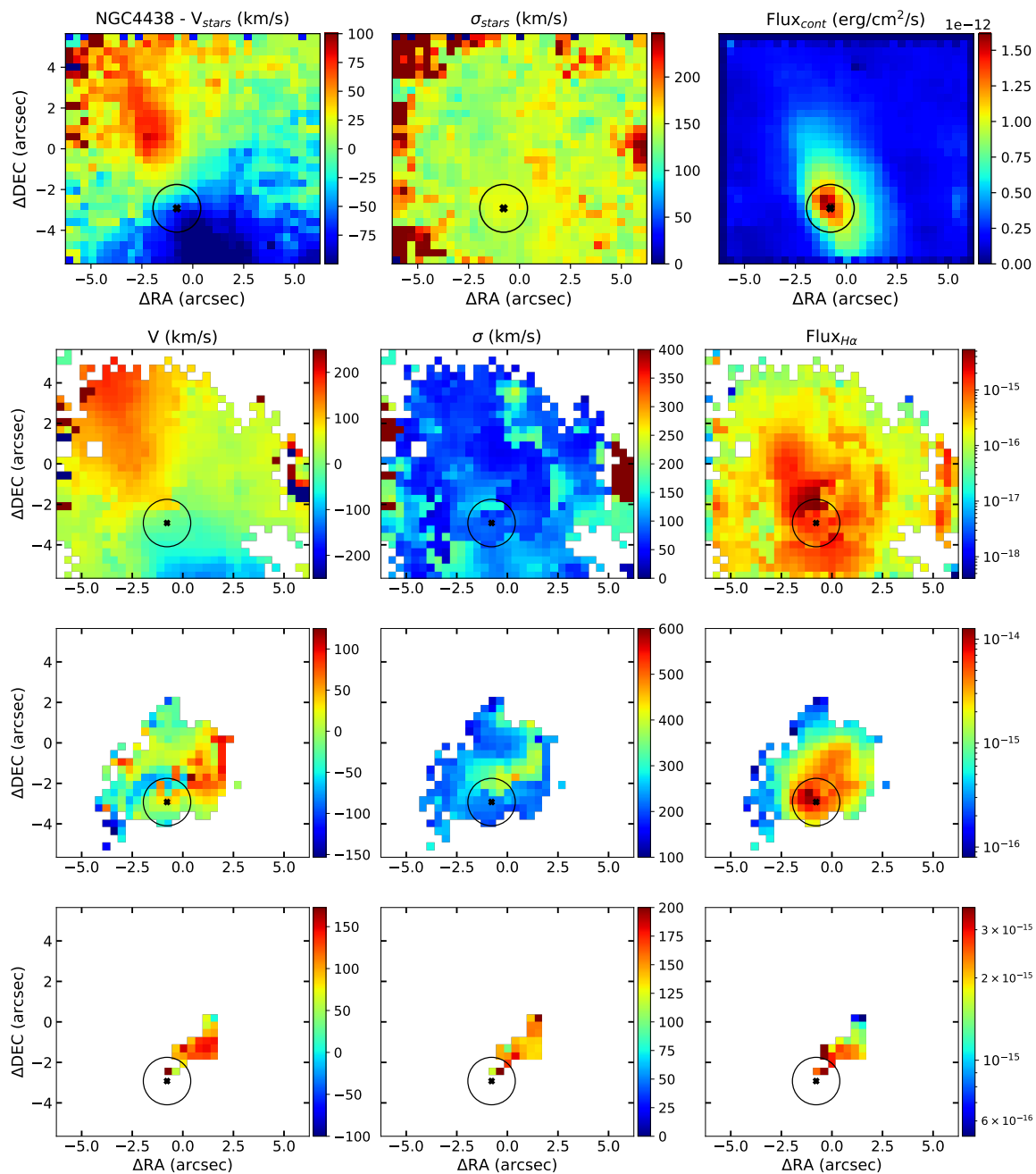
Fig. 5.12 Kinematic maps for the stellar (top panel) and ionised gas components. The spectra of this galaxy was modelled with a primary (second panel), a secondary (third panel) and a third (bottom panel) kinematical components per emission line. Full description in 5.4.

and ionised gas emission can not be explored. For NGC 0266 and NGC 4438 the detection is continuum radio emission, with no signatures of a radio jet, and will be discussed in Sects. 5.5.2 and 5.5.3, respectively.

There is, however, a particular feature that is common for three targets (NGC 1052, NGC 3226 and NGC 3245) in the velocity dispersion maps. That is an enhanced σ region with a 'butterfly'-like shape. For NGC 1052 (see Chapter 4), this feature was found in the direction of the major axis of the galaxy, and it was interpreted as a cocoon of low density, turbulent gas ionised by the AGN and by shocks. It is probably related to the ionised gas outflow in the galaxy, that is probed by the secondary component. However, for NGC 3226 and NGC 3245, this feature is perpendicular to the stellar major axis. Given that both galaxies also have a secondary component, interpreted as an outflow in the case of NGC 1052, it is likely that we are in a similar case, in which the high-σ region for these two objects is also a cocoon produced by an outflow, probed by the secondary component of the gas. For both NGC 3226 and NGC 3245, the secondary component can be consistent with an unresolved, compact outflow, given that their velocities are blueshifted (-91 and -214 km s^{-1}, respectively; see Table 5.3) and their widths are larger than for the primary component in the same spatial region (i.e. within the PSF; for NGC 3226: $\sigma_{\mathrm{gas,N}}^{\mathrm{PSF}}$ =136 vs $\sigma_{\mathrm{gas,S}}^{\mathrm{PSF}}$ =262 km s^{-1}; for NGC 3245: $\sigma_{\mathrm{gas,N}}^{\mathrm{PSF}}$ =154 vs $\sigma_{\mathrm{gas,S}}^{\mathrm{PSF}}$ =198 km s^{-1}). The determination of the energetics, properties and origin of these outflows will be analysed in a future work (Hermosa Muñoz et al. in prep.).

5.5.1 The view of MEGARA on the imaging and long-slit spectroscopic results

In this section we compare the results from the modelling of MEGARA data with our previous results from ground-based[4] long-slit spectroscopic data (Cazzoli et al. 2018 and Chapter 2) and from imaging data (Chapter 3)[5]. As mentioned in Sect. 5.2, all the targets were selected as they were candidates of having an outflow in our previous works Masegosa et al. (2011), Cazzoli et al. (2018) and Chapter 2, except for NGC 5055, that was observed within the MEGADES survey (Chamorro-Cazorla et al. in prep). Our past classification for each work is summarised in Table 5.4.

---

[4]These works analyse both ground-based and space-based nuclear spectra of the galaxies. As they derived differences on the results mainly due to the differing resolutions of the instruments, we will conservatively use here only the ground-based results to do a fair comparison with our (also ground-based) MEGARA data.

[5]This work includes the results from Pogge et al. (2000) and Masegosa et al. (2011)

Table 5.4 Classification of the components for each galaxy in our previous works: (2) Cazzoli et al. (2018), (3) and (4) Chapters 2 and 3, and (5) this chapter (C18, HM20, HM22 and This work, respectively). 'In/Outflow' indicates candidates of hosting an in/outflow, 'Rotation' indicates those for which the kinematical components were consistent with being produced by rotational motions, 'Candidate' indicates those candidates for non-rotational motions, 'Bubble', 'Core-halo' and 'Dusty' categories are defined in Chapter 3.

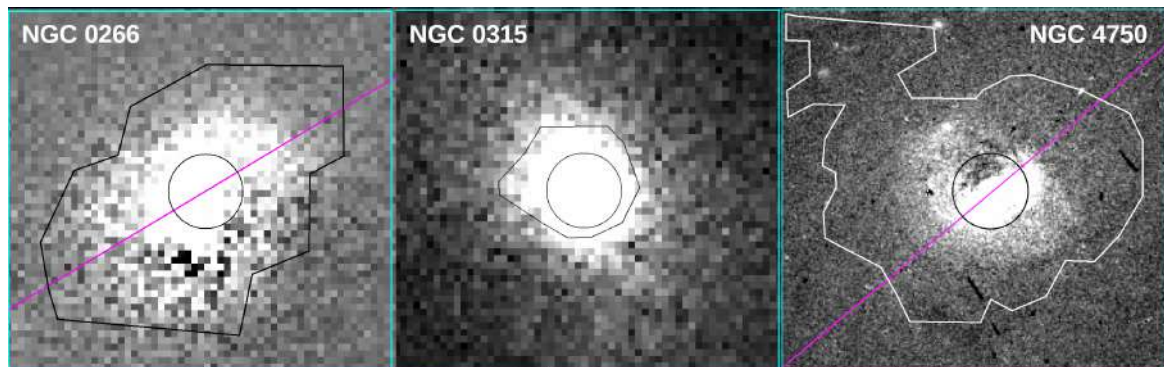| Galaxy	C18	HM20	HM22	This work
(1)	(2)	(3)	(4)	(5)
NGC 0266	Outflow	–	Bubble	Inflow(?)
NGC 0315	Outflow	–	Core-halo	Unresolved
NGC 1052	Outflow	–	Bubble	Outflow
NGC 3226	Outflow	–	Dusty	Outflow
NGC 3245	–	Rotation	Bubble	Outflow
NGC 4438	Rotation	–	Bubble	Outflow
NGC 4750	Candidate	–	Bubble	Outflow
NGC 5055	–	–	Core-halo	No outflow

Fig. 5.13 Comparison of the morphology of the primary component derived from the MEGARA data with the narrow band images of the Hα emission from Chapter 3 for NGC 0266, NGC 0315 and NGC 4750. The inner black circle indicates the PSF; the magenta line indicates the major axis of the stars for reference; and the large black (white for NGC 4750) contours are the profiles of the primary component. The images are cut to the FoV of MEGARA.

We have detected signatures of outflows using all the available data for NGC 1052, that was extensively discussed in Chapter 4, and for NGC 4750. For the rest of the targets there are some discrepancies among the analyses, as it is individually discussed below.

- For NGC 0266, there were signatures of the presence of an outflow with both long-slit spectroscopic and imaging data in our previous works, but the kinematics derived from the MEGARA data are discrepant. The morphology of the Hα emission seen from the primary (and unique) component from MEGARA data closely resembles that detected with the NOT narrow band images (see Fig. 5.13 and Chapter 3). With the NOT data, we observed the ionised gas distributed extended as a bubble oriented emerging north-west from the nucleus. With MEGARA data, we detect the same structure but with kinematic properties not characteristic of outflows (see Fig. 5.4). In the long slit spectroscopic data analysed in Cazzoli et al. (2018), they derived the presence of two kinematical components, being the secondary blueshifted and having a width consistent with an outflow ($v_{\mathrm{gas,S}}^{\mathrm{C18}} = -296 \pm 19\,\mathrm{km\,s^{-1}}$ and $\sigma_{\mathrm{gas,S}}^{\mathrm{C18}} = 475 \pm 50\,\mathrm{km\,s^{-1}}$). However, these components were modelled using the [O I] line instead of the [S II] line, as we use in our analysis of the MEGARA data, and intrinsic differences between the kinematics of both lines may produce discrepancies in the derived kinematics. In fact, this is what we detect, as with MEGARA a single component is sufficient to obtain a good fit of the emission lines. The width of this primary component detected with MEGARA and with the long-slit spectra are consistent, with a central value of $\sigma_{\mathrm{PSF,N}}^{\mathrm{MEGARA}} = 182 \pm 14\,\mathrm{km\,s^{-1}}$ and $\sigma_{\mathrm{gas,N}}^{\mathrm{C18}} = 165 \pm 17\,\mathrm{km\,s^{-1}}$, respectively.

  The maps from MEGARA show a perturbed velocity and a spiral-like Hα flux most likely produced by internal effects of the galaxy rather than by outflows. This galaxy is known to have a central bar (Epinat et al. 2008) that may be causing a gravitational torque and perturbing the gas (see Sect. 5.5.2).

- For both NGC 0315 and NGC 3226 there were hints of an outflow with the long-slit spectra but not with the imaging data. In the case of NGC 0315, the derived velocity dispersion for both the narrow and secondary components in the PSF of MEGARA data and with the ground-based long-slit spectroscopic data (for the [S II] lines) are consistent within 1σ errors ($\sigma_{\mathrm{gas,N}}^{\mathrm{C18}} = 88 \pm 5\,\mathrm{km\,s^{-1}}$ and $\sigma_{\mathrm{gas,S}}^{\mathrm{C18}} = 485 \pm 50\,\mathrm{km\,s^{-1}}$; for MEGARA $\sigma_{\mathrm{PSF,N}}^{\mathrm{MEGARA}} = 195 \pm 38\,\mathrm{km\,s^{-1}}$ and $\sigma_{\mathrm{PSF,S}}^{\mathrm{MEGARA}} = 480 \pm 120\,\mathrm{km\,s^{-1}}$; see Table 5.3). The 'outflow' classification in Cazzoli et al. (2018) was based on the width and the blueshifted velocities derived for the secondary component ($v_{\mathrm{gas,S}}^{\mathrm{C18}} = -209 \pm 148$ km s^{-1}), for which we contrarily find redshifted velocities ($v_{\mathrm{gas,S}}^{\mathrm{MEGARA}} = 96 \pm 77\,\mathrm{km\,s^{-1}}$) but indications of being an outflow, as mentioned in Sect. 5.5. In any case, this

secondary component is unresolved in the PSF region, explaining the general 'core-halo' morphology seen in the imaging data, with no other peculiar morphology (see Chapter 3).

In the case of NGC 3226, the outflow is probed by the unresolved, blueshifted secondary component in the MEGARA data. In Cazzoli et al. (2018), the secondary component was also broad ($\sigma_{\mathrm{gas,S}}^{\mathrm{C18}}$ ~620 km s^{-1}) and blueshifted (v$_{\mathrm{gas,S}}^{\mathrm{C18}}$ ~ -150 km s^{-1}), with a velocity consistent with the results from MEGARA data within 1.5σ, but differing in the velocity dispersion (consistent only within 4σ). This differences could be produced due to the use of the [O I] line to model the remaining emission lines for the long-slit spectrum instead of the [S II] lines as we did with MEGARA data, given that they fell in the limits of the wavelength range (see Fig. B7 in Cazzoli et al. 2018). As mentioned in the case of NGC 1052, these two emission lines can show very different kinematics if they are formed in different regions of the NLR, with the [S II] kinematics resembling more that of Hα, whereas the [O I] behaved really different. In the imaging data this outflow component could not be detected as it is located within the PSF (as for NGC 0315), with no particular features in the Hα flux with respect to the primary component. It was classified as 'Dusty' instead of 'Bubble' in Chapter 3 as there is a dust lane located eastward from the centre (see sharp-divided image in Fig. 2 from Masegosa et al. 2011), despite the innermost contours of the image show a similar morphology than the Hα emission of the secondary component in MEGARA data (see Fig. 2 in Masegosa et al. 2011).

- For both NGC 3245 and NGC 4438, they were classified as outflow candidates based on the imaging morphology ('Bubble' in Chapter 3), whereas the kinematics of the two components derived from the long-slit spectroscopic data were explained with rotational movements in Chapter 2 and Cazzoli et al. (2018), respectively. The case of NGC 4438 will be further discussed in Sect. 5.5.3.

  For NGC 3245, the Hα emission in Masegosa et al. (2011) was extended in the north-south direction, aligned with the slit used with the Palomar spectroscopic data in Chapter 2. The orientation and extension of the ionised gas in the imaging data is consistent with the primary component derived in the MEGARA data. The analysis of the Palomar spectroscopic data derived a secondary component in the emission lines, rather narrow compared with the typical values for the secondary component in the other objects from the sample ($\sigma_{\mathrm{gas,S}}^{\mathrm{HM20}}$ of 136±21 km s^{-1}), and redshifted (94±17 km s^{-1}). However, in the MEGARA data this secondary component is barely resolved out of the PSF, being generally blueshifted (-214±142 km s^{-1}) and with a consistent width

with the long-slit data (198±172 km s^{-1}). In general, the kinematics of the narrow and secondary component are very similar to that of NGC 3226, as was previously discussed (see Sect. 5.5). The most likely origin of the secondary component is an outflow that is producing perturbed kinematics in the primary component found in the emission lines.

- NGC 4750 was classified as a candidate for having an outflow with long-slit spectroscopic data in Cazzoli et al. (2018), based on the kinematics derived from the [O I] line. They found two kinematical components in the emission lines, with the primary being explained with rotational movements, and the secondary, blueshifted ($v_{gas,S}^{C18} = -296\pm21$ km s^{-1}), broad ($\sigma_{gas,S}^{C18} = 380 \pm 42$ km s^{-1}) component as a possible outflow. For our MEGARA data, the secondary component is barely resolved out of the PSF in a bubble-like morphology emerging westwards from the centre up to ~2.5". It is blueshifted (average $v_{gas,S}^{MEGARA} = -92\pm50$ km s^{-1}) and has a average width of 297±41 km s^{-1} (see Table 5.3), consistent with the derived value in Cazzoli et al. (2018).

  The imaging data from Chapter 3 reveals a similar morphology of the Hα gas in the MEGARA data, with a enhanced region ~4" north-east from the centre, corresponding to a star forming region that is less spatially resolved in MEGARA data than in the HST image (see Fig. 5.13). It was classified as a 'Bubble' considering the peculiar morphology of the innermost contours of the HST image (see Fig. 7 in Appendix 2) that, however, are only partially oriented towards the same direction as the secondary component (emerging south-west vs the bubble emerging west). Considering the morphological and the kinematical signatures, this secondary component is likely tracing the emission from a compact, ionised outflow.

- For NGC 5055, we have no prior kinematical information in our works, but we have a morphological classification of the Hα gas as 'Core-halo' in Chapter 3. The Hα ionised gas in the imaging data (see Fig. 2 in Masegosa et al. 2011) is concentrated around the nucleus, where we also see a centrally peaked flux with MEGARA. This galaxy is a spiral system with both spiral arms and star forming regions falling within the MEGARA and HST FoV. The apparent asymmetry in the flux and velocity dispersion maps may be caused by the strong dust features produced by the spiral arms, that are more prominent to the south as already seen in Masegosa et al. (2011), partially obscuring the nuclear region. The star forming regions are proved by the enhanced Hα-flux regions at ~2.5" north-east and ~3" south-west from the centre in the MEGARA

flux map, corresponding to low σ in the corresponding map ($< 50\,\mathrm{km\,s^{-1}}$; see Fig. 5.10). These were reported as an extended emission at a PA$\sim$30° in Masegosa et al. (2011).

In general, considering the velocity map of the primary component, the detected ionised gas emission is more likely associated to a regular gas disc than to non-rotational motions.

5.5.2   Peculiar morphologies of the ionised gas of NGC 0266 and NGC 4750

The two galaxies for which the narrow, primary component shows the most peculiar maps are NGC 0266 and NGC 4750. The ionised gas of NGC 0266 is distributed in the nort-west to south-east direction, such that the Hα flux is more prominent in a spiral-like shape corresponding to a nearly non-rotating region on the primary component velocity, and co-spatial with an enhanced region in the velocity dispersion map. This structure resembles the inner structure ($\leq$100 pc) of the molecular gas of NGC 1808 studied in Audibert et al. (2021). They detected a spiral structure decoupled of the disc kinematics, at a different PA (ΔPA $\sim$ 30°), seen with various tracers both in molecular gas (CO(3-2), HCN(4-3), HCO$^+$(4-3) and CS(7-6)) and with near-infrared IFU data (Busch et al. 2017), consistent with an inflow of gas towards the nucleus (see Fig. 13 in Audibert et al. 2021). This kind of perturbed morphologies have already been seen for other objects (see e.g. Audibert et al. 2019). There are no hints of this galaxy hosting a jet that could be related to the ionised gas, producing the perturbed morphologies, although there is a detection of compact radio emission (Nagar et al. 2005). If we are in the same scenario as for NGC 1808, then the gas here would be driven inwards thanks to the bar in this galaxy (Epinat et al. 2008), and thus the ionised gas would be tracing an inflow.

For NGC 4750 the narrow, primary component of the ionised gas is distributed along the FoV with peculiar kinematical maps (see Fig. 5.9). This galaxy has strong dust lanes from the spiral arms (see e.g. Carollo et al. 2002). The velocity dispersion map is distributed in a spiral-like shape, bordering southward and northward the regions of lowest and highest velocities, respectively. This enhanced-σ region is not co-spatial with the secondary component, that traces the outflow (see Sect. 5.5.1). This peculiar morphology of the primary component may have been produced by the outflow, as for the cases of NGC 1052, NGC 3226 and NGC 3245 (see Sect. 5.5). In this case, the gas could have been perturbed by the emission of the outflow, enhancing the velocity dispersion in the regions of homogeneous velocities. This hypothesis could be further tested once we characterise the properties of the outflowing gas (Hermosa Muñoz et al. in prep.).

5.5.3 The bubble in NGC 4438

NGC 4438 is the only galaxy in our sample (except for NGC 1052, see Chapter 4) for which we resolve three different kinematical components in all the analysed emission lines. The narrowest component is tracing the gas disc, with a regular rotational pattern, a relatively homogeneous σ, and the Hα flux oriented similarly to the disc. However, the secondary and third component are most likely related to the Hα bubble detected in this galaxy, as hinted by its morphology and kinematics.

Kenney & Yale (2002) studied Hα narrowband images of this LINER, as so did afterwards Masegosa et al. (2011), characterising a prominent ionised gas bubble emerging north-west from the nucleus. Its projected length was estimated to be 1 kpc and, despite it was classified as a bipolar outflow, one bubble is more visible north-west of the nucleus, probably due to intrinsic differences in the ISM in the two sides of the galaxy (Kenney & Yale 2002).

The Hα flux derived from the MEGARA data and the previous narrow band images clearly map the bubble emerging from the nucleus (see Sect. 5.4.2 and Fig. 1.5). The velocity map derived for the secondary component in MEGARA data indicates that we are looking at the receding (i.e. redshifted) part of the bubble, whereas the approaching (i.e. blueshifted) part is on the south-east direction, barely detected in our data. The velocity dispersion in the borders of the bubble reaches larger values than for the inner parts (average $\sigma_{gas,S}^{MEGARA}$ ~340 vs ~220 km s^{-1}; see Fig. 5.12). All these kinematical properties and also the morphology of this component are consistent with an outflow. The previous spectroscopic analysis of this object with long-slit spectroscopy did not find strong evidences of an outflow (Cazzoli et al. 2018). It is explained with the fact that the slit was oriented perpendicular to the outflow, so it could not be traced (PA$_{slit}$ = 39° vs PA$_{Bubble}$ ∼ 141°).

Given that the third component in the MEGARA data is oriented in the direction of the outflow (PA~127°), its origin seem also connected to it. In fact it is coincident with the north-western side of the bubble, traced with high-σ by the secondary component, but with differing kinematics. This component is mainly redshifted (v$_{gas,T}^{MEGARA}$ >50 km s^{-1}), but narrower than the secondary component (average $\sigma_{gas,T}^{MEGARA}$ of 135 km s^{-1}). This galaxy has a double-lobed radio continuum source oriented in a similar direction to that of the bubble (PA∼ 125° Hota et al. 2007). The extension of this double-lobed radio emission was estimated to be ~250 pc west and ~730 pc east from the nucleus (Hota et al. 2007). This is consistent with the estimated size of the outflow in the west direction (~300 pc), as extended as the third component in the MEGARA data. In fact Kenney & Yale (2002) confirmed the co-spatiality between this radio emission and the outer ends of the Hα bubble, initially associating the borders of the ionised gas bubble to shocks produced by the interaction of

the radio emission with the ISM as already suggested by Hota et al. (2007), despite a radio jet has not been detected. The X-ray emission was also found to be co-spatial with the ionised gas (Machacek et al. 2004). Considering all the evidences and the kinematics of the third component derived with MEGARA data, it may be tracing the optical counter-part of the radio emission. We will further test this hypothesis by deriving the line ratios and the energetics of the outflow (Hermosa Muñoz et al. in prep.).

5.5.4 The BLR component in LINERs

We found in our data that a very broad component reproduced better the Hα emission line for four LINERs. These detections can be compared with the two previous works searching for this BLR-component based on 1D spectroscopic data in type-1.9 and type-2 LINERs, that are Cazzoli et al. (2018) and Chapter 2, respectively. In particular, Cazzoli et al. (2018) studied six LINERs from our sample, namely NGC 0266, NGC 0315, NGC 3226, NGC 4438 and NGC 4750, and NGC 3245 is studied in Chapter 2. They compare the detections (or non-detections) with previous works in the literature (see e.g. Ho et al. 1997a; Barth et al. 2001; Walsh et al. 2013; Balmaverde & Capetti 2014; Constantin et al. 2015). The only object not included in these works is NGC 5055, for which we do not find a detection of a BLR component in our MEGARA data.

Cazzoli et al. (2018) found a very broad component in Hα for two objects: NGC 0315 (with both ground- and space-based observations) and NGC 4750 (with ground-based data). Similarly, we detected a BLR component for NGC 0315 and NGC 4750 with the following widths: $\text{FWHM}_{\text{MEGARA}} = 2655 \pm 360\,\text{km s}^{-1}$ and $\text{FWHM}_{\text{MEGARA}} = 2188 \pm 300\,\text{km s}^{-1}$, respectively. In Cazzoli et al. (2018), the derived width for NGC 0315 is $\text{FWHM}_{\text{C18}} = 2475 \pm 495\,\text{km s}^{-1}$, which are consistent within the 1σ error, and with results from previous works ($\text{FWHM} \sim 2600$, see Balmaverde & Capetti 2014; Constantin et al. 2015 and Table 5.5). For NGC 4750, the derived width in Cazzoli et al. (2018) is $\text{FWHM}_{\text{C18}} = 2367 \pm 106\,\text{km s}^{-1}$, and the only other detection of this component in previous works comes from Ho et al. (1997a) with $\text{FWHM} \sim 2200\,\text{km s}^{-1}$, being both values consistent with ours within the 1σ error (see Table 5.5).
As in Cazzoli et al. (2018), despite NGC 0266 is a type-1.9 AGN, with ground-based data we do not detect a BLR component (it is however detected in Ho et al. 1997a).
In contrast to Cazzoli et al. (2018), we detect a very broad component for NGC 3226 (also detected in Ho et al. 1997a) with a FWHM of $2305 \pm 153\,\text{km s}^{-1}$ and an integrated velocity of $269 \pm 20\,\text{km s}^{-1}$.

Table 5.5 Properties of the BLR component of the LINERs in comparison to previous detections. Columns indicate: (1) object; (2), (3), (4), (5), (6) and (7) the FWHM of the BLR component in km s^{-1} in this Chapter, Cazzoli et al. (2018), Chapter 2, Ho et al. (1997a); Balmaverde & Capetti (2014); Constantin et al. (2015), respectively. $^{(*)}$ indicates the targets for which we selected the ground-based spectral fit to the BLR component in Cazzoli et al. (2018). The [] symbols indicate when the BLR fit is not well constrained.

Galaxy	FWHM$_{MEGARA}$ (km s^{-1})	FWHM$_{C18}$ (km s^{-1})	FWHM$_{HM20}$ (km s^{-1})	FWHM$_{H97}$ (km s^{-1})	FWHM$_{B14}$ (km s^{-1})	FWHM$_{C15}$ (km s^{-1})
(1)	(2)	(3)	(4)	(5)	(6)	(7)
NGC 0266	–	–	–	1350	–	–
NGC 0315$^{(*)}$	2655±360	2475±495	–	2000	2590	2870
NGC 1052	2350±470	2916±52	–	1950	2240	2800
NGC 3226	2305±153	–	–	2000	–	–
NGC 3245	–	–	2350±14	–	–	4300
NGC 4438	[1980±350]	–	–	2050	–	–
NGC 4750	2188±300	2367±106	–	2200	–	–
NGC 5055	–	–	–	–	–	–

For NGC 4438 the presence of a BLR component is uncertain in MEGARA data, as it was in the modelling of the nuclear spectrum in Cazzoli et al. (2018). In our data, the inclusion of this component improves the χ^2 of the fit <10% for the majority of the spaxels in the PSF (maximum improvement of 30%), with respect to the typical improvement in the other galaxies (always >15%, maximum improvement of >50%). If present, its properties would be a FWHM of 1980±350 km s^{-1} consistent with that detected in Ho et al. (1997a), and an average velocity of 88±36 km s^{-1} (see Table 5.5).

In Chapter 2, a BLR component was present on the HST nuclear spectrum of NGC 3245, although it could not be resolved in the ground-based spectra of the Palomar Survey due to differing spatial resolutions. The same occurs with the MEGARA data, as we did not detect a very broad component in the Hα emission line.

Summarising, we have found consistent results with previous ground-based detected broad components for the majority of type-1.9 LINERs (~60%), and with no detection for the type-2 LINER NGC 3245. The non-detections with the ground-based data of a BLR component in type-1.9 LINERs, as mentioned in Chapter 2, could be a consequence of the low intensity of this AGNs, whose BLR can be diluted if seen with relatively low spatial resolution (due to the long-slit aperture and the spaxel size).

5.6   Summary and future work

In this chapter, we analyse the optical IFS data of eight LINERs observed with MEGARA/GTC with its low resolution mode (R~6000) in different wavelength bands (LR-R, LR-V, LR-B). Prior to the study of the ionised gas properties, a subtraction of the stellar component of the galaxies is required. For that we applied a ᴘPXF modelling (Cappellari & Copin 2003; Cappellari 2017) to the combined data cubes of LR-R and LR-V when both were available (7 LINERs, see Sect. 5.3). After the stellar subtraction we obtained the spectra of the ISM and applied a kinematical decomposition of the optical ionised emission lines available in the wavelength range of each VPH. We used the [S II] lines as reference for modelling the rest of the emission lines as in previous works (Cazzoli et al. 2018; Hermosa Muñoz et al. 2020; Cazzoli et al. 2022).

We derived the kinematical maps from both stellar and gas components per each galaxy (see Sect. 5.4. The stellar component generally is rotating with a regular pattern, with a centrally peaked-σ map, except for NGC 0266 and NGC 0315. In contrast, the ionised gas shows a complex behaviour in our objects, with at least two kinematical components in the majority of the LINERs (75%) and a broad component associated to the BLR in a 50% of them. For two objects, namely NGC 0266 and NGC 5055 we detect a single component in the emission lines that can be explained by an inflow induced by the large-scale bar and by rotational motions of the ionised gas, respectively. For three objects, namely NGC 1052, NGC 3226 and NGC 3245, the primary component has a symmetric rotational pattern, but with a peculiar σ. They have an enhanced-σ region perpendicular (parallel) to the stellar major axis in NGC 3226 and NGC 3245 (NGC 1052) with a 'Butterfly' -like shape. This region is probably triggered by the secondary component, which is typically blueshifted and broad (average $\sigma_S \sim 200 \, \mathrm{km \, s^{-1}}$) explained as an outflow (compact for NGC 3226 and NGC 3245) that produces an expansion of the gas. Finally for NGC 4438 and NGC 4750, we detected a secondary component with a bubble-like shape emerging north-west and west from the centre, respectively, with kinematical properties consistent with being an outflow. For NGC 4438 we also detected a third component that is oriented in the same direction and co-spatial with the outflow and a double-sided radio continuum emission, suggesting that this could be the optical component of the radio emission. Although a jet has not been detected in this galaxy, the energetics will allow us to know if this third component is a part of the outflow or if it is related to the doubled-lobed radio emission.

All the galaxies in our sample were candidates of hosting an outflow from our previous analyses using both imaging and long-slit spectroscopic data (see Cazzoli et al. 2018, Chapters 2 and 4). The MEGARA data has higher spectral resolution than our previous analysis of

the optical spectra, and traces spatially the central regions of our targets. This new analysis allowed us to confirm the presence of outflows for the majority of the sample (five objects accounting with NGC 1052, i.e. ~55% of the sample). Our results have allowed us to characterise and unify all the results coming from various techniques, finding the existence of outflows, mainly nuclear and unresolved for the majority of the LINERs. This reinforces the results from Chapter 3 about outflows being common also in LINERs, and that they can be detected with less time consuming techniques than IFS.

As a future work we will derive the line ratios to understand the ionisation source of each emission, supported with the results from the analysis of the LR-B and HR-R data cubes, which is ongoing (Hermosa Muñoz et al. in prep.). We will estimate the properties of the detected outflows following the expressions in Sect. 1.2 to derive their mass rates, energetics and power, to disentangle their origin and fully characterise them. Additionally, we will study the NaD absorption lines to see if their emission could be related to the ionised gas outflows but tracing its neutral phase (Hermosa Muñoz et al. in prep.).

Chapter 6

Conclusions

In this thesis we have presented studies aimed at constraining for the first time the question of how common are outflows in low luminosity AGNs, in particular searching systematically in LINERs. All the data analysed here are based on long-slit spectroscopy from STIS/HST and the Double Spectrograph/Palomar Survey (Ho et al. 1995), narrow and broad band images from ALFOSC/NOT and HST (Pogge et al. 2000; Masegosa et al. 2011), and integral-field spectroscopic data from MUSE/VLT and MEGARA/GTC. The main conclusions of this thesis are listed below:

- **Optical spectroscopy of type-2 LINERs**: In Chapter 2 (Hermosa Muñoz et al. 2020), we presented a kinematic analysis of the optical emission lines produced by the ionised gas of nine type-2 LINERs, based on ground- (Palomar) and space-based (STIS/HST) spectroscopic data. We performed a kinematical decomposition of the emission lines in the search for: (i) a broad component associated to the BLR in the Balmer lines (Hα), and (ii) hints of outflows as a broad ($\sigma \leq 400\,\mathrm{km\,s^{-1}}$), blueshifted component.

  Our main results indicate that 67% LINERs analysed with the STIS/HST have a BLR component. For three targets (NGC 3245, NGC 4594 and NGC 4736) this component had already been discovered by Constantin et al. (2015), with similar values of flux and FWHM. However, only 25% objects with data from the Palomar survey needed that BLR component. Our study hence highlights the importance of the spatial resolution to detect such an intrinsically faint component in these low-luminosity AGNs. It may not be detected if the starlight from the host galaxy contaminates the pure emission from the nucleus, preventing a correct classification of these LINERs. For the galaxy NGC 4594 we found a BLR component both in the ground- and space-based spectroscopic data, so we proposed its reclassification as a type-1 LINER.

The analysis of the nine LINERs revealed the presence of ionised gas in all the targets consistent with rotational motions, and an additional component of the gas for three and four LINERs in the ground- and space-based data, respectively. For the galaxies NGC 4486 and NGC 4594, both the velocity and velocity dispersion of this component suggest a non-rotational origin, most probably produced by an outflow. Its FWHM is similar to that found for other LINERs, also candidates of hosting an outflow (for type-1.9 Cazzoli et al. 2018).

- **A search for ionised gas outflows in an Hα imaging atlas of nearby LINERs**: Outflows are believed to be ubiquitous within the AGN population, but the total number of LINERs analysed in Chapter 2 was not large enough for any statistically significant conclusion. In Chapter 3 (Hermosa Muñoz et al. 2022) we performed a systematic search for outflows through the analysis of Hα narrow band images with ALFOSC/NOT data of 70 nearby LINERs, classifying the ionised gas morphologies into four main categories. The detection rate of outflows, detected as extended, filamentary or bubble-like gas ('Bubble') is ~32%. The remaining objects were classified as: ~29% with compact circumnuclear gas ('Core-halo'), ~21% with gas along the disc or spiral arms ('Disky'); and there were dust lanes obscuring the central emission for ~11% ('Dusty'). Finally for ~7% of the galaxies the morphological classification was unclear ('Unclear').

  We complemented the imaging data with kinematical data available in the literature for the same targets to confirm (or not) the outflow candidates. We found data for 60 out of the 70 LINERs; among them, 48% had a kinematically identified outflow. Our main result is that at least 1 out of every 3 LINERs in the nearby Universe (z < 0.025) may host an outflow.

  By comparing the results from the morphological classification with those from the kinematical information, we found that a morphological identification of outflows could be affected by orientation effects (less detection probability for the 'Disky' morphology) or by the compactness of the circumnuclear gas ('Core-halo').

  We compared the ionised gas with the soft X-ray emission for 54 targets with available data. We found a correlation in both emissions for ~60% of the LINERs, which suggest a common origin for the ionised and hot gas, as already proposed for more luminous AGNs (Bianchi et al. 2006, 2019b). There was no correlation between the spatial coincidence of both and spectroscopically-confirmed outflows.

- **Unexplored outflows in nearby low luminosity AGNs: The case of NGC 1052**: We followed up the most promising candidates of hosting an outflow by performing a

systematic, spectroscopic analysis in Chapters 4 and 5. We obtained optical IFS data for nine LINERs using MEGARA/GTC and (in one case) MUSE/VLT. Our exploration started with the analysis with the prototypical LINER NGC 1052, which is shown in Chapter 4 (Cazzoli et al. 2022).

The ionised gas in NGC 1052 is extended as a large-scale structure in the polar direction up to ~30″ (~3.3 kpc). We found hints of a bipolar outflow propagating in a region of gas with enhanced turbulence (the 'butterfly'region) and triggering kpc-scale bubbles (referred to as 'polar emission'). Given the derived energetics, the outflow is likely powered by the jet, although some contribution from the AGN is possible. We detected an additional gas component unresolved (inside the PSF region) in both MUSE and MEGARA data.

We also mapped the optically thick neutral gas in the search for the outflow in its neutral gas phase. The velocity field is consistent with a slow rotating disc, whereas the hints of a neutral gas outflow are weak, with a tentative identification in our work.

We confirmed its nature as a type 1.9 LINER with the detection of a BLR component with FWHM of 2427 ± 332 and $2350 \pm 470 \, \text{km s}^{-1}$ for MUSE and MEGARA data, respectively.

- **The MEGARA view of outflows in LINERs**: We analysed the remaining eight LINERs with MEGARA/GTC data in Chapter 5, finding a large variety of morphologies in the gas (traced by different kinematical components). We found at least two components in 75% of the sample and a broad component associated to the BLR in 50%. For NGC 0266 and NGC 5055 we only found one component in the emission lines, with peculiar morphologies for the first one produced by an inflow. For NGC 3226 and NGC 3245 the primary component has regular rotating maps but a central, enhanced σ with a 'Butterfly' shape, probably triggered by an outflow probed by the secondary component in the emission lines of these galaxies (similar to what was found for NGC 1052). For NGC 4438 and NGC 4750 we also found a secondary component with kinematical properties and a bubble-like morphology consistent with an outflow. Additionally for NGC 4438 we found a third component co-spatial with the outflow, interpreted as the optical counterpart of the double-lobed radio emission.

In general, our new analysis, based on IFS data, confirmed the existence of an outflow for the majority of the sample (5/9 including NGC 1052, i.e. 55%) as a generally blueshifted, broad component in the emission lines. Our results have allowed us to characterise and unify all the results coming from the various techniques presented in this thesis, finding the existence of outflows, mainly nuclear and unresolved for

the majority of LINERs. In one hand this agrees with and reinforces the results from Chapter 3 about outflows being common also in LINERs. On the other hand, our results indicate that less time consuming techniques than IFS may be used to detect and quantify outflows in LINER hosts, hence facilitating the study of large samples of LINERs with the required spectroscopic approach.

Chapter 7

Conclusiones

En esta tesis hemos presentado estudios destinados a restringir por primera vez la cuestión de cuán comunes son los 'outflows' en AGNs de baja luminosidad, en particular buscando sistemáticamente su presencia en LINERs. Todos los datos analizados se basan en espectroscopía de rendija larga de STIS/HST y del Double Spectrograph/Palomar Survey (Ho et al. 1995), imágenes de banda estrecha y ancha de ALFOSC/NOT y HST (Pogge et al. 2000; Masegosa et al. 2011), y datos espectroscópicos de campo integral de MUSE/VLT y MEGARA/GTC. Las principales conclusiones de esta tesis se enumeran a continuación:

- **Espectroscopia óptica de LINERs de tipo 2**. En el Capítulo 2 (Hermosa Muñoz et al. 2020), presentamos un análisis cinemático de las líneas de emisión ópticas producidas por el gas ionizado para nueve LINERs de tipo 2. Nos hemos basado en datos espectroscópicos tomados desde tierra (Palomar) y desde el espacio (STIS/HST). Realizamos una descomposición cinemática de las líneas de emisión en busca de: (i) una componente ancha asociada a la BLR en las líneas de Balmer (Hα), y (ii) indicios de 'outflows' como una componente ancha ($\sigma \leq$,400 km s^{-1}) desplazada hacia el azul.

  Nuestros principales resultados indican que para el 67% de los LINERs analizados con el STIS/HST se detecta una componente perteneciente a la BLR. Para tres objetos (NGC 3245, NGC 4594 y NGC 4736) esta componente ya había sido descubierta por Constantin et al. (2015), con valores similares de flujo y FWHM. Sin embargo, sólo el 25% de los objetos con datos del Palomar necesitaban esa componente producida en la BLR. Nuestro estudio destaca la importancia de la resolución espacial para detectar una componente tan intrínsecamente débil en estos AGN de baja luminosidad. Es posible que no se detecte si la luz estelar de la galaxia anfitriona contamina la emisión pura del núcleo, impidiendo una clasificación correcta de estos LINER. En el caso de la

galaxia NGC 4594 encontramos un componente producida en la BLR tanto en los datos espectroscópicos de tierra como de espacio, por lo que proponemos su reclasificación como LINER de tipo 1.

El análisis de los nueve LINERs reveló la presencia de gas ionizado en todos los objetos consistente con movimientos rotacionales, y encontramos una componente adicional del gas para tres y cuatro LINERs en los datos de tierra y de espacio, respectivamente. En el caso de las galaxias NGC 4486 y NGC 4594, tanto la velocidad como la dispersión de la velocidad de esta componente sugieren un origen no rotacional, probablemente producido por un 'outflow'. Su FWHM es similar al encontrado para otros LINERs, también candidatos a albergar 'outflows' (para tipos 1.9 ver Cazzoli et al. 2018).

- **Búsqueda de 'outflows' en gas ionizado en un atlas de imágenes Hα de LINERs cercanos**. Se cree que los 'outflows' son omnipresentes en todos los AGN, pero el número total de LINERs analizados en el Capítulo 2 no es lo suficientemente grande como para llegar a una conclusión estadísticamente significativa. En el Capítulo 3 (Hermosa Muñoz et al. 2022) realizamos una búsqueda sistemática de 'outflows' mediante el análisis de imágenes de banda estrecha en Hα con datos ALFOSC/NOT de 70 LINERs cercanos, clasificando las morfologías del gas ionizado en cuatro categorías principales. La tasa de detección de 'outflows', vistos como gas extendido, filamentoso o en forma de burbuja ('Bubble') es del ~32%. Los objetos restantes se clasificaron como: ~29% de objetos con gas compacto alrededor del núcleo ('Core-halo'), ~21% con gas situado a lo largo del disco o de los brazos espirales ('Disky'); y había bandas de polvo oscureciendo la emisión central en ~11% ('Dusty'). Por último, la clasificación morfológica del 7% de las galaxias no estaba clara ('Unclear').

  Complementamos los datos de las imágenes con datos cinemáticos disponibles en la literatura para los mismos objetos con el fin de confirmar (o no) los candidatos a 'outflows'. Encontramos datos para 60 de los 70 LINER; de ellos, el 48% tenía un 'outflow' identificado cinemáticamente. Nuestro principal resultado es que al menos 1 de cada 3 LINERs en el Universo cercano (z < 0,025) puede albergar un 'outflow'.

  Al comparar los resultados de la clasificación morfológica con los de la información cinemática, descubrimos que la identificación morfológica de los 'outflows' podría verse afectada por efectos de orientación (menor probabilidad de detección para la morfología 'Disky') o por la compacidad del gas cercano al núcleo ('Core-halo').

  Comparamos el gas ionizado con la emisión de rayos-X blandos para 54 objetos con datos disponibles en la literatura. Encontramos una correlación en ambas emisiones para el ~60% de los LINERS, lo que sugiere un origen común para el gas ionizado y

el gas caliente, como ya se había propuesto para AGNs más luminosos (Bianchi et al. 2006, 2019b). No encontramos ninguna correlación entre la coincidencia espacial de ambas emisiones y la existencia de 'outflows' confirmados espectroscópicamente.

- **'Outflows' inexplorados en AGNs cercanos de baja luminosidad: El caso de NGC 1052**. Hemos realizado un seguimiento de los candidatos más prometedores a albergar un 'outflow' mediante un análisis sistemático y espectroscópico en los Capítulos 4 y 5. Obtuvimos datos ópticos de IFS para nueve LINERs utilizando MEGARA/GTC y (en un caso) MUSE/VLT. Nuestra exploración comenzó con el análisis del LINER NGC 1052, que se estudia en el Capítulo 4 (Cazzoli et al. 2022).

  El gas ionizado en NGC 1052 se extiende en una estructura a gran escala en la dirección polar alcanzando distancias de $\sim 30''$ (~ 3.3 kpc). Encontramos indicios de un 'outflow' bipolar que se propaga en una región de gas de gran turbulencia (la llamada 'Butterfly') y que desencadena la emisión de burbujas a escala de kpc (denominadas 'emisión polar'). Dada la energía estimada del 'outflow', es probable que esté impulsado por el 'jet' detectado en radio frecuencias, aunque no se descarta que haya alguna contribución del AGN. Detectamos una componente de gas adicional no resuelta (dentro de la PSF) tanto en los datos de MUSE como de MEGARA.

  También mapeamos el gas neutro en la búsqueda de una correspondencia del 'outflow' en gas ionizado pero en su fase de gas neutro. El campo de velocidad es consistente con un disco en rotación lenta, mientras que los indicios de un'outflow' son débiles, con solamente una identificación tentativa en nuestro trabajo.

  Confirmamos su naturaleza como un LINER de tipo 1.9 con la detección de una componente producida en BLR con FWHM de 2427 ± 332 y 2350 ± 470 km $^{-1}$ para los datos de MUSE y MEGARA, respectivamente.

- **El punto de vista de MEGARA sobre los 'outflows' en LINERs**. Analizamos los ocho LINERs restantes con datos de MEGARA/GTC en el Capítulo 5, encontrando una gran variedad de morfologías en el gas ionizado (trazadas por diferentes componentes cinemáticas). Encontramos al menos dos componentes en el 75% de la muestra y una componente ancha asociada a la BLR en el 50%. En el caso de NGC 0266 y NGC 5055 sólo encontramos una componente por línea de emisión, con morfologías peculiares para la primera galaxia debidas a un 'inflow'. Para NGC 3226 y NGC 3245 la componente primaria presenta mapas de rotación regulares pero una dispersión de velocidad central ensanchada con forma de 'Butterfly', probablemente provocada por un 'outflow'. Este estaría caracterizado por la componente secundaria de las líneas de emisión (similar a lo encontrado para NGC 1052). Para NGC 4438 y NGC 4750

encontramos también una componente secundaria con una morfología de burbuja y propiedades cinemáticas consistentes con un 'outflow'. Además, en el caso de NGC 4438 encontramos una tercera componente que es co-espacial con el 'outflow', que interpretamos como la contrapartida óptica de la emisión de radio detectada en forma de doble lóbulo.

En general, nuestro nuevo análisis basado en los datos del IFS, confirmó la existencia de un 'outflow' para la mayoría de la muestra (5/9 incluyendo NGC,1052, es decir, el 55%) como una componente ancha y generalmente desplazada al azul en las líneas de emisión. Nuestros resultados han permitido caracterizar y unificar todos los resultados procedentes de las distintas técnicas presentadas en esta tesis, encontrando la existencia de 'outflows' principalmente nucleares y no resueltos, para la mayoría de los LINERs. Por un lado, esto concuerda y refuerza los resultados del Capítulo 3 sobre que los 'outflows' son comunes también en los LINERs. Por otro lado, nuestros resultados indican que se pueden utilizar técnicas que consuman menos tiempo de observación que la IFS para detectar y cuantificar los 'outflows' en LINERs, facilitando así el estudio posterior de grandes muestras de LINERs con un enfoque espectroscópico.

Chapter 8

Perspectives and future work

In this thesis we have addressed the topic of ionised gas outflows in LINERs, with a particular focus on characterising their kinematics. In this section we focus on a number of open questions that are not covered here, but will be studied.

Characterisation of the neutral gas to search for outflows

The neutral gas phase, along with the molecular gas phase, is correlated with the presence of star formation in the host galaxies. This makes it very important to characterise the possible outflow and determine if it is influencing the evolution of the host by depleting the amount of cold gas available to form stars.
We know that outflows also have a neutral phase that can be studied with the sodium doublet. We have detected this emission in all of our MEGARA targets, to analyse its properties. Our MEGARA data in principle allow to characterise the neutral gas in terms of its extension, kinematics, density, etc. by using the sodium doublet. We plan to use this information to derive the neutral gas properties and check if there could be hints of a neutral gas outflow correlated (or not) with the ionised gas one.

AGN-driven or jet-driven outflows?

For NGC 1052 the energetics derived for the outflow and the jet indicate that the ionised gas outflow is most likely driven by the jet. In the near future we plan to look for correlations between the jets and the ionised gas outflows in our targets.

List of publications

Main publications in this thesis

- *Optical spectroscopy of type-2 LINERs*.
Authors: **L. Hermosa Muñoz**, S. Cazzoli, I. Márquez, and J. Masegosa.
Published in Astronomy & Astrophysics. Volume 635, A50, 19 pages, March 2020.
DOI: 10.1051/0004-6361/201936680.

- *A search for ionised gas outflows in an Hα imaging atlas of nearby LINERs*.
Authors: **L. Hermosa Muñoz**, I. Márquez, S. Cazzoli, J. Masegosa, and B. Agís-González.
Published in Astronomy & Astrophysics. Volume 660, A133, 31 pages, April 2022.
DOI: 10.1051/0004-6361/202142629.

- *Unexplored outflows in nearby low luminosity AGNs: the case of NGC 1052*.
Authors: S. Cazzoli, **L. Hermosa Muñoz**, I. Márquez, J. Masegosa, Á. Castillo-Morales, A.
Gil de Paz, L. Hernández-García, F. La Franca, and C. Ramos Almeida.
Published in Astronomy & Astrophysics. Volume 664, A135, 32 pages, August 2022.
DOI: 10.1051/0004-6361/202142695.

- *The MEGARA view of outflows low luminosity AGNs*.
Authors: **L. Hermosa Muñoz**, S. Cazzoli, I. Márquez, J. Masegosa et al. in preparation.

Other publications

- *NGC 7469 as seen by MEGARA: new results from high-resolution IFU spectroscopy*.
Authors: S. Cazzoli , A. Gil de Paz, I. Márquez, J. Masegosa, J. Iglesias, J. Gallego, E.
Carrasco, R. Cedazo, M. L. García-Vargas, Á. Castillo-Morales, S. Pascual, N. Cardiel, A.
Pérez-Calpena, P. Gómez-Alvarez, I. Martínez-Delgado and **L. Hermosa Muñoz**.
Published in Monthly Notices of the Royal Astronomical Society. Volume 493, Issue 3,

- *Kinematic and metallicity properties of the Aquarius dwarf galaxy from FORS2 MXU spectroscopy*.

References

Afanasiev, V. L. & Silchenko, O. K. 2007, Astronomical and Astrophysical Transactions, 26, 311

Allard, E. L., Peletier, R. F., & Knapen, J. H. 2005, ApJ, 633, L25

Antonucci, R. 1993, ARA&A, 31, 473

Arribas, S., Colina, L., Bellocchi, E., Maiolino, R., & Villar-Martín, M. 2014, A&A, 568, A14

Arsenault, R., Roy, J. R., & Boulesteix, J. 1990, A&A, 234, 23

Asplund, M., Grevesse, N., Sauval, A. J., & Scott, P. 2009, ARA&A, 47, 481

Audibert, A., Combes, F., García-Burillo, S., et al. 2019, A&A, 632, A33

Audibert, A., Combes, F., García-Burillo, S., et al. 2021, A&A, 656, A60

Avery, C. R., Wuyts, S., Förster Schreiber, N. M., et al. 2021, MNRAS, 503, 5134

Baade, W. & Minkowski, R. 1954, ApJ, 119, 206

Bacon, R., Accardo, M., Adjali, L., et al. 2010, in Proc. SPIE, Vol. 7735, Ground-based and Airborne Instrumentation for Astronomy III, 773508

Bacon, R., Copin, Y., Monnet, G., et al. 2001, MNRAS, 326, 23

Bacon, R., Vernet, J., Borisova, E., et al. 2014, The Messenger, 157, 13

Bai, Z.-R., Zhang, H.-T., Yuan, H.-L., et al. 2017, Research in Astronomy and Astrophysics, 17, 091

Baldi, R. D., Rodríguez Zaurín, J., Chiaberge, M., et al. 2019, ApJ, 870, 53

Baldi, R. D., Williams, D. R. A., McHardy, I. M., et al. 2018, MNRAS, 476, 3478

Baldwin, J. A., Phillips, M. M., & Terlevich, R. 1981, PASP, 93, 5

Balmaverde, B. & Capetti, A. 2013, A&A, 549, A144

Balmaverde, B. & Capetti, A. 2014, A&A, 563, A119

Barentine, J. C. & Kormendy, J. 2012, ApJ, 754, 140

Barth, A. J., Filippenko, A. V., & Moran, E. C. 1999, ApJ, 515, L61

Barth, A. J., Sarzi, M., Rix, H.-W., et al. 2001, ApJ, 555, 685

Battaner, E., Mediavilla, E., Guijarro, A., Arribas, S., & Florido, E. 2003, A&A, 401, 67

Beckmann, R. S., Devriendt, J., Slyz, A., et al. 2017, MNRAS, 472, 949

Beckmann, V. & Shrader, C. R. 2012, Active Galactic Nuclei

Beifiori, A., Courteau, S., Corsini, E. M., & Zhu, Y. 2012, MNRAS, 419, 2497

Belfiore, F., Maiolino, R., Maraston, C., et al. 2016, MNRAS, 461, 3111

Bellstedt, S., Forbes, D. A., Romanowsky, A. J., et al. 2018, MNRAS, 476, 4543

Bertola, F., Corsini, E. M., Beltrán, J. C. V., et al. 1999, ApJ, 519, L127

Bianchi, S., Antonucci, R., Capetti, A., et al. 2019a, MNRAS, 488, L1

Bianchi, S., Guainazzi, M., & Chiaberge, M. 2006, A&A, 448, 499

Bianchi, S., Guainazzi, M., Laor, A., Stern, J., & Behar, E. 2019b, MNRAS, 485, 416

Binette, L., Magris, C. G., Stasińska, G., & Bruzual, A. G. 1994, A&A, 292, 13

Bittner, A., Falcón-Barroso, J., Nedelchev, B., et al. 2019, A&A, 628, A117

Bland-Hawthorn, J., Maloney, P. R., Sutherland, R., et al. 2019, ApJ, 886, 45

Bluck, A. F. L., Maiolino, R., Piotrowska, J. M., et al. 2020, MNRAS, 499, 230

Boardman, N. F., Weijmans, A.-M., van den Bosch, R., et al. 2017, MNRAS, 471, 4005

Boehle, A., Larkin, J. E., Armus, L., & Wright, S. A. 2018, ApJ, 866, 79

Boizelle, B. D., Walsh, J. L., Barth, A. J., et al. 2021, ApJ, 908, 19

Bongiorno, A., Schulze, A., Merloni, A., et al. 2016, A&A, 588, A78

Bosch, G., Hägele, G. F., Amorín, R., et al. 2019, MNRAS, 489, 1787

Bower, C. A., Wilson, A. S., Heckman, T. M., & Richstone, D. O. 1996, in Astronomical Society of the Pacific Conference Series, Vol. 103, The Physics of Liners in View of Recent Observations, ed. M. Eracleous, A. Koratkar, C. Leitherer, & L. Ho, 163

Bower, G. A., Green, R. F., Danks, A., et al. 1998, ApJ, 492, L111

Bower, R. G., Benson, A. J., Malbon, R., et al. 2006, MNRAS, 370, 645

Braun, R., Oosterloo, T. A., Morganti, R., Klein, U., & Beck, R. 2007, A&A, 461, 455

Brodie, J. P., Romanowsky, A. J., Strader, J., et al. 2014, ApJ, 796, 52

Brum, C., Riffel, R. A., Storchi-Bergmann, T., et al. 2017, MNRAS, 469, 3405

Brusa, M., Cresci, G., Daddi, E., et al. 2018, A&A, 612, A29

Busch, G., Eckart, A., Valencia-S., M., et al. 2017, A&A, 598, A55

Calzetti, D., Armus, L., Bohlin, R. C., et al. 2000, ApJ, 533, 682

Canning, R. E. A., Fabian, A. C., Johnstone, R. M., et al. 2011, MNRAS, 417, 3080

Cappellari, M. 2016, ARA&A, 54, 597

Cappellari, M. 2017, MNRAS, 466, 798

Cappellari, M. & Copin, Y. 2003, MNRAS, 342, 345

Cappellari, M. & Emsellem, E. 2004, PASP, 116, 138

Cappellari, M., Emsellem, E., Bacon, R., et al. 2007, MNRAS, 379, 418

Cappellari, M., McDermid, R. M., Alatalo, K., et al. 2013, MNRAS, 432, 1862

Cappellari, M., Renzini, A., Greggio, L., et al. 1999, ApJ, 519, 117

Carniani, S., Marconi, A., Maiolino, R., et al. 2015, A&A, 580, A102

Carollo, C. M., Franx, M., Illingworth, G. D., & Forbes, D. A. 1997, ApJ, 481, 710

Carollo, C. M., Stiavelli, M., Seigar, M., de Zeeuw, P. T., & Dejonghe, H. 2002, AJ, 123, 159

Carrasco, E., Gil de Paz, A., Gallego, J., et al. 2018, in Society of Photo-Optical Instrumentation Engineers (SPIE) Conference Series, Vol. 10702, Ground-based and Airborne Instrumentation for Astronomy VII, ed. C. J. Evans, L. Simard, & H. Takami, 1070216

Casasola, V., Hunt, L. K., Combes, F., García-Burillo, S., & Neri, R. 2011, A&A, 527, A92

Catalán-Torrecilla, C., Castillo-Morales, Á., Gil de Paz, A., et al. 2020, ApJ, 890, 5

Cazzoli, S., Arribas, S., Colina, L., et al. 2014, A&A, 569, A14

Cazzoli, S., Arribas, S., Maiolino, R., & Colina, L. 2016, A&A, 590, A125

Cazzoli, S., Gil de Paz, A., Márquez, I., et al. 2020, MNRAS, 493, 3656

Cazzoli, S., Hermosa Muñoz, L., Márquez, I., et al. 2022, A&A, 664, A135

Cazzoli, S., Márquez, I., Masegosa, J., et al. 2018, MNRAS, 480, 1106

Cepa, J. & Beckman, J. E. 1990, A&AS, 83, 211

Chemin, L., Balkowski, C., Cayatte, V., et al. 2006, MNRAS, 366, 812

Chiaraluce, E., Bruni, G., Panessa, F., et al. 2019, MNRAS, 485, 3185

Cicone, C., Maiolino, R., Sturm, E., et al. 2014, A&A, 562, A21

Cid Fernandes, R., Stasińska, G., Mateus, A., & Vale Asari, N. 2011, MNRAS, 413, 1687

Combes, F., Young, L. M., & Bureau, M. 2007, MNRAS, 377, 1795

Comerón, S., Knapen, J. H., Ramos Almeida, C., & Watkins, A. E. 2021, A&A, 645, A130

Concas, A., Popesso, P., Brusa, M., Mainieri, V., & Thomas, D. 2019, A&A, 622, A188

Constantin, A. & Seth, A. C. 2012, Advances in Astronomy, 2012, 178060

Constantin, A., Shields, J. C., Ho, L. C., et al. 2015, ApJ, 814, 149

Corsini, E. M., Méndez-Abreu, J., Pastorello, N., et al. 2012, MNRAS, 423, L79

Corsini, E. M., Morelli, L., Zarattini, S., et al. 2018, A&A, 618, A172

Cortés, J. R., Kenney, J. D. P., & Hardy, E. 2015, ApJS, 216, 9

Costa, T., Sijacki, D., & Haehnelt, M. G. 2014, MNRAS, 444, 2355

Cresci, G. & Maiolino, R. 2018, Nature Astronomy, 2, 179

Cresci, G., Marconi, A., Zibetti, S., et al. 2015, A&A, 582, A63

Cresci, G., Vanzi, L., Telles, E., et al. 2017, A&A, 604, A101

Currie, M. J., Berry, D. S., Jenness, T., et al. 2014, in Astronomical Society of the Pacific Conference Series, Vol. 485, Astronomical Data Analysis Software and Systems XXIII, ed. N. Manset & P. Forshay, 391

Dahmer-Hahn, L. G., Riffel, R., Ricci, T. V., et al. 2019a, MNRAS, 489, 5653

Dahmer-Hahn, L. G., Riffel, R., Steiner, J. E., et al. 2019b, MNRAS, 482, 5211

Davies, R., Baron, D., Shimizu, T., et al. 2020, MNRAS, 498, 4150

Davies, R. I., Maciejewski, W., Hicks, E. K. S., et al. 2014, ApJ, 792, 101

Davis, T. A. & McDermid, R. M. 2017, MNRAS, 464, 453

de Paz, A. G., Pascual, S., & Chamorro-Cazorla, M. 2020, guaix-ucm/megara-tools: v0.1.0

Díaz-García, S., Moyano, F. D., Comerón, S., et al. 2020, A&A, 644, A38

Dopita, M. A., Ho, I.-T., Dressel, L. L., et al. 2015, ApJ, 801, 42

Dopita, M. A., Koratkar, A. P., Evans, I. N., et al. 1996, in Astronomical Society of the Pacific Conference Series, Vol. 103, The Physics of Liners in View of Recent Observations, ed. M. Eracleous, A. Koratkar, C. Leitherer, & L. Ho, 44

Dopita, M. A. & Sutherland, R. S. 1995, ApJ, 455, 468

Draper, P. W., Berry, D. S., Jenness, T., & Economou, F. 2009, in Astronomical Society of the Pacific Conference Series, Vol. 411, Astronomical Data Analysis Software and Systems XVIII, ed. D. A. Bohlender, D. Durand, & P. Dowler, 575

Dudik, R. P., Satyapal, S., & Marcu, D. 2009, ApJ, 691, 1501

Dullo, B. T., Martínez-Lombilla, C., & Knapen, J. H. 2016, MNRAS, 462, 3800

Elitzur, M. 2006, New Astronomy Reviews, 50, 728, qSO Host Galaxies: Evolution and Environments

Elitzur, M. & Shlosman, I. 2006, ApJ, 648, L101

Emsellem, E., Cappellari, M., Peletier, R. F., et al. 2004, MNRAS, 352, 721

Emsellem, E. & Ferruit, P. 2000, A&A, 357, 111

Ene, I., Ma, C.-P., Veale, M., et al. 2018, MNRAS, 479, 2810

Ene, I., Ma, C.-P., Walsh, J. L., et al. 2020, ApJ, 891, 65

Epinat, B., Amram, P., Balkowski, C., & Marcelin, M. 2010, MNRAS, 401, 2113

Epinat, B., Amram, P., & Marcelin, M. 2008, MNRAS, 390, 466

Erroz-Ferrer, S., Knapen, J. H., Mohd Noh Velastín, E. A. N., Ryon, J. E., & Hagen, L. M. Z. 2013, MNRAS, 436, 3135

Erwin, P. & Debattista, V. P. 2017, MNRAS, 468, 2058

Erwin, P., Pohlen, M., & Beckman, J. E. 2008, AJ, 135, 20

Erwin, P. & Sparke, L. S. 1999, ApJ, 521, L37

Eskridge, P. B. & Pogge, R. W. 1997, ApJ, 486, 259

Fabbiano, G., Heckman, T., & Keel, W. C. 1990, ApJ, 355, 442

Fabian, A. C. 2012, ARA&A, 50, 455

Falcón-Barroso, J., Bacon, R., Bureau, M., et al. 2006a, MNRAS, 369, 529

Falcón-Barroso, J., Balcells, M., Peletier, R. F., & Vazdekis, A. 2003, A&A, 405, 455

Falcón-Barroso, J., Sarzi, M., Bacon, R., et al. 2006b, New A Rev., 49, 515

Falocco, S., Larsson, J., & Nandi, S. 2020, A&A, 638, A67

Feruglio, C., Maiolino, R., Piconcelli, E., et al. 2010, A&A, 518, L155

Filho, M. E., Barthel, P. D., & Ho, L. C. 2002, ApJS, 142, 223

Filippenko, A. V. & Terlevich, R. 1992, ApJ, 397, L79

Finkelman, I., Brosch, N., Funes, J. G., Kniazev, A. Y., & Väisänen, P. 2010, MNRAS, 407, 2475

Fiore, F., Feruglio, C., Shankar, F., et al. 2017, A&A, 601, A143

Fischer, T. C., Crenshaw, D. M., Kraemer, S. B., & Schmitt, H. R. 2013, ApJS, 209, 1

Flores, H., Hammer, F., Puech, M., Amram, P., & Balkowski, C. 2006, A&A, 455, 107

Fluetsch, A., Maiolino, R., Carniani, S., et al. 2021, MNRAS, 505, 5753

Fluetsch, A., Maiolino, R., Carniani, S., et al. 2019, MNRAS, 483, 4586

Font, J., Beckman, J. E., Martínez-Valpuesta, I., et al. 2017, ApJ, 835, 279

Forbes, D. A. 1996, AJ, 112, 1409

Forbes, D. A., Sinpetru, L., Savorgnan, G., et al. 2017, MNRAS, 464, 4611

Foster, C., Spitler, L. R., Romanowsky, A. J., et al. 2011, MNRAS, 415, 3393

Fox, A. J., Bordoloi, R., Savage, B. D., et al. 2015, ApJ, 799, L7

García-Burillo, S., Combes, F., Ramos Almeida, C., et al. 2019, A&A, 632, A61

García-Burillo, S., Fernández-García, S., Combes, F., et al. 2009, A&A, 496, 85

Garcia-Burillo, S., Sempere, M. J., Combes, F., & Neri, R. 1998, A&A, 333, 864

Gerssen, J., Kuijken, K., & Merrifield, M. R. 1999, MNRAS, 306, 926

Gil de Paz, A., Carrasco, E., Gallego, J., et al. 2018, in Society of Photo-Optical Instrumentation Engineers (SPIE) Conference Series, Vol. 10702, Ground-based and Airborne Instrumentation for Astronomy VII, ed. C. J. Evans, L. Simard, & H. Takami, 1070217

Gil de Paz, A., Carrasco, E., Gallego, J., et al. 2016, in Society of Photo-Optical Instrumentation Engineers (SPIE) Conference Series, Vol. 9908, Ground-based and Airborne Instrumentation for Astronomy VI, ed. C. J. Evans, L. Simard, & H. Takami, 99081K

González Delgado, R. M., Cerviño, M., Martins, L. P., Leitherer, C., & Hauschildt, P. H. 2005, MNRAS, 357, 945

González Delgado, R. M., Cid Fernandes, R., Pérez, E., et al. 2004, ApJ, 605, 127

González Delgado, R. M., Pérez, E., Cid Fernandes, R., & Schmitt, H. 2008, AJ, 135, 747

González-Martín, O., Masegosa, J., García-Bernete, I., et al. 2019a, ApJ, 884, 10

González-Martín, O., Masegosa, J., García-Bernete, I., et al. 2019b, ApJ, 884, 11

González-Martín, O., Masegosa, J., Márquez, I., & Guainazzi, M. 2009, ApJ, 704, 1570

González-Martín, O., Masegosa, J., Márquez, I., Guainazzi, M., & Jiménez-Bailón, E. 2009, A&A, 506, 1107

González-Martín, O., Masegosa, J., Márquez, I., Guerrero, M. A., & Dultzin-Hacyan, D. 2006, A&A, 460, 45

González-Martín, O., Masegosa, J., Márquez, I., et al. 2015, A&A, 578, A74

Goudfrooij, P., Hansen, L., Jorgensen, H. E., & Norgaard-Nielsen, H. U. 1994a, A&AS, 105, 341

Goudfrooij, P., Hansen, L., Jorgensen, H. E., et al. 1994b, A&AS, 104, 179

Greene, J. E. & Ho, L. C. 2005, ApJ, 630, 122

Groves, B. A., Dopita, M. A., & Sutherland, R. S. 2004, ApJS, 153, 75

Hameed, S. & Devereux, N. 2005, AJ, 129, 2597

Harms, R. J., Ford, H. C., Tsvetanov, Z. I., et al. 1994, ApJ, 435, L35

Harrison, C. M. 2017, Nature Astronomy, 1, 0165

Harrison, C. M., Alexander, D. M., Mullaney, J. R., et al. 2016, MNRAS, 456, 1195

Harrison, C. M., Alexander, D. M., Mullaney, J. R., & Swinbank, A. M. 2014, MNRAS, 441, 3306

Harrison, C. M., Costa, T., Tadhunter, C. N., et al. 2018, Nature Astronomy, 2, 198

Hawkins, M. R. S. 2004, A&A, 424, 519

Haynes, M. P., Jore, K. P., Barrett, E. A., Broeils, A. H., & Murray, B. M. 2000, AJ, 120, 703

Hazard, C., Mackey, M. B., & Shimmins, A. J. 1963, Nature, 197, 1037

Heckman, T. M. 1980, A&A, 87, 152

Heckman, T. M. & Best, P. N. 2014, ARA&A, 52, 589

Heckman, T. M., Lehnert, M. D., Strickland, D. K., & Armus, L. 2000, ApJS, 129, 493

Hermosa Muñoz, L., Cazzoli, S., Márquez, I., & Masegosa, J. 2020, A&A, 635, A50

Hermosa Muñoz, L., Márquez, I., Cazzoli, S., Masegosa, J., & Agís-González, B. 2022, A&A, 660, A133

Hernández-García, L., González-Martín, O., Márquez, I., & Masegosa, J. 2013, A&A, 556, A47

Hernández-García, L., González-Martín, O., Masegosa, J., & Márquez, I. 2014, A&A, 569, A26

Hernández-García, L., Panessa, F., Bassani, L., et al. 2019, MNRAS, 489, 4049

Hernández-García, L., Vietri, G., Panessa, F., et al. 2018, MNRAS, 478, 4634

Ho, L. C. 2008, ARA&A, 46, 475

Ho, L. C., Filippenko, A. V., & Sargent, W. L. 1995, ApJS, 98, 477

Ho, L. C., Filippenko, A. V., & Sargent, W. L. W. 1993, ApJ, 417, 63

Ho, L. C., Filippenko, A. V., & Sargent, W. L. W. 1997a, ApJS, 112, 315

Ho, L. C., Filippenko, A. V., & Sargent, W. L. W. 2003, ApJ, 583, 159

Ho, L. C., Filippenko, A. V., Sargent, W. L. W., & Peng, C. Y. 1997b, ApJS, 112, 391

Ho, L. C., Greene, J. E., Filippenko, A. V., & Sargent, W. L. W. 2009, ApJS, 183, 1

Hota, A., Saikia, D. J., & Irwin, J. A. 2007, MNRAS, 380, 1009

Huchtmeier, W. K. 1994, A&A, 286, 389

Huchtmeier, W. K. & Richter, O.-G. 1986, A&AS, 64, 111

James, P. A. & Percival, S. M. 2016, MNRAS, 457, 917

Jarvis, M. E., Harrison, C. M., Thomson, A. P., et al. 2019, MNRAS, 485, 2710

Józsa, G. I. G., Oosterloo, T. A., Morganti, R., Klein, U., & Erben, T. 2009, A&A, 494, 489

Kadler, M., Kerp, J., Ros, E., et al. 2004a, A&A, 420, 467

Kadler, M., Ros, E., Lobanov, A. P., Falcke, H., & Zensus, J. A. 2004b, A&A, 426, 481

Kakkad, D., Mainieri, V., Vietri, G., et al. 2020, A&A, 642, A147

Kaneda, H., Ishihara, D., Onaka, T., et al. 2011, PASJ, 63, 601

Kang, D. & Woo, J.-H. 2018, ApJ, 864, 124

Karachentsev, I. D. & Makarov, D. A. 1996, AJ, 111, 794

Katkov, I. Y., Moiseev, A. V., & Sil'chenko, O. K. 2011, ApJ, 740, 83

Kauffmann, G., Heckman, T. M., Tremonti, C., et al. 2003, MNRAS, 346, 1055

Kenney, J. D. P. & Yale, E. E. 2002, ApJ, 567, 865

Kennicutt, R. C. & Evans, N. J. 2012, ARA&A, 50, 531

Kent, S. M. 1990, AJ, 100, 377

Kewley, L. J., Groves, B., Kauffmann, G., & Heckman, T. 2006, MNRAS, 372, 961

Knapen, J. H., Cepa, J., Beckman, J. E., Soledad del Rio, M., & Pedlar, A. 1993, ApJ, 416, 563

Knapen, J. H., Shlosman, I., Heller, C. H., et al. 2000, ApJ, 528, 219

Koopmann, R. A. & Kenney, J. D. P. 2006, ApJS, 162, 97

Koopmann, R. A., Kenney, J. D. P., & Young, J. 2001, ApJS, 135, 125

Kormendy, J. 1979, ApJ, 227, 714

Kormendy, J. 1984, ApJ, 287, 577

Kormendy, J., Bender, R., Ajhar, E. A., et al. 1996, ApJ, 473, L91

Kormendy, J. & Ho, L. C. 2013, ARA&A, 51, 511

Kormendy, J. & Richstone, D. 1995, ARA&A, 33, 581

Koss, M., Trakhtenbrot, B., Ricci, C., et al. 2017, ApJ, 850, 74

Krajnović, D., Weilbacher, P. M., Urrutia, T., et al. 2015, MNRAS, 452, 2

Kuo, C.-Y., Lim, J., Tang, Y.-W., & Ho, P. T. P. 2008, ApJ, 679, 1047

Lakhchaura, K., Werner, N., Sun, M., et al. 2018, MNRAS, 481, 4472

Laurikainen, E. & Salo, H. 2017, A&A, 598, A10

Laurikainen, E., Salo, H., Buta, R., & Knapen, J. H. 2011, MNRAS, 418, 1452

Lehnert, M. D., Tasse, C., Nesvadba, N. P. H., Best, P. N., & van Driel, W. 2011, A&A, 532, L3

Leroy, A. K., Schinnerer, E., Hughes, A., et al. 2021, arXiv e-prints, arXiv:2104.07739

Leroy, A. K., Walter, F., Martini, P., et al. 2015, ApJ, 814, 83

Li, J.-T. 2015, MNRAS, 453, 1062

López-Cobá, C., Sánchez, S. F., Anderson, J. P., et al. 2020, AJ, 159, 167

Luo, R., Woo, J.-H., Karouzos, M., et al. 2021, ApJ, 908, 221

Ma, C.-P., Greene, J. E., McConnell, N., et al. 2014, ApJ, 795, 158

Machacek, M., Nulsen, P. E. J., Jones, C., & Forman, W. R. 2006, ApJ, 648, 947

Machacek, M. E., Jones, C., & Forman, W. R. 2004, ApJ, 610, 183

Maiolino, R., Russell, H. R., Fabian, A. C., et al. 2017, Nature, 544, 202

Markwardt, C. B. 2009, in Astronomical Society of the Pacific Conference Series, Vol. 411, Astronomical Data Analysis Software and Systems XVIII, ed. D. A. Bohlender, D. Durand, & P. Dowler, 251

Márquez, I., Durret, F., González Delgado, R. M., et al. 1999, A&AS, 140, 1

Márquez, I., Masegosa, J., Durret, F., et al. 2003, A&A, 409, 459

Márquez, I., Masegosa, J., González-Martin, O., et al. 2017, Frontiers in Astronomy and Space Sciences, 4, 34

Márquez, I. & Moles, M. 1996, A&AS, 120, 1

Martins, L. P., González Delgado, R. M., Leitherer, C., Cerviño, M., & Hauschildt, P. 2005, MNRAS, 358, 49

Masegosa, J., Márquez, I., Ramirez, A., & González-Martín, O. 2011, A&A, 527, A23

Mason, R. E., Lopez-Rodriguez, E., Packham, C., et al. 2012, AJ, 144, 11

Matthews, T. A. & Sandage, A. R. 1963, ApJ, 138, 30

Mazzalay, X., Maciejewski, W., Erwin, P., et al. 2014, MNRAS, 438, 2036

McKernan, B., Ford, K. E. S., & Reynolds, C. S. 2010, MNRAS, 407, 2399

Mediavilla, E., Arribas, S., García-Lorenzo, B., & del Burgo, C. 1997, ApJ, 488, 682

Mingozzi, M., Cresci, G., Venturi, G., et al. 2019, A&A, 622, A146

Moellenhoff, C. & Bender, R. 1989, A&A, 214, 61

Molaeinezhad, A., Falcón-Barroso, J., Martínez-Valpuesta, I., et al. 2016, MNRAS, 456, 692

Molina, M., Eracleous, M., Barth, A. J., et al. 2018, ApJ, 864, 90

Molyneux, S. J., Harrison, C. M., & Jarvis, M. E. 2019, A&A, 631, A132

Morganti, R. 2017, Frontiers in Astronomy and Space Sciences, 4, 42

Morganti, R. & Oosterloo, T. 2018, A&A Rev., 26, 4

Morganti, R., Oosterloo, T., Tadhunter, C., Bernhard, E. P., & Raymond Oonk, J. B. 2021, A&A, 656, A55

Morganti, R., Oosterloo, T. A., Tadhunter, C. N., van Moorsel, G., & Emonts, B. 2005, A&A, 439, 521

Mosenkov, A., Rich, R. M., Koch, A., et al. 2020, MNRAS, 494, 1751

Mukherjee, D., Bicknell, G. V., Wagner, A. Y., Sutherland, R. S., & Silk, J. 2018, MNRAS, 479, 5544

Mulcahey, C. R., Prichard, L. J., Krajnović, D., & Jorgenson, R. A. 2021, MNRAS, 504, 5087

Müller-Sánchez, F., Prieto, M. A., Hicks, E. K. S., et al. 2011, ApJ, 739, 69

Müller-Sánchez, F., Prieto, M. A., Mezcua, M., et al. 2013, ApJ, 763, L1

Nagar, N. M., Falcke, H., & Wilson, A. S. 2005, A&A, 435, 521

Nagar, N. M., Falcke, H., Wilson, A. S., & Ho, L. C. 2000, ApJ, 542, 186

Nakashima, S., Koyama, K., Wang, Q. D., & Enokiya, R. 2019, ApJ, 875, 32

Nemmen, R. S., Storchi-Bergmann, T., & Eracleous, M. 2014, MNRAS, 438, 2804

Netzer, H. 2013, The Physics and Evolution of Active Galactic Nuclei

Netzer, H. 2015, ARA&A, 53, 365

Newville, M., Stensitzki, T., Allen, D. B., & Ingargiola, A. 2014, LMFIT: Non-Linear Least-Square Minimization and Curve-Fitting for Python

Nicholson, K. L., Reichert, G. A., Mason, K. O., et al. 1998, MNRAS, 300, 893

Noel-Storr, J., Baum, S. A., Verdoes Kleijn, G., et al. 2003, ApJS, 148, 419

Nyland, K., Davis, T. A., Nguyen, D. D., et al. 2017, ApJ, 845, 50

Oke, J. B. & Gunn, J. E. 1982, PASP, 94, 586

Onori, F., La Franca, F., Ricci, F., et al. 2017a, MNRAS, 464, 1783

Onori, F., Ricci, F., La Franca, F., et al. 2017b, MNRAS, 468, L97

Oosterloo, T., Morganti, R., Tadhunter, C., et al. 2019, A&A, 632, A66

Osterbrock, D. E. & Ferland, G. J. 2006, Astrophysics of gaseous nebulae and active galactic nuclei, 2nd. ed. by D.E. Osterbrock and G.J. Ferland. Sausalito, CA: University Science Books, 2006

Osterbrock, D. E., Fulbright, J. P., Martel, A. R., et al. 1996, PASP, 108, 277

Padovani, P. 2017, Nature Astronomy, 1, 0194

Padovani, P., Miller, N., Kellermann, K. I., et al. 2011, ApJ, 740, 20

Pagotto, I., Corsini, E. M., Sarzi, M., et al. 2019, MNRAS, 483, 57

Pandya, V., Greene, J. E., Ma, C.-P., et al. 2017, ApJ, 837, 40

Papaderos, P., Gomes, J. M., Vílchez, J. M., et al. 2013, A&A, 555, L1

Pascual, S., Cardiel, N., Gil de Paz, A., et al. 2019, in Highlights on Spanish Astrophysics X, ed. B. Montesinos, A. Asensio Ramos, F. Buitrago, R. Schödel, E. Villaver, S. Pérez-Hoyos, & I. Ordóñez-Etxeberria, 227–227

Pascual, S., Cardiel, N., Picazo-Sanchez, P., Castillo-Morales, A., & de Paz, A. G. 2020, guaix-ucm/megaradrp: v0.10.1

Pascual, S., Cardiel, N., Picazo-Sanchez, P., Castillo-Morales, A., & Gil De Paz, A. 2021, guaix-ucm/megaradrp: v0.11

Paturel, G., Andernach, H., Bottinelli, L., et al. 1997, A&AS, 124, 109

Pereira-Santaella, M., Colina, L., García-Burillo, S., et al. 2016, A&A, 594, A81

Pereira-Santaella, M., Colina, L., García-Burillo, S., et al. 2020, A&A, 643, A89

Pérez-Díaz, B., Masegosa, J., Márquez, I., & Pérez-Montero, E. 2021, MNRAS, 505, 4289

Pérez-Montero, E. 2014, MNRAS, 441, 2663

Perna, M., Arribas, S., Catalán-Torrecilla, C., et al. 2020, A&A, 643, A139

Perna, M., Arribas, S., Colina, L., et al. 2022, arXiv e-prints, arXiv:2202.02336

Perna, M., Arribas, S., Pereira Santaella, M., et al. 2021, A&A, 646, A101

Perna, M., Lanzuisi, G., Brusa, M., Mignoli, M., & Cresci, G. 2017, A&A, 603, A99

Peters, W. & Kuzio de Naray, R. 2017, MNRAS, 469, 3541

Pignatelli, E., Corsini, E. M., Vega Beltrán, J. C., et al. 2001, MNRAS, 323, 188

Pogge, R. W., Maoz, D., Ho, L. C., & Eracleous, M. 2000, ApJ, 532, 323

Ponti, G., Hofmann, F., Churazov, E., et al. 2019, Nature, 567, 347

Predehl, P., Sunyaev, R. A., Becker, W., et al. 2020, Nature, 588, 227

Pu, S. B., Saglia, R. P., Fabricius, M. H., et al. 2010, A&A, 516, A4

Raimundo, S. I. 2021, A&A, 650, A34

Ramos Almeida, C., Martínez González, M. J., Asensio Ramos, A., et al. 2016, MNRAS, 461, 1387

Ramos Almeida, C. & Ricci, C. 2017, Nature Astronomy, 1, 679

Randall, S. W., Forman, W. R., Giacintucci, S., et al. 2011, ApJ, 726, 86

Randall, S. W., Nulsen, P. E. J., Jones, C., et al. 2015, ApJ, 805, 112

Rest, A., van den Bosch, F. C., Jaffe, W., et al. 2001, AJ, 121, 2431

Revalski, M., Meena, B., Martinez, F., et al. 2021, ApJ, 910, 139

Ricci, T. V., Steiner, J. E., & Menezes, R. B. 2014, MNRAS, 440, 2419

Ricci, T. V., Steiner, J. E., & Menezes, R. B. 2015, MNRAS, 451, 3728

Riffel, R. A., Storchi-Bergmann, T., Riffel, R., et al. 2021, MNRAS, 504, 3265

Rose, M., Tadhunter, C., Ramos Almeida, C., et al. 2018, MNRAS, 474, 128

Roy, A., Nath, B. B., Sharma, P., & Shchekinov, Y. 2016, MNRAS, 463, 2296

Rupke, D. S., Veilleux, S., & Sanders, D. B. 2002, ApJ, 570, 588

Rupke, D. S. N. & Veilleux, S. 2013, ApJ, 768, 75

Ruschel-Dutra, D., Storchi-Bergmann, T., Schnorr-Müller, A., et al. 2021, MNRAS, 507, 74

Saglia, R. P., Opitsch, M., Erwin, P., et al. 2016, ApJ, 818, 47

Sakamoto, K., Okumura, S., Minezaki, T., Kobayashi, Y., & Wada, K. 1995, AJ, 110, 2075

Sánchez, S. F., Kennicutt, R. C., Gil de Paz, A., et al. 2012, A&A, 538, A8

Sánchez, S. F., Walcher, C. J., Lopez-Cobá, C., et al. 2021, Rev. Mexicana Astron. Astrofis., 57, 3

Sánchez-Gallego, J. R., Knapen, J. H., Wilson, C. D., et al. 2012, MNRAS, 422, 3208

Sandage, A. 1965, ApJ, 141, 1560

Sanders, R. L., Shapley, A. E., Kriek, M., et al. 2016, ApJ, 816, 23

Sarzi, M., Falcón-Barroso, J., Davies, R. L., et al. 2006, MNRAS, 366, 1151

Sarzi, M., Kaviraj, S., Nedelchev, B., et al. 2016, MNRAS, 456, L25

Sarzi, M., Shields, J. C., Schawinski, K., et al. 2010, MNRAS, 402, 2187

Saturni, F. G., Vietri, G., Piconcelli, E., et al. 2021, A&A, 654, A154

Scarlata, C., Stiavelli, M., Hughes, M. A., et al. 2004, AJ, 128, 1124

Schmidt, M. 1963, Nature, 197, 1040

Schmidt, M., Schneider, D. P., & Gunn, J. E. 1995, AJ, 110, 68

Schmidt, T. M., Bigiel, F., Klessen, R. S., & de Blok, W. J. G. 2016, MNRAS, 457, 2642

Seyfert, C. K. 1943, ApJ, 97, 28

Shapiro, K. L., Cappellari, M., de Zeeuw, T., et al. 2006, MNRAS, 370, 559

Sharp, R. G. & Bland-Hawthorn, J. 2010, ApJ, 711, 818

Shields, G. A. 1999, PASP, 111, 661

Shields, J. C., Rix, H.-W., Sarzi, M., et al. 2007, ApJ, 654, 125

Silk, J. 2013, ApJ, 772, 112

Silk, J. & Mamon, G. A. 2012, Research in Astronomy and Astrophysics, 12, 917

Singh, R., van de Ven, G., Jahnke, K., et al. 2013, A&A, 558, A43

Singha, M., Husemann, B., Urrutia, T., et al. 2022, A&A, 659, A123

Spitzer, L. 1978, Physical processes in the interstellar medium

Stasińska, G., Vale Asari, N., Cid Fernandes, R., et al. 2008, MNRAS, 391, L29

Steiner, J. E., Menezes, R. B., Ricci, T. V., & Oliveira, A. S. 2009, MNRAS, 395, 64

Storchi-Bergmann, T., Schimoia, J. S., Peterson, B. M., et al. 2017, ApJ, 835, 236

Sturm, E., Lutz, D., Verma, A., et al. 2002, A&A, 393, 821

Su, M., Slatyer, T. R., & Finkbeiner, D. P. 2010, ApJ, 724, 1044

Sugai, H., Hattori, T., Kawai, A., et al. 2005, ApJ, 629, 131

Tacchella, S., Dekel, A., Carollo, C. M., et al. 2016, MNRAS, 457, 2790

Tombesi, F., Cappi, M., Reeves, J. N., et al. 2013, MNRAS, 430, 1102

Tremmel, M., Quinn, T. R., Ricarte, A., et al. 2019, MNRAS, 483, 3336

Trinchieri, G., Pellegrini, S., Fabbiano, G., et al. 2008, ApJ, 688, 1000

Trussler, J., Maiolino, R., Maraston, C., et al. 2020, MNRAS, 491, 5406

Tsai, A.-L., Matsushita, S., Kong, A. K. H., Matsumoto, H., & Kohno, K. 2012, ApJ, 752, 38

Ulrich, M.-H. 1975, PASP, 87, 965

Urry, C. M. & Padovani, P. 1995, PASP, 107, 803

Valdes, F., Gupta, R., Rose, J. A., Singh, H. P., & Bell, D. J. 2004, ApJS, 152, 251

van den Bosch, F. C., Ferrarese, L., Jaffe, W., Ford, H. C., & O'Connell, R. W. 1994, AJ, 108, 1579

van Dokkum, P. G. 2001, PASP, 113, 1420

Veilleux, S., Cecil, G., & Bland-Hawthorn, J. 2005, ARA&A, 43, 769

Veilleux, S., Cecil, G., Bland-Hawthorn, J., et al. 1994, ApJ, 433, 48

Veilleux, S., Maiolino, R., Bolatto, A. D., & Aalto, S. 2020, A&A Rev., 28, 2

Veilleux, S. & Osterbrock, D. E. 1987, ApJS, 63, 295

Venturi, G., Cresci, G., Marconi, A., et al. 2021, A&A, 648, A17

Venturi, G., Nardini, E., Marconi, A., et al. 2018, A&A, 619, A74

Villar-Martín, M., Cabrera-Lavers, A., Humphrey, A., et al. 2018, MNRAS, 474, 2302

Vogelsberger, M., Genel, S., Springel, V., et al. 2014, Nature, 509, 177

Walsh, J. L., Barth, A. J., Ho, L. C., et al. 2008, AJ, 136, 1677

Walsh, J. L., Barth, A. J., Ho, L. C., & Sarzi, M. 2013, ApJ, 770, 86

Walsh, J. L., Barth, A. J., & Sarzi, M. 2010, ApJ, 721, 762

Wardle, M. & Knapp, G. R. 1986, AJ, 91, 23

Watkins, A. E., Mihos, J. C., Harding, P., & Feldmeier, J. J. 2014, ApJ, 791, 38

Westfall, K. B., Cappellari, M., Bershady, M. A., et al. 2019, AJ, 158, 231

Wild, V., Rosales-Ortega, F., Falcón-Barroso, J., et al. 2014, A&A, 567, A132

Wilson, C. D., Cridland, A., Foyle, K., et al. 2013, ApJ, 776, L30

Wrobel, J. M. 1984, ApJ, 284, 531

Wylezalek, D., Flores, A. M., Zakamska, N. L., Greene, J. E., & Riffel, R. A. 2020, MNRAS, 492, 4680

Yıldız, M. K., Peletier, R. F., Duc, P. A., & Serra, P. 2020, A&A, 636, A8

Young, L. M., Bureau, M., & Cappellari, M. 2008, ApJ, 676, 317

Appendix A

Additional material from Chapter 2

A.1 Stellar modeling and subtraction for Palomar spectra

The starlight modeling and subtraction to the ground-based spectra is presented here for the eight available LINERs. The stellar continuum in the observed spectra was modeled using the PPXF method as it was in Cazzoli et al. (2018) (Sect. 2.3).
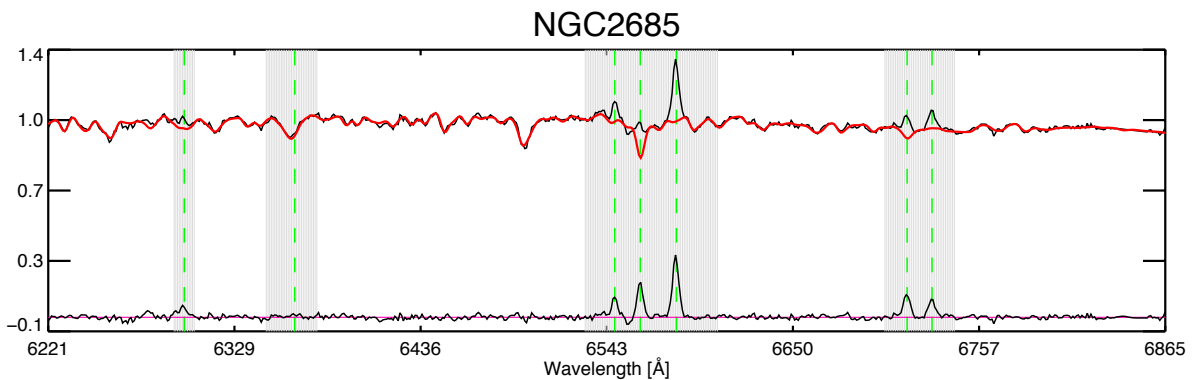
Fig. A.1 Optical ground-based Palomar spectrum of NGC 2685. The original data is shown in black; the red line indicates the modeled stellar spectrum that matches the observed stellar continuum. The spectrum used for the kinematical decomposition (i.e., data − model) is also presented. Green dashed lines show the rest-frame position of the [O I], [N II]-Hα, and [S II] lines. Gray bands indicate the regions masked to perform the stellar modeling. The magenta line indicates the zero level as reference.
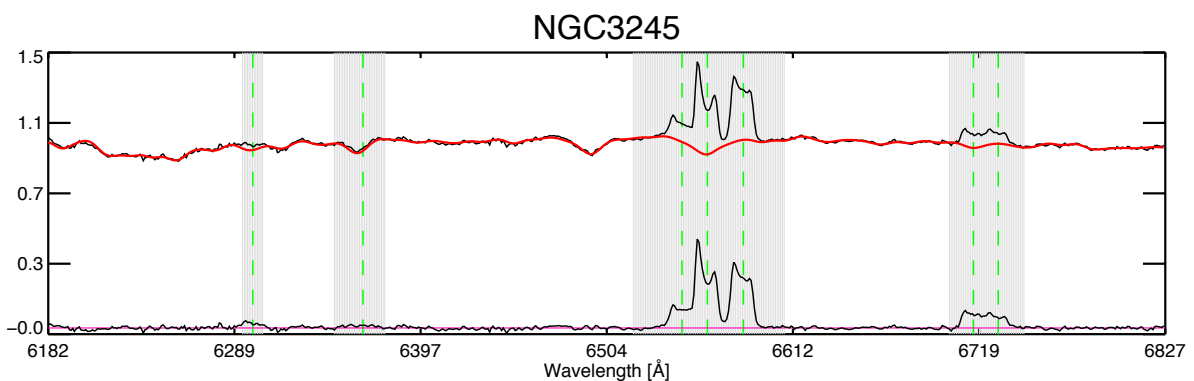
Fig. A.2 Same as Fig. A.1 but for NGC 3245.
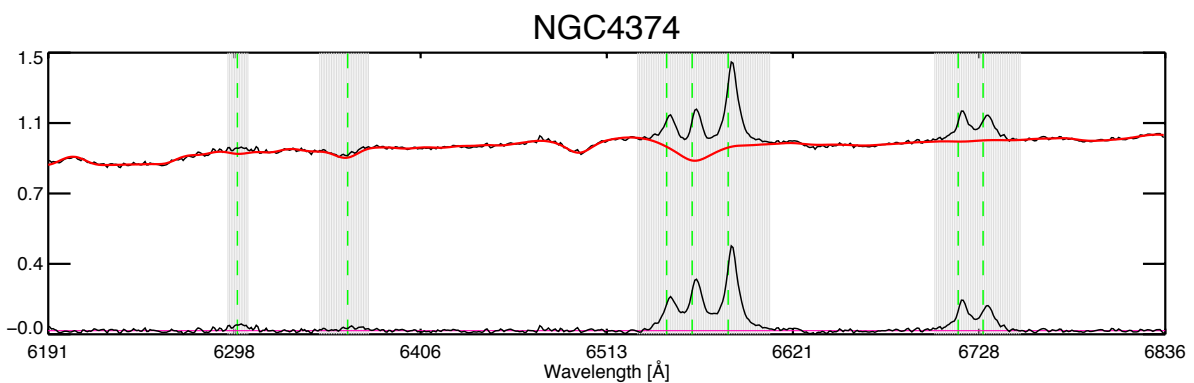
Fig. A.3 Same as Fig. A.1 but for NGC 4374.
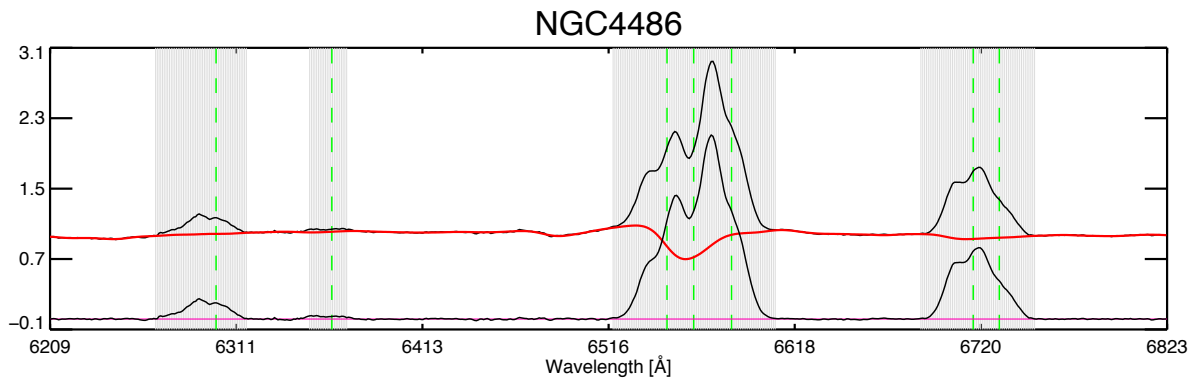
Fig. A.4 Same as Fig. A.1 but for NGC 4486.
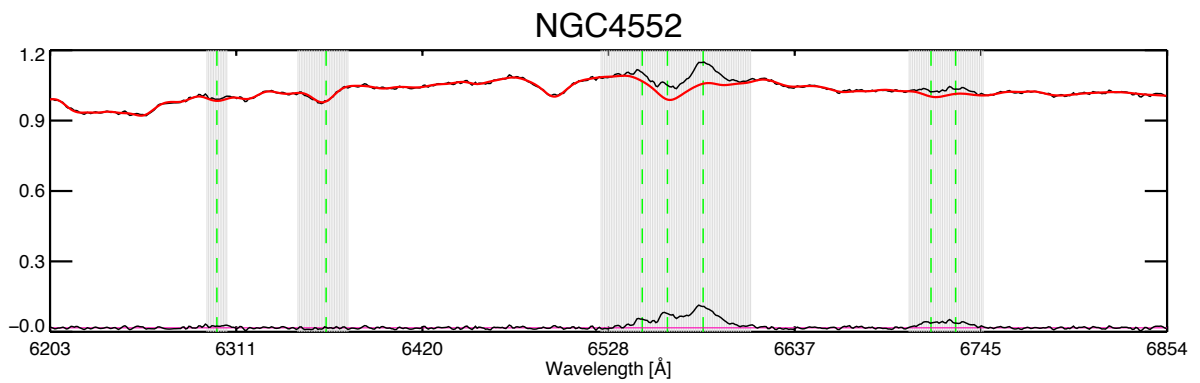
Fig. A.5 Same as Fig. A.1 but for NGC 4552.
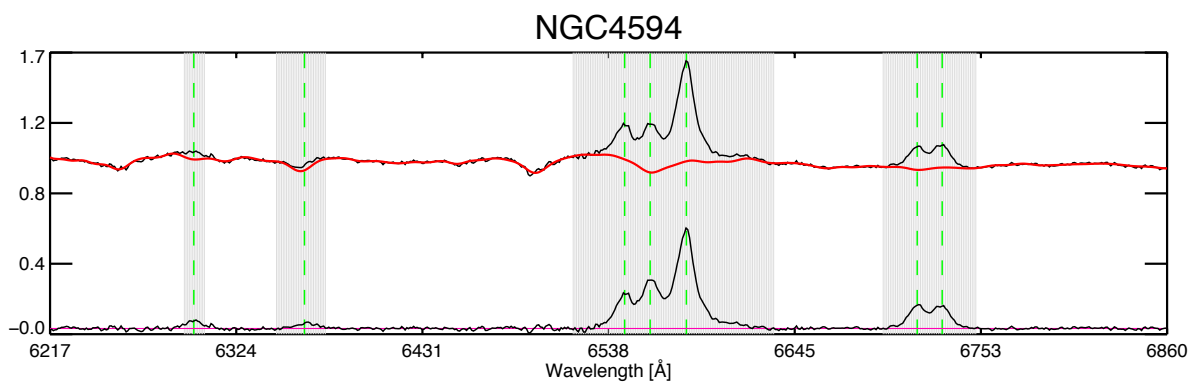
Fig. A.6 Same as Fig. A.1 but for NGC 4594.
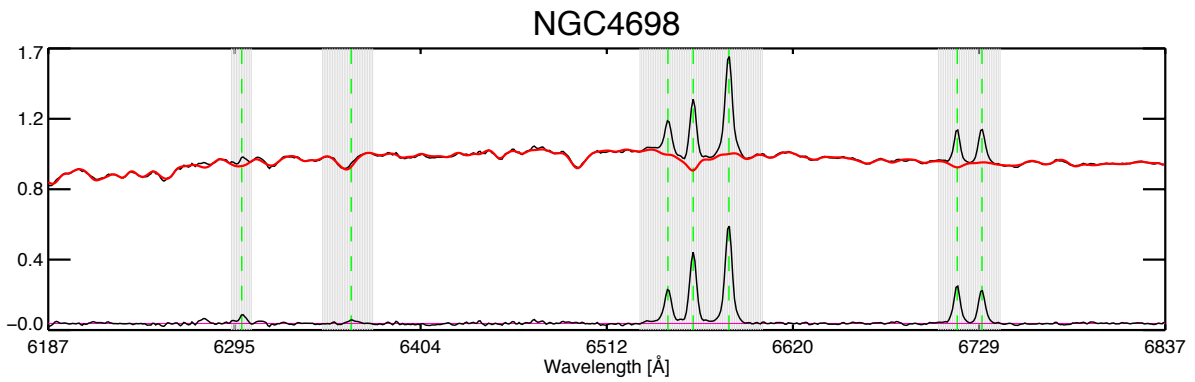
Fig. A.7 Same as Fig. A.1 but for NGC 4698.
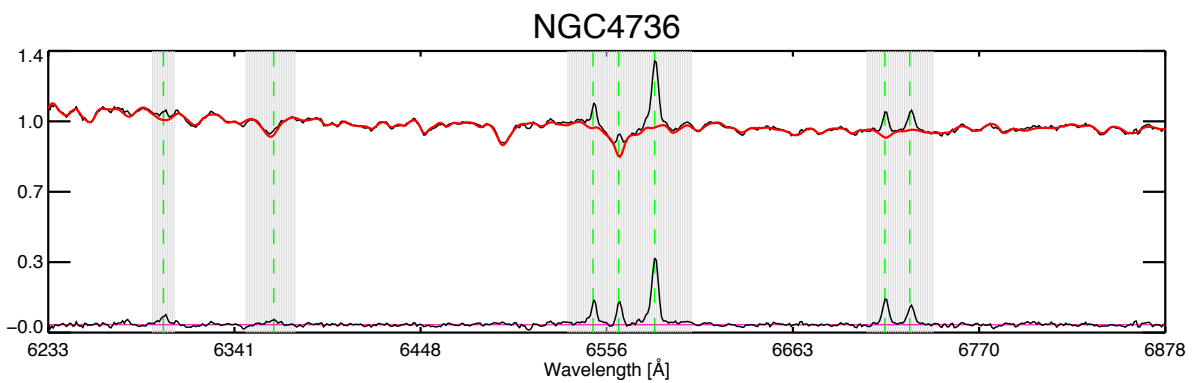
Fig. A.8 Same as Fig. A.1 but for NGC 4736.

A.2   Spectra modeling for each galaxy

We present HST images from the archive and the spectra analyzed in this manuscript for each LINER. They are arranged as follows:

- Top: Sharp divided (Márquez & Moles 1996; Márquez et al. 1999, 2003) HST image of the galaxy in the inner $10''$x$10''$. The HST filters are summarized in Table 2.2, column 9. Sharp-divided images are very useful for tracing asymmetries in the light distribution, such as bars, spiral arms, dust lanes, and rings. The method consists of dividing the original image by that obtained from the convolution with a median filter of 30 pixels. This technique allows the subtraction of the diffuse background emission facilitating the detection of small-scale variations and rouses the notion of a possible presence of both dust extinguished, and more luminous regions (e.g., Masegosa et al. 2011). The galaxy ID is indicated in the panel title. White and yellow continuous lines represent the slit used to obtain the HST/STIS and Palomar spectrum (when available), respectively. The angular scale of 1"of the image in parsecs (see Table 2.1 column 6) is indicated in the right-upper part of the image. The white dashed line indicates the PA of the major axis (see Tab. 2.1).

- Bottom-left: Line modeling of the HST/STIS spectra (see Sect. 2.3 for details). We marked each Gaussian component with different colors (identical colours mark the same kinematic components). Green lines represent the narrow component; when present, blue lines represent the secondary component, and purple lines, the broad component. The red curve shows the total contribution of all the components. The continuum range selected to calculate the standard deviation is plotted in yellow. Residuals from the fits are in the middle/lower panels. We have included the residuals of the fit without the broad component for those objects in which this component was necessary (labeled as: 'Res 1') for comparison. When the two are plotted, the final fit residuals are labeled as 'Res 2'. In these panels, the orange lines indicate the 3σ limits. If the [O I] lines are not present, their restframe position is indicated in gray in both the spectrum and residual. Wavelengths are restframe.

- Bottom-right: Line modeling for the Palomar data (same description as in previous panel) after stellar continuum modeling and subtraction (see Sect. 2.3 and Appendix A.1). The flux is in arbitrary units.
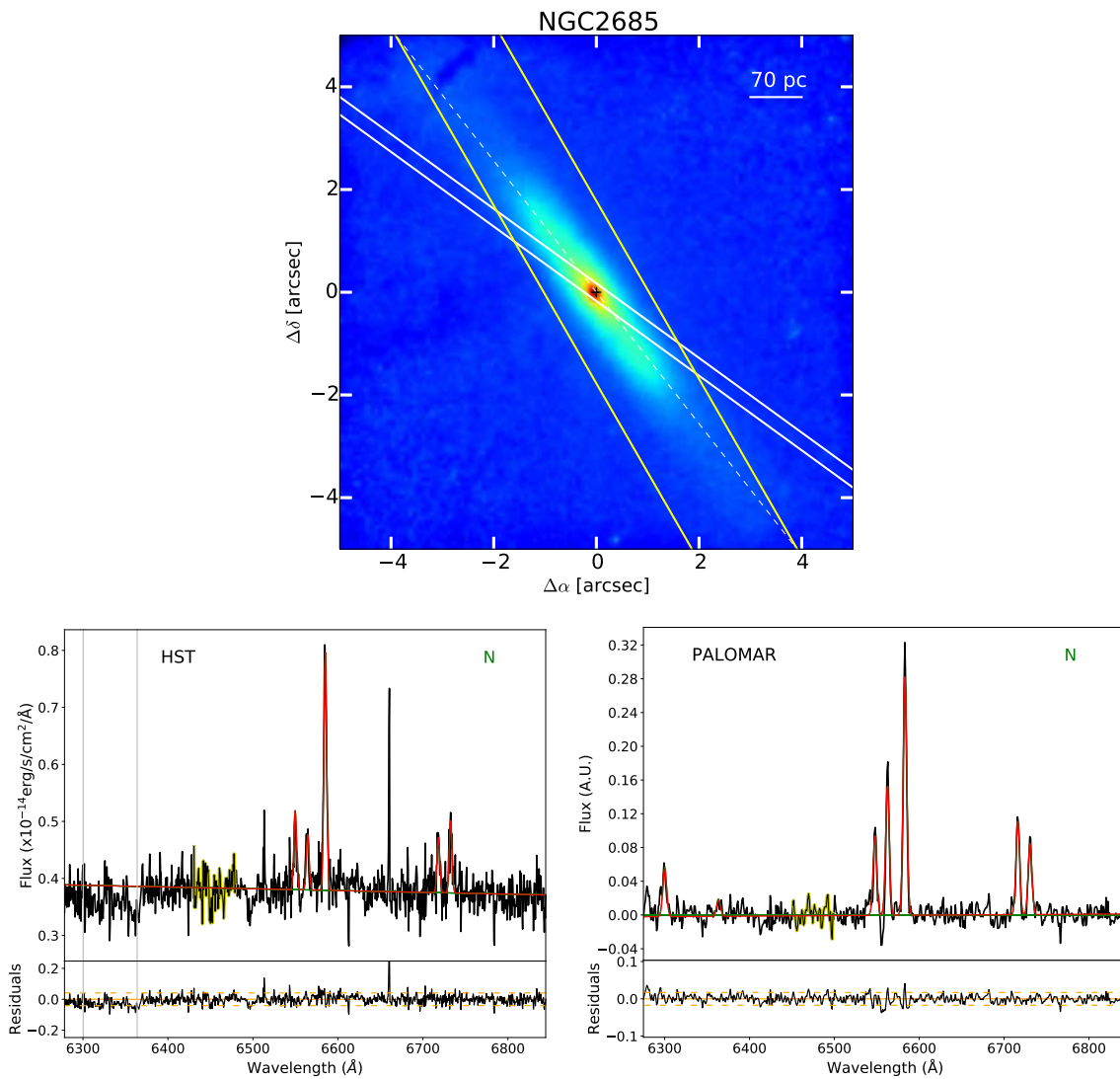
Fig. A.9 (General description in Appendix A.2). NGC 2685: The Hα-[NII] lines are unblended in both spectra. [O I] lines are not present in the HST/STIS spectrum, thus [S II] lines were used to model the other profiles. In the Palomar spectrum, [O I] lines are visible, however, no significant improvement was seen by using them to model the rest of the emission lines. All the lines are well-reproduced with a single narrow Gaussian component.
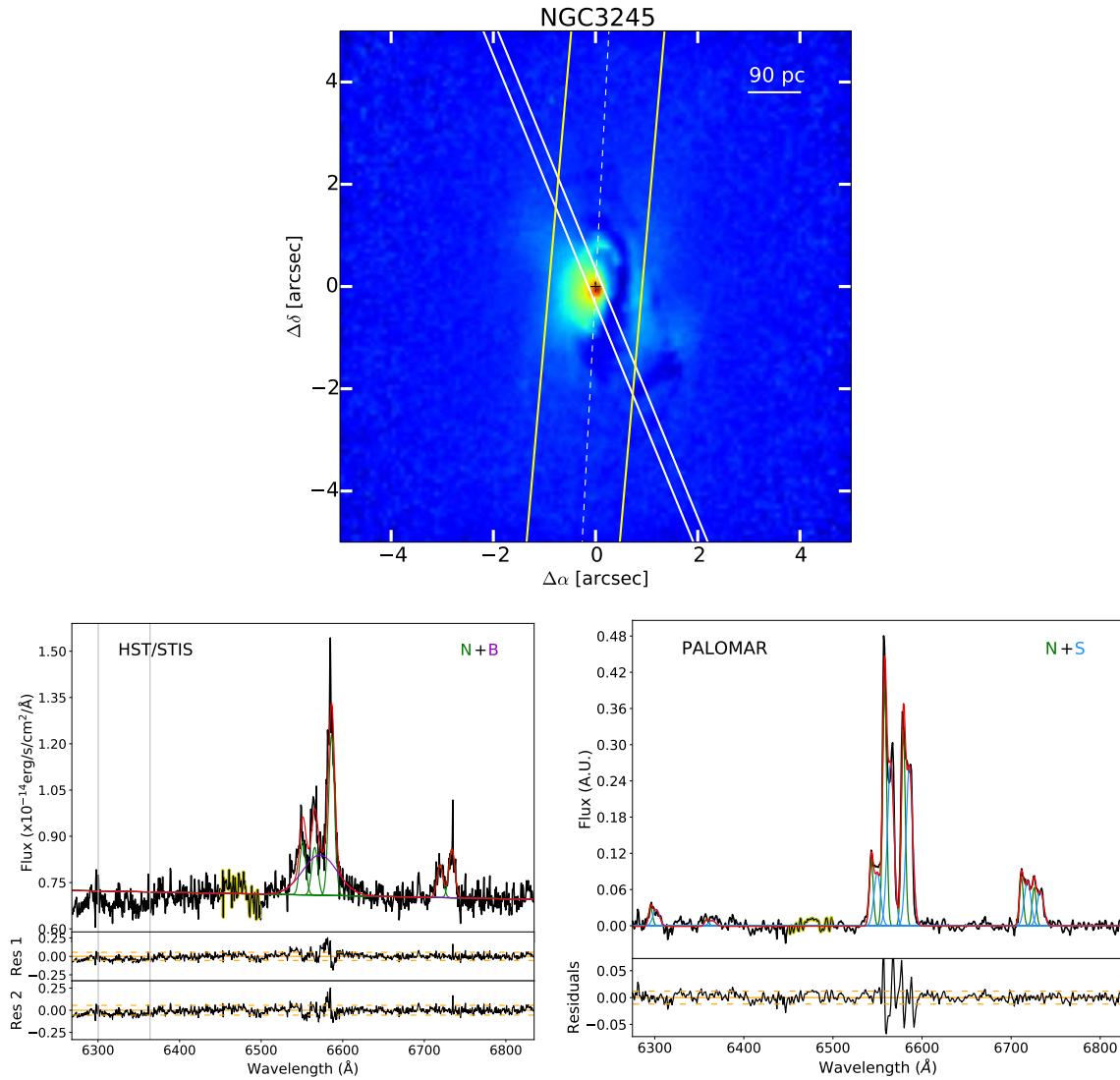
Fig. A.10 (General description in Appendix A.2). NGC 3245: For HST/STIS spectra, emission lines are modeled with a single narrow Gaussian component. The residuals were improved by adding a broad component to Hα. [O I] lines are not visible. In the Palomar spectrum, the double-peaked line profiles are modeled with two Gaussian components. As the [O I] line is rather faint, [S II] lines have been used for the modeling. Hα does not require any BLR-originated component.
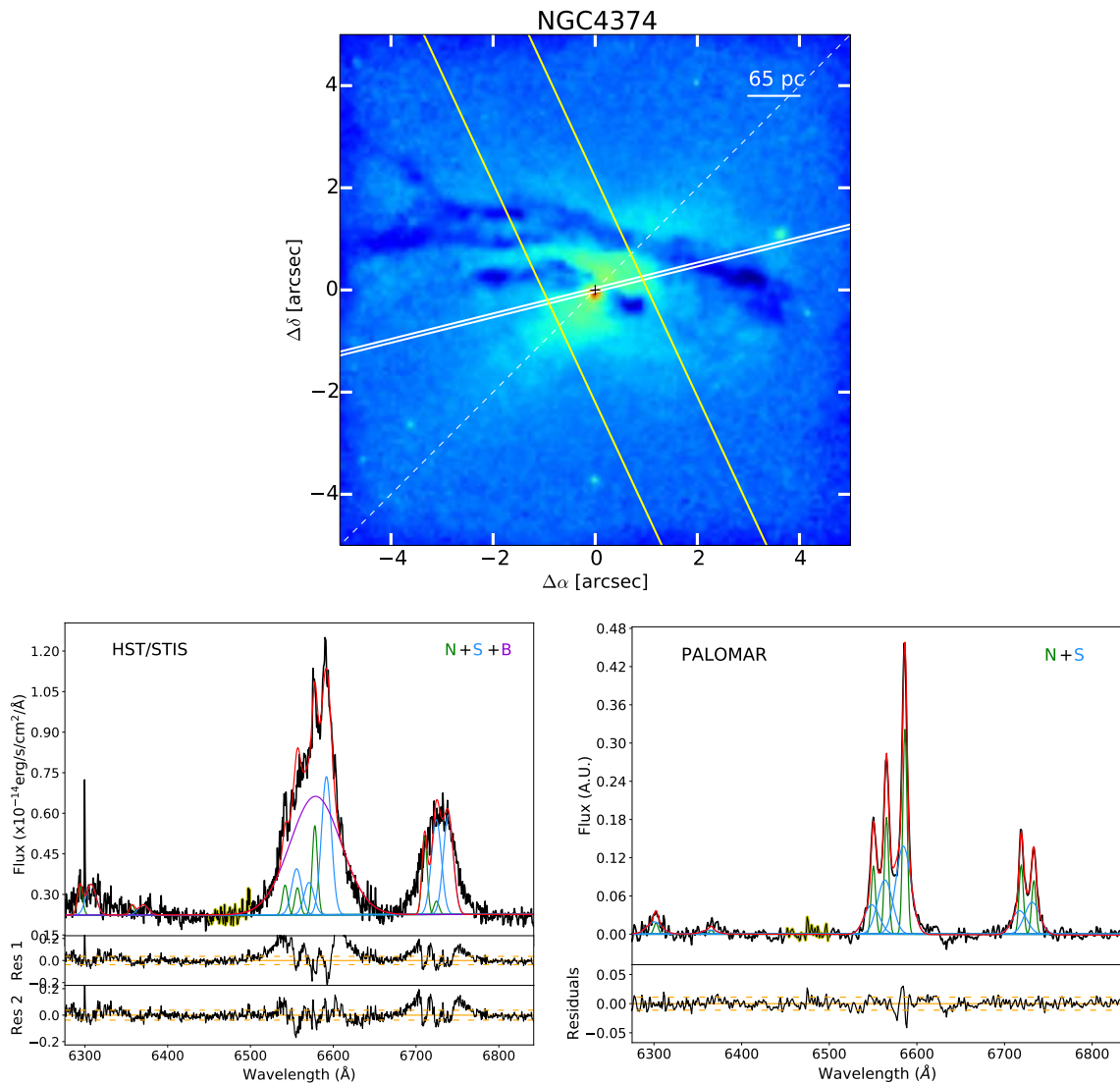
Fig. A.11 (General description in Appendix A.2). NGC 4374: In the HST/STIS spectrum, [S II] lines are severely blended, and only the [O I]λ6300Å line is visible (with low S/N). This complicated the modeling for the other lines, so the fit was performed considering the narrow peaks of [N II]-Hα blend (see Sect. 2.3), which results in high residuals under the [S II] lines. A broad component is needed in this decomposition. For the Palomar spectrum, all the emission lines are well-modeled with two Gaussian components.
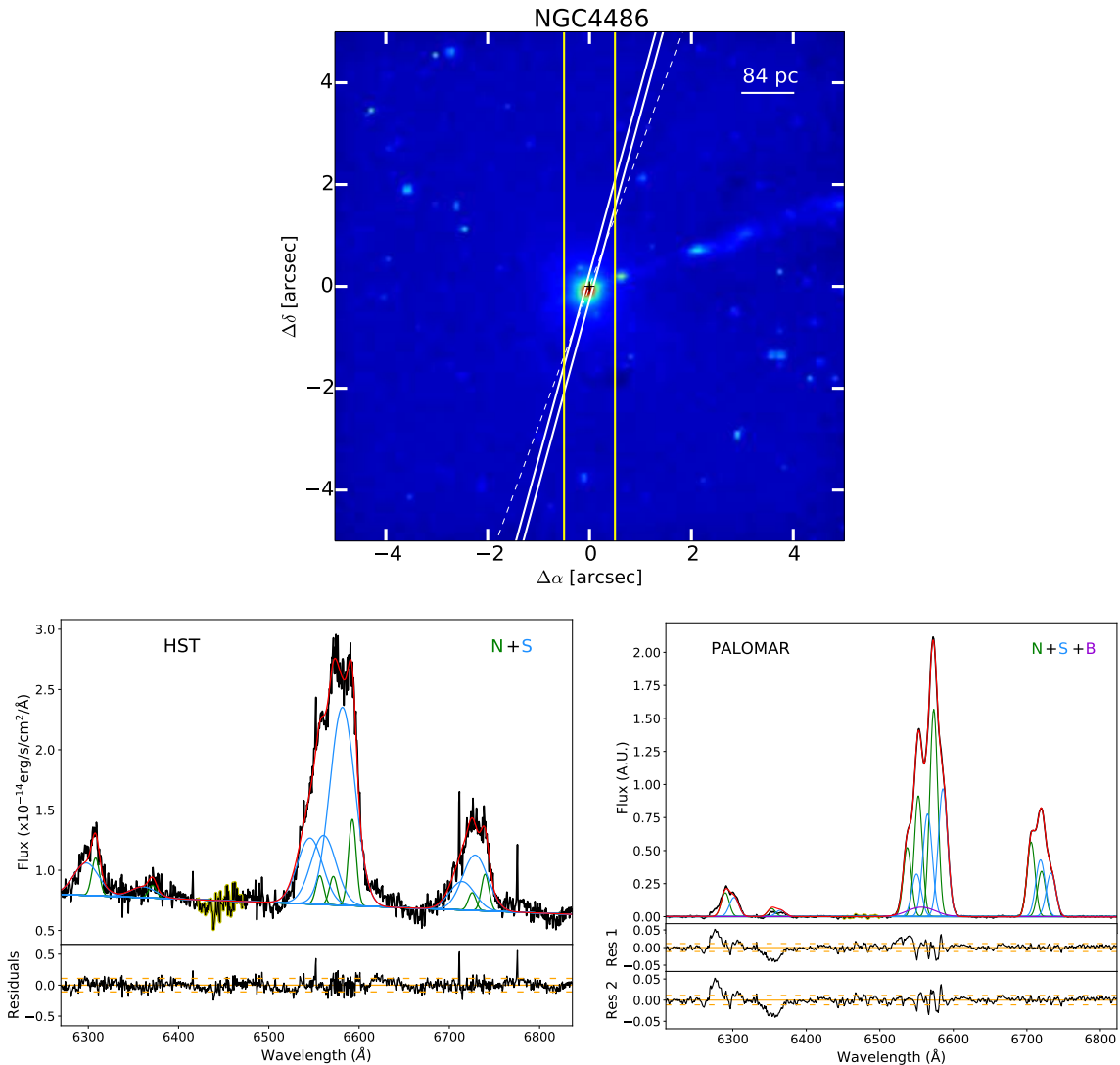
Fig. A.12 (General description in Appendix A.2). NGC 4486: In the HST/STIS spectrum, two components are required to model the broad [O I] and [S II] emissions. No broad component is needed to model the Hα line profile. For the Palomar spectrum, two components have been used to reproduce the [S II] and [O I] lines, but a very faint broad component is used for Hα.
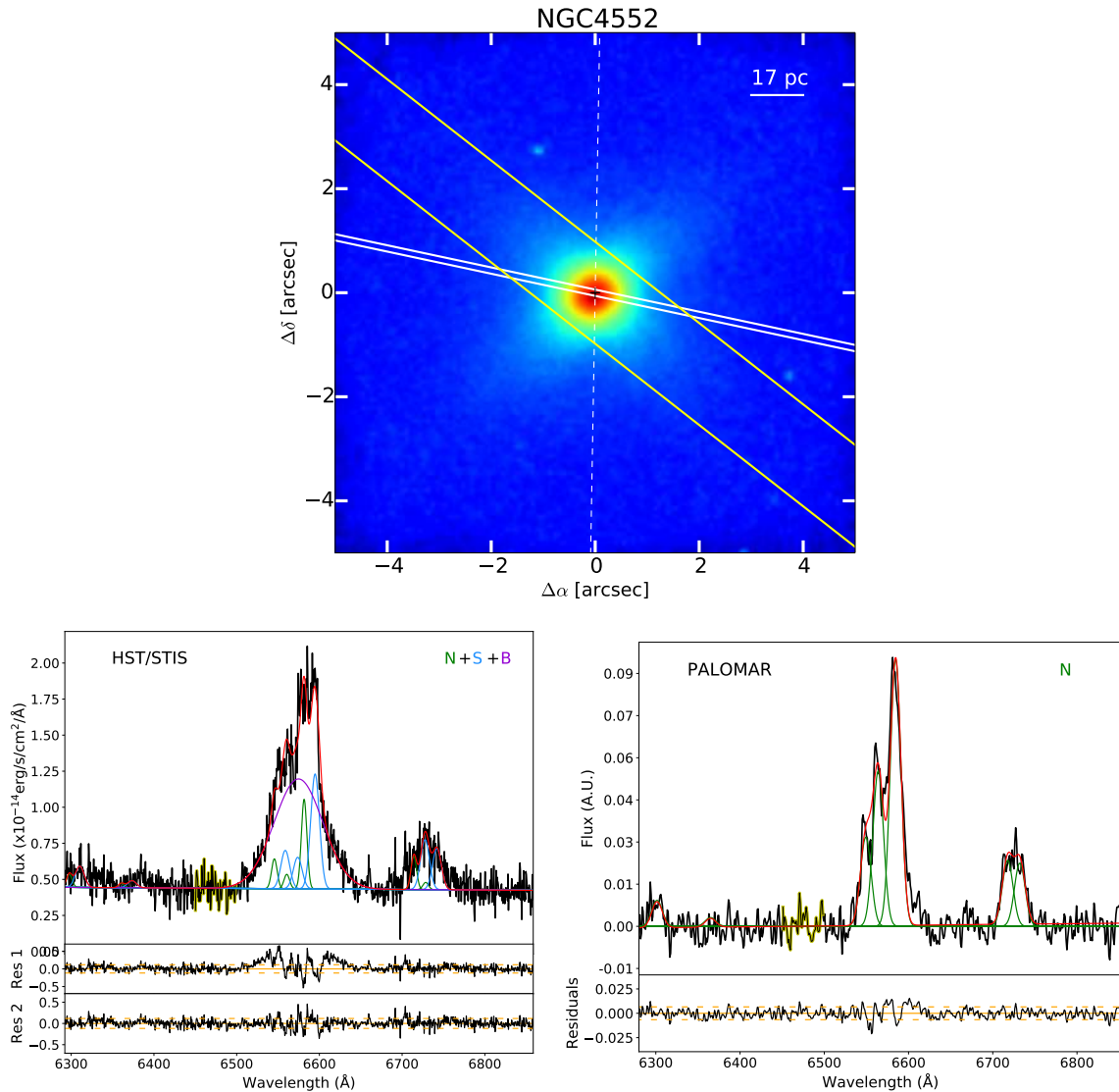
Fig. A.13 (General description in Appendix A.2). NGC 4552: For HST/STIS spectrum, a second and a broad component were necessary to model emission lines. [O I] lines are very noisy and weak, thus they could not be used as a template for forbidden lines and narrow Hα. A broad component is not required to fit the Hα profile. On the contrary, for the Palomar spectrum, all the emission lines can be reproduced with only a single component.
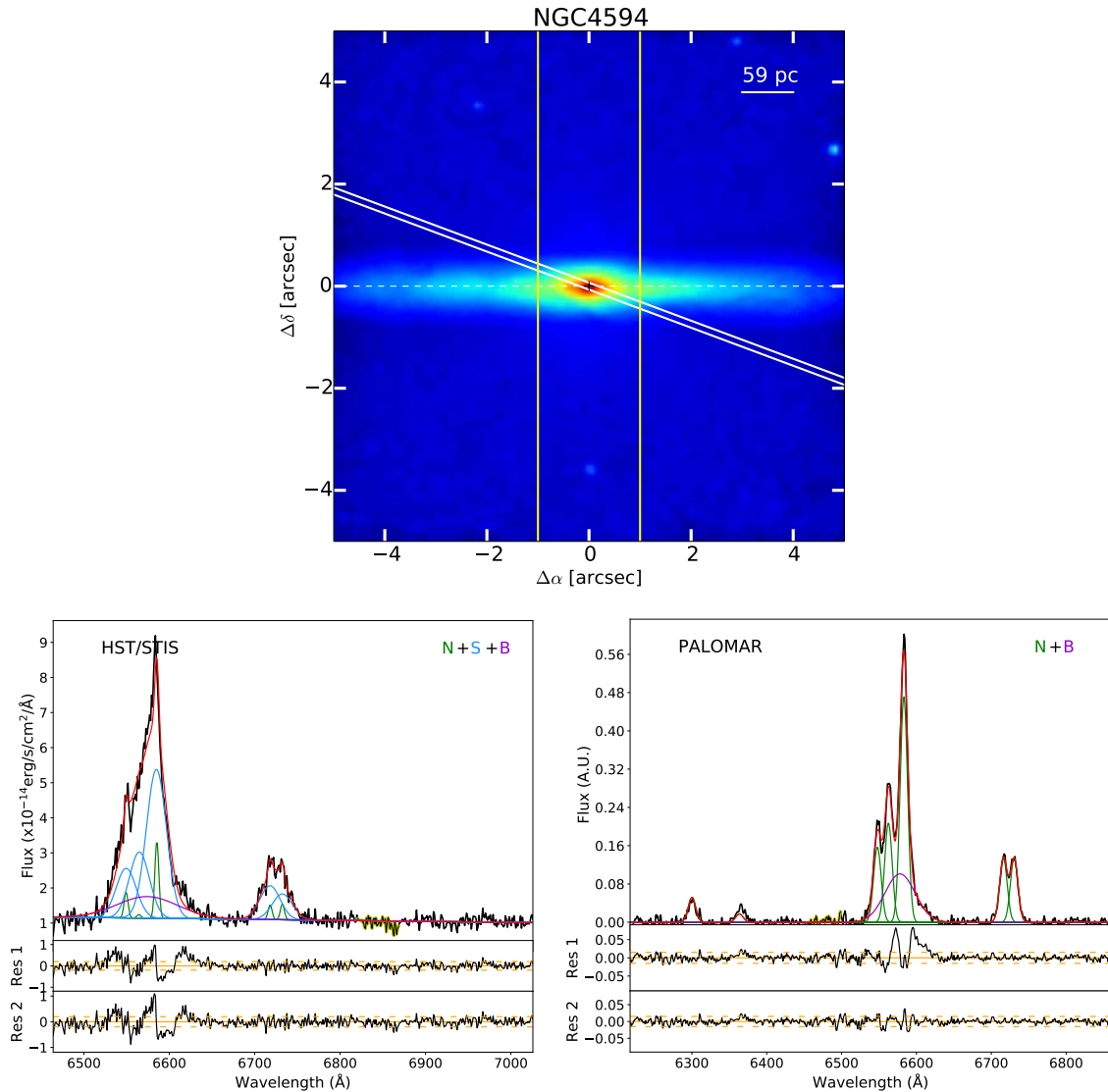
Fig. A.14 (General description in Appendix A.2). NGC 4594: Wavelength coverage of HST/STIS spectrum does not include [O I] lines. The [S II] lines have separate narrow profile peaks and a broader profile underneath. A broad component for Hα is to improve the fit. This broad component is also needed for the Palomar spectrum, although a single narrow Gaussian is sufficient for the forbidden lines.
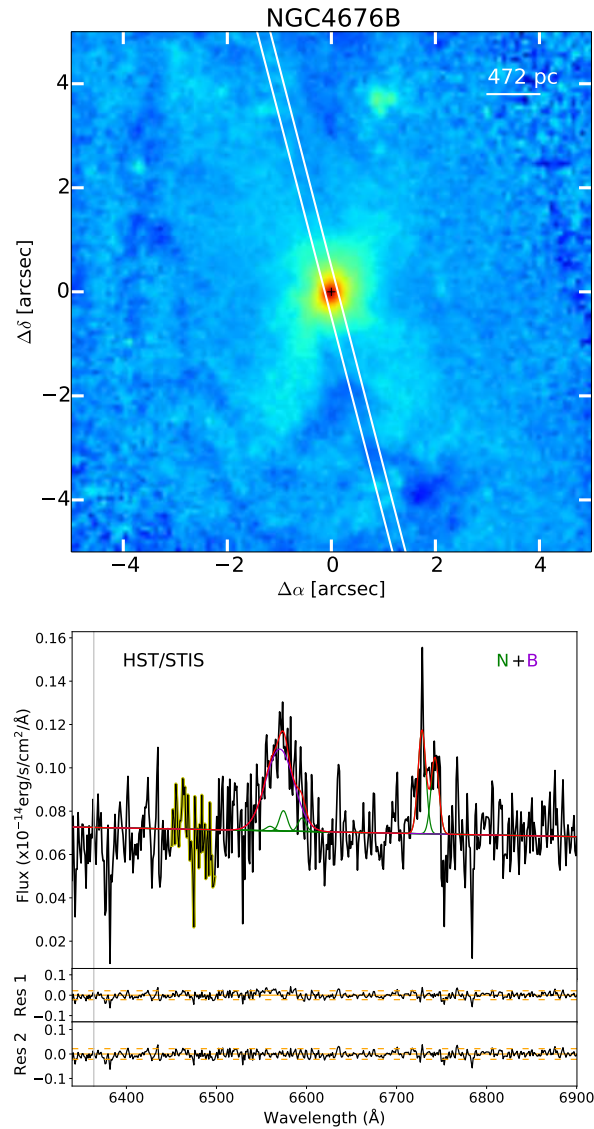
Fig. A.15 (General description in Appendix A.2). NGC 4676B: S/N of HST/STIS spectrum is generally low, and the quality of the fitting could be hampered. Both this and the wavelength range starting at 6340 Å make the [O I] lines not visible, so only the S-method could be applied. The fit slightly improves by adding a broad component. There is no Palomar spectrum for this galaxy. The PA is not indicated, as this galaxy belongs to an interacting system, and there is no clear determination of it.
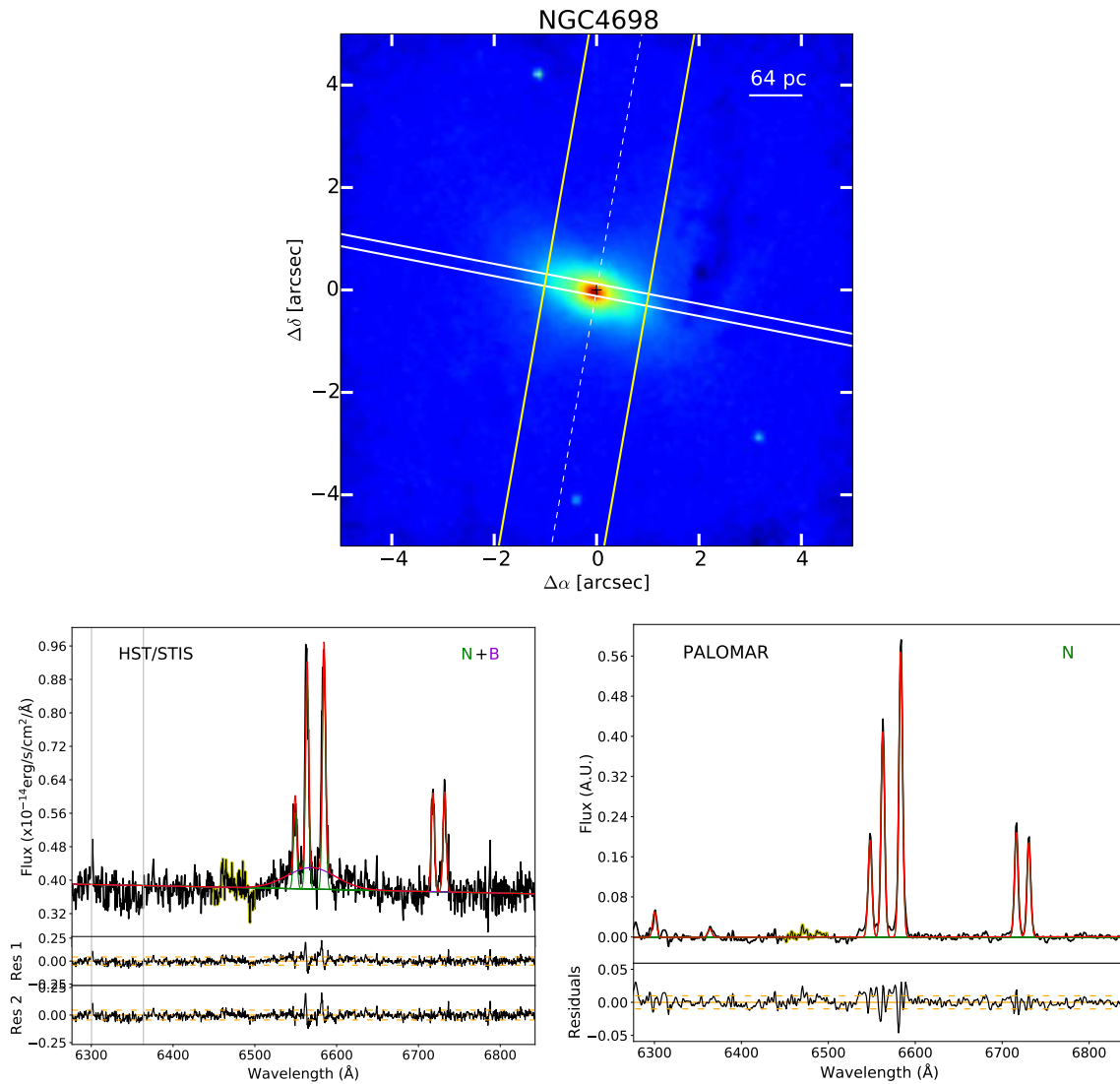
Fig. A.16 (General description in Appendix A.2). NGC 4698: [O I] lines are not visible in HST/STIS spectrum. A narrow Gaussian component is sufficient to fit [S II] lines, and a broad component in Hα to improve the modeling, although its contribution to the global fit is rather weak. For the Palomar data a single narrow component is sufficient to model the lines.
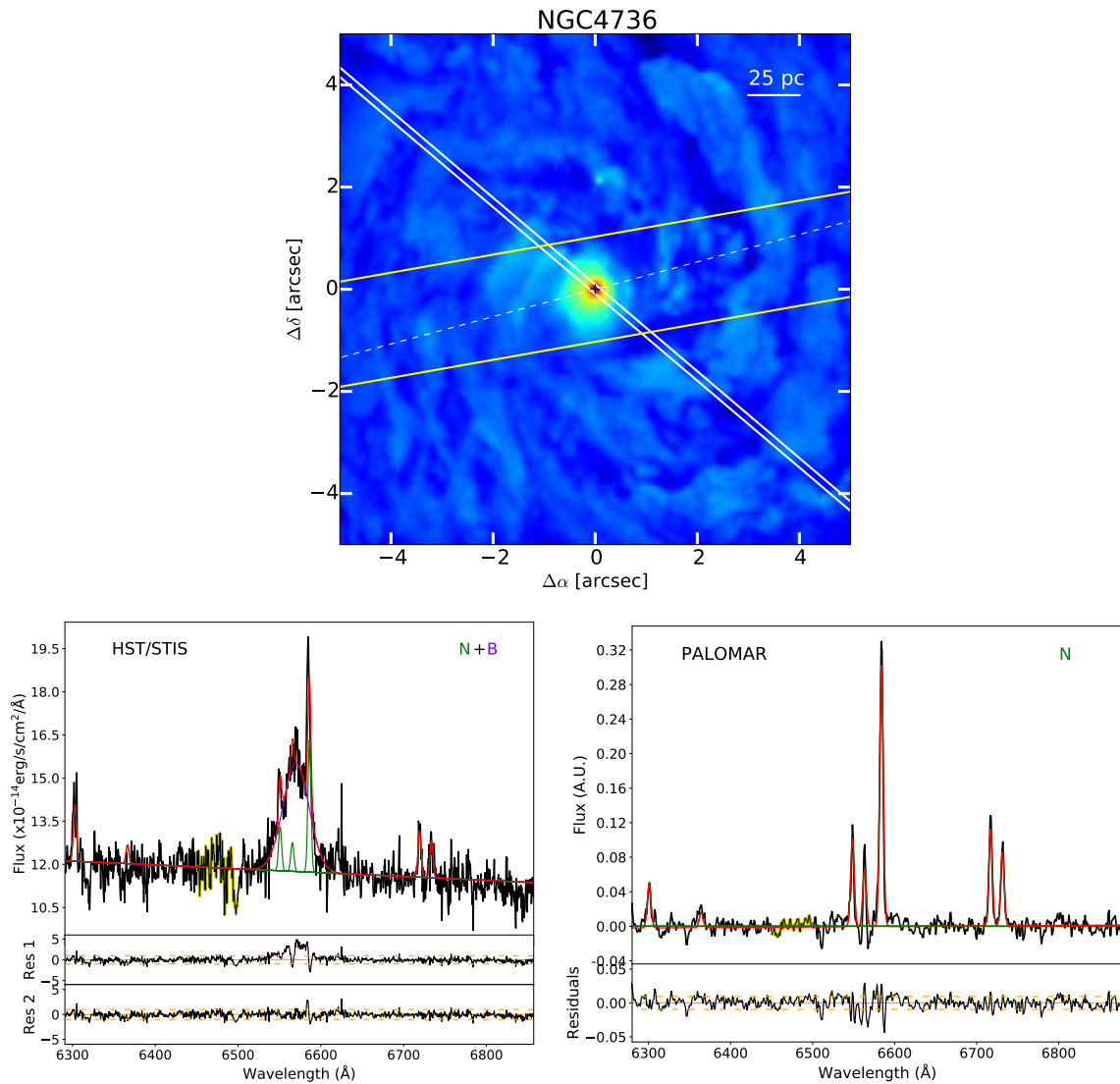
Fig. A.17 (General description in Appendix A.2). NGC 4736: Both [S II] and [O I] lines are unblended in the HST/STIS spectrum and they clearly present narrow profiles. In the Hα-[NII] lines a broad component is visible, as already reported by Constantin et al. (2015). For the Palomar spectrum, a narrow component is sufficient for fitting all the emission lines considered in our study.

Appendix B

Additional material from Chapter 3

B.1 Individual comments on galaxies

NGC 0266 (see Fig. B.1): The Hα emission of this barred galaxy was studied by Epinat et al. (2008). These authors obtained the velocity maps with data from the GHASP survey, finding gas with disturbed morphology, that could be consistent with past interactions. Considering all the regions with Hα emission of NGC 0266 (out to ~2'), we only find emission along the spiral arms and extended in the centre (see upper panel of Fig. B.1). In the work by Epinat et al. (2008), they detected additional gas distributed along the major axis of the galaxy, following the spiral arms but also randomly distributed, with large voids of gas near the centre.

NGC 0410 (see Fig. B.1): It belongs to a small group of galaxies together with NGC0407 and NGC0414 (non-active systems). We have classified the emission of this object as 'Core-halo' (see Table 3.1). No extended Hα emission has been reported previously (Lakhchaura et al. 2018). This galaxy is also included in the MASSIVE survey (Ma et al. 2014), but only the stellar kinematics is shown (Ene et al. 2020).

NGC 0841 (see Fig. B.1): González Delgado et al. (2008) characterised this galaxy as hosting a nuclear spiral and a dust lane using F547M HST imaging. Our sharp-divided image also suggests a ring-like nuclear structure. The Hα image shows strong emission in the nucleus and clumpy emission regions along the disc, probably associated to multiple star forming regions. Thus, we classified it as 'Disky'. The HI data of this system show a perturbed morphology indicative of its interaction with NGC 0834 (not in this sample), located south-east of our galaxy, although both systems are optically undisturbed (Kuo et al. 2008). In fact, the ionised and neutral gas of this galaxy follow a rotation pattern (Cazzoli et al. 2018).

NGC 2685 (see Fig. B.1): This galaxy shows a complex structure, hosting an inner, polar ring and an outer ring, proposed to correspond to a warped disc, oriented as the galaxy disc (Józsa et al. 2009). The H I gas morphology is disturbed with the presence of non-circular motions (likely due to the interaction between these two different rings), although its rotation curve is nearly that of a spiral (Józsa et al. 2009). Boardman et al. (2017) studied the [O III] kinematics for this galaxy within the ATLAS^{3D} survey, finding a disturbed velocity map, probably ascribed to gas accretion. In Hermosa Muñoz et al. (2020) the long-slit spectrum analysed shows very narrow line profiles (σ ~65 kms^{-1}) in both space- and ground-based spectra, although neither was oriented in the direction in which we see an extended ionised emission (PA~120°; see middle-down panel in Fig. B.1). This asymmetric emission coming from the nucleus, extending up to 10 arcsec, was also pointed out by Ulrich (1975) using long-slit spectroscopy around the [O II]λ3727Å line. Eskridge & Pogge (1997) obtained optical spectroscopy to study the H II regions of the galaxy and Hα imaging data where they traced the nuclear emission, stating that the asymmetry probably is produced due to extinction effects. In our work we ascribe this emission to the possible presence of an outflow, probably not detected kinematically due to the orientation of the slit (e.g. PA=38° and 54° in Hermosa Muñoz et al. 2020).

NGC 3185 (see Fig. B.2): We have classified the ionised gas emission of this galaxy as 'Disky', with a clear unresolved nuclear structure that was proposed to be a ring in several works (James & Percival 2016; Laurikainen & Salo 2017), coincident with the radio emission in Chiaraluce et al. (2019). In these works the nature of the ring is ascribed to a bar that is driven star formation in the nucleus. Laurikainen & Salo (2017) also supports that view, finding an 'X-shape' in their image, usually present in barred galaxies. On the contrary, Díaz-García et al. (2020) defines the nuclear enhanced star forming region not as a ring, but as a circumnuclear starburst for NGC 3185.

NGC 3379 (see Fig. B.2): We classified the ionised gas in this galaxy as 'Bubble', as we found evidence for extended Hα emission with an elongated shape in the innermost parts of the image (~4"). This substructure (PA~41°) is spatially coincident with a nuclear dust lane at a PA~50° (Masegosa et al. 2011). Watkins et al. (2014) also found extended emission when studying this galaxy. The Hα emission shows no particular asymmetric structures and no evidences of any previous merger interactions. When they apply a elliptical fitting to the brightness profile, their residuals show an 'X'-like shape, just as seen in our SD image (see Fig. B.2), usually present in barred systems. Trinchieri et al. (2008) discovered the presence of outflowing emission near the centre with a width of ~ 800 pc (larger than the

apparent width in our Hα image ~300 pc) with deep soft X-ray Chandra observations. Using kinematic data, Shapiro et al. (2006) obtained information within the SAURON sample of the stellar and gaseous component of this galaxy. They found a regular rotating gas disc and also evidences of non-rotational motions.

NGC 3414 (see Fig. B.2): This is a peculiar S0 galaxy, with a faint disc over a prominent bulge (Koopmann & Kenney 2006). In our images, the Hα morphology is classified as an 'Bubble'. Our results show the nuclear emission with a non-symmetric shape that could be due to the presence of dust in the south-west direction, as previously reported. Specifically, the analysis in the R band with HST data done by Rest et al. (2001) suggest the presence of dust in the nucleus. This is also confirmed by Koopmann & Kenney (2006), as they found centrally concentrated ionised gas distorted by the presence of dust. Sarzi et al. (2006) studied this galaxy using SAURON data, finding a spiral pattern in the gas distribution, that was generally rotating perpendicularly to the stellar component.

NGC 3507 (see Fig. B.2): We have classified the ionised gas morphology of this galaxy as 'Disky'. Previous Hα imaging from the literature (Sánchez-Gallego et al. 2012) trace the large scale ionised gas distribution that is also seen in our images, but with worse seeing (theirs 1.3" vs ours 1.0"). The CO map from the PHANGS-ALMA survey, which provides the CO(2-1) line emission at about 1" resolution (Leroy et al. 2021), traces molecular gas along the dust-lanes seen in the sharp-divided images, broadly resembling the ionised gas emission. A detailed analysis of the CO kinematics would reveal whether the atomic gas is participating from the putative outflow indicated by the Hα morphology.

NGC 3608 (see Fig. B.3): We have classified the Hα morphology of this galaxy as 'Disky'. Similarly, Goudfrooij et al. (1994a) found the distribution of ionised gas to be nearly face-on and symmetric, with no evidences of dust absorption. Afanasiev & Silchenko (2007) found evidences of the ionised gas rotating perpendicular to the stars, with complex stellar kinematics (counter rotating components). They found no evidences of outflows, although they do see a strong variation of the gas photometric and kinematic major axes at ~ 1-4 arcsec from the nucleus, that would indicate the presence of polar gas rotation. They claim the existence of a inclined gaseous ring of ~ 200 pc, which would be coincident with the inner contours of our Hα image. This galaxy was observed within the ATLAS3D sample, but the weakness of the measured emission lines avoid any kinematical analysis.

NGC 3628 (see Fig. B.3): The nuclear emission in this galaxy is classified as 'Dusty' given the large amount of dust that prevents from seen the galactic centre. At larger scales (up to 100") Fabbiano et al. (1990) reported for the first time the presence of an outflow in this galaxy, based on Hα observations, reporting that it is coincident with an X-ray plume. This work was latter supported by several other studies in other wavelength bands. Specifically, Tsai et al. (2012) reported the existence of is a sub-kpc scale outflow north of the disc, detected with CO(1-0) emission, expanding at 50 km s^{-1} outwards of the galaxy. This was confirmed by Cicone et al. (2014) using also molecular gas observations, and they mention that this outflow is spatially coincident with a large scale plasma outflow ($\sim$ 10 kpc) that was detected with soft X-ray observations with Chandra. The outflow studied by Tsai et al. (2012) is described as being a weak bubble coming through a central and larger outflow (Roy et al. 2016). Sharp & Bland-Hawthorn (2010) observed this galaxy with the AAOmega IFS, finding filamentary emission and outflowing gas, with evidences of large-scale shocks. We also see signatures of a large scale outflow in our data, out of the dust lane (up to ~80"), seen in Fig. 3.4.

NGC 3642 (see Fig. B.3): As in our image, Pogge et al. (2000) detect a strong nuclear source surrounded by some diffuse circumnuclear Hα emission. We have classified this emission as 'Disky', concentrated along the spiral arms, with no outflowing signatures. Scarlata et al. (2004) describe the nuclear region of this galaxy as being elongated, probably due to a dust lane, from where dusty spiral arms emerge. The kinematic study performed by Cazzoli et al. (2018) suggest the presence of two kinematic components in the nuclear spectrum, being the broadest component a candidate signature of a nuclear outflow.

NGC 3884 (see Fig. B.3): The Hα morphology of our image shows a rather elongated structure along the galaxy disc (see last row of Fig. B.3); we classified it as 'Core-halo'. The soft X-ray emission is coincident with the ionised gas (see Fig. 3.5). Despite the simple distribution of the ionised gas, in Cazzoli et al. (2018) they modelled the emission lines of the ionised gas with two kinematic components. The broadest component is blueshifted and was interpreted as a possible nuclear outflow.

NGC 3898 (see Fig. B.4): In our image we find that the distribution of the Hα gas is extended and Disky. This is consistent with previous works as Hameed & Devereux (2005) with data from the CCD imager of the Kitt Peak National Observatory, or Pignatelli et al. (2001), using imaging data from the Vatican Advanced Technology Telescope and spectra from the Isaac Newton Telescope. This latter work found that that the distribution of the ionised gas is

smooth within the bulge of the galaxy, but rather clumpy within the disc, due to the presence of H II regions. From this work, we can infer from the distribution of these regions that both the gas and stellar components are coincident in the same plane. On the contrary Carollo et al. (2002) reported an irregular nuclear emission with strong dust component with data from NICMOS/HST. They found red nuclear emission with elongated features, surrounded by a large scale disc or bar-like structure connected with a spiral feature north-east from the nucleus.

NGC 3945 (see Fig. B.4): In our Hα image we see clear hints of filamentary emission (up to ∼15"), which we have classified as 'Bubble'. This emission could be co-spatial with some internal features mentioned in previous works such as a pseudo-bulge (R∼4" Kormendy 1979), two bars (R∼2-3" Erwin & Sparke 1999) or a lens which is coincident with the larger bar (R∼26" Dullo et al. 2016). Laurikainen et al. (2011) identified the barlens for the first time oriented along the minor axis of the galaxy, however Erwin & Debattista (2017) stated that instead that feature resembles to be associated to a larger inner/nuclear disc.

NGC 4125 (see Fig. B.4): This elliptical galaxy contains a disc (e.g. van den Bosch et al. 1994; Goudfrooij et al. 1994b) and filamentary nuclear dust (e.g. Goudfrooij et al. 1994a; Braun et al. 2007), visible in our sharp-divided image, that lead us to a 'Dusty' morphological classification. This galaxy is not detected with radio emission(Filho et al. 2002), H I or CO gas (Wilson et al. 2013). The soft-X rays are much more extended and not correlated with the ionised gas, that is however correlated with the PAH emission (Kaneda et al. 2011). Pu et al. (2010) obtained the long slit spectrum of the nucleus, finding evidences of rotation along both the major and minor axes of the galaxy, and young stellar populations in the centre, which could indicate the existence of material coming from a past merger. They found the ionised gas to be oriented along the major axis of the galaxy (as we see it in our Hα image), following non-rotational motions, no ascribed to outflows.

NGC 4143 (see Fig. B.4): Our Hα morphology is classified as 'Unclear', given that the image shows extended emission along the galaxy disc, but part of the gas (or even the whole emission) could be associated to a possible outflow (see Cazzoli et al. 2018). The nuclear spectra of this galaxy was studied by Cazzoli et al. (2018) based on TWIN/CAHA observations. They found two kinematic components in the ionised gas, with the broadest component consistent with an outflow.

NGC 4203 (see Fig. B.5): The ionised gas morphology in our data set is classified as 'Unclear', as there is some extended emission that cannot be classified as coming from the disc or from outflowing emission exclusively from imaging data. Yıldız et al. (2020) characterised the object as a spiral-like, HI-rich, dusty galaxy (their Fig. C1), and gave an extinction map oriented east-west, in contrast to the north-south orientation of the Hα emission in our image. The nuclear spectrum of this galaxy has complicated profiles with several components (Storchi-Bergmann et al. 2017; Cazzoli et al. 2018). Stellar and gas kinematics from IFU spectroscopy were obtained by Boardman et al. (2017) with the Mitchell spectrograph. The derived gas kinematics, even with sparser spatial resolution, seem to indicate that non-rotational motions, associated to outflows, could be present roughly along the north-south direction.

NGC 4261 (see Fig. B.5): The Hα emission is concentrated near the nucleus, thus we classified it as 'Core-halo'. We find a correlation in the orientation of the soft X-ray emission and the ionised gas, although the first is much more extended (>15"from the centre). Baldi et al. (2019) published Hα and [O III] images obtained with HST, showing a notably less extended Hα emission (maximum 3"vs our ≥5") and more asymmetric (more emission to the west) than what we find. Boizelle et al. (2021) used high resolution (about 0.2") CO observations with ALMA, finding that the molecular gas extends 2"on both sides along the north-south axis. The molecular gas kinematics can be globally reproduced by a rotating disc model.

NGC 4278 (see Fig. B.5): This HI-rich (Yıldız et al. 2020), elliptical galaxy hosts a regular disc (Sarzi et al. 2006). The ionised gas morphology is classified here as 'Core-halo' as it is centrally concentrated (see also Masegosa et al. 2011). In Cazzoli et al. (2018) the emission lines of the nuclear spectrum show two kinematic components, one of them consistent with an inflow.

NGC 4321 (see Fig. B.5): This galaxy has been studied in different wavelength bands. Specifically, the ionised gas emission (e.g. Arsenault et al. 1990; Cepa & Beckman 1990; Knapen et al. 2000), the molecular gas (e.g. Sakamoto et al. 1995; Garcia-Burillo et al. 1998) and the HI emission, which is coincident with the optical disc (Knapen et al. 1993). Our Hα morphological image is classified as 'Disky' as it clearly follows the disc of the galaxy, the separation of the 4 spiral arms and several star forming regions (also visible in molecular gas Garcia-Burillo et al. 1998). The central region was analysed with SAURON IFS data (Allard et al. 2005), that reported an enhancement of the Hβ emission in the ring as well as two dust lanes at the end of the bar of the galaxy. The existence of dust in the disc plane makes the

definition of the spiral arms difficult (Scarlata et al. 2004).

NGC 4450 (see Fig. B.6): This barred spiral galaxy was classified as hosting a truncated star forming disc at ~60" from the nucleus, given the non-continuous Hα emission at large scales (Koopmann et al. 2001; Chemin et al. 2006). In the innermost parts of the galaxy (i.e. 5" from the centre) we find the Hα emission concentrated in a 'Core-halo' morphology. This is in agreement with the image on Koopmann et al. (2001), where the nuclear emission is not extended further out to the galaxy (<10"), except for some sparse regions at larger scales (~30", i.e.~3 kpc). Cortés et al. (2015) obtained the velocity field for this galaxy, finding two plateaus at a distance ~5" from the centre, that suggested the presence of an additional rotating component. The [O III] emission has an offset of 25° with respect to the main stellar component, that was ascribed to the recent acquisition of gas into the galaxy (Cortés et al. 2015). This additional component is also confirmed by Cazzoli et al. (2018), who detected a secondary component in the forbidden lines, although it was interpreted as outflows/inflows.

NGC 4457 (see Fig. B.6): This face-on galaxy has many star forming regions, clearly visible in our Hα image (classified as 'Disky'), found only in the inner 30" (Cortés et al. 2015). This galaxy is known to host a radio jet, although the PA is not reported in the literature (see Nemmen et al. 2014, and references therein). Both the stellar and the ionised gas components are rotating, but non-circular motions have been detected. This is seen in the gas velocity map, that is more disturbed than that of the stars, specially along the stellar kinematic minor axis (Cortés et al. 2015). In our image it is clearly visible an Hα arm in the approaching side of the galaxy, as in previous works (Chemin et al. 2006; Cortés et al. 2015). The gas kinematic centre has the most blue-shifted velocities (Chemin et al. 2006), and its centre is not spatially coincident with the stellar kinematic centre (Cortés et al. 2015). In the work by Cortés et al. (2015), they suggest that the arm and the velocity maps of the ionised gas component are indicative of ram pressure stripping effects.

NGC 4459 (see Fig. B.6): This unbarred lenticular galaxy has an extended dust disc up to ~8" from the nucleus (Pagotto et al. 2019, and references therein). The ionised gas morphology is classified here as 'Bubble', as it shows two small blobs south from the nucleus, in the direction of the molecular gas kinematic minor axis (Young et al. 2008). The blobs are not seen in previous kinematic maps of the ionised gas (Hβ line in Sarzi et al. 2006). The Hα emission is extended up to ~ 10" from the nucleus in the west-east direction (in agreement with Koopmann et al. 2001), concentrated in a disc as the Hβ emission (Sarzi et al. 2006, 2010). Various works have studied the molecular gas traced by the CO in the galaxy (Combes

et al. 2007; Young et al. 2008; Davis & McDermid 2017) which is detected along an oval shape, similar to that of the Hα, coincident with dust lanes (visible in our sharp-divided image, see third, right panel in Fig. B.6). The concentrated molecular gas suggests the existence of ongoing circumnuclear star formation (Sarzi et al. 2006). The kinematic information of the CO (2-1) suggest a regular rotating disc (Davis & McDermid 2017).

NGC 4494 (see Fig. B.6): This elliptical galaxy is characterised by an inner edge-on dusty ring of star formation (Forbes 1996). So far, our study is the first one focused on the ionised gas of this galaxy. In our image the Hα emission shows a 'Core-halo' morphology, extended up to 40" from the nucleus (with a 3σ-detection). Foster et al. (2011) found a double structure in the global kinematics derived from individual globular clusters, which they ascribe to a recent gas-rich merger, although we do not see any feature of this in the ionised gas. The stellar kinematics was further studied within the ATLAS3D survey (Krajnović et al. 2015) and the SLUGGS survey (Brodie et al. 2014), in which they found a regular rotation pattern, particularly flat in the outer parts of the galaxy.

NGC 4589 (see Fig. B.7): The ionised gas in this elliptical galaxy shows a 'Core-halo' morphology with a dust lane along the minor axis also seen in previous works (Moellenhoff & Bender 1989; Goudfrooij et al. 1994a). Moellenhoff & Bender (1989) performed a spectroscopic study of the object that revealed complex gas and stellar kinematics, with gas moving along several position angles. They associated these motions to a previous merger. This latter event may also have caused the minor-axis dust lane by accretion of external material. The ionised gas is co-spatial with the dust lane as it already settled down, which is consistent with being produced in an old merger (Moellenhoff & Bender 1989).

NGC 4596 (see Fig. B.7): It is a strong barred galaxy (Kent 1990; Gerssen et al. 1999; Laurikainen & Salo 2017) with a faint dust spiral and a compact source in the nucleus (González Delgado et al. 2008). Our image of the Hα emission reveals an outflow-like morphology, with an asymmetric profile with respect to the nucleus. Falcón-Barroso et al. (2006a) studied this galaxy within the SAURON sample (Bacon et al. 2001), mentioning the misalignment in the kinematic and photometric axes of this galaxy, due to a bar. The stellar and gaseous component are aligned, both with a regular rotation pattern. In the SAURON map, the Hβ gas is centrally concentrated (Falcón-Barroso et al. 2006a), similar to what we see for Hα in our image.

NGC 4698 (see Fig. B.7): Our Hα image has a morphology that we classified as 'Core-halo'. Erroz-Ferrer et al. (2013) included this object in their sample, where they also obtained Hα imaging with ALFOSC/NOT. They were only interested in the double-ring structure seen at large scales, hence the comparison of the nuclear region with the published Hα image is not possible. Bertola et al. (1999) reported that the nuclear disc of gas and stars are rotating perpendicularly with respect to the galaxy main disc, most probably as a result of acquisition of external gas (Corsini et al. 2012). Cortés et al. (2015) spatially studied resolved stellar and ionised gas kinematics, and suggested that this Virgo cluster galaxy is the product of an ancient merger. They also concluded that the ionised gas kinematics (traced with [O III] in the central 5") is non-planar. In Hermosa Muñoz et al. (2020) the line profiles are narrow (σ ~90 kms^{-1}) for both space- and ground-based spectroscopic data.

NGC 4750 (see Fig. B.7): The morphology of the Hα gas of this galaxy, 'Bubble', is correlated with the soft X-ray emission (see Sect. 3.5.2). Carollo et al. (2002) reported the presence of spiral features emerging from the nucleus, stronger in the north-east direction, using NICMOS/HST images. They found evidence of strong dust features and star formation. In our data, specially in the sharp-divided image, we also detect the spiral arms and the presence of dust. However, the gas seems to be outflowing from the nucleus rather than being distributed along the spiral arms, and we do not detect star-forming regions. In Cazzoli et al. (2018) the nuclear spectrum show features of an outflow (broad component in forbidden lines and narrow Hα). Indeed, the slit is oriented towards the outflow detected by our imaging data (PA = 231°).

NGC 4772 (see Fig. B.8): The Hα emission of this galaxy is classified here as 'Core-halo'. Haynes et al. (2000) reported a centrally peaked emission surrounded by diffuse gas affected by the presence of a dust lane, coincident with HI gas. They suggest that this galaxy may have gone through a merger that spread out the gas through the disc. Falcón-Barroso et al. (2006a) detected ionised gas with SAURON data that was oriented in the north-west and south-west direction, possibly coming from a ring out of the main galactic plane. Although there could be other interpretations as the main stellar and gas components of this galaxy are known to co-rotate. In our image we detect a nuclear source both in the ionised and soft X-ray emissions, that is diffuse and extended for Hα in the same direction as in Falcón-Barroso et al. (2006a).

NGC 5077 (see Fig. B.8): In our image the Hα gas seems to follow the galactic spiral arms or disc; thus we classified it as a 'Disky' morphology. The analysis of MUSE IFS data by

Raimundo (2021) confirmed the presence of a stellar distinct, counter-rotating core with complex gas dynamics. In fact, our Hα distributions are very similar. She reports the discovery of a nuclear outflow, consistent with a hollow cone intersecting the plane of the sky.

NGC 5363 (see Fig. B.8): The galaxy is classified as I0 in NED database, although the images may contradict this classification due to an inner spiral structure (Finkelman et al. 2010). In our Hα image this internal structure is seen, as in Finkelman et al. (2010), although is not detected in the R broad-band image. This galaxy shows an internal dust lane that obscures the nuclear emission, and extends further out from the nucleus (Finkelman et al. 2010). No outflow/inflow signatures are seen neither in the sharp-divided image nor in the pure Hα image in the nuclear region. However, at larger scales in our image there is extended emission, whose nature is not clear. This lead to our classification as 'Unclear'.

NGC 5746 (see Fig. B.8): This is an edge-on, quiescent spiral galaxy, with no evidences of recent mergers (Barentine & Kormendy 2012; Mosenkov et al. 2020). Our image shows a heavily obscured nucleus due to a dust lane that prevents from seeing the nuclear Hα emission. Integral field spectroscopy is reported only for the extraction of the stellar kinematics, from which the presence of a bar in determined (Molaeinezhad et al. 2016; Peters & Kuzio de Naray 2017).

NGC 5813 (see Fig. B.9): The most notable feature of this elliptical is that it hosts a kinematically decoupled core (Kormendy 1984; Krajnović et al. 2015). Carollo et al. (1997) reported the presence of a dust lane along the major axis of the galaxy, stating that the dust itself may be suggesting the existence of the two reported cores. Our image of the ionised gas reveals that is very extended emission (see Fig. 3.4) with filamentary structures that resemble an outflow. In previous Hα observations with the Imager on the SOAR telescope, Randall et al. (2011) reported the presence of filaments co-spatial with the radio emission and with cool gas. They also reported that part of the central Hα emission is anti-correlated with some inner X-rays cavities, although we do find a rough correlation with the soft X-ray emission. With MUSE IFU data, Krajnović et al. (2015) identified two counter-rotating components (visible in the emission lines) and a disturbed velocity dispersion in the stellar component. The Hα-[N II] emission revealed the presence of knots and filaments along the polar direction of the galaxy, also visible in our image. Both lines have a uniform velocity dispersion and both approaching and receding velocities with respect to the systemic velocity of the galaxy (Krajnović et al. 2015). The origin of this emission is explained in Krajnović et al. (2015) as being related to the X-rays cavities and the jet

activity, due to the interaction of the gas filaments with the plasma, being a gas reservoir of the galaxy rather than an inflow or an outflow. Despite its complex kinematics and its double nucleus, this galaxy is not believed to have gone through a major merger (Randall et al. 2015).

NGC 5838 (see Fig. B.9): This is an inclined lenticular galaxy ($i = 72°$, see Table. B.1), with a thin bar (Molaeinezhad et al. 2016; Laurikainen & Salo 2017), fast, regular disc rotation (Emsellem et al. 2004). There is reported minor axis rotation, probably produced by asymmetry effects in the velocity maps due to the presence of a nuclear dust disc (Falcón-Barroso et al. 2003). This dust disc is subtle, but visible in our broad-band image. Our narrow-band image precludes to interpret if the gas is lying in the galaxy disc or it may be produced by outflowing processes given its asymmetry. Sarzi et al. (2006) found a regular dust disc and a relatively small scale of the gas distribution (maximum extension up to ~10" north-east from the nucleus), being Hβ similar to our Hα distribution. These authors remarked its similarity with NGC 4459, both in the gas distribution and in the kinematic maps, whose ionised gas we classified here as an 'Bubble'(see individual comments for that galaxy).

NGC 5957 (see Fig. B.9): This galaxy has previous observations with the NOT telescope in the broad R filter, studied in the work by Erwin et al. (2008). However, they could not determine all their properties due to problems with the sky subtraction. Similarly, our observations of this galaxy suffered from poor sky conditions and high clouds (see Sect. 3.2), which is translated into a flux loss; we cannot state anything about the ionised gas morphology beyond the pure nuclei, due to the low signal-to-noise.

NGC 6482 (see Fig. B.9): This galaxy is the brightest object of its fossil group (Corsini et al. 2018). The ionised gas in our image has a 'Core-halo' morphology. The object was studied in the context of the MASSIVE survey (Ma et al. 2014), were Ene et al. (2018) found a regular rotation pattern in the stellar component, well aligned with the photometric axis. They found that it is one of the galaxies with more warm gas from the sample, extended up to 16 kpc, in contrast to the ionised gas that goes up to 4 kpc. They associated it to cooling flows that may be connected to the X-ray emission in the system (Pandya et al. 2017). Corsini et al. (2018) analysed the stellar and gaseous components of the galaxy via long-slit spectroscopy, finding a young stellar population that may have been produced by a recent merger or AGN feedback processes.

NGC 7331 (see Fig. B.10): This is a highly inclined spiral galaxy ($i = 72°$, see Table B.1) located in a group along other 4 galaxies (NGC 7335, NG 7336, NGC 7337, and NGC 7340).

The Hα gas is asymmetric, resembling an outflow-like morphology. Mediavilla et al. (1997) studied the ionised gas emission, in particular the [O III] lines, that were modelled with 3 different components associated to: systemic velocity, a blueshifted component and a redshifted component. They interpret the components as coming from a disc and a shell of gas, although they do not discard the presence of an outflow/inflow. Battaner et al. (2003) suggest the existence of a massive stellar formation ring, through which there is infalling matter into the inner regions of the galaxy. Inflowing and outflowing material in this galaxy were also found using H I data from the THINGS survey (Schmidt et al. 2016).

NGC7743 (see Fig. B.10): We have classified the ionised gas morphology as 'Core-halo'. The analysis of both long-slit and IFS spectroscopic data made by Katkov et al. (2011) conclude that the ionised gas present several components in the inner 1-2", one of them probably produced by the interaction of the jet from the AGN with the ambient interstellar medium. This could be related to what we see in our image, that the Hα contours in that regions shows a slightly different orientation than the outer contours (north-south vs northeast-southwest). The H$_2$ velocity field derived from K-band IFS with SINFONI allowed Davies et al. (2014) to conclude that the molecular gas is outflowing from the AGN.
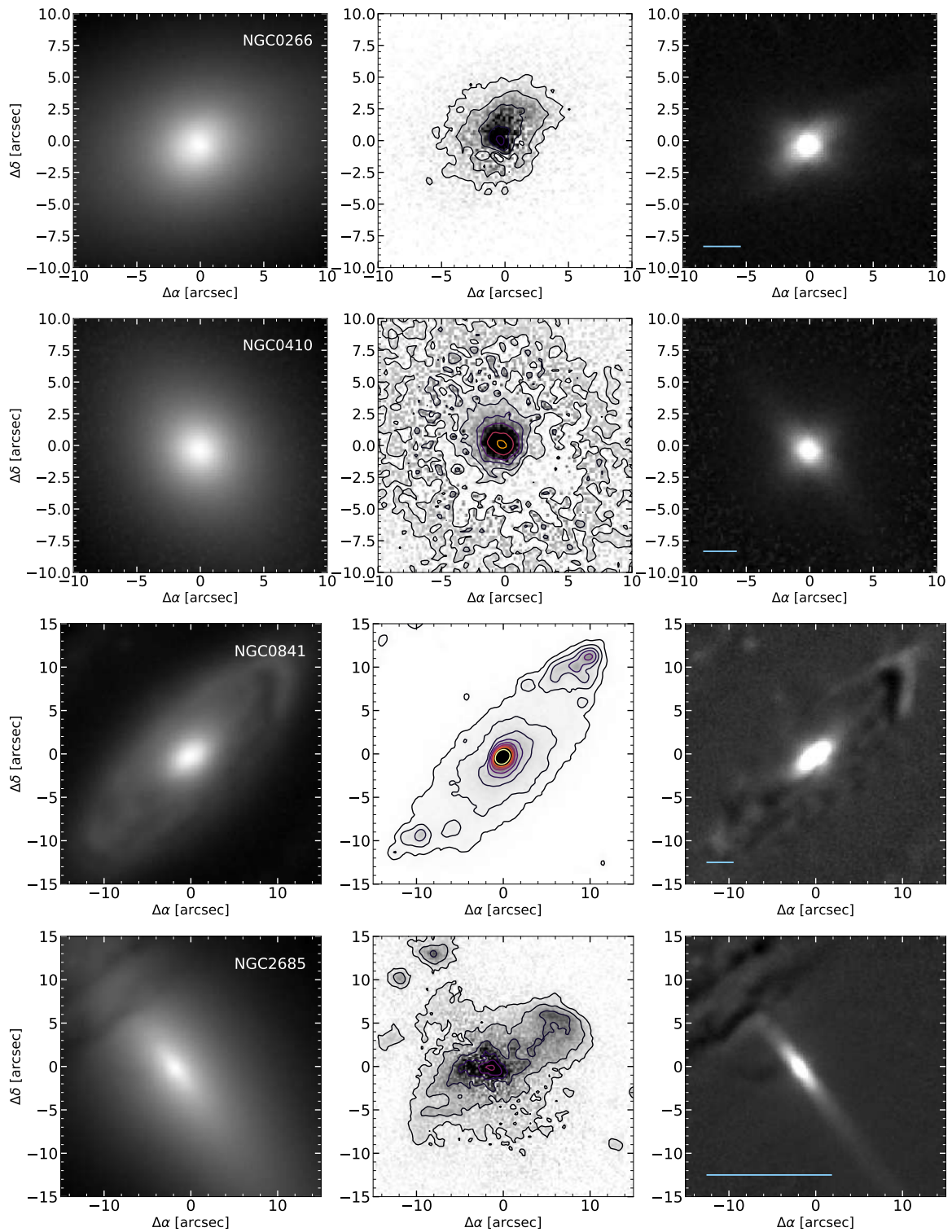
B.2 Hα and sharp-divided images

Fig. B.1 *Left:* Original NF image. *Middle:* Hα image of NGC 0266, NGC 0410, NGC 0841 and NGC 2685 with contours at 3σ (black), 7σ (black), 15σ (black), 25σ (dark-purple), 40σ (purple), 60σ (light-purple), 80σ (red), 100σ (orange) and 150σ (yellow) levels. *Right:* Sharp-divided BF image. The blue line indicates the 1 kpc scale.
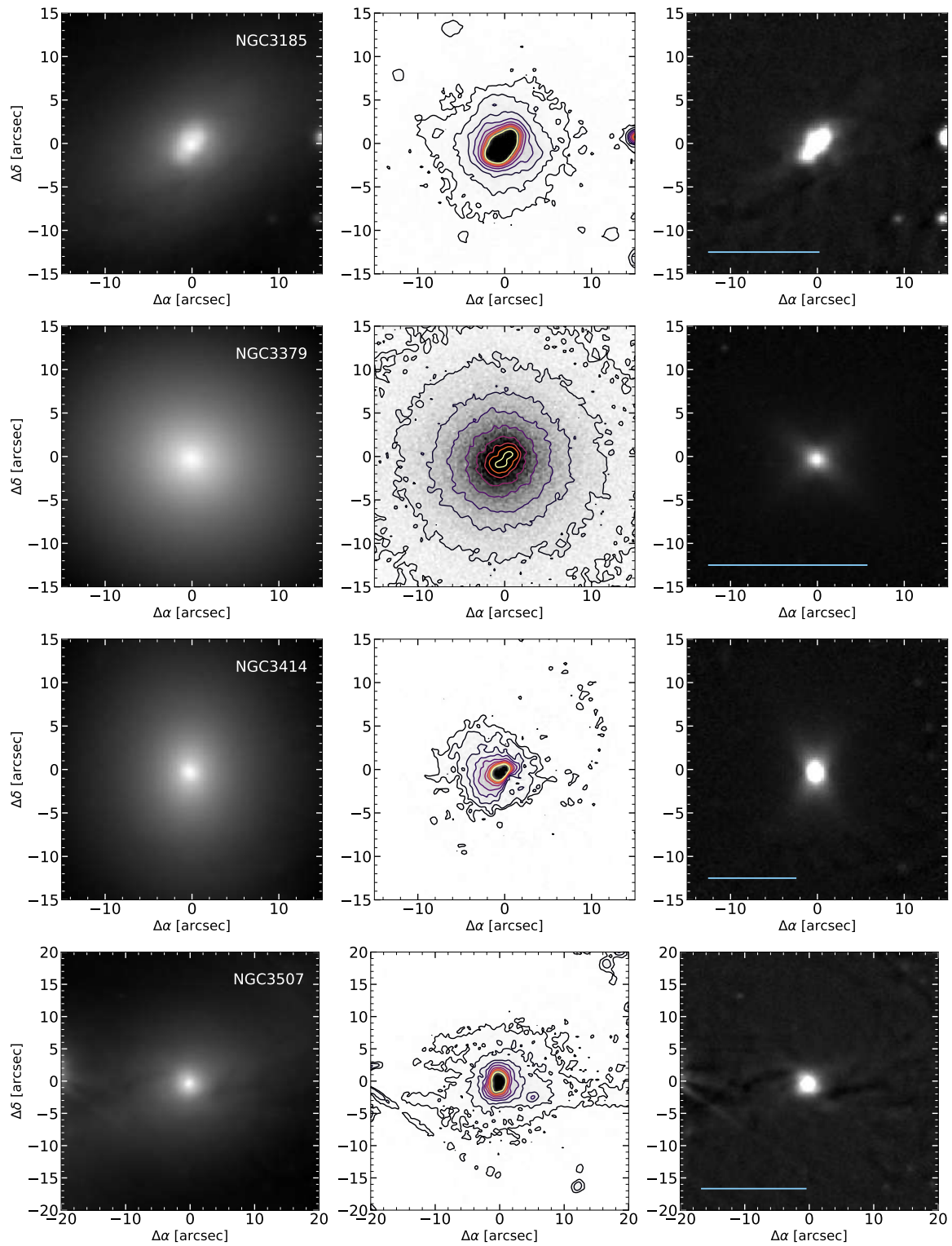
Fig. B.2 NGC 3185, NGC 3379, NGC 3414 and NGC 3507 Hα emission. The complete description is in Fig. B.1.
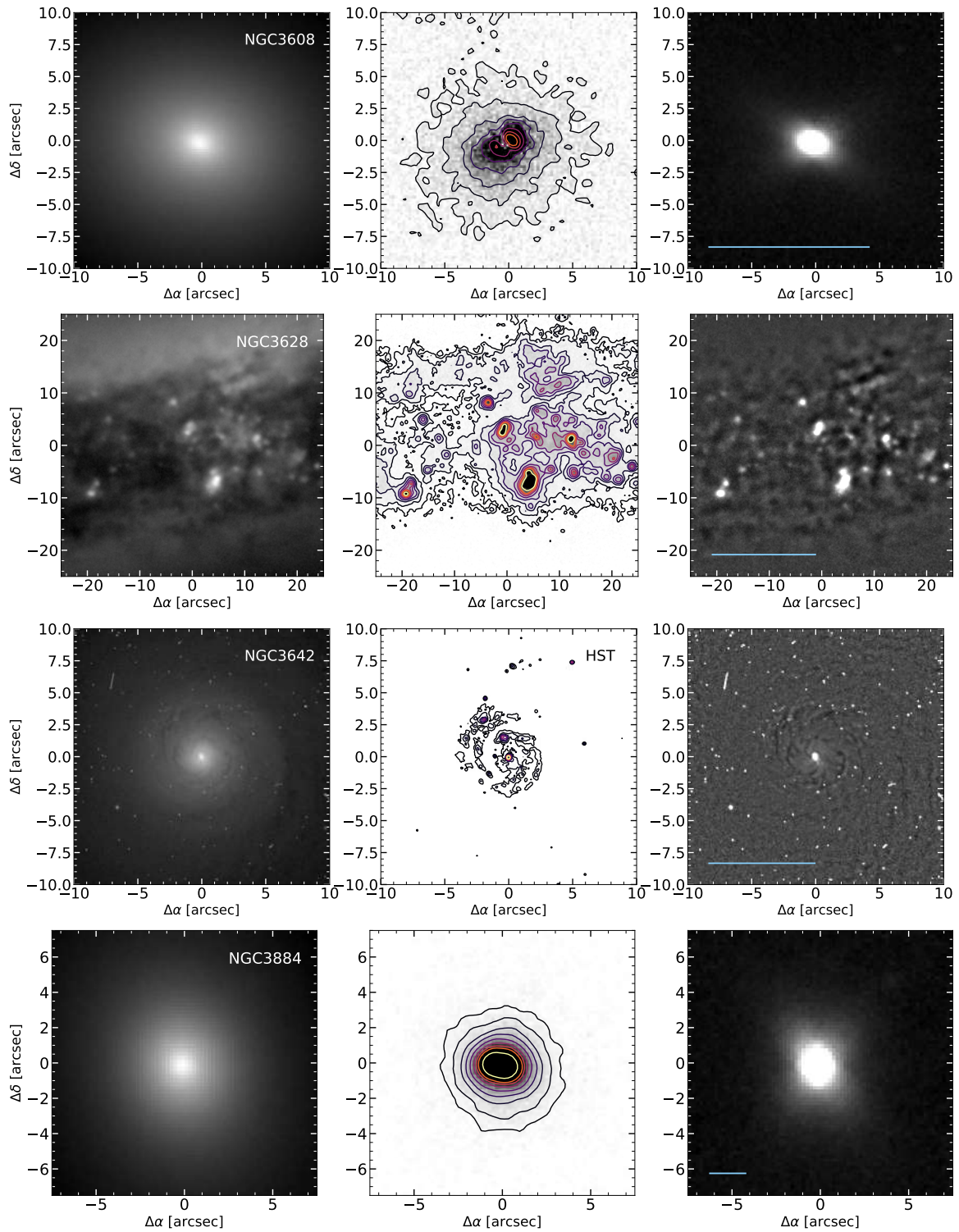
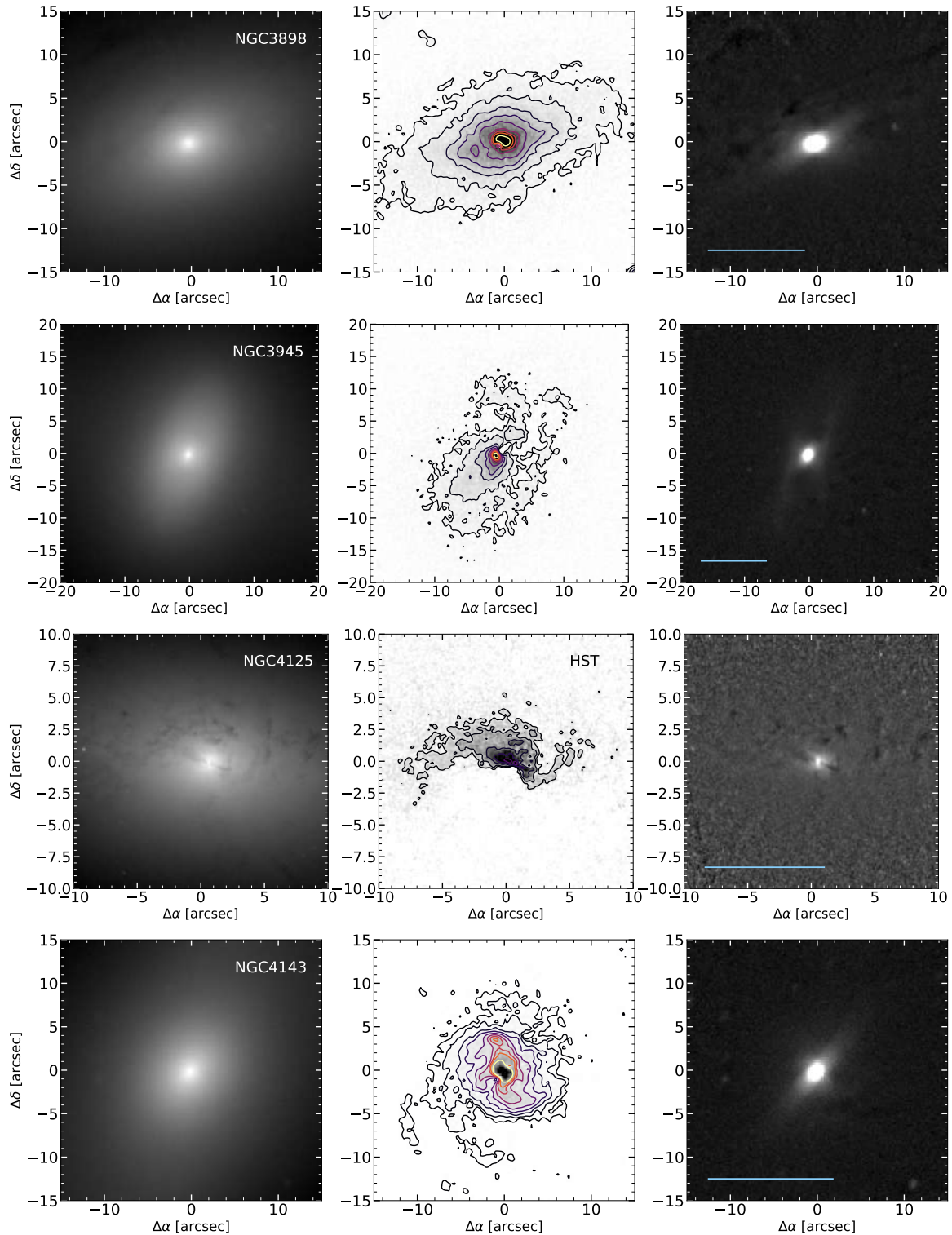Fig. B.3 NGC 3608, NGC 3628, NGC 3642 and NGC 3884 Hα emission. The complete description is in Fig. B.1.

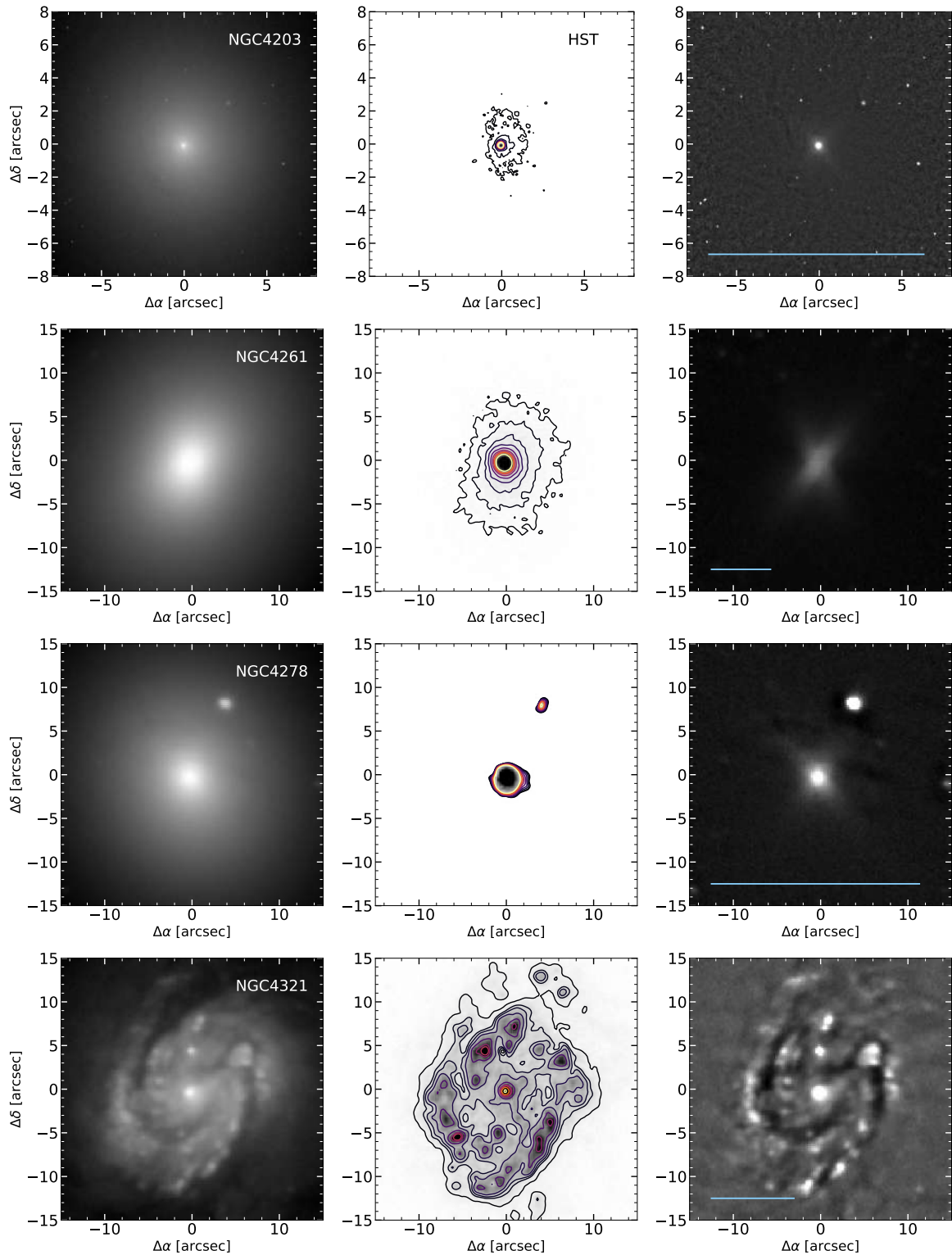Fig. B.4 NGC 3898, NGC 3945, NGC 4125 and NGC 4143 Hα emission. The complete description is in Fig. B.1.

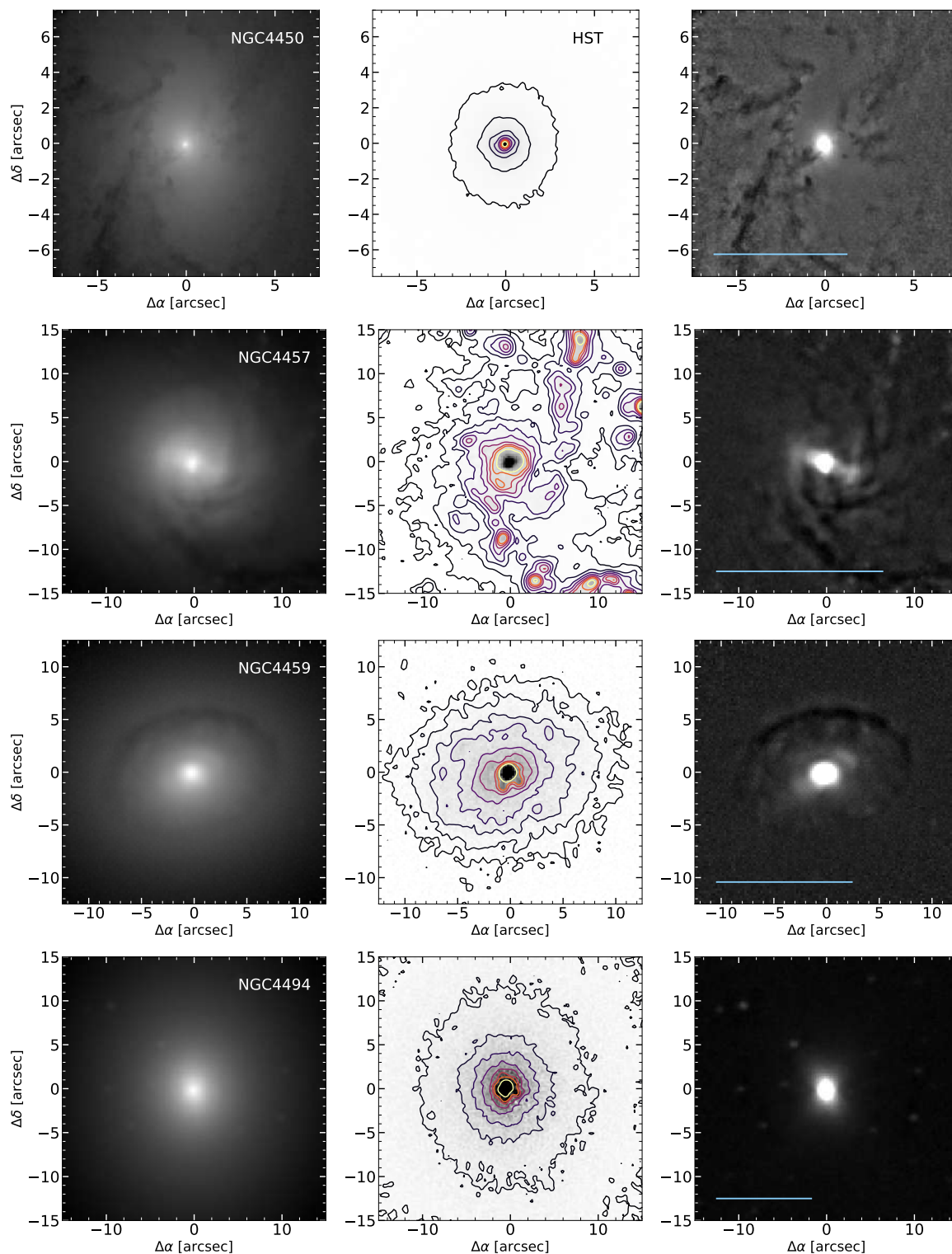Fig. B.5 NGC 4203, NGC 4261, NGC 4278 and NGC 4321 Hα emission. The complete description is in Fig. B.1.

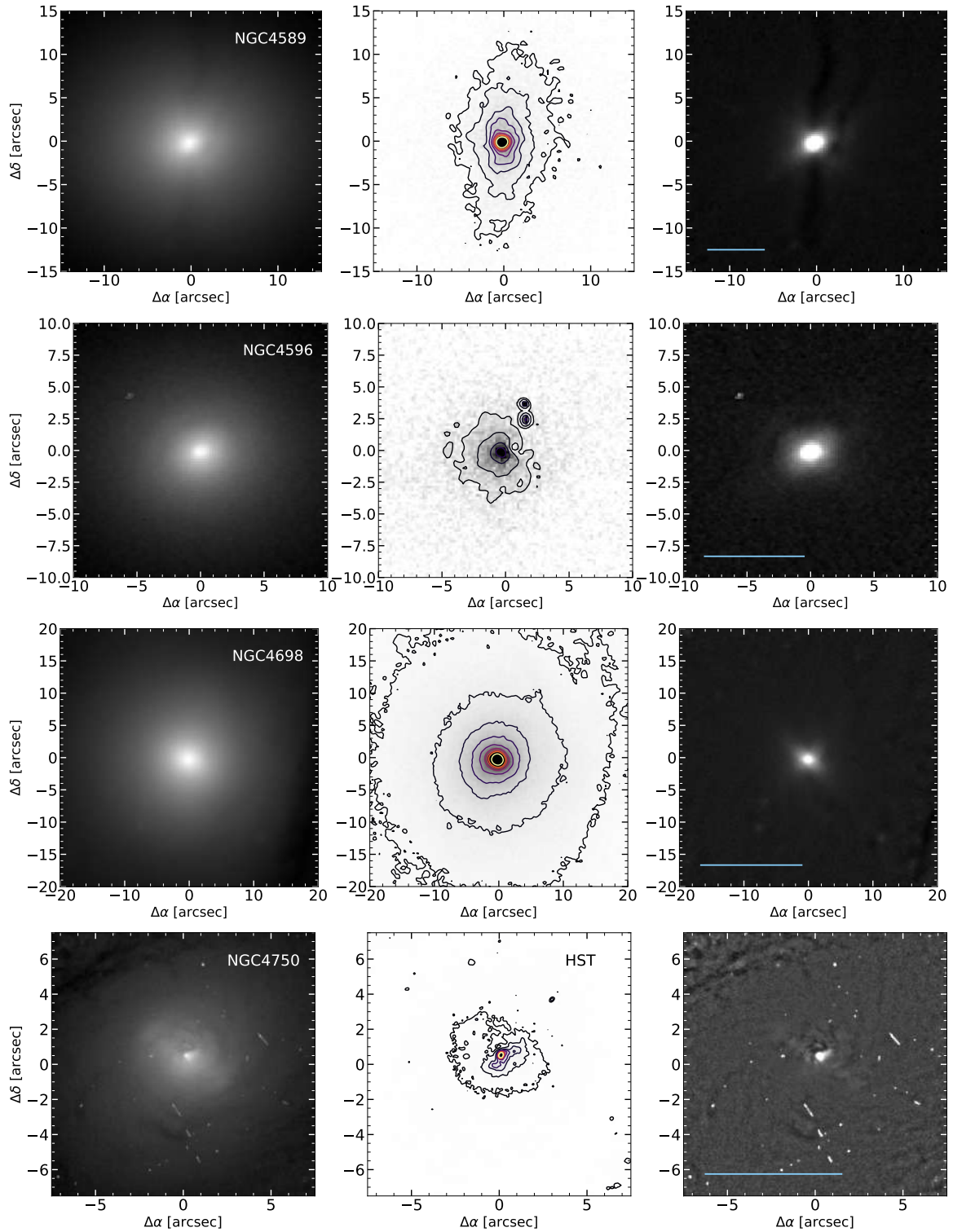Fig. B.6 NGC 4450, NGC 4457, NGC 4459 and NGC 4494 Hα emission. The complete description is in Fig. B.1.

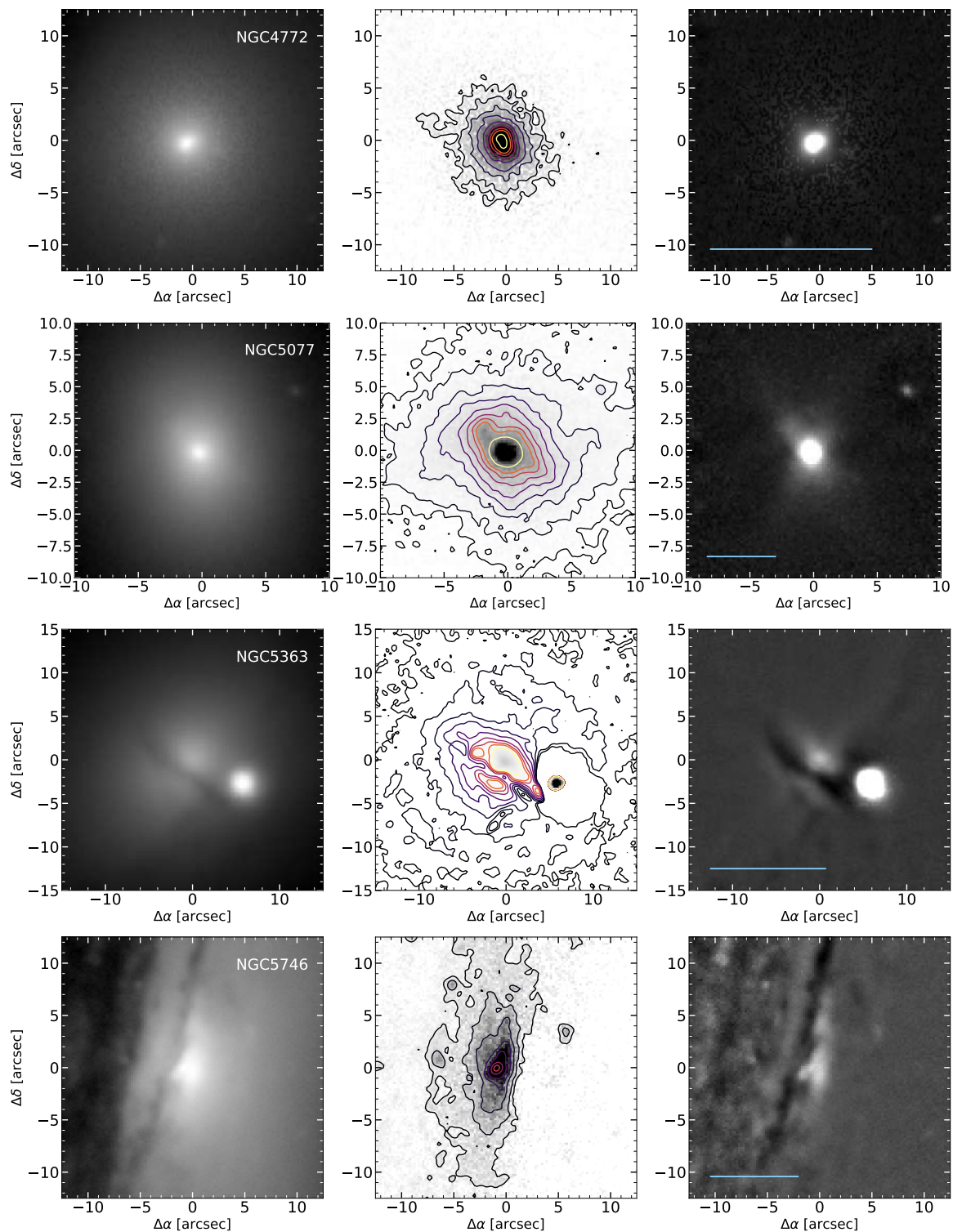Fig. B.7 NGC 4589, NGC 4596, NGC 4698 and NGC 4750 Hα emission. The complete description is in Fig. B.1.

Fig. B.8 NGC 4772, NGC 5077, NGC 5363 and NGC 5746 Hα emission. The complete description is in Fig. B.1.
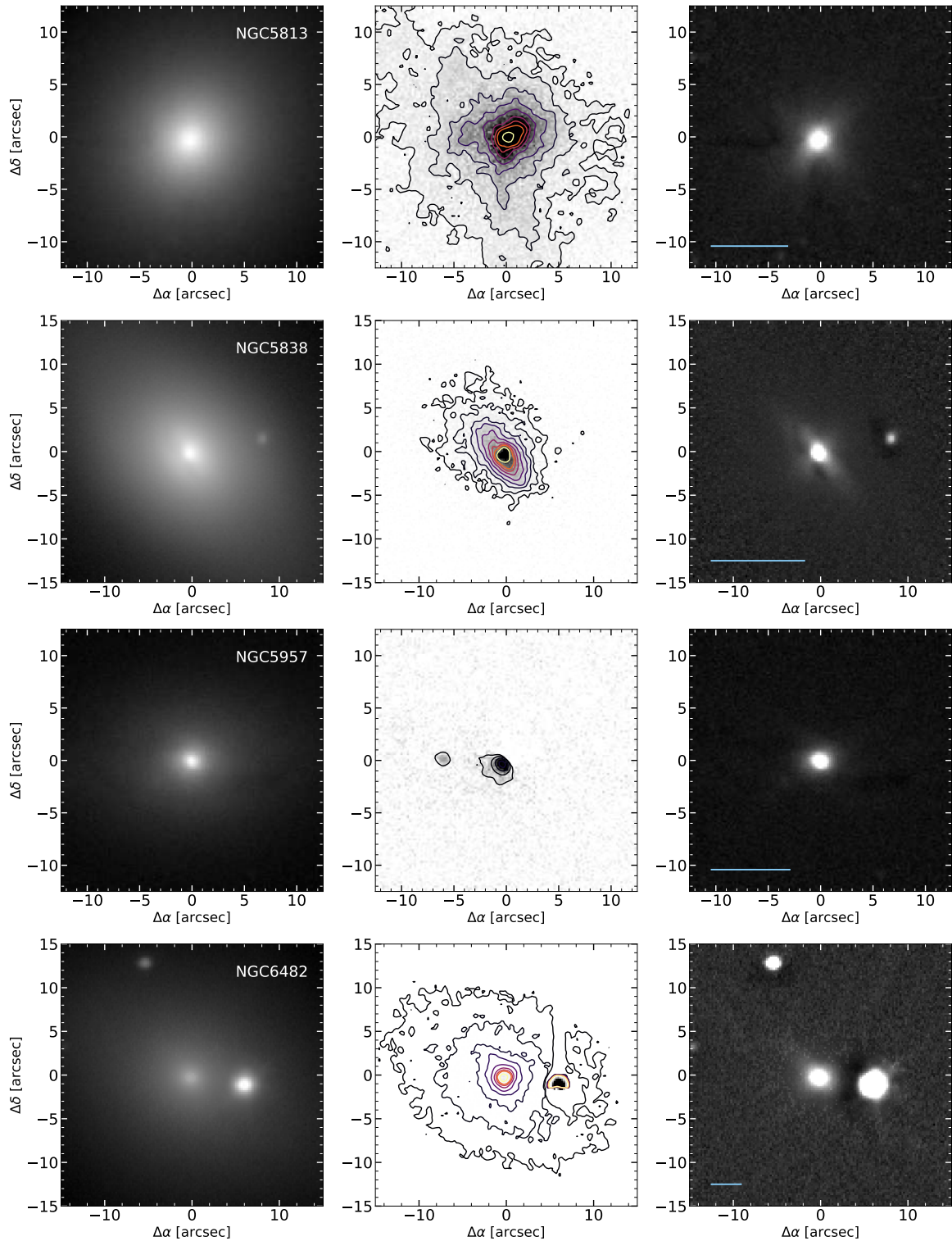
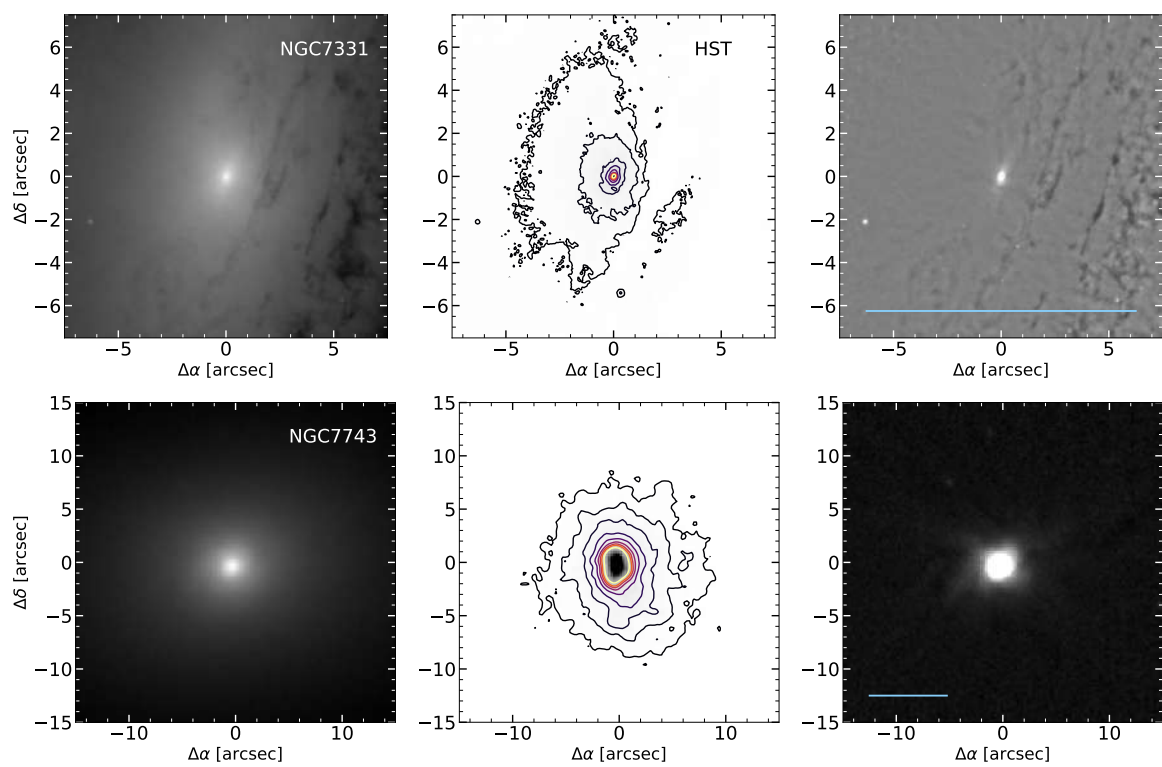Fig. B.9 NGC 5813, NGC 5838, NGC 5957 and NGC 6482 Hα emission. The complete description is in Fig. B.1.

Fig. B.10 NGC 7331 and NGC 7743 Hα emission. The complete description is in Fig. B.1.

B.3   Additional tables

Table B.1 General properties for all the 70 LINERs in Chapter 3. The line separates the new observed targets from those selected from Masegosa et al. (2011) and Pogge et al. (2000).

#	ID	Other name	RA (hh mm ss)	DEC (dd mm ss)	Morphology	z	Scale (pc as^{-1})	i (deg)	V mag	L_{bol} (10^X) (erg s^{-1})
	(1)	(2)	(3)	(4)	(5)	(6)	(7)	(8)	(9)	(10)
1	NGC 0266	UGC 508	00 49 47.80	+32 16 39.79	SB(rs)ab	0.0155	351	12	11.8	–
2	NGC 0410	UGC 735	01 10 58.90	+33 09 06.81	E+	0.0177	395	–	11.5	42.25
3	NGC 0841	IRAS 02082+3715	02 11 17.36	+37 29 49.80	(R')SAB(s)ab	0.0151	339	57	13.1	–
4	NGC 2685	IRAS 08517+5855	08 55 34.71	+58 44 03.83	(R)SB0+pec	0.0030	70	60	11.4	42.35
5	NGC 3185	HCG 44c	10 17 38.56	+21 41 17.70	(R)SB(r)a	0.0041	79	48	12.2	42.68
6	NGC 3379†	M 105	10 47 49.59	+12 34 53.85	E1	0.0030	55	–	9.3	41.44
7	NGC 3414	IRAS 10485+2814	10 51 16.21	+27 58 30.36	S0 pec	0.0049	100	44	11.1	41.39
8	NGC 3507	UGC 6123	11 03 25.36	+18 08 07.62	SB(s)b	0.0033	62	32	–	<40.51
9	NGC 3608	UGC 6299	11 16 58.95	+18 08 55.26	E2	0.0041	80	–	10.6	41.51
10	NGC 3628	IRAS 11176+1351	11 20 16.97	+13 35 22.86	Sb	0.0028	51	–	9.5	41.47
11	NGC 3642	IRAS 11194+5920	11 22 17.89	+59 04 28.25	SA(r)bc	0.0053	121	34	12.2	–
12	NGC 3884	UGC 6746	11 46 12.18	+20 23 29.93	SA(r)0/a	0.0233	496	51	12.6	–
13	NGC 3898	IRAS 11465+5621	11 49 15.37	+56 05 03.69	SA(s)ab	0.0039	91	55	10.7	<42.08
14	NGC 3945	IRAS 11506+6056	11 53 13.73	+60 40 32.00	SB(rs)0	0.0043	100	50	10.8	40.66
15	NGC 4125	IRAS 12055+6527	12 08 06.02	+65 10 26.90	E6 pec	0.0060	107	–	9.7	<42.04
16	NGC 4143	UGC 7142	12 09 36.06	+42 32 03.00	SAB(s)0	0.0032	70	52	12.1	–
17	NGC 4203	IRAS 12125+3328	12 15 05.05	+33 11 50.38	SAB0-	0.0036	77	21	11.6	–
18	NGC 4261	3C 270	12 19 23.22	+05 49 30.78	E2-3	0.0074	148	–	11.1	42.60
19	NGC 4278†	IRAS 12175+2933	12 20 06.82	+29 16 50.72	E1-2	0.0021	42	–	10.2	42.53
20	NGC 4321	M 100	12 22 54.83	+15 49 18.54	SAB(s)bc	0.0052	106	32	9.5	42.03
21	NGC 4450	IRAS 12259+1721	12 28 29.63	+17 05 05.81	SA(s)ab	0.0065	134	43	10.9	–

Table B.1 Continue.

#	ID	Other name	RA (hh mm ss)	DEC (dd mm ss)	Morphology	z	Scale (pc as^{-1})	i (deg)	V mag	L_{bol} (10^X) (erg s^{-1})
(1)		(2)	(3)	(4)	(5)	(6)	(7)	(8)	(9)	(10)
22	NGC 4457	IRAS 12264+0350	12 28 59.01	+03 34 14.09	(R)SAB(s)0/a	0.0029	53	32	10.6	42.12
23	NGC 4459	IRAS 12264+1415	12 29 00.01	+13 58 42.14	SA(r)0+	0.0040	78	41	10.3	39.90
24	NGC 4494	IRAS 12288+2603	12 31 24.10	+25 46 30.91	E1-2	0.0045	93	–	9.8	40.31
25	NGC 4589	IRAS 12353+7428	12 37 24.99	+74 11 30.92	E2	0.0066	155	–	10.7	42.23
26	NGC 4596	IRAS 12373+1027	12 39 55.95	+10 10 34.10	SB(r)0+	0.0063	128	43	10.5	40.00
27	NGC 4698	IRAS 12458+0845	12 48 22.91	+08 29 14.58	SA(s)ab	0.0034	64	53	10.7	42.05
28	NGC 4750	IRAS 12483+7308	12 50 07.27	+72 52 28.72	(R)SA(rs)ab	0.0054	129	24	12.1	–
29	NGC 4772	UGC 8021	12 53 29.16	+02 10 06.16	SA(s)a	0.0035	65	62	11.3	–
30	NGC 5077	UGCA 347	13 19 31.67	-12 39 25.07	E3-4	0.0094	188	–	11.7	–
31	NGC 5363	IRAS 13356+0529	13 56 07.21	+05 15 17.18	I0?	0.0038	76	51	10.2	43.09
32	NGC 5746	IRAS 14424+0209	14 44 55.92	+01 57 18.01	SAB(rs)b	0.0058	120	–	10.6	41.75
33	NGC 5813	UGC 9655	15 01 11.23	+01 42 07.13	E1-2	0.0065	138	–	10.5	42.08
34	NGC 5838	IRAS 15029+0217	15 05 26.26	+02 05 57.59	SA0-	0.0045	94	72	10.8	42.51
35	NGC 5957(*)	IRAS 15330+1212	15 35 23.21	+12 02 51.36	(R')SAB(r)b	0.0061	134	–	12.3	–
36	NGC 6482	UGC 11009	17 51 48.81	+23 04 18.99	E	0.0131	296	–	11.3	42.64
37	NGC 7331	IRAS 22347+3409	22 37 04.01	+34 24 55.87	SA(s)b	0.0038	80	72	9.4	41.76
38	NGC 7743	IRAS 23417+0939	23 44 21.14	+09 56 02.69	(R)SB(s)0+	0.0057	138	32	12.4	<42.86
39	IC 1459	IRAS 22544-3643	22 57 10.61	-36 27 44.00	E3-4	0.0060	131	–	10.5	–
40	NGC 0315	UGC 00597	00 57 48.88	+30 21 08.81	E+	0.0165	370	52	11.6	43.30
41	NGC 0404	IRAS 01066+3527	01 09 27.02	+35 43 05.27	SA0(s)	-0.0002	-	–	10.6	–
42	NGC 1052	IRAS 02386-0828	02 41 04.80	-08 15 20.75	E4	0.005	108	–	11.0	42.77
43	NGC 2639	IRAS 08400+5023	08 43 38.08	+50 12 20.00	(R)SA(r)a	0.0111	242	54	11.8	<41.59

Table B.1 Continue.

#	ID	Other name	RA (hh mm ss)	DEC (dd mm ss)	Morphology	z	Scale (pc as^{-1})	i (deg)	V mag	L_{bol} (10^X) (erg s^{-1})
	(1)	(2)	(3)	(4)	(5)	(6)	(7)	(8)	(9)	(10)
44	NGC 2681	IRAS 08499+5130	08 53 32.73	+51 18 49.30	(R)SAB(rs)0/a	0.0023	24	–	10.9	42.58
45	NGC 2787	IRAS 09148+6924	09 19 18.56	+69 12 12.00	SB0+(r)	0.0023	60	51	11.3	<40.34
46	NGC 2841	IRAS 09185+5111	09 22 02.63	+50 58 35.47	SA(r)b	0.0021	49	66	10.2	40.75
47	NGC 3226	ARP 094	10 23 27.01	+19 53 54.68	E2 pec	0.0044	86	–	12.9	42.33
48	NGC 3245	IRAS 10244+2845	10 27 18.39	+28 30 26.56	SA0^0(r)	0.0044	90	58	10.8	42.29
49	NGC 3607	UGC 06297	11 16 54.66	+18 03 06.50	SA0^0(s)	0.0031	58	62	10.0	42.07
50	NGC 3623	M 65	11 18 55.96	+13 05 32.00	SAB(rs)a	0.0027	48	77	9.3	<40.91
51	NGC 3627	M 66	11 20 15.03	+12 59 29.58	SAB(s)b	0.0024	42	65	10.3	42.72
52	NGC 3718	ARP 214	11 32 34.85	+53 04 04.52	SB(s)a pec	0.0033	76	62	10.7	–
53	NGC 3998	UGC 06946	11 57 56.13	+55 27 12.92	SA0^0(r)	0.0035	82	34	11.3	42.85
54	NGC 4036	IRAS 11588+6210	12 01 26.75	+61 53 44.81	S0$^-$	0.0046	108	69	10.8	42.43
55	NGC 4111	UGC 07103	12 07 03.13	+43 03 56.59	SA0$^+$(r)	0.0026	59	85	10.8	<41.89
56	NGC 4192	M 98	12 13 48.29	+14 54 01.20	SAB(s)ab	-0.0005	–	78	10.8	–
57	NGC 4314	IRAS 12200+3010	12 22 31.82	+29 53 45.19	SB(rs)a	0.0032	67	27	10.6	<40.63
58	NGC 4374	M 84	12 25 03.74	+12 53 13.14	E1	0.0034	65	–	9.8	42.84
50	NGC 4438	IRAS 12252+1317	12 27 45.59	+13 00 31.78	SA(s)0/a pec	0.0002	–	71	10.9	<42.36
60	NGC 4486	M 87	12 30 49.42	+12 23 28.04	E	0.0043	84	–	9.0	42.35
61	NGC 4552	M 89	12 35 39.81	+12 33 22.83	E0-1	0.0011	17	–	10.1	40.78
62	NGC 4579	M 58	12 37 43.52	+11 49 05.50	SAB(rs)b	0.0051	101	38	10.3	42.70
63	NGC 4594	M 104	12 39 59.43	-11 37 22.99	SA(s)a	0.0034	59	68	8.6	41.50
64	NGC 4636	UGC 07878	12 42 49.83	+02 41 15.99	E0-1	0.0031	57	–	9.9	<40.56
65	NGC 4696	ABELL 3526:BCG	12 48 49.27	-41 18 40.04	cD1 pec	0.0099	193	–	10.3	41.51

Table B.1 Continue.

#	ID	Other name	RA (hh mm ss)	DEC (dd mm ss)	Morphology	z	Scale (pc as^{-1})	i (deg)	V mag	L$_{bol}$ (10^X) (erg s^{-1})
(1)		(2)	(3)	(4)	(5)	(6)	(7)	(8)	(9)	(10)
66	NGC 4736	M 94	12 50 53.06	+41 07 13.65	(R)SA(r)ab	0.0010	25	36	9.5	40.13
67	NGC 5005	IRAS 13086+3719	13 10 56.23	+37 03 33.14	SAB(rs)bc	0.0032	70	63	10.7	<43.16
68	NGC 5055	M 63	13 15 49.33	+42 01 45.40	SA(rs)bc	0.0017	40	56	8.6	41.09
69	NGC 5846	UGC 09706	15 06 29.28	+01 36 20.25	E0-1	0.0057	121	–	10.2	<42.34
70	NGC 5866	M 102	15 06 29.49	+55 45 47.57	SA0+	0.00001	13	68	11.3	41.60

Notes. Columns indicate: (3) RA and (4) DEC: coordinates; (5) Morphology, (6) z and (7) scale distance: from the Local Group from NED; (8) i: inclination angle from Ho et al. (1997a); (9) V magnitude from HyperLeda; and (10) bolometric luminosity estimated from (González-Martín et al. 2009). [*] indicates galaxies observed with high clouds; [†] indicates targets already analysed in Masegosa et al. (2011).

Table B.2 Observing log of HST data.

ID	Instrument	Filename (.fits)	Proposal ID	P.I.	Obs. date (yy-mm-dd)	Exp. time (s)	Filter
(1)	(2)	(3)	(4)	(5)	(6)	(7)	(8)
NGC 3642	ACS/WFC	hst_9788_41_acs_wfc_f658n	9788	L. Ho	2003-12-16	700	F658N
	ACS/WFC	hst_9788_41_acs_wfc_f814w	9788	L. Ho	2003-12-16	120	F814W
NGC 4125	WFPC2	hst_11966_15_wfpc2_f658n_wf	11966	M. Regan	2009-01-30	2100	F658N
	WFPC2	hst_06587_23_wfpc2_f555w_wf	6587	D.Richstone	1997-03-15	1400	F555W
NGC 4203	ACS/WFC	hst_9788_72_acs_wfc_f658n	9788	L. Ho	2003-07-18	700	F658N
	ACS/WFC	hst_9788_72_acs_wfc_f814w	9788	L. Ho	2003-07-18	120	F814W
NGC 4450	WFPC2	hst_11966_18_wfpc2_f658n_wf	11966	M. Regan	2009-01-31	1800	F658N
	WFPC2	hst_05375_04_wfpc2_f555w_wf	5375	V.Rubin	1994-05-09	520	F555W
NGC 4750	ACS/WFC	hst_9788_b4_acs_wfc_f658n	9788	L. Ho	2004-05-20	700	F658N
	ACS/WFC	hst_9788_b4_acs_wfc_f814w	9788	L. Ho	2004-05-20	120	F814W
NGC 7331	WFC3	hst_14202_01_wfc3_uvis_f657n	14202	D.Milisavljevic	2015-08-22	2400	F657N
	WFC3	hst_14202_01_wfc3_uvis_f814w	14202	D.Milisavljevic	2015-08-22	1350	F814W

Notes. Columns indicate: (1) galaxy name; (2) observing instrument; (3) file name of the image as indicated in the archive; (4) proposal ID of the observations; (5) Principal Investigator of the proposal; (6) date of the observation; (7) exposure time; (8) filter used, also from the HST archive.

Table B.3 Observing log of ALFOSC/NOT data.

Observing campaign (1)	Observing date (yy-mm-dd) (2)	Observed galaxies (3)	Exposure time NF-BF (s) (4)	Airmass (5)	Seeing (6)
GT-Jan2019	2019-01-03	NGC 0841/NGC 2685/NGC 3185/NGC 3884/NGC 4278	1200 (300)	1.01-1.42	0.7″-1.5″
	2019-01-04	NGC 0266/NGC 0410/NGC 3414/NGC 4143	1200 (300)	1.03-1.7	0.6″-1.8″
	2019-01-05	NGC 3507/NGC 4698/NGC 4772	1200 (300)	1.06-1.5	0.7″-1.3″
GT-May2019	2019-05-31	NGC 3628	1200 (300)	1.10-1.30	0.8″-0.9″
	2019-06-01	NGC 5363	1200 (100)	1.09-1.16	0.9″-1.6″
GT-Jan2020	2020-01-25	NGC 3379	1200 (300)	1.04-1.19	0.7″-0.9″
	2020-01-26	NGC 3608/NGC 3945/NGC 4596	1200 (300)	1.07-1.29	0.6″-0.9″
GT-Jun2021	2021-06-11	NGC 4494	1200 (100)	1.18-1.30	0.8″-0.9″
	2021-06-12	NGC 6482	1200 (300)	1.04-1.10	0.8″-1.0″
OT-Mar2020	2020-03-29	NGC 3898/NGC 4321/NGC 4457/NGC 4459 NGC 5746/NGC 5813/NGC 5957	1200 (300)	1.03-1.21	0.6″-1.1″
OT-Jun2020	2020-06-08	NGC 5077	1200 (300)	1.33-1.43	0.7″-0.8″
	2020-06-09	NGC 4589	1200 (300)	1.54-1.70	0.7″-1.0″
Other	2020-11-09	NGC 7743	1200 (100)	1.12-1.39	0.7″-0.8″
	2021-02-15	NGC 4261 & NGC 5838	1200 (100)	1.10-1.42	0.8″-1.1″

Columns indicate: (1) observing campaign; (2) date of the observation; (3) number of galaxies observed ; (4) exposure time for the narrow (broad) filter; (5) range of the airmass; (6) seeing range during the observations.

Appendix C

Additional material from Chapter 4

C.1 Background/foreground emission

To account for the external (background or foreground) emission from sources different from NGC 1052, from the white-light MUSE frame shown in Fig. C.1, we create a 'sharp-divided' image (see Márquez et al. 1999, 2003). This is obtained by dividing the original image by a filtered version of it (generated using the `IRAF` using the command 'median' with a box of 15 pixels per side). In the final sharp-divided image the identification of features departing from axisymmetry is facilitated (see e.g. Cazzoli et al. 2018, Hermosa Muñoz et al. 2020, 2022). Then we used the sharp-divided image as input for the `EXTRACTOR` tool as part of the Graphical Astronomy and Image Analysis (`GAIA`; Draper et al. 2009) package through the `STARLINK` software (Currie et al. 2014) currently supported by the East Asian Observatory. We considered a 4σ threshold, a minimum area of 8 pixels (in order to avoid the inclusion of noise-spikes), and MUSE parameters from the manual (detector gain: 1.1 ADU/e^-, readout noise: $2.6\,e^-$, and saturation $65\,000\,e^-$). With these prescriptions, we generated a catalogue of putative background and foreground objects.

The catalogue is composed of 104 objects (excluding the NGC 1052 nucleus), which are shown in Fig. C.1 in different colours and listed in Table C.1 along with their positions. Of these, 18 (in red in Fig. C.1) are present in the NED database (within less than 3″ from the position measured in the MUSE field) being classified either as 'Infrared source', 'Radio source', 'X-ray Source', 'UltraViolet Source', or 'Star Cluster'.

We visually inspected the spectra of the remaining 85 objects. For the large majority of these spectra (74 out of 85, green symbols in Fig. C.1) the Hα line is clearly visible, either in emission or in absorption, at the same redshift of NGC 1052 (see Table 4.1). Hence, we consider these sources as part of the galaxy. The remaining 11 of the 85 sources are mostly located at the edge of the MUSE field of view with barely detected emission or absorption

lines in their (noisy) spectra. Hence these will be considered as non-detections (yellow symbols in Fig. C.1).

Only in two cases do the spectra show a strong continuum and evident emission-line features, typically of emission-line galaxies. These are ID numbers 1 and 19 in Table C.1, and are marked in cyan in Fig. C.1. Source 1 has a counterpart in NED with identification SDSS-CGB 67616.02, but with no redshift mentioned. In our data the Hα emission is observed at a wavelength of 6761.86 Å, resulting in a redshift measurement of 0.0303. Source 19 is not present in the NED database (within 3″ of its measured position). The Hα emission peaks at 7999.09 Å, hence the redshift is ~0.2189. The spectra of both galaxies are shown in Fig. C.2, along with an example of the spectrum of a source having Hα in emission or absorption at the same redshift as NGC 1052, for comparison.

The emission from the two external galaxies was masked out from the final MUSE datacube used for the analysis, whereas that of sources at the same redshift of NGC 1052 were included.
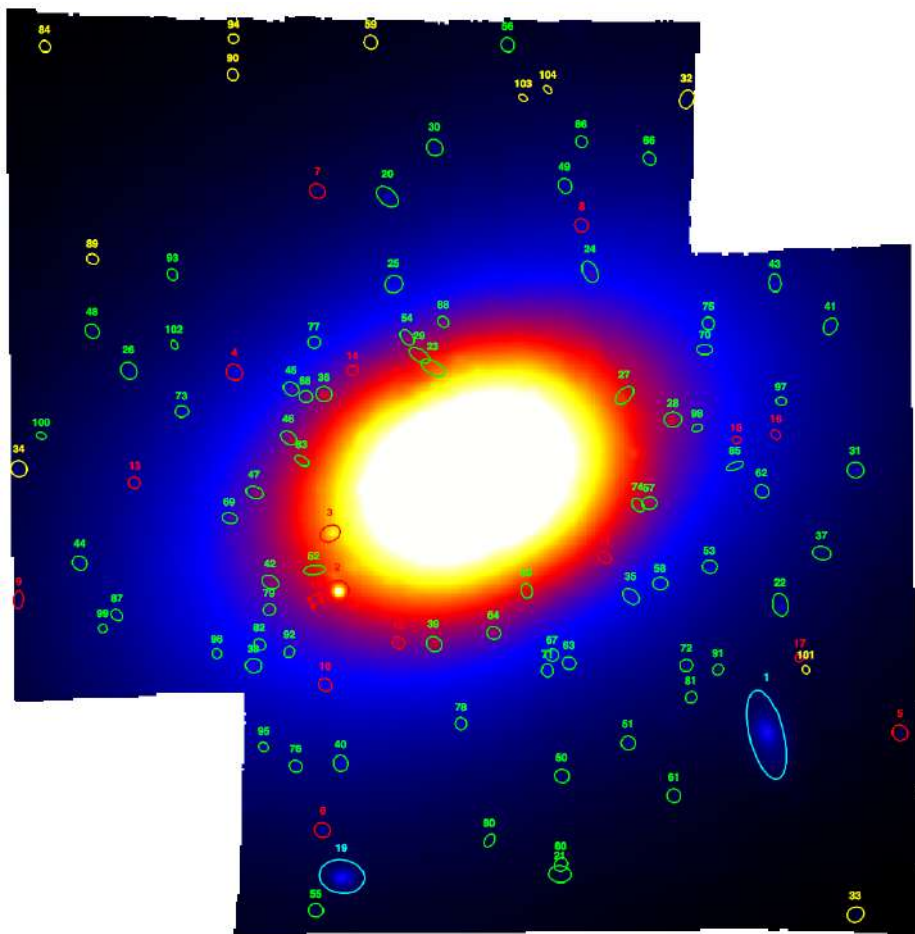
Fig. C.1 White light image of NGC 1052 from MUSE datacube. The different symbols indicate the sources listed in Table C.1. See text for the colour-coding.
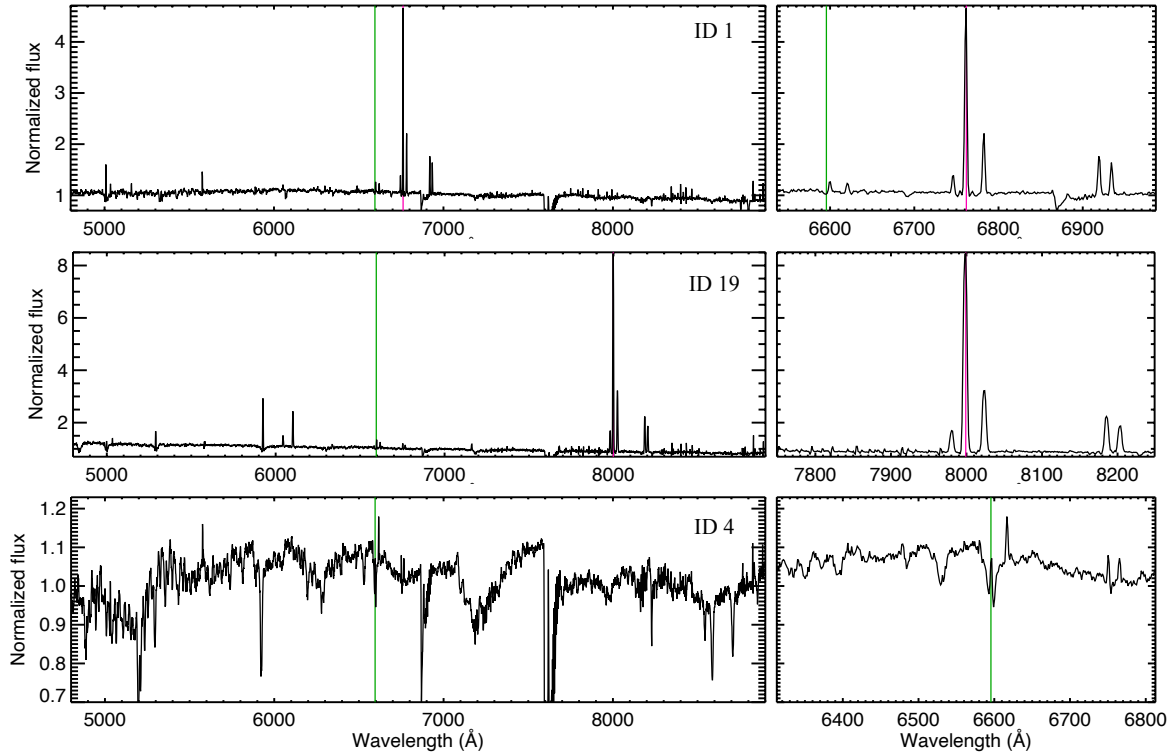
Fig. C.2 Spectra of the objects with ID numbers 1, 19, and 4 from Table C.1 (see also Fig. C.1). The right panel shows a zoomed-in view of the spectra region around Hα. The green lines indicate the wavelength of Hα at the redshift of NGC 1052 (z = 0.005, Table 4.1). The magenta lines in the first and second panels indicate the wavelength of Hα at the corresponding redshift (see text for details).

Table C.1 Coordinates of the sources in Fig. C.1.

ID	RA	DEC	ID	RA	DEC
1	$02^h41^m02^s.928$	$-08^d15^m43^s.83$	53	$02^h41^m03^s.276$	$-08^d15^m28^s.56$
2	$02^h41^m05^s.558$	$-08^d15^m30^s.79$	54	$02^h41^m05^s.130$	$-08^d15^m07^s.72$
3	$02^h41^m05^s.601$	$-08^d15^m25^s.56$	55	$02^h41^m05^s.689$	$-08^d15^m59^s.77$
4	$02^h41^m06^s.188$	$-08^d15^m10^s.90$	56	$02^h41^m04^s.546$	$-08^d14^m40^s.81$
5	$02^h41^m02^s.112$	$-08^d15^m43^s.65$	57	$02^h41^m03^s.646$	$-08^d15^m22^s.78$
6	$02^h41^m05^s.649$	$-08^d15^m52^s.50$	58	$02^h41^m03^s.579$	$-08^d15^m30^s.09$
7	$02^h41^m05^s.680$	$-08^d14^m54^s.42$	59	$02^h41^m05^s.370$	$-08^d14^m39^s.94$
8	$02^h41^m04^s.063$	$-08^d14^m57^s.53$	60	$02^h41^m04^s.187$	$-08^d15^m55^s.61$
9	$02^h41^m07^s.527$	$-08^d15^m31^s.64$	61	$02^h41^m03^s.496$	$-08^d15^m49^s.37$
10	$02^h41^m05^s.631$	$-08^d15^m39^s.31$	62	$02^h41^m02^s.957$	$-08^d15^m21^s.70$
11	$02^h41^m03^s.922$	$-08^d15^m27^s.70$	63	$02^h41^m04^s.139$	$-08^d15^m37^s.31$

Table C.1 Continue.

ID	RA	DEC	ID	RA	DEC
12	$02^h41^m05^s.184$	$-08^d15^m35^s.46$	64	$02^h41^m04^s.599$	$-08^d15^m34^s.58$
13	$02^h41^m06^s.801$	$-08^d15^m20^s.94$	65	$02^h41^m04^s.398$	$-08^d15^m30^s.73$
14	$02^h41^m05^s.465$	$-08^d15^m10^s.73$	66	$02^h41^m03^s.645$	$-08^d14^m51^s.49$
15	$02^h41^m05^s.694$	$-08^d15^m31^s.53$	67	$02^h41^m04^s.243$	$-08^d15^m36^s.59$
16	$02^h41^m02^s.874$	$-08^d15^m16^s.55$	68	$02^h41^m05^s.750$	$-08^d15^m13^s.10$
17	$02^h41^m02^s.729$	$-08^d15^m36^s.84$	69	$02^h41^m06^s.217$	$-08^d15^m24^s.14$
18	$02^h41^m03^s.114$	$-08^d15^m17^s.05$	70	$02^h41^m03^s.308$	$-08^d15^m08^s.82$
19	$02^h41^m05^s.529$	$-08^d15^m56^s.71$	71	$02^h41^m04^s.270$	$-08^d15^m37^s.98$
20	$02^h41^m05^s.251$	$-08^d14^m54^s.93$	72	$02^h41^m03^s.421$	$-08^d15^m37^s.51$
21	$02^h41^m04^s.194$	$-08^d15^m56^s.50$	73	$02^h41^m06^s.510$	$-08^d15^m14^s.44$
22	$02^h41^m02^s.843$	$-08^d15^m32^s.02$	74	$02^h41^m03^s.715$	$-08^d15^m22^s.96$
23	$02^h41^m04^s.973$	$-08^d15^m10^s.48$	75	$02^h41^m03^s.285$	$-08^d15^m06^s.45$
24	$02^h41^m04^s.011$	$-08^d15^m01^s.75$	76	$02^h41^m05^s.813$	$-08^d15^m46^s.69$
25	$02^h41^m05^s.211$	$-08^d15^m02^s.88$	77	$02^h41^m05^s.699$	$-08^d15^m08^s.16$
26	$02^h41^m06^s.835$	$-08^d15^m10^s.75$	78	$02^h41^m04^s.801$	$-08^d15^m42^s.82$
27	$02^h41^m03^s.800$	$-08^d15^m13^s.00$	79	$02^h41^m05^s.974$	$-08^d15^m32^s.48$
28	$02^h41^m03^s.503$	$-08^d15^m15^s.19$	80	$02^h41^m04^s.625$	$-08^d15^m53^s.43$
29	$02^h41^m05^s.054$	$-08^d15^m09^s.35$	81	$02^h41^m03^s.391$	$-08^d15^m40^s.44$
30	$02^h41^m04^s.963$	$-08^d14^m50^s.46$	82	$02^h41^m06^s.033$	$-08^d15^m35^s.63$
31	$02^h41^m02^s.383$	$-08^d15^m19^s.77$	83	$02^h41^m05^s.773$	$-08^d15^m18^s.93$
32	$02^h41^m03^s.417$	$-08^d14^m46^s.06$	84	$02^h41^m07^s.348$	$-08^d14^m41^s.28$
33	$02^h41^m02^s.384$	$-08^d16^m00^s.15$	85	$02^h41^m03^s.123$	$-08^d15^m19^s.40$
34	$02^h41^m07^s.524$	$-08^d15^m19^s.67$	86	$02^h41^m04^s.062$	$-08^d14^m49^s.94$
35	$02^h41^m03^s.759$	$-08^d15^m31^s.27$	87	$02^h41^m06^s.908$	$-08^d15^m32^s.94$
36	$02^h41^m05^s.640$	$-08^d15^m12^s.88$	88	$02^h41^m04^s.909$	$-08^d15^m06^s.31$
37	$02^h41^m02^s.590$	$-08^d15^m27^s.32$	89	$02^h41^m07^s.055$	$-08^d15^m00^s.61$
38	$02^h41^m06^s.070$	$-08^d15^m37^s.54$	90	$02^h41^m06^s.197$	$-08^d14^m43^s.84$
39	$02^h41^m04^s.966$	$-08^d15^m35^s.60$	91	$02^h41^m03^s.227$	$-08^d15^m37^s.91$
40	$02^h41^m05^s.537$	$-08^d15^m46^s.41$	92	$02^h41^m05^s.853$	$-08^d15^m36^s.28$
41	$02^h41^m02^s.538$	$-08^d15^m06^s.70$	93	$02^h41^m06^s.567$	$-08^d15^m02^s.00$
42	$02^h41^m05^s.969$	$-08^d15^m29^s.96$	94	$02^h41^m06^s.193$	$-08^d14^m40^s.57$
43	$02^h41^m02^s.878$	$-08^d15^m02^s.77$	95	$02^h41^m06^s.010$	$-08^d15^m44^s.94$
44	$02^h41^m07^s.135$	$-08^d15^m28^s.21$	96	$02^h41^m06^s.295$	$-08^d15^m36^s.44$
45	$02^h41^m05^s.840$	$-08^d15^m12^s.39$	97	$02^h41^m02^s.838$	$-08^d15^m13^s.51$

Table C.1 Continue.

ID	RA	DEC	ID	RA	DEC
46	$02^h41^m05^s.855$	$-08^d15^m16^s.83$	98	$02^h41^m03^s.354$	$-08^d15^m15^s.93$
47	$02^h41^m06^s.065$	$-08^d15^m21^s.81$	99	$02^h41^m06^s.994$	$-08^d15^m34^s.16$
48	$02^h41^m07^s.059$	$-08^d15^m07^s.15$	100	$02^h41^m07^s.370$	$-08^d15^m16^s.66$
49	$02^h41^m04^s.164$	$-08^d14^m53^s.94$	101	$02^h41^m02^s.688$	$-08^d15^m37^s.91$
50	$02^h41^m04^s.181$	$-08^d15^m47^s.57$	102	$02^h41^m06^s.556$	$-08^d15^m08^s.38$
51	$02^h41^m03^s.776$	$-08^d15^m44^s.57$	103	$02^h41^m04^s.420$	$-08^d14^m45^s.94$
52	$02^h41^m05^s.698$	$-08^d15^m28^s.87$	104	$02^h41^m04^s.269$	$-08^d14^m45^s.20$

Notes. 'ID' indicates the sources numbered in Fig. C.1. 'RA' and 'DEC' are the coordinates from MUSE data.

C.2   Spectral maps

The first part of this appendix is devoted to presenting the ionised gas velocity, velocity dispersion, and flux maps for NGC 1052 from MUSE and MEGARA data, for the two spatially resolved components detected (Sect. 4.4). In the second part, we show maps for the line ratios of the standard diagnostic diagrams used to pinpoint the ionisation mechanisms of the ISM gas in NGC 1052.

As for the figures in the main text, north is at the top and east to the left in all the panels. The centre (0,0) is identified with the photometric centre (see Fig. 4.1). The black solid line indicates the major axis of the stellar rotation (i.e. 122°, Table 4.2). The dot-dashed square indicates the MEGARA field of view, as in Fig. 4.8.

Flux intensity maps are in units of $\mathrm{erg\,s^{-1}\,cm^{-2}}$ and mJy for MUSE and MEGARA, respectively, and are displayed in logarithmic scale. Line fluxes are not converted to a common unit as we are mainly interested in the analysis of line ratios and we do not compare directly the line fluxes of the two data sets (e.g. due to differences in spatial resolution).
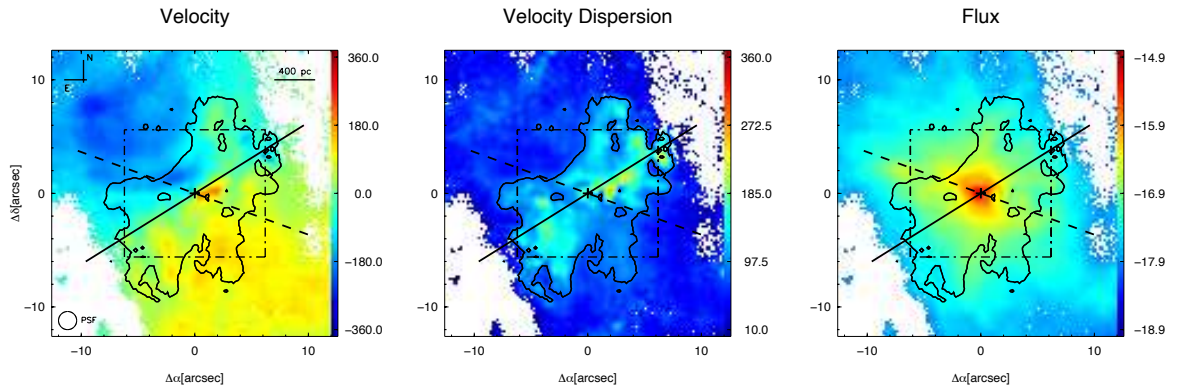
Fig. C.3 [O III]5007Å velocity field (km s^{-1}), velocity dispersion (km s^{-1}), and flux intensity (erg s^{-1} cm^{-2}) maps for the narrow component. The maps are as in the lower panel of Fig. 4.5, and are included here as reference. The black solid line indicates the major axis of the stellar rotation (Table 4.2). The dashed lines indicate the orientation of the radio jet (Table 4.1).
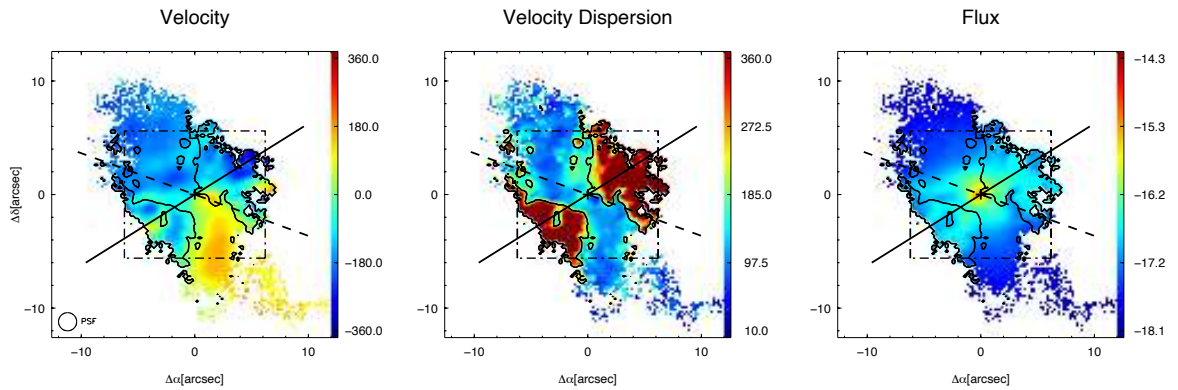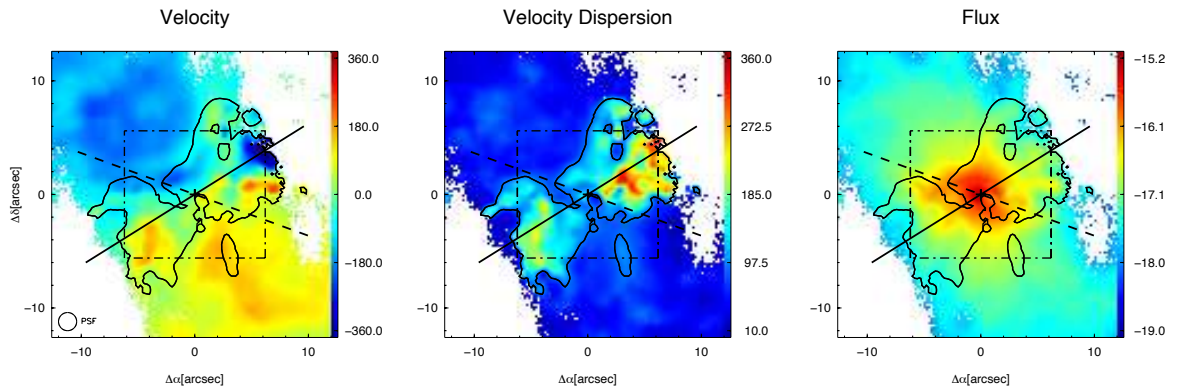

Fig. C.4 As in Fig. C.3, but for [OI]λ6300.

Fig. C.5 As in Fig. C.3, but for Hα.
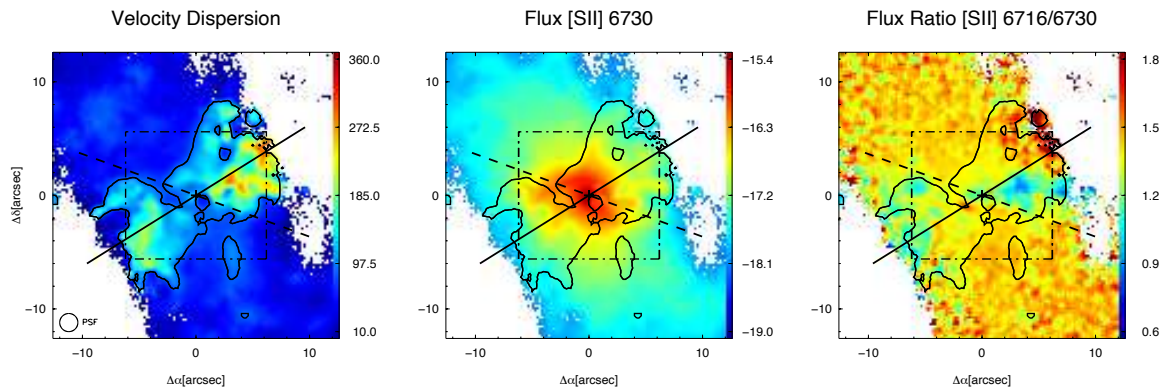
Fig. C.6 Maps of velocity dispersion and flux for the [S II]λ6730 line, and the [S II] flux ratio for the primary component. The lines, symbols, and contours are as in Fig. C.3.
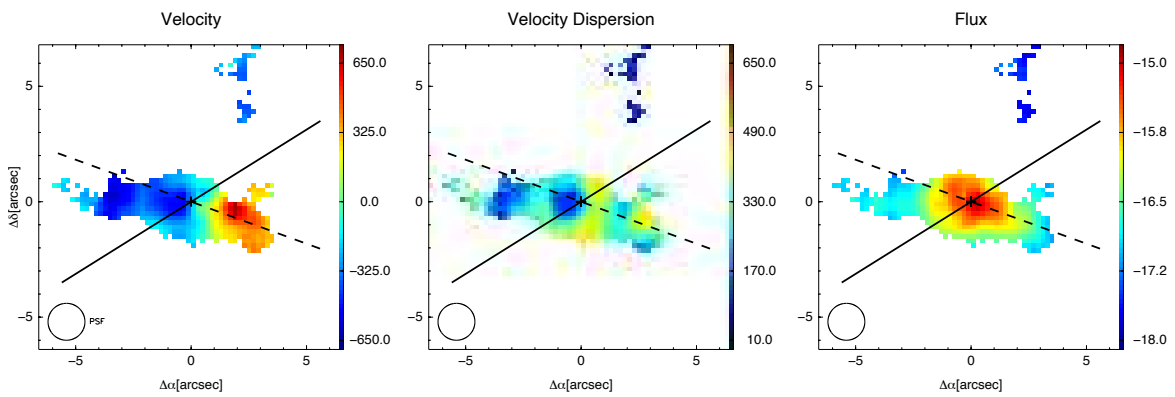
Fig. C.7 As in Fig. C.3, but for the second component and for a smaller field of view (similar to the MEGARA footprint).
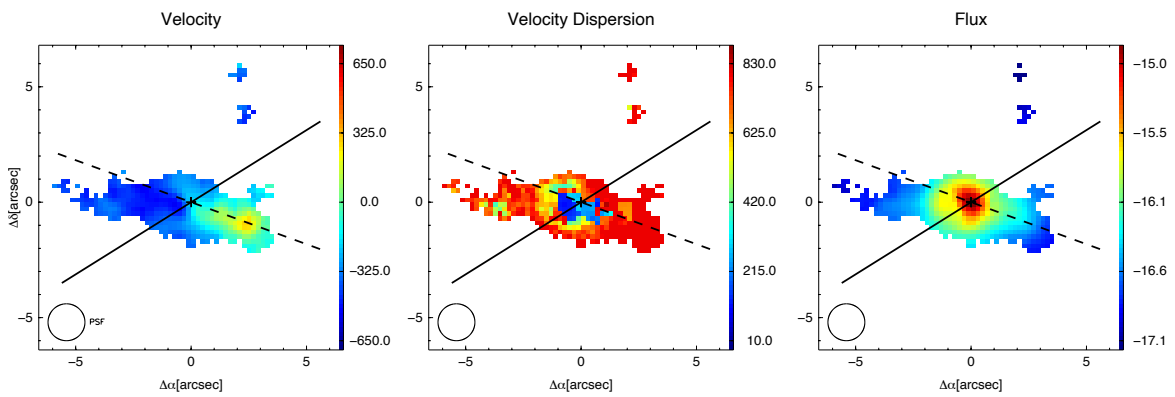
Fig. C.8 As in Fig. C.7, but for [OI]λ6300.
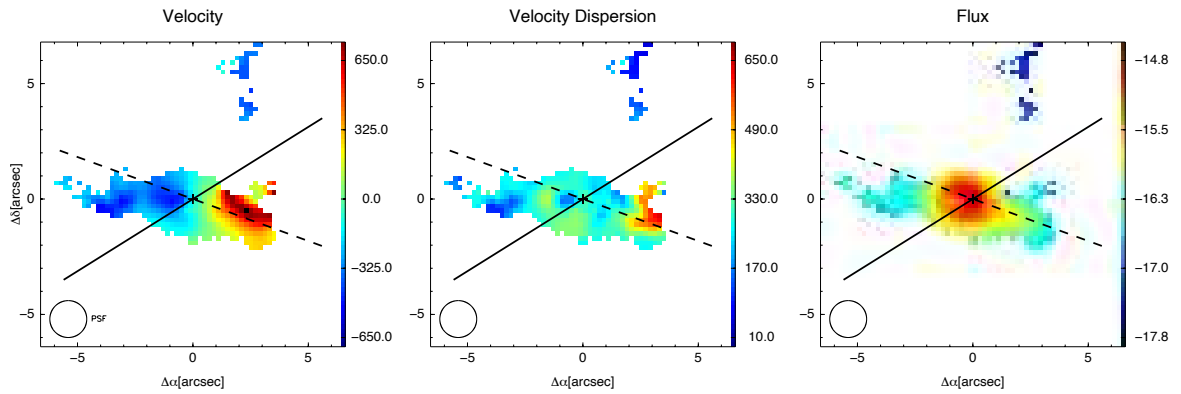
Fig. C.9 As in Fig. C.7, but for Hα.
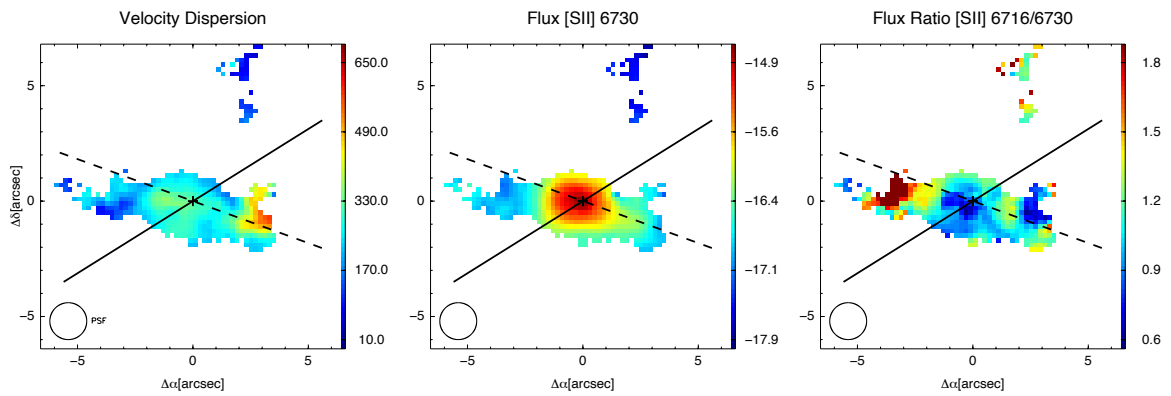
Fig. C.10 As in Fig. C.6, but for the second component and for a smaller field of view (similar to the MEGARA footprint, see Fig. C.7).
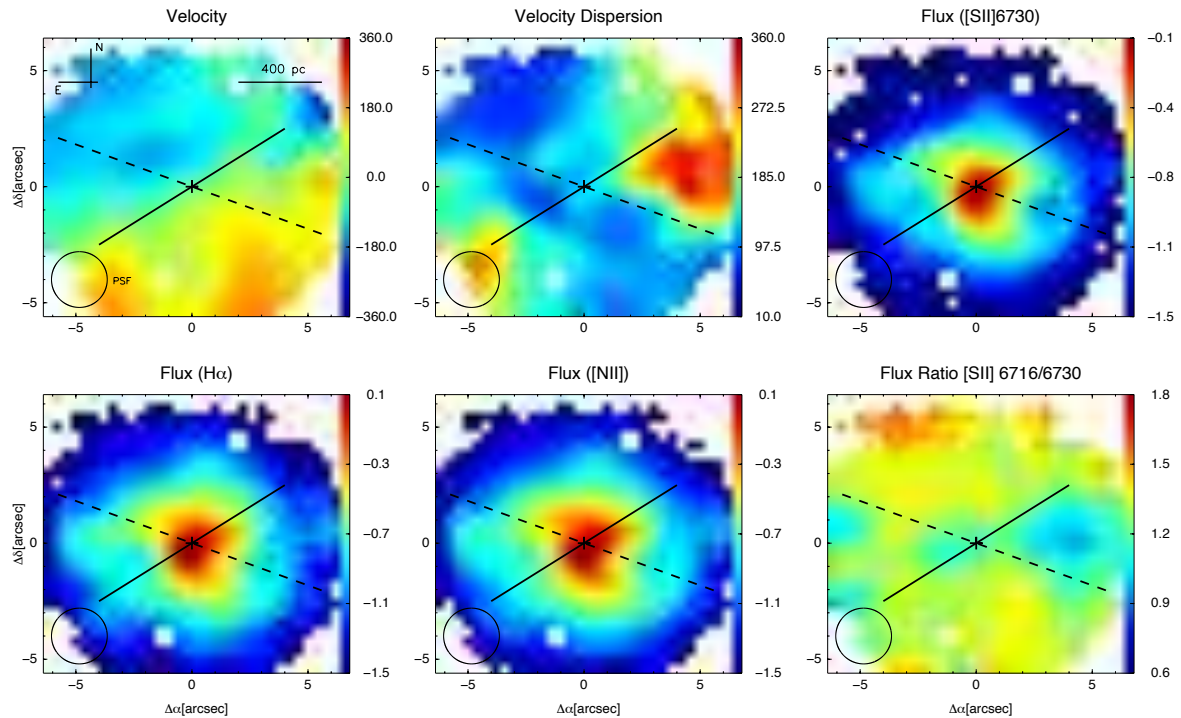
Fig. C.11 Maps of velocity, velocity dispersion, and flux maps for the narrow component from the MEGARA cube. The flux maps correspond to the lines tied together, e.g. the [S II] doublet and Hα-[N II] complex, see Sect. 4.3.3. The lines and symbols are as in Fig. C.3.
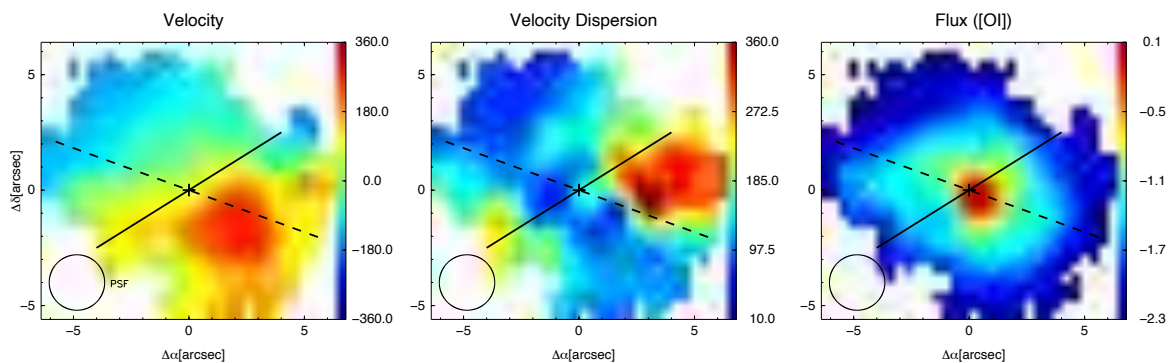
Fig. C.12 Same as Fig.C.11, but for [O I]. This line has been modelled separately from [S II] (see Sect. 4.3.3).
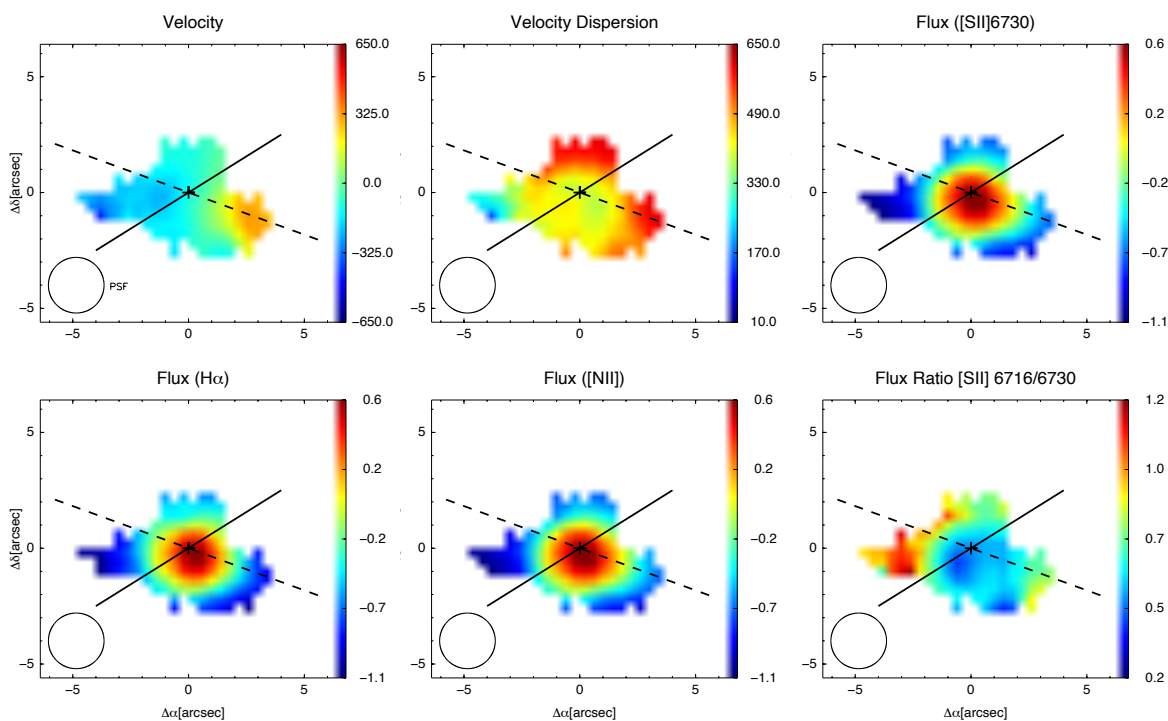
Fig. C.13 As in Fig. C.11, but for the second component.
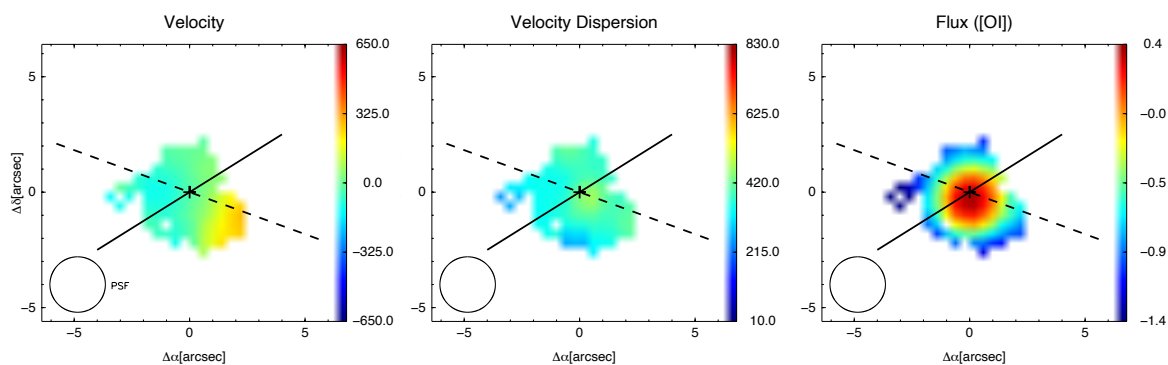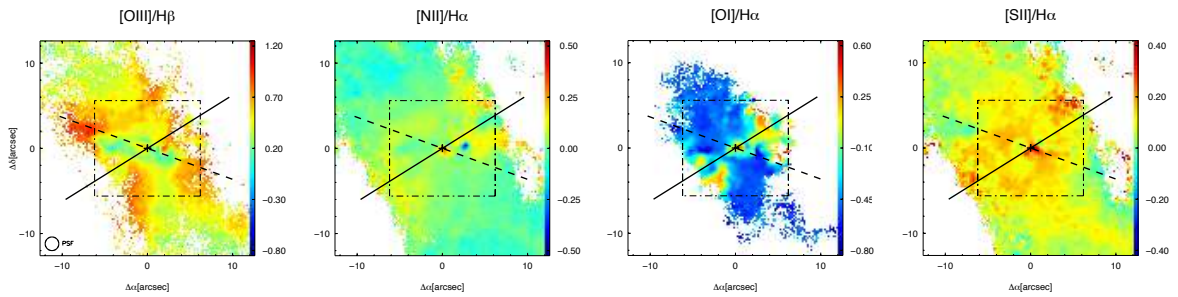

Fig. C.14 As in Fig. C.13, but for the [O I] line.

Fig. C.15 Maps of the standard BPT line ratios (labelled at the top) for the narrow component (see also Fig. 4.6). The lines are as in Fig. C.3.
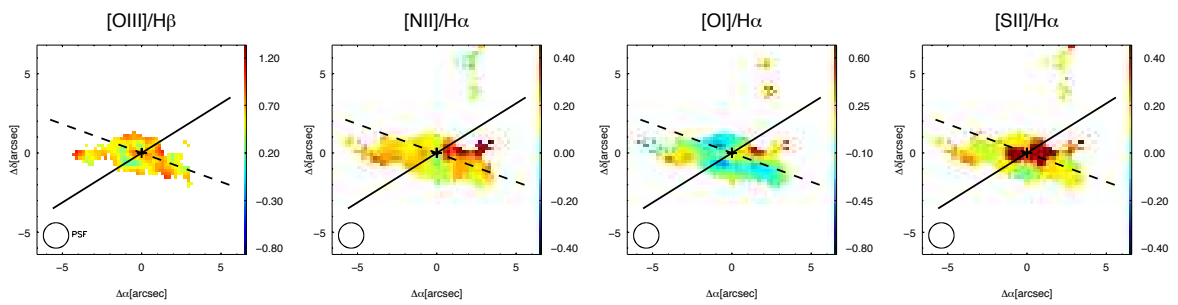

Fig. C.16 As in Fig. C.15, but for the second component and for a smaller field of view (similar to the MEGARA footprint, see e.g Fig. C.7).
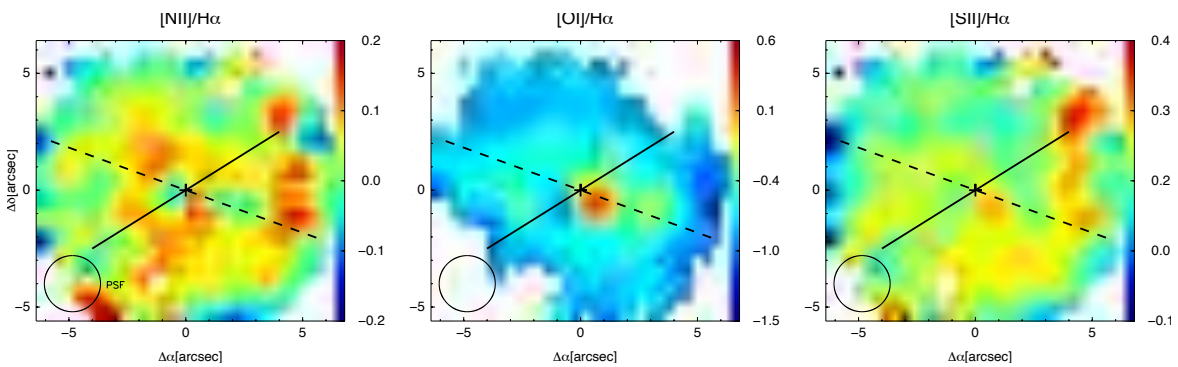

Fig. C.17 Maps of the standard BPT line ratios (labelled on the top) for the narrow component. The lines are as in Fig. C.3.
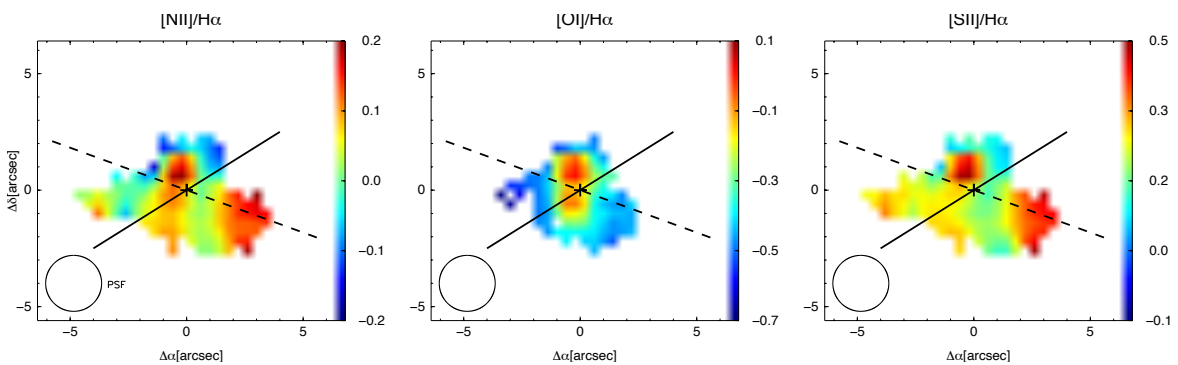

Fig. C.18 As in Fig. C.17, but for the second component. The long-dashed line gives the PA of the 20 cm emission (Table 4.1), as in Fig. C.7.

C.3 Position-velocity and position-dispersion diagrams

This appendix is devoted to the present position-velocity (P-V, top) and position-dispersion (P-σ, bottom) for the primary component used to model the emission lines in NGC 1052 (MUSE data).

Both diagrams suggest that the kinematics of the stars is completely decoupled from that of the ionised gas. The stellar P-V and P-σ curves show a clear signature of a rotating disc, whereas this is not the case for the gas component. Specifically, along both major and minor photometric axis (left and centre panels) the ionised gas shows a very perturbed P-V curve as well as an asymmetric and not centrally peaked P-σ curve.

The curves extracted from the slit aligned according to the radio jet do not show any intriguing features.
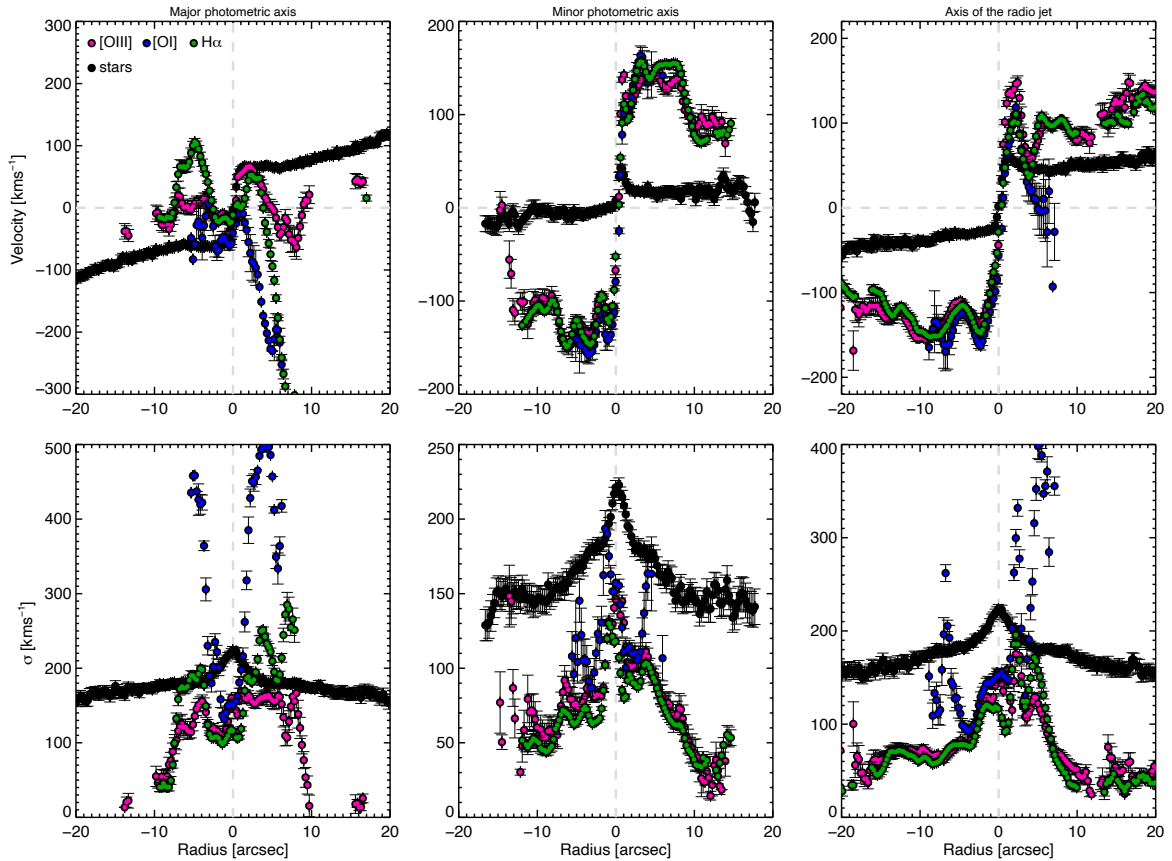
Fig. C.19 Position-velocity (P-V, top) and position-dispersion (P-σ, bottom) curves of the stellar (black) and gas component of NGC 1052 from the MUSE data. Specifically, the gas component is probed via the [O III] (magenta), [O I] (blue), and H α (green) emission lines. Similarly to Fig. 4.11 the curves were obtained considering a pseudo-slit 1″ in width aligned according to the major (left) and minor (centre) axis of the rotation, as well as the axis of the radio jet (right). The position angles are listed in Tables 4.1 and 4.2. Velocities are centred to the kinematic centre, and the radius is calculated as the distance from the photometric centre. The grey dashed lines show zero points for position and velocity, as reference.